Vol. 47, No. 2, 2026

Chemical and Process Engineering: New Frontiers

PAN
POLSKA AKADEMIA NAUK

Polish Academy of Sciences

Commitee of Chemical and Process Engineering

ISSN 2300-1925

Vol. 47 No. 2 2026

Chemical and Process Engineering: New Frontiers

Polish Academy of Sciences
Committee of Chemical and Process Engineering

Editorial Team

Editor-in-Chief
Andrzej I. Stankiewicz
Delft University of Technology, Netherlands
Warsaw University of Technology, Poland

Executive Editor
Paweł Sobieszuk
Warsaw University of Technology, Poland

Technical Editor
Barbara Zakrzewska
West Pomeranian University of Technology, Szczecin, Poland

Language Editor
Marek Stelmaszczyk
West Pomeranian University of Technology, Szczecin, Poland

Editorial Office

ul. Waryńskiego 1
00-645 Warszawa
Poland

email: office.cpe@pw.edu.pl

Typesetting in LATEX:
Drukarnia Braci Grodzickich Sp. j.
Hiacyntowa 31, 05-077 Warszawa

Chemical and Process Engineering: New Frontiers, 2026, 47(2), e129
DOI: 10.24425/cpe.2026.158127

Conversion of hydrogen to ammonia as a method of increasing energy density – a simulation study

Michalina Miller[1], Karol P. Nowacki[1], Maciej Kopiński[1], Michał Zmyślony[1], Alicja Wasilewska[1], Piotr T. Mitkowski[2], Szymon Woziwodzki*[2]

[1] Poznań University of Technology, Chemical Engineering Research Club, ul. Berdychowo 4, 61-131 Poznań, Poland.
[2] Poznań University of Technology, Faculty of Chemical Technology, Institute of Chemical Technology and Engineering, ul. Berdychowo 4, 61-131 Poznań, Poland.

*** Corresponding author, e-mail:**
szymon.woziwodzki@put.poznan.pl

Presented at
5th Seminar on Practical Aspects of Chemical Engineering PAIC 2025, 22–23 September 2025, Zaniemyśl, Poland.
Guest Editors: Andżelika Krupińska and Sylwia Włodarczak.

Article info:
Received: 13 January 2026
Revised: 20 February 2026
Accepted: 24 April 2026

Abstract
In light of the current efforts of harnessing hydrogen as a potential carbon free energy source alternative to fossil fuels, ammonia has emerged as one of the possible candidates for an effective hydrogen storage method, due to its significantly simplified storage conditions. In this work, the Haber-Bosch process for ammonia synthesis was studied for three scales of production, in the aspect of energy efficient reactor design and optimal operational conditions, with the use of a process simulator, allowing for the manipulation of desired plant parameters in a wide range of values. Moreover, the energy balance of the process has been included in the research process allowing for the visualization of energetic cost of increasing the energy density of the system. The obtained data provides a basis for analysing the Haber-Bosch process in the context of ammonia conversion for hydrogen storage.

Keywords
energy density, ammonia synthesis, hydrogen storage, process simulation

1. INTRODUCTION

Ammonia has remained as one of the most important chemicals produced worldwide, owing to its key role in the manufacture of nitrogen fertilizers and, more recently, as a hydrogen and energy carrier. The global annual production of ammonia exceeds 200 Mt/year and relies almost exclusively on the Haber–Bosch process. This process consumes 1–2% of the world's total energy supply and 3–5% of global natural gas production (de la Hera et al., 2024). The associated CO_2 emissions are estimated at nearly 400 Mt/year. At such a large global production scale, even small relative improvements in process efficiency or carbon intensity translate into substantial absolute benefits. This makes the Haber-Bosch process an attractive subject for systematic simulation-based studies and justifies a critical review of existing modelling work across different production scales.

2. BACKGROUND AND LITERATURE REVIEW

This chapter summarises the current state of knowledge on the conversion of hydrogen to ammonia as a solution aimed at increasing the useful energy density of the system in energy storage and transport applications. The overview is organised into five subsections, which lead from a systemic perspective on the role of ammonia in energy systems and the power-to-ammonia concept, through a reference to the industrial starting point of the Haber–Bosch process as a reference system and contemporary downscaling trends, to aspects key to simulation analyses: reactor and synthesis loop modelling, operating dynamics, and quantitative assessment of energy consumption and energy parameters in consistent kWh/kg NH_3 units.

2.1. Power-to-ammonia in energy systems

Ammonia is currently being analysed as an energy vector and part of the electricity-to-fuel/storage medium conversion chain in the power-to-ammonia concept, rather than solely as a chemical product (Jabarivelisdeh et al., 2022; Smith et al., 2020). This approach links NH_3 synthesis to the energy and emission balance of the entire system, in which the variability of energy supply (e.g. from renewable energy sources) forces the process to be evaluated under dynamic conditions and partial loads (Fahr et al., 2025; Smith et al., 2020; Verlysen et al., 2021). Small-scale energy-oriented analyses show that in P2A (Power to ammonia) it is crucial to break down energy consumption into stages (H_2 production, N_2 production, synthesis loop) and to assess the efficiency-flexibility-unit cost trade-off (de la Hera et al., 2024; Lin et al., 2020). From an implementation perspective, it is also important to determine the safe operating range and flexibility constraints resulting from the apparatus and thermodynamics of the Haber–Bosch loop (Cheema and Krewer, 2018; Fahr et al., 2025).

© 2026. The Author(s). This is an open-access article distributed under the terms of the Creative Commons Attribution (CC-BY 4.0, https://creativecommons.org/licenses/by/4.0/), which permits unrestricted use, distribution, and reproduction in any medium, provided the original author and source are credited.

2.2. Haber–Bosch: reference and downscaling

Classic large-scale installations serve as a reference system for assessing the energy efficiency, stability and maturity of technological solutions, as illustrated by the description of a large scale installation based on proven technology (Rüther et al., 2005). In this approach, the synthesis loop (compression, multi-bed reactor, recirculation, NH_3 separation) is treated as a reference system for loss analysis, optimisation and control solution design (Araújo and Skogestad, 2008; Flórez-Orrego and de Oliveira Junior, 2017; Luyben, 2012). At the same time, pressure to integrate with non-stationary energy generation and to lower investment barriers is driving research towards small scale, modularity and continuous operation as a design paradigm for installations adapted to distributed power supply (Garrote, 2020; Seifert et al., 2012). In this trend, techno-economic and energy analyses of small-scale methods based on Haber-Bosch technology point to a change in the cost and energy structure and to sensitivity to the choice of loop configuration and operating conditions (de la Hera et al., 2024; Lin et al., 2020). At the same time, concepts for process intensification are being developed as a 'bridge' between the classic system and distributed production, in which the reorganisation of heat exchange and the densification of equipment have the potential to reduce scale limitations (Garrote, 2020; Spatolisano and Pellegrini, 2023).

2.3. Reactor and synthesis loop: modelling and dynamics

Modelling based on differential equations forms the basis for describing the synthesis reactor and the entire loop, from stationary models to dynamic and optimisation analyses (Amin et al., 2013; Dashti et al., 2006; Flórez-Orrego and de Oliveira Junior, 2017). Reactor models (most often similar to Plug Flow Reactor – PFR with heterogeneous kinetics) allow quantitative investigation of the influence of temperature, pressure and composition on conversion and on temperature distributions determining cooling requirements (Amin et al., 2013; Dashti et al., 2006; Shamiri and Aliabadi, 2021). An exergetic approach to modelling and optimising industrial units allows the identification of loss locations and the interpretation of limitations to energy efficiency improvements (Flórez-Orrego and de Oliveira Junior, 2017).

In industrial practice, a 3-bed reactor is commonly used, in which the exothermicity of the equilibrium reaction requires controlled heat removal between the beds, which ensures that the temperature is maintained within the catalyst activity window and limits the decrease in thermodynamic drive (Luyben, 2012; Rüther et al., 2005). 3-bed configurations differ primarily in the method of heat removal: interstage cooling using inter-bed exchangers or cooling by injecting cold gas (quench) between the beds (Luyben, 2012; Rosbo et al., 2023). Comparisons of reactor configurations in terms of cooling methods indicate that the method of heat removal affects the temperature distribution in the beds, conversion and intensification potential (Khademi and Sabbaghi, 2017). Design and control analyses of the cooled reactor show a strong coupling between temperature profile, chemical equilibrium and operational stability, making heat removal a critical degree of design freedom (Luyben, 2012; Shamiri and Aliabadi, 2021).

Flexible operation of the Haber–Bosch loop requires dynamic tools, as the process is non-linear and prone to instability phenomena (Morud and Skogestad, 1998; Verlysen et al., 2021). Reactor instability mechanisms and their consequences for the selection of controlled variables are a classic starting point for designing synthesis loop control structures (Araújo and Skogestad, 2008; Morud and Skogestad, 1998). In P2A terms, dynamic sensitivity analysis and stabilisation strategies (including for a quench reactor) indicate that the selection of operating trajectories, equipment limitations and anti-surge requirements affect the achievable load range and transient responses (Rosbo et al., 2023; Verlysen et al., 2021). Dynamic simulations of high load flexibility installations show that power consumption and loop conditions vary with load, and the ability to reduce pressure and compression power depends on the operating strategies adopted (Fahr et al., 2025). Determining the safe operating area for P2A designs formalises the operating constraints that determine the acceptable range of parameters and system stability (Cheema and Krewer, 2018).

2.4. H_2 to NH_3 conversion: energy and energy density (kWh/kg NH_3)

In analysing the increase in 'system energy density' through H_2 to NH_3 conversion, it is crucial to distinguish between the energy chemically stored in NH_3 and the energy expenditure of conversion throughout the P2A chain (Jabarivelisdeh et al., 2022; Smith et al., 2020). Smith et al. (2020) assume a lower limit for the energy 'contained' in the carrier equal to the Lower Heating Value (LHV) of ammonia, 5.17 kWh/kg NH_3. Jabarivelisdeh et al. (2022) use an energy value of 5.75 kWh/kg NH_3 for the product for their production pathway comparisons (Jabarivelisdeh et al., 2022). Smith et al. (2020) also give the LHV energy of the stoichiometric amount of hydrogen needed to produce 1 kg NH_3 as 5.92 kWh/kg NH_3, which is the reference point for the energy balance of the conversion.

The energy cost of conversion in an electrified chain strongly depends on the stage of H_2 production, as confirmed by literature balances (Lin et al., 2020; Smith et al., 2020). For the electrolysis-based variant (60% efficiency). Smith et al. (2020) report a total energy demand of 10.61 kWh/kg NH_3, of which 9.86 kWh/kg NH_3 is accounted for by H_2 production and approximately 0.75 kWh/kg NH_3 by N_2 separation and compression in the synthesis loop (Smith et al., 2020). In the same study, the reference ranges for best available techniques (BAT) are 7.61–8.83 kWh/kg NH_3, which allows P2A assessments to be set against industrial energy benchmarks (Smith et al., 2020).

On a small scale, Lin et al. (2020) report total energy consumption of 9.36–9.70 kWh/kg NH_3 for the all-electric configuration, with energy attributed to the synthesis loop alone of 0.37–0.71 kWh/kg NH_3, which explicitly separates the energy cost of NH_3 production from the cost of the Haber–Bosch part. For the reference large-scale case based on SMR, Lin et al. (2020) report a total consumption of 8.89 kWh/kg NH_3, and an energy consumption of the synthesis loop alone of 1.28 kWh/kg NH_3, which serves as a reference point for scale and configuration comparisons.

De la Hera et al. (2024) present small-scale energy simulations directly in P2A logic, reporting a total consumption of 214–217 kWh/kmol NH_3, which corresponds to 12.57–12.74 kWh/kg NH_3 after conversion. The authors also provide a share distribution of energy consumption, which is dominated by electrolysis (e.g. $\sim$ 80.6%), with a significant share attributable to H_2 synthesis ($\sim$ 18.6%) and N_2 production having a marginal share ($\sim$ 0.818%), which supports the analysis of the energy expenditure structure in P2A (de la Hera et al., 2024).

2.5. Summary of the literature collection

The literature review forms a coherent chain of argumentation: systemic and energy-emission studies place P2A in the context of energy balance and the role of NH_3 as a carrier (Jabarivelisdeh et al., 2022; Smith et al., 2020), while classic large-scale technology provides a reference system for design and control solutions (Araújo and Skogestad, 2008; Rüther et al., 2005) Development trends towards small scale, modularity and intensification require an assessment of the flexibility-energy trade-off (de la Hera et al., 2024; Garrote, 2020; Lin et al., 2020; Seifert et al., 2012; Spatolisano and Pellegrini, 2023). The methodological core remains reactor and loop modelling (stationary and dynamic) and operational stability analysis, which determine whether energy consumption reduction is achievable in the real P2A operating area (Amin et al., 2013; Cheema and Krewer, 2018; Dashti et al., 2006; Fahr et al., 2025; Flórez-Orrego and de Oliveira Junior, 2017; Khademi and Sabbaghi, 2017; Luyben, 2012; Morud and Skogestad, 1998; Rosbo et al., 2023; Shamiri and Aliabadi, 2021; Verlysen et al., 2021).

This study analysed simulation performance under operating conditions such as ammonia production intensity, including simultaneous changes in key process variables such as reactor pressure, ammonia concentration in the recirculation/feed stream, H_2 to N_2 molar ratio, total feed mass flow rate, and reactor inlet temperature, while tracking energy consumption consistently across the entire operating range.

In addition, special case studies were conducted on changes in parameters such as reactor pressure, ammonia concentration in the feed loop, H_2 to N_2 molar ratio, total feed mass, and reactor inlet temperature, and the results obtained were compared with those reported in the literature for all operating ranges.

Table 1 presents selected production scale values. Lin et al. (2020) analyzed two conceptual variants of the process. In two configurations, a high-pressure reactor operating at 200 bar was used, and the product was separated by condensation (RXN–CON system, i.e. reactor–condenser). In the variant by (Lin et al., 2020), on the other hand, the reactor operates under low pressure (8 bar), and the product is obtained in liquid form through absorption. In contrast, in Garrote (2020) production was divided into four scales: 75%, 50% and 25% of the nominal production of 45540 kg/h of ammonia. A multi-tube reactor was used in each of them, with 250, 200, 150, and 100 tubes, respectively, depending on the scale of production.

Table 1. Scope of literature overview on ammonia synthesis using the Haber–Bosch process.

Order ID	Source	Method	Reactor type	NH_3 production, kg/h
1	Spatolisano and Pellegrini, 2023	AS	3BR–AIIC	9350
2	Rosbo et al., 2023	MM	3BR–AQCR	4031
3	Shamiri and Aliabadi, 2021	MM	3BR–AQCR	20083
4	Verlysen et al., 2021	AS	FR–1	80
5a	Garrote, 2020	AS	FR–250	45540
5b	Garrote, 2020	AS	FR–200	34155
5c	Garrote, 2020	AS	FR–150	22770
5d	Garrote, 2020	AS	FR–100	11385
6a	Lin et al., 2020	AS	3BR–AQCR	2284
6b	Lin et al., 2020	AS	3BR–AQCR	2428
7	Cheema and Krewer, 2018	MM	3BR–AQCR	100
8	Flórez-Orrego and Oliveira, 2017	AS	3BR–AIIC	41667
9	Luyben, 2012	AS	3BR–AQCR	71053
10	Araújo and Skogestad, 2008	AS	3BR–AQCR	70958

Abbreviations: AS – Aspen simulation; MM – mathematical model; FR–x – flow reactor, where x is number of tubes; 3BR – 3-bed reactor; AQCR – adiabatic quench cooled reactor; AIIC – adiabatic indirect intercooling.

3. SIMULATION MODELS AND METHODS

In this project, AVEVA Process Simulation is used to model ammonia synthesis. The first step, before beginning work on the simulation, was a selection of suitable thermodynamic model for the considered conditions and substances. A preliminary selection was made, leaving only models that were not limited by high temperatures (350–500°C) and pressures (150–250 bar) of the Haber Bosch process. A particularly important

part of the simulation that is highly dependent on the chosen model is the product separation through condensation, as then the system functions in the vapour-liquid equilibrium (VLE). Two chosen thermodynamic models: Soave–Redlich–Kwong (SRK) and Soave–Redlich–Kwong Modified Panagiotopoulos–Reid (SRKM), were compared to the experimental data of VLE equilibrium of a three component, NH_3–H_2–N_2 system with considered ammonia concentrations (10% and 20%) (Michels et al., 1950). The results have been shown in Figure 1.

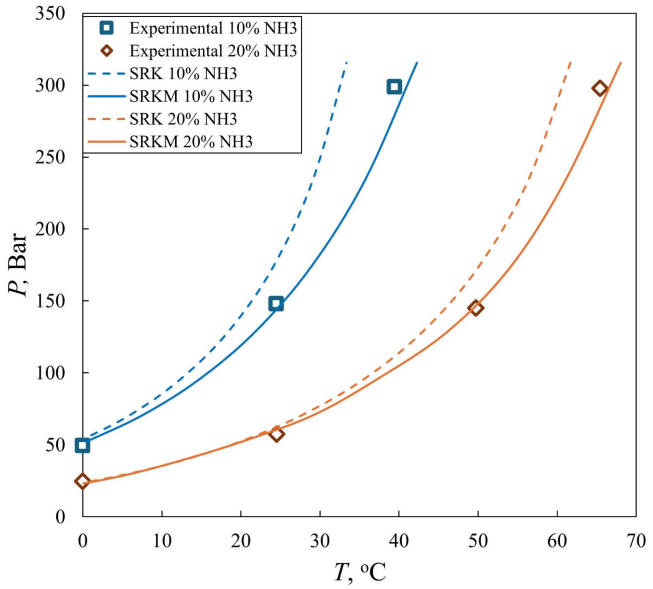


Figure 1. Comparison of experimental data (Michels et al., 1950) and two thermodynamic models (SRK, SRKM) for two ammonia concentrations as a PT curve.

Based on the data presented in Figure 1, the SRKM model has proven to be a better candidate for the considered process. The model improves the accuracy of predictions for strongly asymmetric mixtures of polar and nonpolar components compared to the SRK model, by using an asymmetric mixing rule (AVEVA™ Process Simulation, 2025). The model is described by Eq. (1):

$$P = \frac{RT}{V-b} - \frac{a(T)}{V(V+b)} \tag{1}$$

where a and b are parameters specific to the considered system, defined by Eq. (2) and Eq. (3) respectively:

$$b = \sum_i x_i \frac{0.08664 R T_{c,i}}{P_{c,i}} \tag{2}$$

$$a(T) = \sum_i \sum_j x_i x_j a_{ij} \tag{3}$$

The prepared simulation has been split into 3 sub-flowsheets using the *Flag* model. This solution has several benefits, it is used not only to improve the convergence of recycles through iterative sequential updates, rather than by solving it simultaneously, but it also makes the simulation clearer, splitting it visually into smaller subsections. The considered subsections are: Feed preparation, Reactor, and Condensation and Recycle, which have been discussed in further detail in their own sections.

3.1. Feed preparation

In the prepared simulation, the AVEVA naming convention has been utilized. Each element was given a name according to the formula: A_B, where A is the subsection code: S – substrate preparation section, R – reaction section, M – main condensation and recycle section, and B is the name of the model: S – stream, XV – valve, V – drum, K – compressor, HDR – junction, R – reactor bed, E – heat exchanger.

Figure 2 depicts the first part of the simulation involving the compression and heating of the substrates before their mixing.

The hydrogen and nitrogen feeds are correlated with the molar ratio expressed by Eq. (4):

$$R_{H_2/N_2} = \frac{F_{S_H_2}}{F_{S_N_2}} \tag{4}$$

where $F_{S_H_2}$ and $F_{S_N_2}$ are the molar streams of hydrogen and nitrogen, respectively. This approach has several advantages. The equation allows hydrogen mass flow to be the only variable necessary for analysing the capacity of the installation. Additionally, the R_{H_2/N_2} coefficient in the equation was used as a changing parameter in the following case studies to demonstrate the influence of the ratio of the hydrogen and nitrogen flow on the selected observed parameters. The value of the coefficient has been chosen based on the stoichiometry of the reaction, Eq. (5), with slight positive and negative deviations in the case study, i.e. varying between 2.8 and 3.2:

$$3H_2 + N_2 \leftrightarrow 2NH_3 \tag{5}$$

$$\Delta H = -46.2 \left[\frac{\text{kJ}}{\text{mol}_{NH_3}}\right] \tag{6}$$

The hydrogen source in the simulation had no impurities and the studied mass flow rates in the simulation were chosen and tuned based on the desired product flow rate. The ammonia synthesis process is sensitive to impurities that are present in air like oxygen or carbon oxides. The impact of impurities on the process was not the focus of this work. That is why the nitrogen source consisted of 100% pure nitrogen.

Both substrates are firstly inserted into buffer tanks through valves that are used to calculate the pressure drop. Next, a series of compressors (S_K1-3) heighten the pressure of the gases to the desired amount, i.e. 200 bar. For the hydrogen stream, an additional heat exchanger S_E1 is also needed as an in-between cooling step. The gases are then combined in the S_HDR1 junction and the mixture is transported to the next part of the simulation with the use of *Flag 1*, which has been used in order to visually split the simulation into multiple smaller regions, while improving the integrity of numerical calculations.

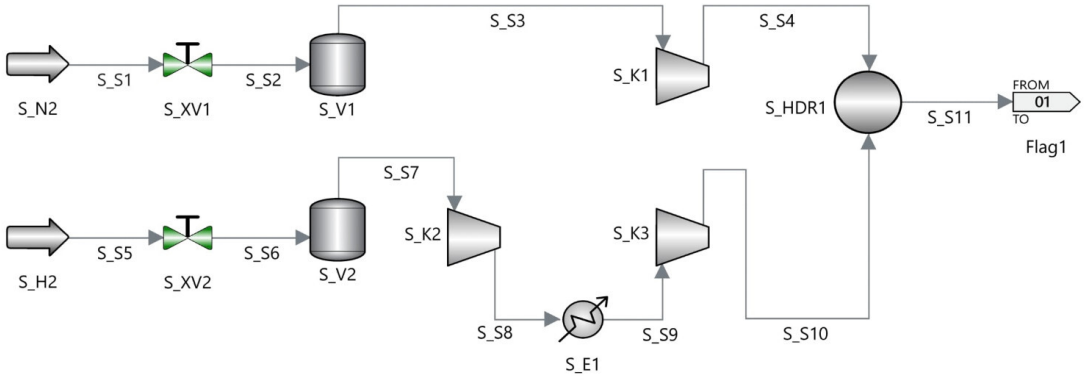


Figure 2. Source section: preparation of the nitrogen and hydrogen streams.

3.2. Reactor

Currently, the standard design solution in ammonia synthesis via the Haber–Bosch process is a three-bed reactor. The catalytic bed is divided into three consecutive reaction sections, separated by cooling zones and by throttling/flow-distribution elements. This architecture enables the temperature to be maintained within limits acceptable for both the catalyst and the equipment, while allowing operation as close as possible to the thermodynamic optimum (a compromise between reaction kinetics and equilibrium constraints). The three-bed configuration constitutes a common starting point both for stability and control analyses of the ammonia converter (Morud and Skogestad, 1998) and for studies aimed at increasing the flexibility and energy efficiency of the Haber–Bosch synthesis loop (Araújo and Skogestad, 2008; Rosbo et al., 2023).

In industrial practice, two dominant approaches to temperature control in three-bed systems are employed. The first, most commonly used, is the AQCR (adiabatic quench cooled reactor) concept, in which interstage cooling is achieved by mixing the hot post-reaction gas with a stream of "cold" synthesis gas (quench) prior to feeding the mixture to the next catalytic bed. The second approach is adiabatic indirect cooling, which involves heat removal in a heat exchanger integrated into the reactor or located externally (external interstage coolers). In both cases, the objective is to limit the temperature rise associated with the strongly exothermic nature of ammonia synthesis and to maintain a favourable temperature profile along successive bed sections.

In this work, Figure 3, the AQCR variant was selected due to its advantageous engineering features: simpler mechanical implementation (no additional heat-exchange equipment in the interstage line), reduced capital expenditures, and lower cooling energy demand owing to the use of a lower-temperature base stream as the quench medium.

For simulation purposes, the three-bed reactor was represented as a series of three tubular reactors (R1–R3) corresponding to the three catalytic-bed sections, with interstage cooling implemented in mixing headers (nodes combining the post-reaction stream with the quench feed). Fresh synthesis gas is supplied from node Flag1 (graphical representation of data from stream S_S11 from the source section in Figure 2) and then mixed in the header with the recycle gas stream Rcy1. In the industrial plant, the start-up heat exchanger is installed upstream of the header to preheat the feed during start-up. This unit was omitted from the simulation flowsheet because, under steady-state operation, its contribution to the overall energy balance is omitted since the required preheating of the mixture upstream of the first bed is provided by the recycle stream, and the calculated heat duty of the start-up exchanger approaches zero.

In the presented simulation, the conversion of substrates to ammonia was kept at around 20%. However, in the literature the conversion values varied between 14.4 % and 30% as reported in Table 2. In an article Cheema and Krewer (2018) reported a conversion rate closer to the higher range of values reaching a result of 24.5%. In the work of Smith et al. (2020), due to the use of a ruthenium (Ru) catalyst (the process temperature is relatively lower, ranging from 573.15 K to 673.15 K). However, in (Shamiri and Aliabadi, 2021), optimisation of the conversion process increased it from 15.24 to 15.45%.

Table 2. Conversion values per one reactor pass reported in literature.

Publication	Conversion [mol. %]	Pressure range [bar]	Temperature range [°C]
de la Hera et al., 2024	14.4–23.8	160–295	350–540
Smith et al., 2020	15	150–250	300–400
Shamiri and Aliabadi, 2021	15.45	87.2	358–466
Cheema and Krewer, 2018	24.5	200	350–500
Jabarivelisdeh et al., 2022	20–30	100–250	350–550

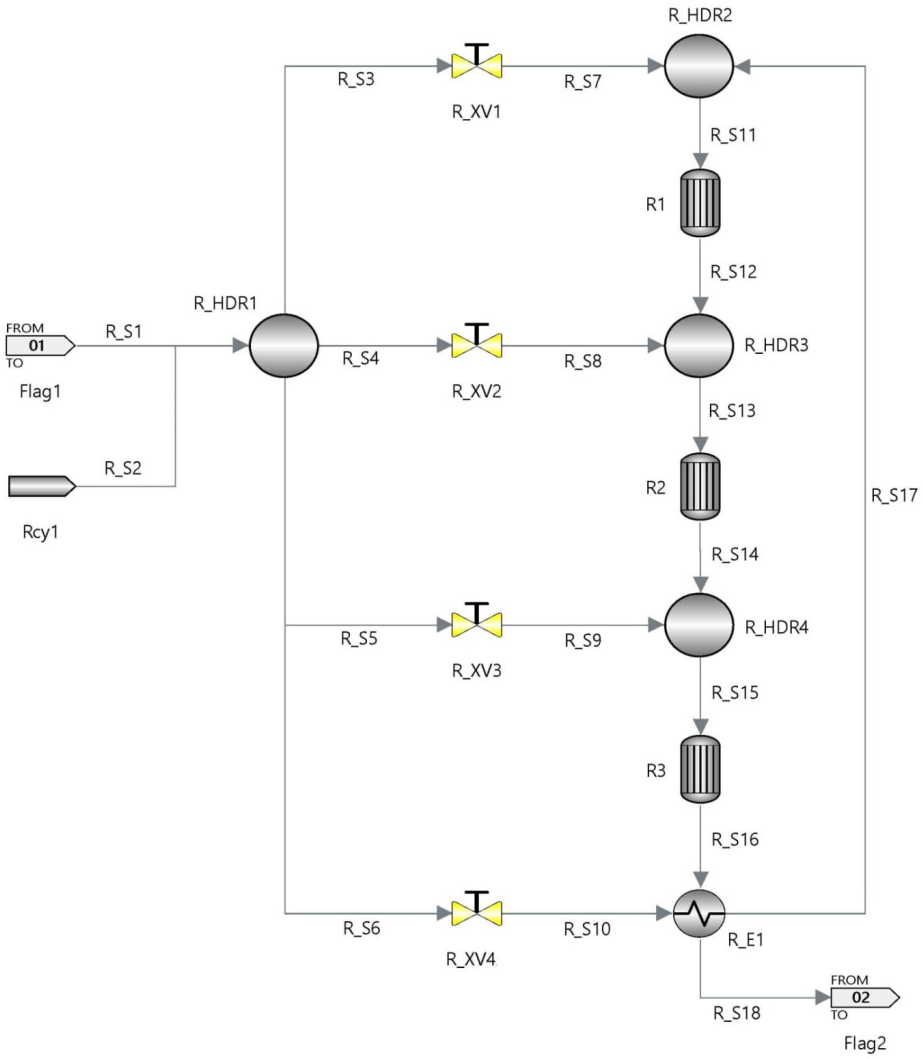


Figure 3. Reaction section: representation of adiabatic quench cooled reactor in process simulator.

An analysis of available models of three-bed ammonia synthesis reactors shows that both industrial and small-scale units employ strictly increasing volumes of consecutive catalyst beds. For reactors with constant diameter, typical volume ratios fall within the ranges: ($V_1/V_3 = 0.35$–0.5) and ($V_2/V_3 = 0.6$–0.7). The reactor sizes reported in the literature along with the production scales have been shown in Table 3.

Based on these observations, a unified, dimensionless description of bed size was adopted in this work, in which the volume of the third bed is used as a reference ($V_3 = 100\%$). The volumes of the other two beds are defined as fixed fractions of V_3:

$$V_1 = 0.35 \cdot V_3 \quad (7)$$

$$V_2 = 0.65 \cdot V_3 \quad (8)$$

The choice of 35–65–100 proportions correspond to the lower bounds of the ranges reported in the literature (Araújo and Skogestad, 2008; Fahr et al., 2025; Lin et al., 2020; Morud and

Table 3. Relative size of catalytic beds.

Source	V_{1BR} [m^3]	V_{2BR} [m^3]	V_{3BR} [m^3]	Ratio of $V_{1BR} : V_{2BR} : V_{3BR}$
Fahr et al., 2025	17.1	27.9	43.4	39:64:100
Shamiri and Aliabadi, 2021	12.7	22	32	40:69:100
Morud and Skogestad, 1998	6.69	9.63	15.2	44:63:100
Araújo and Skogestad, 2008	6.69	9.64	15.2	44:63:100
Rosbo et al., 2023	1.4	2	3.2	43:63:100
Lin et al., 2020 RXN-ABS variant	1	2	3	33:67:100
Lin et al., 2020 RXN-CON variant	0.5	0.7	1	50:70:100

Skogestad, 1998; Rosbo et al., 2023; Shamiri and Aliabadi, 2021) included in Table 3. On the one hand, this preserves consistency with industrial solutions; on the other, it helps to reduce the overall pressure drop while maintaining a large completing volume in the third bed (Dashti et al. 200; Khademi and Sabbaghi 2017; Luyben, 2012; Shamiri and Aliabadi 2021).

Table 4 summarises the adopted values of individual bed volumes for selected reactor configurations.

Table 4. Size of bed's reactor in this work.

Production [t/h]	V_{1BR} [m^3]	V_{2BR} [m^3]	V_{3BR} [m^3]	D [mm]	L/D [m/m]
0.3	0.12	0.23	0.35	500	7.2
11.5	4.76	8.85	13.61	1700	7.1
23	9.09	16.88	25.96	2100	7.1

The smallest production scale considered, 300 kg/h of NH_3, was selected as potentially feasible in a containerised installation, assuming a modular layout and scalability by adding identical modules. The dimensions of the individual beds were determined based on literature data, adopting 35% and 65% of the volume of a three-bed reactor (3BR), respectively. The production level of 23000 kg/h NH_3 was selected – in line with the findings of (de la Hera et al., 2024) – as economically most favourable, whereas 11500 kg/h NH_3 serves as an intermediate scale, linking the container-level installation concept with the largest case under consideration.

3.2.1. Catalyst

The most commonly used catalysts are amorphous materials based on iron with various additives, including K_2O, Al_2O_3, and CaO, several also contained cobalt as one of the dopants (AntenChem, 2025; Syamcat, 2026). The parameters of commercially available ammonia synthesis catalysts are listed in Table 5.

The porosity and grain size of the catalyst are needed for the calculation of pressure drop in the reactor. In the simulation, the Ergun pressure drop model was chosen to calculate the pressure drop ΔP of gas flowing through a catalytic bed. The model is described by the equations:

$$1000 \cdot \Delta P_{\text{elem}} = \left(\frac{150 \cdot \mu \cdot v \cdot (1-\varepsilon)^2}{d_{\text{cat}}^2 \cdot \varepsilon^3} + \frac{1.75 \cdot \rho \cdot v \cdot |v| \cdot (1-\varepsilon)}{d_{\text{cat}} \cdot \varepsilon^3} \right) \cdot L_{\text{elem}} \quad (9)$$

$$v \cdot \rho \cdot \left(\frac{\pi}{4 \cdot D^2} \right) = F \cdot \text{MW} \quad (10)$$

The objective of the aforementioned equations is to calculate the pressure drop of the catalytic bed by summing the calculated pressure drop of each individual submodel. Eq. (9) is the core element and is known as the Ergun equation (Esence et al., 2017). Its result – the pressure drop of the discrete element of the catalytic bed – is the outcome of summing the viscous and inertial terms inside the parentheses. Eq. (10) shows a basic correlation between variables by equating two formulas for mass flow rate, which the program uses to lower the degrees of freedom.

For the simulation, a porosity of 0.45 and a catalyst diameter of 3 mm – the most common value offered by catalyst suppliers (Table 5) – were chosen to calculate the pressure drop. Packing density is a parameter that is heavily dependent on catalyst particle size. It takes on a wide range of values. However, the parameter needed for the calculation of the pressure drop through the Ergun model is particle density, which is why a value of 3500 kg/m^3 was chosen. Operational temperature and pressure are the conditions under which the catalyst is active. They were taken into consideration while planning the flow rates and temperatures of the gases delivered into the reactor. Iron-based ammonia synthesis catalysts are also sensitive to impurities, particularly oxygen and carbon oxides,

Table 5. Parameters of commercially available catalysts used in ammonia synthesis.

Source	Chemical composition	ε [m^3/m^3]	ρ_p [kg/L]	ρ [kg/L]	d_{cat} [mm]	T_o [°C]	p_o [MPa]
Zhulin Carbon, 2010	Fe_3O_4, K_2O, Al_2O_3, CaO, MgO	0.46	2.8–3.0	n.s.	1.5–9.4	500	n.s.
Syamcat, 2026	Fe–Co	0.45	2.4–3.2	n.s.	1.5–13	n.s.	n.s.
AntenChem, 2025	Fe_3O_4, K_2O, Al_2O_3, CaO, Co_3O_4	0.45	2.2–3.0	n.s.	1.5–3.0	n.s.	n.s.
Dengzhuochem, 2025	Fe_3O_4, K_2O, Al_2O_3, CaO	n.s.	2.3–3.2	n.s.	1.5–3.0	350–530	10–40
Stanford Advanced Materials	$Fe_{(1-x)}O$, Al_2O_3, K_2O, CaO	n.s.	3.0–3.4	n.s.	1.5–13	330–500	10–32
Catalystzeolite, 2025	Fe_3O_4	0.46	2.2–2.4	3.5–3.6	1.5–13	350–500	10–31.4

Abbreviations: n.s. – not specified.

which may contaminate the source gas streams. However, the effect of impurities was not the focus of this work, which is why pure nitrogen and hydrogen were chosen as substrates.

3.2.2. Reaction kinetics

The Temkin and Pyzhev model (Temkin and Pyzhev, 1940) was chosen as the model describing the heterogeneous reactions occurring on the surface of the iron catalyst. The model is suited for high-pressure, high-temperature reactions with VLE equilibrium, which are the characteristics of the process that is the focus of this work. The reaction rate of the model is described as the difference between the rate of the ammonia synthesis reaction and the ammonia decomposition reaction, which depend on the partial pressures of the gas mixture components. The denominator of the fractions has been increased by the value of 10^{-5} in order to prevent numerical errors when partial pressures of either ammonia or hydrogen reach the value of zero. The following semi-empirical Eq. (11) shows the method of calculating the reaction rate:

$$r = \frac{k_1 \cdot p_{N_2} \cdot p_{H_2}^{1.5}}{p_{NH_3} + 10^{-5}} - \frac{k_2 \cdot p_{NH_3}}{p_{H_2}^{1.5} + 10^{-5}} \tag{11}$$

The classic Arrhenius equation was used to calculate the reaction rate constants k_1 and k_2. The pre-exponential constant A_i and the activation energy E_i have been chosen according to Table 6:

$$k_i = A_i \cdot \exp\left(-\frac{E_i}{RT}\right) \tag{12}$$

Table 6. Parameters in the Arrhenius equation (AVEVA™ Process Simulation, 2024).

i	A_i	E_i, kJ/mol
1	5	87.3
2	$7.02 \cdot 10^{12}$	200

3.3. Condensation and recycling

Figure 4 shows the section representing the condensation and recycle stream to the reactor section. The process has been described in more detail in Sections 3.3.1 and 3.3.2.

3.3.1. Condensation

The third subsection of the simulation begins with model *Flag2*, importing data from the Reactor sub-simulation described in the previous section. To condense ammonia, the high-pressure cooling method has been chosen, in which the gaseous mixture is cooled down, first in the exchanger M_E1 and later in the drum M_V1. The reaction product is separated from the unreacted gases and uncondensed leftover ammonia at 25 °C. The condensation parameters have been analysed based on phase diagrams of a mixture of ammonia and the unreacted hydrogen and nitrogen with the molar ratios corresponding to the ratios at the outlet of the reactor. Condensation pressure is dictated by the outlet reactor pressure and in the considered process is equal to around 200 bar. During the process of condensation, the ratios between the ingredients of the vapour phase change, as the less volatile ammonia passes into the liquid phase and its molar fraction

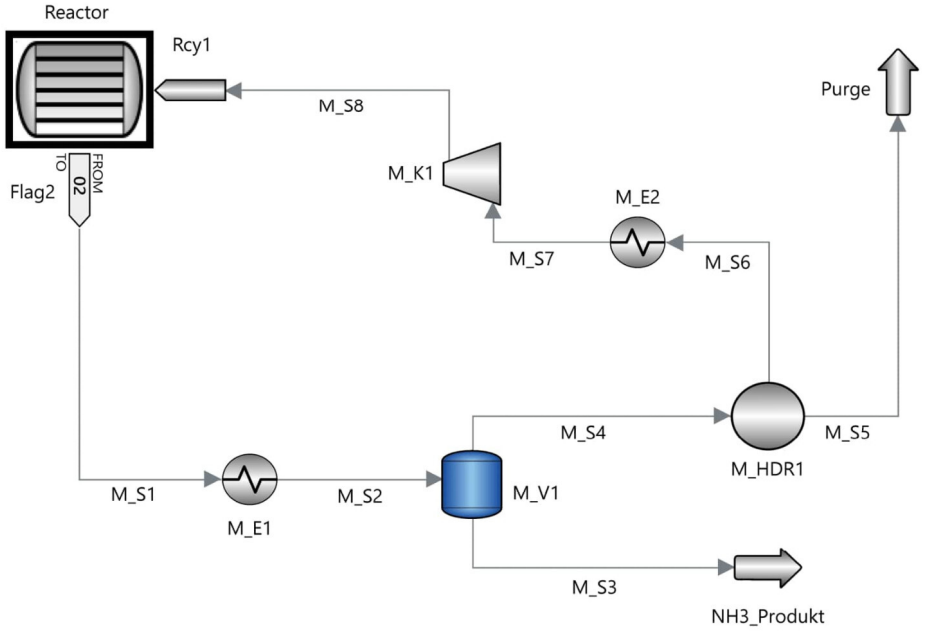


Figure 4. Product condensation and recycling of substrates.

in the vapour phase lowers. This causes the temperature required for condensation to lower as well. Figure 5 shows the Enthalpy – Temperature diagram for mixtures containing 20% (outlet reactor ammonia concentration) of ammonia and stoichiometric ratio of hydrogen and nitrogen.

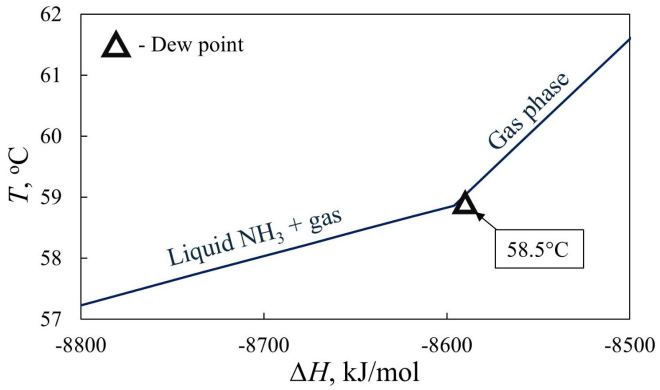


Figure 5. Phase diagram of the mixture with 20% NH_3 in the vapour phase at 200 bar.

An important issue, when it comes to choosing the right condensation conditions is the available cooling media that can be used to lower the system temperature by the required amount. Generally, it is advantageous to use tap water as a cooling medium, as it is widely available and does not need any additional preparation. However this method of cooling is limited with the minimum achievable temperature, which in practice does not go below 20 °C. The obtained liquid is separated from the uncondensed gases and is treated as the product of the installation. The purity of the obtained product is kept around 99%.

3.3.2. Recycle

The remaining stream of gases M_S4 is appropriately prepared and then recycled back into the reactor. The preparation process includes splitting the stream into two parts in the M_HDR1 junction: the main recycled stream M_S6 and the purge stream M_S5, which is discarded to prevent accumulation of unreacted substrates, which unfortunately leads to the unavoidable loss of part of the substrates and product.

The parameter *OutRatio*, expressed by Eq. (13), was defined as the ratio of the purge stream (M_S5) and the recycle stream (M_S4). This parameter was used to control the amount of gases removed from the installation through the purge stream:

$$\text{OutRatio} = \frac{W_{\text{M_S5}}}{W_{\text{M_S4}}} \tag{13}$$

The typical amount of gases discarded into the purge streams oscillates around 1–2% of the primary stream M_S4. The effect of changing this parameter on our simulation has been analysed with the use of a case study. It is important to note that the use of a purge stream can be a cause of environmental and safety concerns, as the gases from the installation could be released into the atmosphere and therefore they should be collected, e.g. in additional storage tanks.

After the stream split, the major portion of the gases is then reheated in the heat exchanger M_E2 and recompressed by the compressor M_K1, to match the parameters of the primary substrate stream flowing into the reactor. Obtaining the right parameters of the recycled gas plays a key role in the functioning of the junction R_HDR1 (see Fig. 3) that introduces the recycled stream back to the reaction section. The pressure and temperature need to be carefully balanced to guarantee the right conditions in the reactor.

4. RESULTS

4.1. Reactor fine-tuning

The considered ammonia synthesis reaction is an exothermic reaction, which causes changes in the temperature distribution within the reactor. This distribution is dependent on the reaction rate on each of the three catalyst beds. Figure 6 shows the temperature gradients over the length of the reactor.

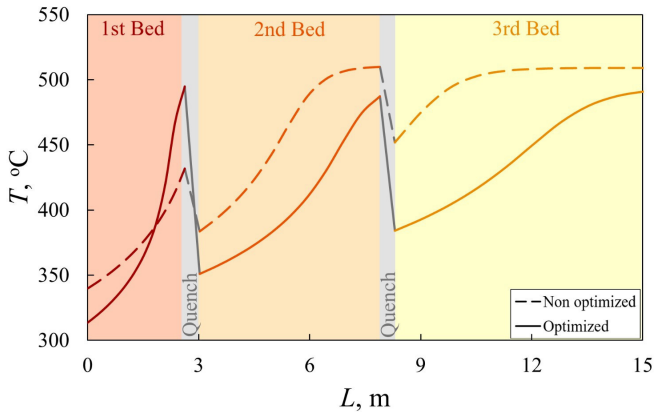


Figure 6. Temperature profile in the reactor for the 23000 kg/h scale.

In order to prevent the decrease of conversion rate while fine-tuning the reactor temperature to keep the catalyst temperature under 500 °C, an optimization tool was used. The tool works by changing several specified variables in predefined ranges as well as keeping observed parameters above or below a given value. The changed variables were: the percentage of the feed stream going through the valves XV1-XV4, controlled by the valve opening degree, as well as the reactor inlet temperature, controlled by the temperature on the junction R_HDR2. During the process, the molar fraction of ammonia in the stream exiting the reactor has been monitored to prevent the drop of reaction rate.

In Figure 6 temperature profiles for reactor before and after the use of the optimization tool have been shown. The procedure was done for all three scales, the results have been shown in Table 7.

Table 7. Comparison of various scales of ammonia production before and after the use of the optimization tool.

Parameter	23000 kg/h NH_3		11500 kg/h NH_3		300 kg/h NH_3	
	before	after	before	after	before	after
Reactor inlet temperature [°C]	340	313.8	340	309.4	340	309.6
R_XV1 [%]	2.34	11.65	11.90	14.92	32.27	15.11
R_XV2 [%]	30	33.81	30	33.96	30	33.93
R_XV3 [%]	30	46.67	30	47.76	30	47.71
R_XV4 [%]	37.66	7.87	28.10	3.37	7.73	3.25
R_S18 y_{NH_3} [mol. %]	18.71	20.87	19.24	20.94	19.24	20.94

4.2. Premises

To analyse the influence of selected variables on the process performance, a case study method has been utilized. Case study allows for automatic changing of specified variables through a range of values, while simultaneously collecting the data of the observed variables. Table 8 summarises the specified and observed parameters that have been analysed through the case study in the built simulation.

Table 8. Summary of the case study.

Case study	Variable 1	Range	Variable 2	Range	Observed parameters
CS1	M_V1.T	20–45 °C	–	–	W_{NH_3} [kg/h], Q [kJ/kg$_{NH_3}$], z_{M_S5} [mol. % NH_3], W_{M_S5} [kg/h]
CS2	OutRatio	1.2–5.2%	R_{H_2/N_2}	2.8–3.2	W_{NH_3} [kg/h], Q [kJ/kg$_{NH_3}$]

4.2.1. Case study 1: Condensation temperature

For the first case study, the impact of changing the condensation temperature was analysed. Temperature ranges (20–45°C) were chosen based on the previously presented H–T phase diagrams (Fig. 5). The case study was done for all three scales. Figure 7 depicts the changes of corrected ammonia stream.

The observed changes of product stream with changing condensation temperature show a clear advantage of using low condensation temperatures. However, the slope of the obtained curve grows as the temperature rises, which might suggest

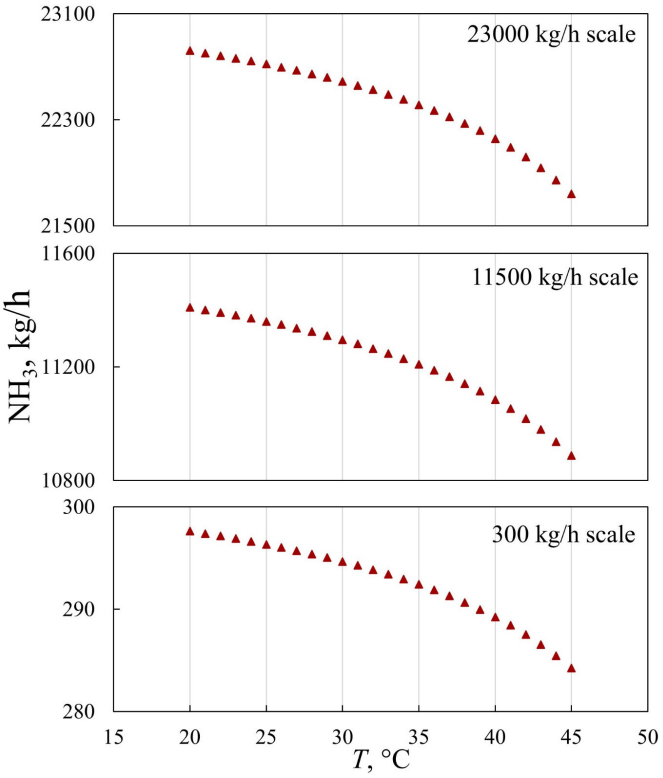


Figure 7. Ammonia flow mass content in the product stream depending on condensation temperature.

a greater tolerance for temperature fluctuations in the lower range of condensation temperatures. Additionally, the case study shows noticeable similarities between the considered scales.

Further analysis has been conducted based on the highest scale of production, as the obtained trends do not differ significantly between the different scales.

Due to the worsening of condensation conditions with growing temperatures, the percentage of leftover ammonia in the vapour phase grows. With the presence of the purge stream, this leads to a higher amount of product loss. Figure 8 depicts the changes in the aforementioned parameters depending on the condensation temperatures.

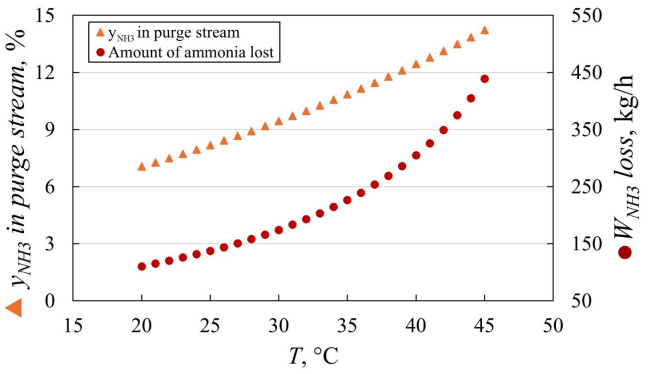


Figure 8. Changes in % of ammonia in the purge stream and loss of product depending on condensation temperature.

The impact of condensation temperature on the energetic requirement of production was analysed next. Figure 9 shows different types of energy demanded by the process per kilogram of produced ammonia: electricity, the heating energy and the cooling energy. Electricity is the energy powering the compressors which increase the pressure of the gases to the desired amount. It is calculated as the sum of the energy usage of all four compressors used in the process. The heating energy is the energy delivered into the system in the heat exchangers heating the gas mixture. It is only used to heat the recycle stream after the condensation step. The cooling energy is the energy taken from the system in the heat exchangers cooling the gas mixture. The heat is taken away by the cooling medium – water. It is used in the substrate preparation step to prevent the temperature of hydrogen from rising too high after its compression, and also in the condensation step, to allow for the separation of the product from the unreacted gases.

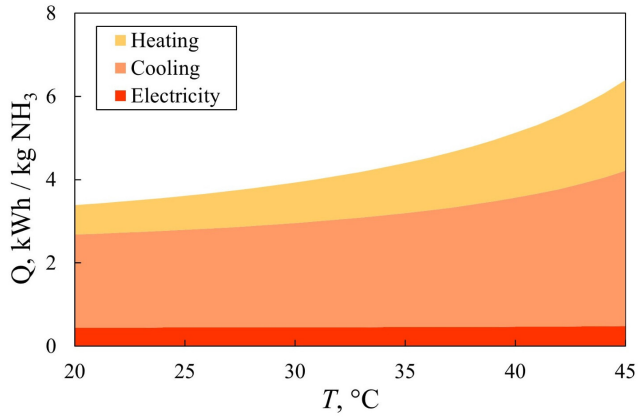


Figure 9. Energy per 1 kg of ammonia produced depending on the condensation temperature.

Based on Figure 9 it can be concluded that lowering the condensation temperature is advantageous from both the production as well as the energetic cost perspective. Both the sum of cooling and heating energies grow with the increase of condensation temperatures. The temperature of 20 °C seems to be the optimal choice, as it improves the efficiency of the process without the need for more expensive cooling media, as it can be achieved by using water as a cooling medium.

4.2.2. Case study 2: Substrate ratio and purge

The following case study shows the impact of changes in the fraction of the purge stream removed from the installation and the ratio of H_2 to N_2 (R_{H_2/N_2}).

The first observed parameter was the ammonia stream. Figure 10 depicts the changes in ammonia stream for the largest scale.

Figure 10 shows clear improvement of ammonia production with lower *OutRatio* and ratio of the substrates around 3. The differences between the results for lowest and highest values of *OutRatio* are quite significant, losing over 2000 kg/h of product. However, the stoichiometry seems to have a lesser impact on the product stream, as even the values for the highest and lowest examined ratios of 3.2 and 2.8 show less than 800 kg/h difference from the highest obtained production at the ratio of 3.

The impact of the change of the studied variables has also been analysed in the context of changing energy requirements per 1 kg of produced ammonia. Figures 11 with 12 show a total of four heatmaps, demonstrating the influence of changing *OutRatio* and stoichiometry on the sum of energy used per 1 kg of ammonia as well as the changes of three types of energy: cooling, heating and electric energy. The total energy, as well as the cooling and heating energy show similar trends, as for all of them, the stoichiometric ratio of 3 shows a clear value decrease. What can also be observed, is that with the increasing *OutRatio*, the results for different stoichiometric ratios seem to be closer in value, which is demonstrated on the heatmaps with a smoother colour gradient. However, when considering the electrical energy used for the compression of the gases, the trend varies significantly from the previous examples, as the energy per 1 kg of ammonia quickly rises with the increase of *OutRatio*, for all considered stoichiometries. However, the electricity used in the process constitutes only a small percentage of the total energy and that is why its influence on the total energy trends is negligible.

4.2.3. Process energy requirement and energy density

In this study, ammonia is treated as an energy carrier in which the energy supplied during the synthesis process is stored in the form of chemical energy. The cumulative enthalpy demand along the entire process pathway, including compression and heat exchange, constitutes a measure of the energy input required to produce this carrier. This approach is complementary to the definition of energy density based on the lower heating value of ammonia, which describes the maximum amount of energy that can be recovered during combustion. Considering both perspectives enables a coherent thermodynamic assessment of ammonia as an energy carrier.

In order to show the thermodynamic impact of the process, changes of the enthalpies of substrates and product streams were analysed, which were the stream enthalpy values (ΔH), molar flow rates (F) and enthalpy streams rate ($\hat{H}$).

Table 9 presents exemplary data for the lowest scale of ammonia production. The domination of negative enthalpy streams in the process is caused by the exothermic nature of the reaction and the heat delivered by the product stream during the condensation step. Due to this, the process, in a thermodynamic sense, leads to the release of energy from the system,

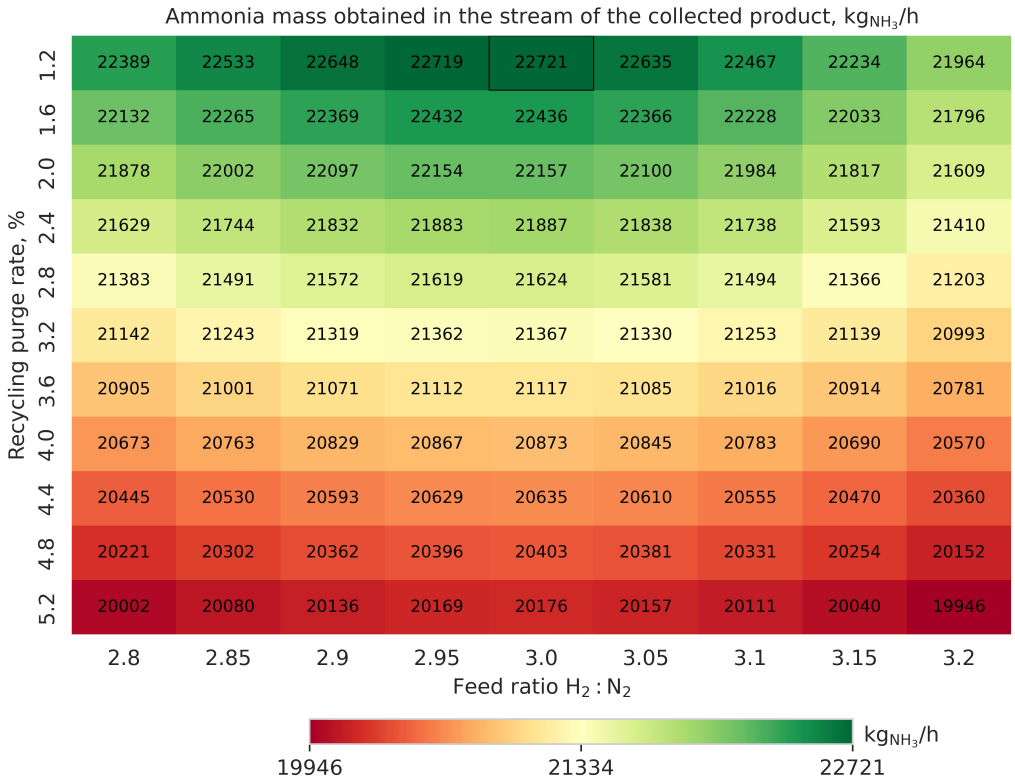


Figure 10. Heat map of ammonia flow mass content in the product stream of the biggest production scale.

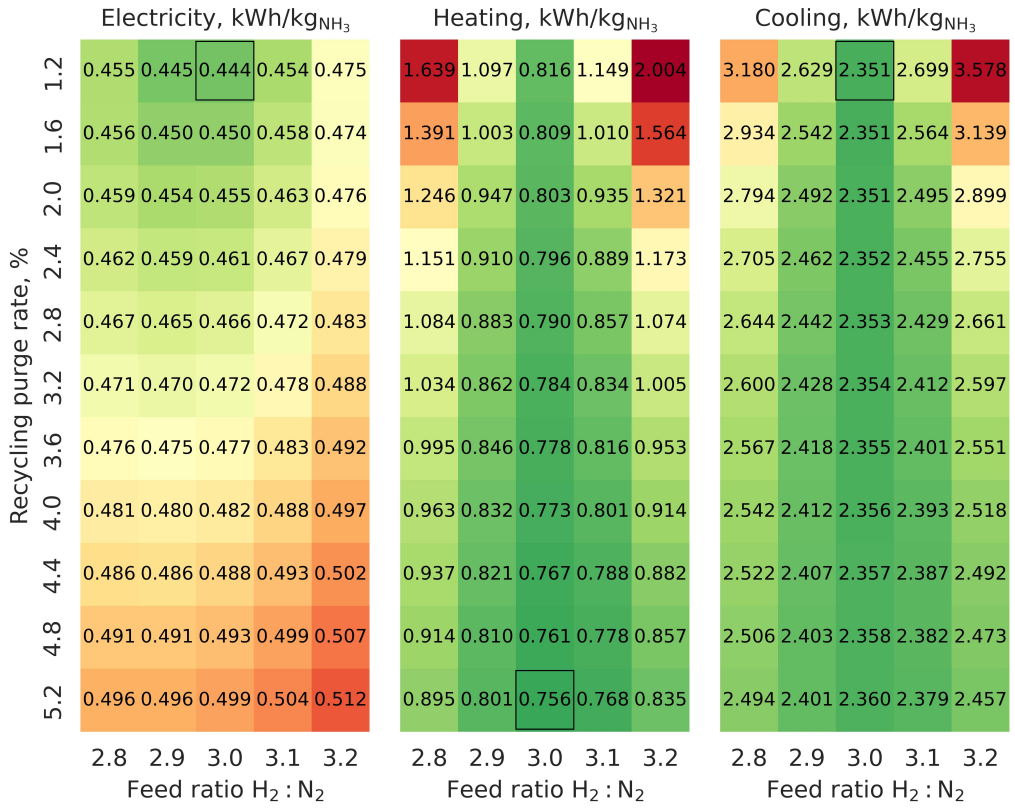


Figure 11. Heat maps of kWh of energy per 1kg of produced ammonia, broken down by energy type: electricity, heating, cooling.

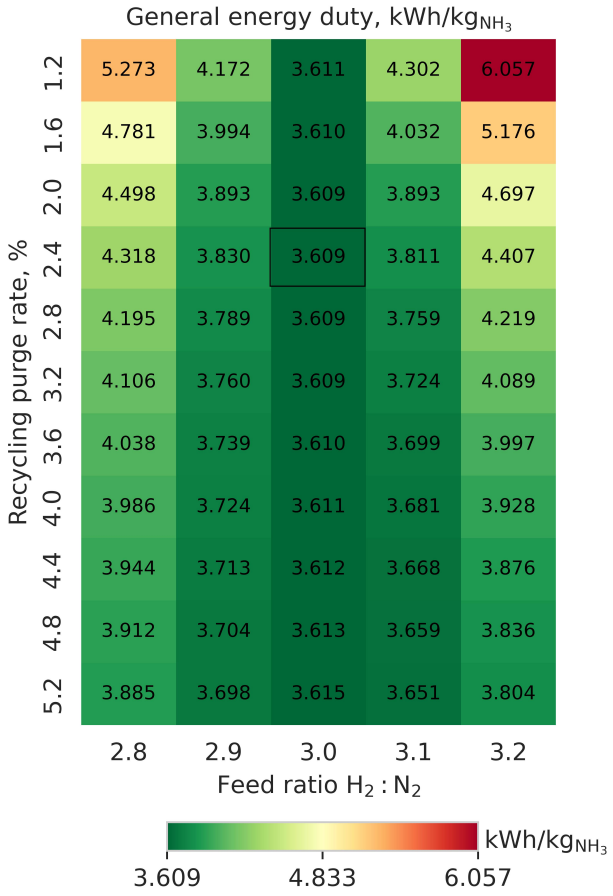


Figure 12. Heat map of kWh of total energy per 1kg of produced ammonia, the result of aggregating the constituent types of energy: electricity, heating and cooling.

Table 9. Enthalpy data of the input and output streams of the process for the lowest scale of ammonia production.

Stream	ΔH [kJ/kmol]	F [kmol/h]	$\hat{H}$ [kJ/h]
S_H_2	1603	27.5	44045
S_N_2	–5686	9.2	–52065
NH_3_Product	–65831	17.7	–1166583
Purge	–3857	1.3	–4997

which has both positive and negative consequences. Although the exothermic nature of the process allows for lower energy consumption of the installation, it can negatively influence the energy density of the produced product, as some of the chemical energy of hydrogen is released during the synthesis process.

The process energy requirement as part of energy density of the system was analysed in more detail, as it has been split into three categories: the duty of the heating of heat exchangers, the duty of the cooling of heat exchangers and the electricity power of the compressors. In order to avoid cancellation of the signs, all of the values have been summed up as an absolute value, avoiding the negative sign. Table 10 and Figure 13 demonstrate the energy consumption of the system.

Table 10. Summary of process energy requirement.

Scale	Electricity [kW]	Cooling [kW]	Heating [kW]	Sum [kW]
23000 kg/h NH_3	10092.7	53447.8	18573.8	82114.3
11500 kg/h NH_3	5030.5	26654.7	9234.1	40919.2
300 kg/h NH_3	130.9	695.2	241.1	1067.2

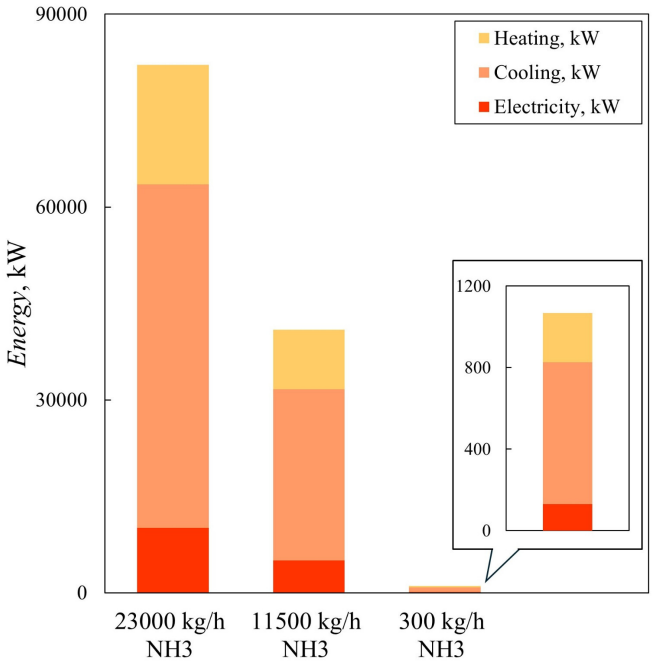


Figure 13. Heating, cooling and electricity demands for three scales of production.

Figure 13 shows clear domination of cooling energy as the biggest part of the total energy consumed by the process. This is caused by the need to vastly lower the temperature of the outlet reactor mixture in order to separate ammonia from the unreacted gases. The temperatures analysed through the case study (20–45°C) are temperatures achievable with using water as a cooling medium. In the prepared simulation, cooling energy was lowered by implementing the quench cooling, which cools the reaction mixture by mixing a cooler stream of gases with the hot stream exiting the catalytic bed.

Compared to the cooling energy, heating energy and electricity used for compression are relatively low. That is because the considered reaction is exothermic, which allows for the heating of the substrates by the outlet reactor mixture. The gases are also heated through the compression process. In order to further minimize the demand of heating energy, a more complex system could be considered, which recycles the heat taken from the cooling of the product in the condensation step.

In the presented analysis, compressor power demand was calculated based on idealized compression work. To better reflect realistic operating conditions at the pre-design stage, addi-

tional losses associated with non-ideal compression behaviour were considered. An isentropic efficiency of 75% which was assumed for all compressors and that of 80% for heat exchangers are conservative engineering assumptions. Furthermore, the model accounts for heat exchangers to ensure realistic thermal management across the system. These efficiency values were kept constant across all investigated production scales. The impact of these assumptions was analysed for all three production scales (i.e. 300, 11 500 and 23 000 kg/h NH_3), and the resulting compressor efficiencies and effective electrical energy consumption are summarized in Tables 11–12.

Table 11. Compressor and heat exchanger efficiency.

Parameter	Efficiency [%]
Compressor Izentropic efficiency	75
Heat Exchanger efficiency	80

Table 12. Compressor and heat exchanger efficiency.

Equipment type	Equipment ID	Power/heat duty [kW] 300 kg/h NH_3	11500 kg/h NH_3	23000 kg/h NH_3
Compressor	S_K1	3	125	250
	S_K2	68	2599	5199
	S_K3	59	2256	4513
	M_K4	1	51	131
Heat exchanger	M_E1	–459	–17590	–35272
	M_E2	241	9234	18574
	S_E1	–63	–2416	–4833
	M_V1	–173	–6649	–13343

Ammonia synthesis has been considered as a method of increasing the energy density of hydrogen produced through environmentally friendly methods. This approach solves the problems concerning the problematic storage conditions of hydrogen. In the simulation, energy densities of substances have been defined for the source stream of hydrogen and the process product with Eqs. (14)–(17), respectively:

$$\text{Energy Density}_{H_2} = \text{LHV}_{H_2} \cdot \rho_{H_2} \quad (14)$$

$$\text{Energy Density}_{H_2KG} = \text{LHV}_{H_2} \quad (15)$$

$$\text{Energy Density}_{NH_3} = \text{LHV}_{NH_3} \cdot \rho_{NH_3} \quad (16)$$

$$\text{Energy Density}_{NH_3KG} = \text{LHV}_{NH_3} \quad (17)$$

The described parameters were used to evaluate changes in the suitability of hydrogen and ammonia as energy carriers for storage and transport, by defining energy density in a two-way approach: a mass basis, as Lower Heating Value (LHV), described with Eq. (15) and Eq. (17), with a unit of MJ/kg, and a volume basis described with Eq. (14) and Eq. (16), with a unit of MJ/m^3.

In order to better visualize the change in the parameters, the following ratios were defined with Eqs. (18)–(19):

$$\text{Energy Density Ratio} = \frac{\text{Energy Density}_{NH_3}}{\text{Energy Density}_{H_2}} \quad (18)$$

$$\text{Energy Density Ratio_KG} = \frac{\text{Energy Density}_{NH_3KG}}{\text{Energy Density}_{H_2KG}} \quad (19)$$

The calculated values are shown in Table 13.

Table 13. Change in LHV based energy density.

Hydrogen energy density[1] [MJ/m^3]	Hydrogen energy density [MJ/kg]	Product energy density [MJ/m^3]	Product energy density[2] [MJ/kg]	Energy Density Ratio	Energy Density Ratio KG
72.9	119.9	11402	18.6	156	0.16

[1] Energy density per 1 m^3 of hydrogen at 80 °C and 8.9 bar.
[2] Energy density per 1 m^3 of ammonia at 25 °C and 200 bar.

The data shown in Table 13 demonstrate how the ammonia synthesis process affects the energy density of the system. There is a considerable increase in the energy per volume, showing the improvement of storage and transport efficiency when ammonia is used as an energy carrier, as it allows more amount of energy to be kept in a smaller volume. However, a noticeable trade-off appears to be the energy density considered in the context of mass, as 1 kg of ammonia is able to deliver less energy than 1 kg of hydrogen. The impact of the hydrogen conversion to ammonia on the energy density of the system is shown in Figure 14.

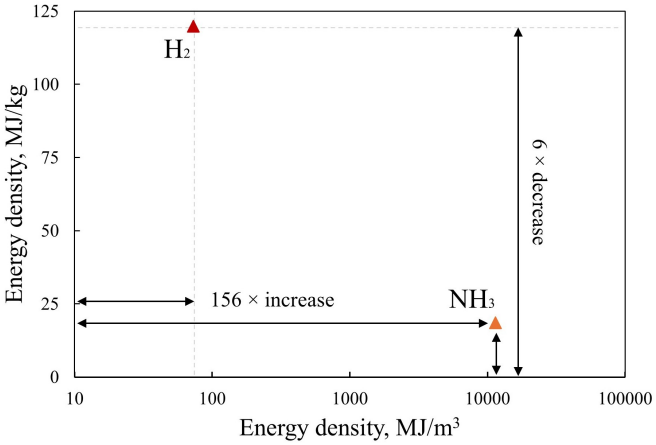


Figure 14. Obtained changes of energy density.

5. CONCLUSIONS

Based on the results presented in this work it can be concluded that the presented process is a promising solution for increasing the energy density of hydrogen, which in light

of current attempts aimed at promoting renewable energy sources as feasible alternatives to fossil fuels, stands as an important area of development. The created simulation operates within the range of optimal conditions sufficient at the pre-engineering stage and demonstrates high numerical stability allowing it to be subjected to numerous experiments and further tuning for the needs of a specific application.

The proposed solution has been analysed from production efficiency and energetic cost perspectives, which show the importance of selecting the proper process conditions to balance the energy consumption with maximum amount of obtainable product. The analysis of the different types of energy used in the process allows for a better understanding of the possible improvements to the process, which help with implementing solutions of circular economy. The study also contributes to the development of the research area related to the conversion of hydrogen to ammonia by presenting the impacts of possible divergence from stoichiometric ratio of reagents, which are common in the industry.

From the industrial perspective, the developed installation demonstrates the potential for effectively utilizing ammonia synthesis process as a potential method for hydrogen storage in a form with higher energy density, ensuring safer conditions. This technology is applicable not only in large-scale industrial installations but also in smaller, decentralized energy systems.

ACKNOWLEDGEMENTS

The work was financed by the Ministry of Science and Higher Education.

The authors would like to thank AVEVA Group Limited for providing software and technical support.

SYMBOLS

a	constant in the SRKM model
A	pre-exponential factor, $\mathrm{mol}/(\mathrm{s}\cdot\mathrm{m}^3\cdot\mathrm{atm}^{1.5})$, $\mathrm{mol}\cdot\mathrm{atm}^{0.5}/(\mathrm{s}\cdot\mathrm{m}^3)$
b	constant in the SRKM model
D	reactor diameter, m
d_{cat}	catalyst particle diameter for Ergun pressure drop correlation, mm
DP	reactor pressure drop, Pa
DP_{elem}	pressure drop per reactor element, Pa
E	activation energy, J/mol
F	molar flowrate, kmol/h
ΔH	enthalpy, kJ/mol
$\hat{H}$	enthalpy stream, kJ/h
k	reaction rate constant, $\mathrm{mol}/(\mathrm{s}\cdot\mathrm{m}^3\cdot\mathrm{atm}^{1.5})$, $\mathrm{mol}\cdot\mathrm{atm}^{0.5}/(\mathrm{s}\cdot\mathrm{m}^3)$
L	reactor length, m
L_{elem}	reactor element length, m
MW	molecular weight, kg/kmol
N_{e}	number of segments used in the Reactor, –
p	pressure, bar, kPa
Q	energy consumption per 1 kg of ammonia, kWh/kg
R	gas constant, $\mathrm{J}/(\mathrm{mol}\cdot\mathrm{K})$
r	reaction rate, $\mathrm{kmol}/(\mathrm{s}\cdot\mathrm{m}^3)$
$R_{\mathrm{H_2/N_2}}$	molar feed ratio of hydrogen to nitrogen, –
T	temperature, °C
v	velocity of fluid in tubes, m/s
V	volume, m^3
W	mass flow rate, kg/h
x	molar fraction in the liquid phase, mol/mol
y	molar fraction in the gas phase, mol/mol
z	molar fraction in the gas and liquid phase, mol/mol

Greek symbols

ε	void fraction, $\mathrm{m}^3/\mathrm{m}^3$
μ	viscosity, $\mathrm{Pa}\cdot\mathrm{s}$
ρ	mass density, kg/L

Subscripts

1, 2	number of component
$\mathrm{NH_3}, \mathrm{H_2}, \mathrm{N_2}$	compound type
p	packing density
o	operational

REFERENCES

Amin M.R., Sharear S., Siddique N., Islam S., 2013. Simulation of ammonia synthesis. *Am. J. Chem. Eng.*, 1, 59–64. DOI: 10.11648/j.ajche.20130103.11.

AntenChem, 2025. *Ammonia synthesis catalyst ATA207*. Available at: https://antenchem.com.

Araújo A., Skogestad S., 2008. Control structure design for the ammonia synthesis process. *Comput. Chem. Eng.*, 32, 2920–2932. DOI: 10.1016/j.compchemeng.2008.03.001.

AVEVA, 2024. *AVEVA™ Process Simulation Version 8.0.0.2238. Example simulation: CC13 - Ammonia Reactor Dynamic PFR*.

AVEVA, 2025. *AVEVA™ Process Simulation. Equations for the SRKM method*. Available at: https://aveva.com.

Catalystzeolite, 2025. *Synteza amoniaku Katalizator na bazie żelaza do syntezy amoniaku i produkcji amoniaku*. Available at: https://catalystzeolite.com.

Cheema I.I., Krewer U., 2018. Operating envelope of Haber–Bosch process design for power-to-ammonia. *RSC Adv.*, 8, 34926–34936. DOI: 10.1039/C8RA06821F.

Dashti A., Khorsand K., Marvast M.A., Kakavand M., 2006. Modeling and simulation of ammonia synthesis reactor. *Petroleum Coal*, 48, 15–23.

de la Hera G., Ruiz-Gutiérrez G., Viguri J.R., Galán B., 2024. Flexible green ammonia production plants: small-scale simulations based on energy aspects. *Environments*, 11, 71. DOI: 10.3390/environments11040071.

Dengzhuochem, 2025. *Ammonia synthesis catalyst DZC-A110*. Available at: https://dengzhuochem.com_37/36.html.

Esence T., Bruch A., Molina S., Stutz B., Fourmigué J.-F., 2017. A review on experience feedback and numerical modeling of packed-bed thermal energy storage systems. *Sol. Energy*, 153, 628–654. DOI: 10.1016/j.solener.2017.03.032.

Fahr S., Kender R., Bohn J.-P., Rehfeldt S., Peschel A., Klein H., 2025. Dynamic simulation of a highly load-flexible Haber–Bosch plant. *Int. J. Hydrogen Energy*, 102, 1231–1242. DOI: 10.1016/j.ijhydene.2025.01.039.

Flórez-Orrego D., de Oliveira Junior S., 2017. Modeling and optimization of an industrial ammonia synthesis unit: an exergy approach. *Energy*, 137, 234–250. DOI: 10.1016/j.energy.2017.06.157.

Garrote J., 2020. *Modularisation of the Haber-Bosch process for small-scale ammonia production*. MEng Research project, CE30122, University of Bath.

Jabarivelisdeh B., Jin E., Christopher P., Masanet E., 2022. *Ammonia production processes from energy and emissions perspectives: A technical brief*. Technical report, C-THRU Project, University of California, Santa Barbara. Available at: https://c-thru.org.

Khademi M.H., Sabbaghi R.S., 2017. Comparison between three types of ammonia synthesis reactor configurations in terms of cooling methods. *Chem. Eng. Res. Des.*, 128, 306–317. DOI: 10.1016/j.cherd.2017.10.021.

Lin B., Wiesner T., Malmali M., 2020. Performance of a small-scale Haber process: a techno-economic analysis. *ACS Sustainable Chem. Eng.*, 8, 15517–15531. DOI: 10.1021/acssuschemeng.0c04313.

Luyben W.L., 2012. Design and control of a cooled ammonia reactor. In: Rangaiah G.P., Kariwala V. (Eds.), *Plantwide control: Recent developments and applications*. Wiley, Chichester, 273–292. DOI: 10.1002/9781119968962.ch13.

Michels A., Skelton G.F., Dumoulin E., 1950. Gas-liquid phase equilibrium in the system ammonia-hydrogen-nitrogen. *Physica*, 16, 831–838. DOI: 10.1016/0031-8914(50)90092-9.

Morud J.C., Skogestad S., 1998. Analysis of instability in an industrial ammonia reactor. *AIChE J.*, 44, 888–895. DOI: 10.1002/aic.690440414.

Rosbo J.W., Ritschel T.K.S., Hørsholt S., Huusom J.K., Jørgensen J.B., 2023. Flexible operation, optimisation and stabilising control of a quench cooled ammonia reactor for power-to-ammonia. *Comput. Chem. Eng.*, 176, 108316. DOI: 10.1016/j.compchemeng.2023.108316.

Rüther J., Larsen J., Lippmann D., Claes D., 2005. 4000 mtpd ammonia plant based on proven technology. *50th Annual Safety in Ammonia Plants and Related Facilities Symposium (AIChE Ammonia Safety Symposium)*, Toronto, Canada, 46, 312–319. Available at: https://conferencespot.org.

Seifert T., Sievers S., Bramsiepe C., Schembecker G., 2012. Small scale, modular and continuous: a new approach in plant design. *Chem. Eng. Process. Process Intensif.*, 52, 140–150. DOI: 10.1016/j.cep.2011.10.007.

Shamiri A., Aliabadi N., 2021. Modeling and performance improvement of an industrial ammonia synthesis reactor. *Chem. Eng. J. Adv.*, 8, 100177. DOI: 10.1016/j.ceja.2021.100177.

Smith C., Hill A.K., Torrente-Murciano L., 2020. Current and future role of Haber–Bosch ammonia in a carbon-free energy landscape. *Energy Environ. Sci.*, 13, 331–344. DOI: 10.1039/C9EE02873K.

Spatolisano E., Pellegrini L.A., 2023. Haber-Bosch process intensification: a first step towards small-scale distributed ammonia production. *Chem. Eng. Res. Des.*, 195, 651–661. DOI: 10.1016/j.cherd.2023.06.031.

Stanford Advanced Materials, 2026. *CM4014 (Discontinued) Ammonia Synthesis Catalyst (Ferrous Ammonia)*. Available at: https://www.samaterials.com/ammonia-synthesis-catalyst-ferrous-ammonia.html.

Syamcat, 2026. *Ammonia synthesis catalysts with strong thermal stability for ammonia plant. Syamcat Catalyst Manufacturer*. Available at: https://www.syamcat.com/pid18424749/Ammonia-Synthesis-Catalysts-with-Strong-Thermal-Stability-for-Ammonia-Plant.htm.

Temkin M.I., Pyzhev V., 1940. Kinetics of ammonia synthesis on promoted iron catalysts. *Acta Physicochim. URSS*, 12, 327.

Verlysen K., Parente A., Contino F., 2021. How sensitive is a dynamic ammonia synthesis process? Global sensitivity analysis of a dynamic Haber-Bosch process (for flexible seasonal energy storage). *Energy*, 232, 121016. DOI: 10.1016/j.energy.2021.121016.

Zhulin Carbon, 2010. *Iron catalyst for ammonia synthesis*. Available at: https://made-in-china.com.

Chemical and Process Engineering: New Frontiers, 2026, 47(2), e130
DOI: 10.24425/cpe.2026.158128

Improvement of antifouling resistance of polymer membranes using CuO nanoparticle incorporation-long-term performance evaluation

Maciej Szwast, Daniel Polak, Andrzej Krasiński

Warsaw University of Technology, Faculty of Chemical and Process Engineering, Waryńskiego 1, 00-645 Warsaw, Poland

Abstract
Long-term biofouling significantly limits continuous membrane filtration operated under constant transmembrane pressure, causing progressive hydraulic resistance and permeate flux instability. This study examined the long-term performance of polypropylene capillary membranes modified with a thin polysulfone layer containing CuO nanoparticles under cross-flow microfiltration with *Escherichia coli*. The focus was on operational stability during extended filtration rather than short-term material properties. Scanning electron microscopy, X-ray fluorescence, and capillary porosimetry confirmed that the modification was confined to the near-surface region without altering intrinsic pore structure or initial hydraulic permeability. Ninety-six-hour continuous filtration tests showed similar initial fluxes for both membranes. However, CuO-modified membranes exhibited a markedly slower flux decline. Consequently, cumulative permeate production was approximately 43% higher compared to unmodified membranes. Hermia model analysis indicated that fouling followed the intermediate pore-blocking mechanism in all cases. To account for time-dependent biofouling dynamics, the model was extended using a Weibull formulation, allowing separation of fouling time scale from intensity. The generalized model revealed a lower initial fouling rate and significantly longer characteristic fouling time for CuO-modified membranes, indicating delayed transition to high-resistance conditions. From a process-engineering standpoint, bacteriostatic surface modification effectively enhances long-term operational stability.

Keywords
membrane biofouling, long-term filtration, Hermia model, Weibull model, bacteriostatic modification

* **Corresponding author, e-mail:**
maciej.szwast@pw.edu.pl

Article info:
Received: 13 January 2026
Revised: 24 March 2026
Accepted: 27 April 2026

1. INTRODUCTION

Microorganisms such as bacteria, fungi and other microorganisms are ubiquitous and in real industrial operations it is difficult to eliminate the adverse effects resulting from their presence. Biofouling remains one of the most significant problems limiting the effectiveness of long-term membrane processes in water filtration applications (Alnumani et al., 2024; Zhang et al., 2022). Biofilm formation by bacteria, fungi, and other microorganisms leads to the formation of a dense, resistant layer that accelerates material aging and dramatically increases flow resistance of filtration media (fibrous filters or membranes), thus reducing the efficiency and economic viability of the system (Gaylarde and Morton, 1999; Momba et al., 2000; Vishwakarma, 2020). Biofilm is an organized structure stabilized by a matrix of extracellular polymeric substances (EPS) secreted from cells, which facilitate adhesion of bacteria and promote the rapid increase in filtration resistance early in membrane life (Di Martino, 2018; Salama et al., 2016).

More precisely, biofilm can be defined as a structured microbial consortium irreversibly attached to a surface and embedded in a self-produced EPS matrix composed of polysaccharides, proteins, lipids and extracellular DNA. This matrix provides mechanical stability, enhances resistance to hydrodynamic shear, and creates a diffusion barrier that limits mass transfer of nutrients and antimicrobial agents. As a consequence, once established on a membrane surface, biofilm significantly alters local transport conditions and promotes progressive hydraulic resistance buildup.

In membrane systems operated under constant transmembrane pressure (TMP), biofilm development manifests as a time-dependent decline in permeate flux. The accumulation of cells and EPS within and on the membrane structure leads to pore constriction, partial or complete pore blocking, and eventually formation of a cake-like layer. Unlike purely inorganic or colloidal fouling, biofouling is dynamic and evolves due to microbial growth, EPS secretion, structural rearrangement of the deposited layer, and possible detachment events. Therefore, the rate of resistance increase is rarely constant over time, which complicates predictive modelling of long-term performance.

One of the methods being intensively developed to improve the resistance of separation materials to biofouling is their modification using additives having confirmed antibacterial properties (Desiriani et al., 2023; Geng et al., 2022; Younas et al., 2016). The effectiveness of metals and metal oxides such as Ag, Cu, ZnO and CuO, especially in the form of dispersed nanoparticles, is widely described in the literature, and their effects include both bactericidal and bacteriostatic effects (Asamoah et al., 2020; Dadi et al., 2019; Dehghani et al., 2019; Krasiński et al., 2025; Pandey et al., 2021). The latter mechanism, which slows down the growth of microor-

© 2026. The Author(s). This is an open-access article distributed under the terms of the Creative Commons Attribution (CC-BY 4.0, https://creativecommons.org/licenses/by/4.0/), which permits unrestricted use, distribution, and reproduction in any medium, provided the original author and source are credited.

ganisms and limits the rate of surface colonization, is particularly important for the membrane durability and the stability of process parameters. Our previous studies confirmed that CuO nanoparticles exhibit significant bacteriostatic properties against microorganisms relevant to water-quality assessment, including common indicator species, as demonstrated in dynamic tests conducted according to the ASTM E2149-13a standard (Szwast et al., 2023).

However, in vitro studies, typically conducted on solid substrates or in simple contact systems, do not fully capture the complexity of phenomena occurring under real membrane operating conditions, where variable flow regimes, mass-transfer processes, repeated passage of the medium through the porous structure, and the development of biofilm under hydrodynamic stresses all play a significant role.

From a mechanistic standpoint, the decline in permeate flux during membrane filtration is commonly interpreted using classical pore-blocking models, among which the Hermia model is one of the most frequently applied frameworks. The Hermia approach distinguishes between four principal fouling regimes: complete blocking, standard blocking, intermediate blocking, and cake formation. Each regime reflects a distinct physical mechanism of pore obstruction or surface coverage. Although originally derived for constant-pressure dead-end filtration, the model is widely used for analysing cross-flow microfiltration and ultrafiltration data due to its ability to relate flux decline to dominant fouling mechanisms.

Nevertheless, in long-term biologically active systems, fouling rarely proceeds at a constant rate assumed in the simplest Hermia formulations. The interaction between microbial growth kinetics, EPS (extracellular polymeric substance) accumulation, and hydrodynamic shear may lead to time-dependent changes in fouling intensity. Therefore, a more comprehensive theoretical framework is required to adequately describe resistance development under realistic operating conditions.

Consequently, the natural next step in research on antibiofouling materials is to move from model tests to verifying membrane properties under conditions as close as possible to those in operation (Tian et al., 2023). In the present study, this challenge was addressed by using polypropylene membranes modified with CuO nanoparticles. The aim of the research was to determine the extent to which the previously confirmed antibacterial properties of CuO translate into a real reduction of biofouling on the membrane surface in a flow-through filtration system operated at constant transmembrane pressure, by monitoring the evolution (decrease) of time-dependent permeate flux. In this approach, the decline in permeate flux is considered a direct measure of the increasing flow resistance associated with fouling and biofouling.

In addition to assessing the effectiveness of CuO in a real process, it was also important to determine the additive's effect on the dynamics of resistance buildup (i.e. clogging of pores), its ability to inhibit early stages of colonization, and any differences in fouling mechanisms compared to unmodified membranes. In particular, we were interested in answering the question of whether the bacteriostatic effect of CuO, previously demonstrated in vitro, is a relevant assessment method and could be strong enough to significantly delay the achievement of critical membrane resistance values in conditions very similar to the realistic operation of membrane filtration systems.

The novelty of the present work lies in combining long-term (96 h) uninterrupted cross-flow filtration under constant TMP with time-resolved flux monitoring and mechanistic modelling of fouling dynamics. In contrast to studies focused primarily on short-term antibacterial assays or material characterization, this study evaluates membrane performance from a process-engineering perspective, linking bacteriostatic surface modification with quantitative analysis of resistance development and dominant fouling regimes.

By integrating experimental long-term filtration data with Hermia-based modelling, the study aims not only to identify the prevailing fouling mechanism but also to assess whether bacteriostatic modification alters the temporal characteristics of resistance buildup. Such an approach provides a bridge between material-level antibacterial properties and system-level operational stability.

Therefore, the present study addresses a key process-engineering problem related to the long-term stability of membrane filtration systems operated under constant transmembrane pressure in biologically active environments. By combining long-term cross-flow filtration experiments with time-resolved analysis of permeate flux decline, this work aims to quantify how bacteriostatic membrane modification influences the dynamics of hydraulic resistance buildup under realistic operating conditions. Such an approach enables direct assessment of membrane performance from the perspective of process continuity, operational stability, and effective operating time, which are critical parameters in the design and operation of membrane-based separation systems.

2. MATERIALS AND METHODS

In the present study, capillary polypropylene membranes with an average pore size of 0.2 μm (3M, model MF-PP S6/2) were employed. Polysulfone (PSf, Sigma–Aldrich) and nanometric copper(II) oxide nanopowder (according to specification the particle size < 50 nm based on TEM; surface area ≈ 29 m^2/g; CuO nanoparticles, Sigma–Aldrich, product no. 544868) was used as the inorganic modifier. N-methyl-2-pyrrolidone (NMP, Pol-Aura) served as the primary solvent, filtered tap water was used as the secondary (nonsolvent) phase, whereas filtered water treated with activated carbon was employed as the process medium in microfiltration experiments to isolate the effects of other compounds, including chlorine or ozone.

2.1. Membrane preparation

In presented research the commercially available polypropylene membranes (used as reference) and in-house modified membranes with enhanced antibacterial properties were utilized. The functional coating was deposited onto the outer surface of the polypropylene membranes using the dip-coating technique. In this procedure, the membrane was immersed in the modifying solution and subsequently withdrawn at a precisely controlled speed of 20 mm/min to achieve uniform layer formation. Dip-coating was performed using the NIMA Dip Coater (KSV NIMA Dip Coaters). The withdrawal speed was low enough to enable formation of an ultrathin and integral coating layer.

To generate a functional porous layer on the membrane surface, the coated membranes were subsequently subjected to a wet phase inversion process. For this purpose, the membranes covered with the film-forming solution were immersed in a water bath, where water, acting as a non-solvent, replaced the primary solvent (NMP) in the polymer solution. This exchange induced a liquid–solid phase transition, resulting in the development of a porous structure within the deposited layer.

The modifying formulation consisted of 11% (w/w) polysulfone (PSf) solution in NMP supplemented with 2% (w/w) CuO nanoparticles, calculated in relation to the mass of PSf. The fabrication procedure and properties of this type of composite material have been discussed in detail in the authors' previous work (Szwast et al., 2023).

2.2. Membrane characterization

A set of instrumental methods was used to characterize the obtained heterogeneous membranes, enabling the assessment of morphological parameters and filtration properties. The effectiveness of coating the supporting membrane with the modifying layer was determined by scanning electron microscopy (SEM) using a PhenomPro G2 microscope (PhenomWorld, Eindhoven, The Netherlands) equipped with a holder that did not require sample sputtering. The membranes were also subjected to X-ray fluorescence (XRF) analysis to confirm the presence of copper on their surface, which is crucial for the bacteriostatic properties associated with CuO nanoparticles. The bacteriostatic properties of these nanoparticles and the heterogeneous membranes containing CuO produced by our team have been demonstrated in previous studies conducted on agar media (Szwast et al., 2023). XRF analyses were performed using an X-ray Fluorescence Spectrometer (Epsilon 3XLE, Malvern PANalytical Ltd, Malvern, Worcestershire, UK).

The effect of modification on material structure was also assessed by capillary porosimetry, comparing unmodified and modified membranes using a PMI Capillary iPore-1200A apparatus (Porous Materials, Inc., Ithaca, NY, USA).

2.3. Filtration tests

Long-term studies of the membrane filtration process were conducted on a large-scale research setup supplied by Polymemtech (Warsaw, Poland). This setup included a replaceable membrane module (Mem), a 10-liter feed tank (Tk), and product tanks (permeate and retentate), which were not used in this experiment, as both streams were recirculated to the feed tank. The setup was equipped with a centrifugal pump (PM), pressure transducers (P) located upstream (in the feed stream) and downstream (in the retentate stream) of the membrane module, and flow transducers (F) installed in the permeate and retentate lines. The setup was also equipped with a heat exchanger (HE), which enabled temperature control of the liquid circulating in the system. The valve configuration allowed for continuous recirculation of both flows to the feed tank, allowing the process to run for several days without the need for feed replenishment or product removal. The configuration of the experimental setup used in this study is presented in Fig. 1. In current research the system was equipped with a three-port module, developed in-house, containing a bundle of 40 tubular (capillary) membranes with the length of 1 m and the inner diameter of 1.8 mm, which results in 0.27 m^2 of total filtration area. The module operated in a cross-flow configuration. The applied configuration allows for continuous operation of the membrane module over several days under controlled hydraulic conditions, enabling direct observation of time-dependent resistance development. From a process-engineering perspective, this setup represents a simplified model of industrial cross-flow microfiltration units operated without intermediate cleaning, making it suitable for evaluating long-term process stability rather than short-term material performance.

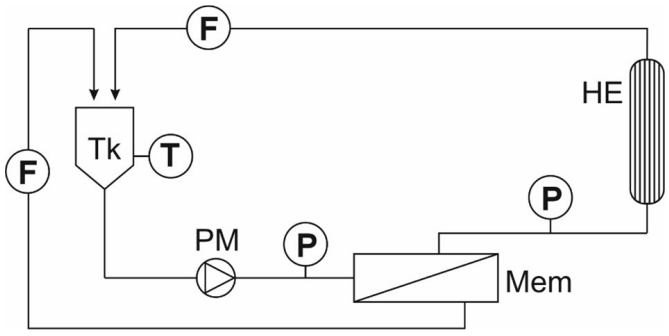


Figure 1. Experimental setup; F – flow transducer, HE – heat exchanger, Mem – membrane module, P – pressure transducer, PM – pump, T – temperature transducer, Tk – tank.

The control and monitoring system was equipped with a recorder enabling storage of process data at one-minute intervals. The control system guaranteed also a stable temperature of the feed water.

The measurements were conducted continuously for 96 hours, maintaining constant system operating parameters, in particular the feed pressure at 0.5 bar and the feed temperature

at 294 K. Once daily, a portion of the bacterial suspension was introduced into the system and a diluted nutrient was continuously supplied to the feed tank to maintain bacteria life functions (the procedure is describe in more detail *Section* 2.4). Other process variables, such as the permeate flow rate – whose variability served as a measure of bacterial growth leading to membrane fouling – were derived quantities taking values dependent on the current operating conditions.

Following the completion of the modified membrane testing, water samples were analysed to assess the stability of copper additive on the membranes' surface. This study aimed to determine whether Cu^{2+} ions or fine fractions of CuO particles were released into the permeate and retentate streams during long-term filtration. Visocolor ECO Copper cuvette tests (Macherey–Nagel) were used to determine Cu^{2+} ion concentration. The concentration range of this method was 0.1–1.5 mg/L, where the lower limit corresponds to the detection threshold.

2.4. Determination of bacterial content in the water

In this study, bacterial cultures of *Escherichia coli* Castellani & Chalmers (ATCC 8739) were used. The water was inoculated with *E.coli* by the injection of 1 mL of bacterial suspension ($3–5 \cdot 10^8$ CFU/mL) once per day to obtain the initial concentration of cells in the feed tank in the range of 10^3–10^4 CFU/mL. The nutrient was supplied directly to the tank with the flow rate of 10 mL/day (concentration of the Luria-Bertani broth was 2.5 g/L). The same procedure was used for reference and modified membranes (a comparative study) to enable verifying the impact of modifications on the membrane biofouling rate. Throughout the process, *E. coli* bacterial content in the feed water and permeate were monitored. Samples of the feed water were taken from the feed tank immediately after the bacteria were added (bacteria were injected once per day) to verify their initial concentration, which was expected to be in the afore-mentioned desired range (i.e., 10^3–10^4 CFU/mL). Petri dishes with a solidified culture medium consisting of bacteriological agar and LB broth (Miller) were used for this purpose. A water sample in the amount of 0.1 mL was spread on the surface of the culture medium, and after 24 hours of incubation, the CFU count was determined and then converted to concentration (per 1 mL of water).

In the present study, the feed solution was prepared from filtered tap water and inoculated with a controlled culture of *E. coli*, which served as a model microorganism representing biofouling-forming bacteria. Due to the use of filtered tap water and the closed recirculation configuration of the experimental setup, the development of other microbial populations during the experiment was considered unlikely. The applied experimental design was therefore intended to provide controlled conditions enabling the analysis of biofouling dynamics associated with a well-defined bacterial species.

For the permeate samples, a similar estimation of the concentration of viable bacteria after passing the membrane was carried out based on water inoculations in Petri dishes. The bacterial concentration was determined immediately after feeding a fresh portion of bacteria into the system and after 1, 2 and 4 hours. No growth in colonies in the Petri dishes was observed in any case. However, it is reported in the literature that in certain situations bacteria can go into so-called VBNC state, which stands for viable but nonculturable (Liu et al., 2023). It refers to a situation where bacteria are alive but cannot grow on standard lab media. They often enter VBNC state in response to environmental stress, e.g., a shortage of nutrients or interaction with compounds having a detrimental effect on their living functions. They do not proliferate (divide), so they often do not form colonies, but to some extent are metabolically active and can contribute to biofilm formation. Therefore, MicroSnap Total tests from Hygiena Diagnostics GmbH were also used for measuring the total viable bacterial count, which is a method certified by Association of Official Analytical Chemists (AOAC). It includes incubating a sample to allow bacterial growth and produce biomarkers, which are then measured using a luminometer. The test is a two-step procedure involving enrichment and a detection phase. First, the sample is incubated with a special growth medium that also contains enzymes to reduce background ATP. During the 7-hour incubation, bacteria multiply and produce more biomarkers. An aliquot of the enriched sample is transferred to a detection device, which is then activated. This releases bioluminescent reagents that react with the biomarkers produced by the bacteria. The resulting light emission was measured using EasyTouch luminometer from Hygiena Diagnostics GmbH, providing a quantitative result in RLU units, which is correlated with a bacterial count.

Additionally, membrane fragments collected after the filtration experiments were placed onto standard culture media to assess the potential presence and viability of bacteria adhering to the membrane surface. This procedure allowed verification of whether microorganisms remained associated with the membrane material after the filtration process.

3. RESULTS AND DISCUSSION

3.1. Membrane characterization

The composite membranes produced by dip-coating were subjected to morphological evaluation. SEM images were taken without sputtering, allowing direct observation of the modified membrane surface and comparison to unmodified membranes (Fig. 2). The SEM image of the unmodified membrane (Fig. 2A) shows a characteristic microporous structure of moderate regularity; some pores are partially obscured, likely due to local polymer melting during the fabrication process. The pore structure is characterized by a distinct orientation parallel to the capillary axis, which is typical for capillary polymer membrane formation technologies.

The image of the modified membrane (Fig. 2B) shows the presence of CuO nanoparticles deposited on the surface. The visible bright clusters are several micrometres in size (approx. 4-6 µm), indicating the tendency of CuO nanoparticles to agglomerate, a phenomenon commonly observed and reported in the literature (Dumitriu et al., 2016; Sotto et al., 2011). In this case, agglomeration is not necessarily undesirable; effective attachment of CuO nanoparticles to the surface of the microporous membrane and their presence on this surface are crucial. The surface of the original membrane is transparent through the applied layer, which suggests that the transport and separation properties of the modified membrane will not change significantly compared to the unmodified membrane.

Cross-sectional images of the capillaries were also captured, but the thickness of the layer formed during the dip-coating process proved too small to be clearly captured in SEM observations. This is beneficial from the perspective of membrane functionality: with confirmed surface modification, no additional, thick layer was observed, which could increase flow resistance and impair transport properties.

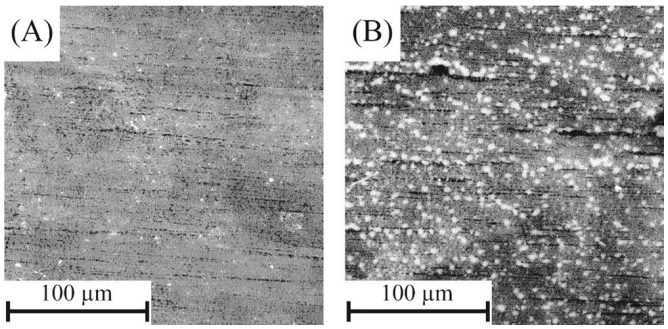


Figure 2. SEM images (1000× magnification): (A) outer surface of the unmodified membrane; (B) outer surface of the modified membrane with visible agglomerates of CuO nanoparticles.

The SEM images indicate that CuO nanoparticles embedded in a polysulfone matrix were successfully introduced into the surface region of the microporous capillary membrane. A similar material system was previously used to create a membrane exhibiting bacteriostatic properties (Szwast et al., 2023). In this context, it was important to ensure that Cu-containing species remained accessible at or near the membrane surface, as achieving the bacteriostatic effect, and thus antibiofouling properties, requires the availability of copper to enable interaction with bacterial cells (Banerjee et al., 2011; Khan and Shakoor, 2023).

X-ray fluorescence (XRF) was used to map the elements present in the near-surface region of the modified membrane and compare them with the unmodified membrane. The results of this analysis are summarized in Table 1.

The XRF measurement results are consistent with the conclusions drawn from the SEM analysis. A very high sulphur content was detected in the modified membrane, originating from the polysulfone, indicating the presence of a thin PSf layer in the near-surface region of the membrane. At the same time, the copper signal appeared only in the modified membrane, confirming the effective introduction of Cu-containing species into this region.

Table 1. XRF analysis results.

Compound	Unit	Unmodified membrane	Modified membrane
Mg	%	0.006	0.000
Al	%	0.025	0.002
Si	%	0.169	0.006
P	%	0.255	0.008
S	%	0.000	0.889
Cl	%	0.146	0.065
Ca	%	0.312	0.016
Fe	%	0.021	0.001
Cu	**%**	**0.000**	**0.011**
Ag	%	0.071	0.003

It is worth emphasizing that, due to the finite penetration depth of XRF, this technique does not exclusively probe the outermost surface. Nevertheless, the combined SEM and XRF results indicate that the polysulfone layer formed during dip-coating is thin and likely discontinuous, and does not constitute a thick, continuous barrier fully isolating CuO nanoparticles from the external environment. This is crucial for the assumed bacteriostatic effect, as either direct contact between bacteria and exposed CuO nanoparticles or the diffusion of copper ions through a thin polymer layer may contribute to antibacterial activity. Partial encapsulation of CuO nanoparticles may therefore be beneficial, as it can moderate copper release and enhance the long-term stability of the antibiofouling effect.

In addition to the elements characteristic of the modifying layer (S and Cu), a number of other elements were also detected in both membranes, such as Al, Si, P, Ca, Fe, and Ag. Their presence is typical for capillary polypropylene membranes and results primarily from the use of inorganic fillers, stabilizers, and technological additives used in the polymer production process. However, such information is not provided by manufacturers. The slight differences in their concentrations between the unmodified and modified membranes can be attributed to the partial obscuration of the PP surface by a thin polysulfone layer, which naturally affects the intensity of the XRF signal from deeper layers of the material. This is particularly noticeable in the case of elements with relatively low content, whose signal may be subject to local fluctuations dependent on the microscopic heterogeneity of the surface. It is also worth noting that the presence of chlorine in the modified membrane at a higher level than in the unmodified membrane may result from residual salts or reagents used in the preparation of the dip-coating solution. This is not a disturbing artifact but only indicates the introduction of additional ingredients as a result of modification.

From the perspective of the filtration and separation properties of modified membranes, the potential change in pore size and distribution introduced by the modification process is crucial. Ideally, modified membranes would be identical in this respect to unmodified membranes, but complete preservation of identical porosity parameters is impossible due to the application of an additional polymer layer to their surface. The results of pore size distribution analyses for the unmodified and modified membranes are presented in Fig. 3 and Table 2.

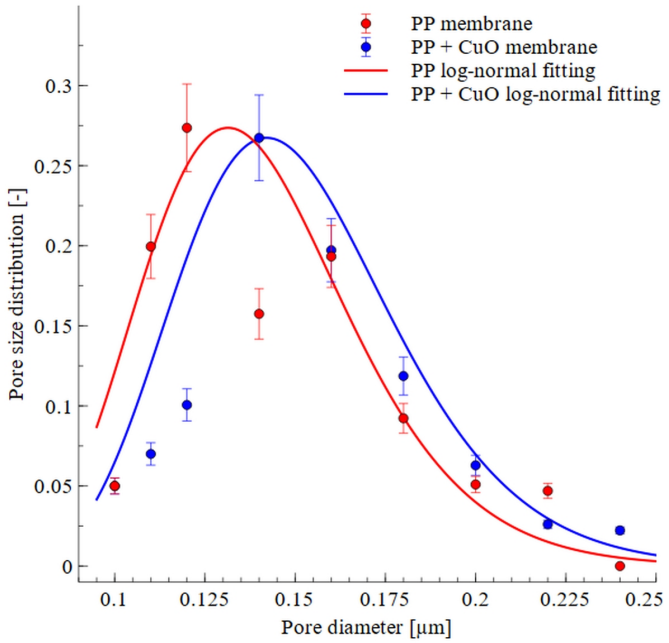


Figure 3. Pore size distribution in unmodified and modified membranes.

Table 2. Statistical parameters of pore size distribution.

Parameter	Unmodified membrane	Modified membrane
Arithmetic mean pore diameter [μm]	0.141	0.152
Standard deviation, SD [μm]	0.032	0.032
Mode (maximum at diameter, [μm])	0.12	0.14
Log-normal μ_{ln}	−1.984	−1.908
Log-normal σ_{ln}	0.214	0.209
Geometric mean pore diameter [μm]	0.139	0.150
Median (log-normal) pore diameter [μm]	0.139	0.150
R^2 (log-normal fit)	0.690	0.748

Analysis of the pore size distributions shown in Fig. 3 indicates that modification of polypropylene membranes with a polysulfone layer containing CuO nanoparticles does not lead to significant changes in their porosity in terms of filtration and separation properties. The pore distribution curves for the unmodified membrane (red line) and the modified membrane (blue line) are similar in shape and width, confirming the preservation of the essential microporous structure after the modification process. However, a slight shift in the main distribution peak for the modified membrane toward larger pore diameters is noticeable. This may be due to partial occlusion of the smallest pores by the thin polysulfone layer, which is consistent with SEM observations indicating the presence of a discontinuous, very thin polymer coating on the capillary surface. At the same time, the lack of a significant decrease in the proportion of larger pores and the similar profile of both curves suggest that the modifying layer does not create any significant additional resistance to mass transport. The statistical analysis summarized in Table 2 confirms the qualitative observations from Fig. 3. The arithmetic mean pore diameter increases only slightly from 0.141 μm for the unmodified membrane to 0.152 μm after modification, while the standard deviation remains essentially unchanged (0.032 μm for both samples). Similarly, the parameters of the log-normal distribution indicate only a minor shift of the distribution toward larger pore diameters without a noticeable change in dispersion. Although the coefficients of determination obtained for the log-normal fitting are moderate ($R^2 \approx 0.69$–0.75), the overall statistical analysis supports the conclusion that the modification does not significantly alter the pore structure of the membrane.

The obtained results allow us to conclude that the modification process does not significantly affect the filtration properties of the membranes, which is beneficial from the point of view of maintaining their functionality while potentially giving them anti-biofouling properties.

3.2. Filtration performance

The studies were conducted in a cross-flow filtration system using three separate membrane modules. In the first series of experiments, a module containing unmodified membranes was used and pure water was filtered (red line in Fig. 4). In the second series, a new, identical membrane module was used and pure water containing a bacterial suspension was filtered (blue line in Fig. 4). In the third series of studies, a module equipped with membranes modified with CuO nanoparticles was used and filtered tap water with the addition of a bacterial suspension was filtered (green line in Fig. 4). The time course of changes in permeate flux is shown in Fig. 4a.

Figure 4a shows the actual permeate flux values obtained in three test series. It should be noted that the initial flux values are very similar, which is particularly important when comparing the properties of unmodified and modified membranes. This result was expected given the similar porosity parameters obtained in the porosimetric analysis (Fig. 3). The curves presented in Fig. 4a show local deviations from the trend, resulting primarily from momentary pump disturbances and small fluctuations in feed pressure, as recorded by the

monitoring system. Therefore, it was decided to normalize the measured data to the operating pressure and to the initial permeate flux value. Based on this processed data, the graph shown in Fig. 4b was prepared. It is crucial that the similar initial permeate flux values in all three measurements ensure that the normalization performed does not introduce interpretation errors and allows for a reliable comparative analysis of changes occurring during filtration.

A slight decline in permeate flux during pure water filtration (red line in Fig. 4a) is typically attributed to membrane compaction and surface relaxation phenomena. Even in the absence of foulants, polymer chains may rearrange upon long-term contact with water, leading to increased hydraulic resistance (Persson et al., 1995). In addition, trace organic impurities and dissolved gases can adsorb or accumulate within the pores, contributing to a gradual permeability loss (van der Bruggen et al., 2002).

In studies involving bacteria, the decreases in permeate flux are clearly more pronounced. In the long term, flux values for both membranes tend to similarly low levels, but the rate of flux degradation for the unmodified membrane (slope of blue line in Fig. 4a) is significantly greater than for the membrane modified with CuO nanoparticles (green line in Fig. 4a).

Integration of the permeate flux curves indicates that the modified membranes produced nearly 43% more permeate over 96 hours of operation. From an operational standpoint, this result corresponds to a substantially slower increase in hydraulic resistance and an extended effective operating time of the membrane module under constant transmembrane pressure, which is directly relevant for maintaining stable throughput and reducing process interruptions in continuous filtration systems.

A significant result of the measurements is that samples taken from the permeate streams in all three filtration variants always showed a complete absence of bacteria. This means that the membranes used maintained full selectivity towards the bacterial culture and effectively retained microbial cells regardless of the membrane type and process conditions.

A preliminary analysis of the permeate flux curves for filtration using modified and unmodified membranes already provides a clearly positive answer regarding the membranes antibiofouling properties, which was the main goal of this research. However, to deepen the analysis and consider potential fouling mechanisms, the remainder of this manuscript will attempt to mathematically describe the observed phenomena.

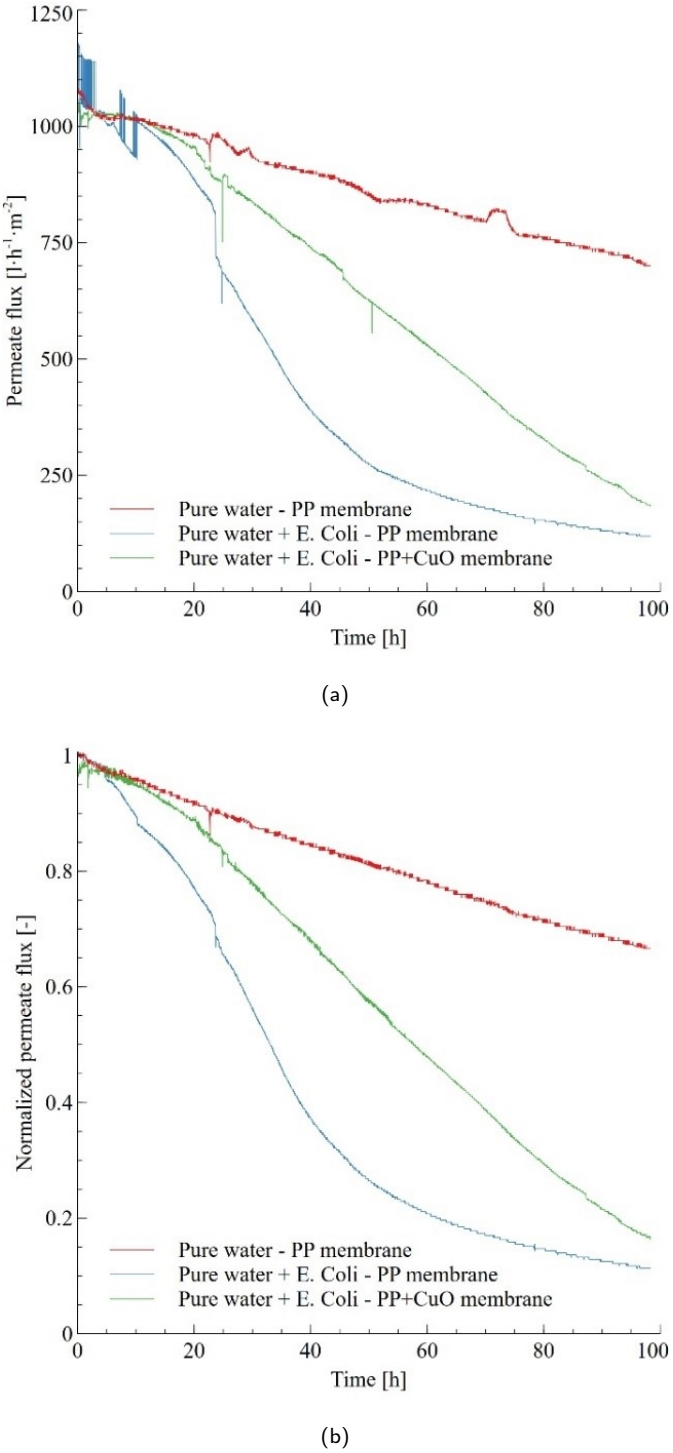
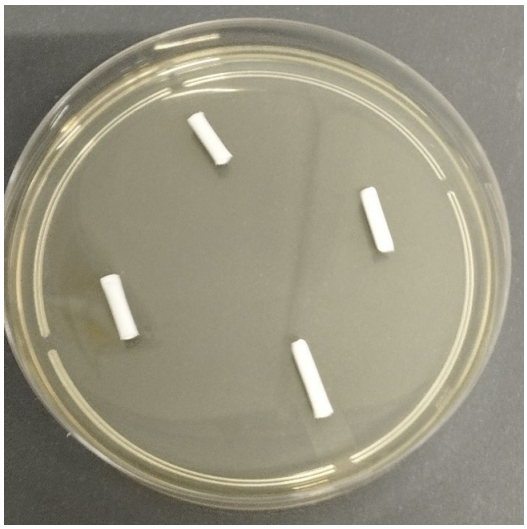


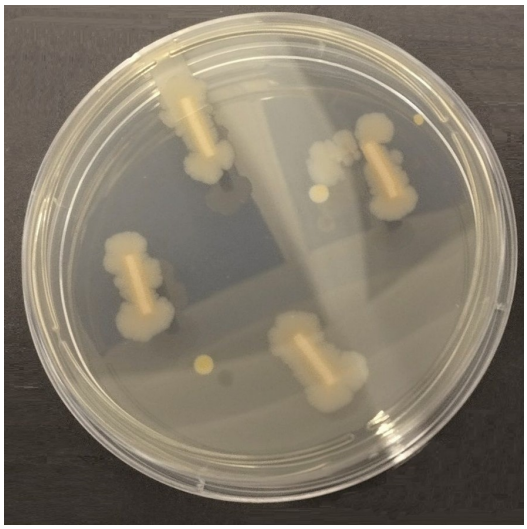
Figure 4. Permeate flux values for three filtration variants; (a) Actual measured values, (b) Normalized values.

Figure 5 shows the growth of bacterial cultures around membrane fragments placed in Petri dishes: (a) initial state and (b) image after 24 hours of incubation. Figure 5b clearly shows the appearance of bacterial colonies on solid support adjacent to the membrane fragments. The observed growth indicates the migration of live bacterial cells from the membrane surface to the agar medium, where they could multiply under favourable conditions. The arrangement of colonies around the samples suggests that viable bacteria were present on the membrane surface after the filtration process and then demonstrated the ability to colonize the surrounding medium, indicating a lack of bactericidal effect. These observations confirm that any interactions between the membrane and microorganisms were bacteriostatic, not lethal, limiting local surface colonization but not eliminating live cells at test conditions, which to some extent seems to be contrary to previous results (Szwast et al.,

2023). However, it should be emphasized that experimental conditions in the present work and in the ASTM test differ significantly in contact time and composition of the surrounding medium (e.g., the presence of nutrient).



(a)



(b)

Figure 5. The growth of bacterial cultures around the membrane fragments on the Petri dishes: (a) initial, (b) after 24h of incubation.

After completing the tests involving CuO-modified membranes, copper was analysed in the retentate and permeate streams after 96 hours of continuous operation of the membrane module. Within the detection limits of the analytical method used, no Cu was detected in either the permeate or retentate. This result, of course, does not definitively confirm the absence of CuO nanoparticle released from the membrane surface, but it does indicate that the degradation of active layer (if any) is negligible and should not affect the quality of the purified stream or the durability of the membrane's functional properties.

3.3. Model analysis of biofouling mechanisms

In long-term membrane operation, fouling rarely develops at a constant rate, as assumed in classical pore-blocking models. From a process-engineering perspective, the intensity of resistance buildup often changes over time due to evolving surface coverage, restructuring of deposited material, and biological activity. Therefore, while the Hermia model provides a useful first-order description of dominant fouling mechanisms, an extended formulation capable of capturing time-dependent fouling dynamics is required to better reflect real operating conditions.

In the literature on the mathematical description of fouling and biofouling, models based on the Hermia approach are commonly used (Niu et al., 2022; Shams et al., 2022). It allows for the description of permeate flux changes as a function of time by relating them to the dominant fouling mechanism. The general form of the Hermia model equation is presented in Eq. (1) (Pereira et al., 2023).

$$\frac{\mathrm{d}^2 t}{\mathrm{d}V^2} = k\left(\frac{\mathrm{d}t}{\mathrm{d}V}\right)^n \tag{1}$$

where t is the filtration time [s], V is the permeate volume [m^3], k is the fouling rate [unit depends on n value] and n is the exponent defining the fouling mechanism [−]. The fouling constant k has units dependent on the value of exponent n and can be expressed as $s^{1-n}m^{3n-6}$. For the mechanisms considered in this study the corresponding units are: $s{\cdot}m^{-6}$ for $n = 0$, m^{-3} for $n = 1$, $s^{-0.5}m^{-1.5}$ for $n = 1.5$, and s^{-1} for $n = 2$.

Different fouling mechanisms can be described using the Hermia model by selecting an appropriate value of the exponent n, which determines the dominant pore-blocking regime. When $n = 2$, the model represents complete blocking, whereas $n = 1.5$ corresponds to standard blocking. A value of $n = 1$ describes intermediate blocking, while $n = 0$ is associated with cake formation. The choice of the exponent thus allows the observed decline in permeate flux to be linked directly to the physical nature of the fouling phenomena occurring on and within the membrane structure. A graphical interpretation of the described fouling phenomena is presented in Figure 6.

To determine the mechanism responsible for fouling and biofouling in the studies presented in this paper, the Hermia model was fitted to the results presented in Fig. 4b, covering the three analysed filtration variants. For each variant and for all four values of the exponent n, the model coefficient was estimated by selecting the parameter k using the least squares method. The Bayesian Information Criterion (BIC) was then calculated to assess the quality of the model fit (Lee et al., 2014). The best model was the one for which the BIC value reached its minimum (Zhang et al., 2023), indicating the most adequate description of the observed changes in permeate flux density. The calculated k, BIC, R^2, and RMSE values are collected in Table 3.

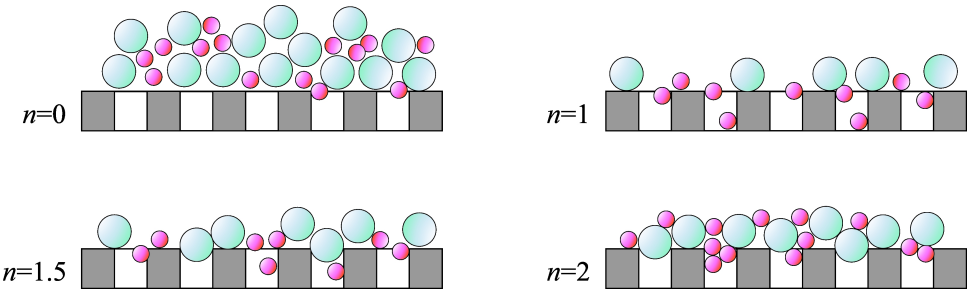


Figure 6. Graphical interpretation of the fouling phenomena described by Hermia equation: $n = 0$ is associated with cake formation, $n = 1$ describes intermediate blocking, $n = 1.5$ corresponds to standard blocking, $n = 2$ represents complete blocking.

Table 3. Calculated values of the k coefficient and the BIC criterion, R^2 and RMSE for Hermia model fits.

		Pure water–PP membrane	Pure water + *E. coli* – PP membrane	Pure water + *E. coli* –PP+CuO membrane
$n = 2$	k	0.0042	0.0224	0.0126
	BIC	−66917	−32647	−30691
	R^2	0.998	0.979	0.976
	RMSE	0.003	0.063	0.074
$n = 1.5$	k	0.0045	0.0293	0.0149
	BIC	−64075	−28415	−27989
	R^2	0.998	0.969	0.945
	RMSE	0.004	0.089	0.093
$n = 1$	k	0.0048	0.0378	0.0176
	BIC	−58465	−25504	−26129
	R^2	0.998	0.949	0.921
	RMSE	0.007	0.115	0.109
$n = 0$	k	0.0056	0.0633	0.0245
	BIC	−51376	−22052	−23692
	R^2	0.991	0.903	0.875
	RMSE	0.012	0.154	0.134

Analysis of the data presented in Table 3 indicates that for all filtration variants, the best model fit (lowest BIC value) was obtained for $n = 2$. The analysis of both R^2 and RMSE values also indicates that the best fit is obtained for $n = 2$. This means that the fouling process is best described by the complete blocking regime. In this case, the increase in filtration resistance occurs in a mixed mode, meaning it is not solely determined by membrane surface blocking or pore blocking. This mechanism is commonly observed in ultrafiltration and microfiltration processes of biological and colloidal solutions, where partial particle deposition on the surface and their penetration into the porous structure simultaneously occur (AlSawaftah et al., 2022; Yang et al., 2022). Figure 6 presents the measurement data obtained for three filtration variants, along with the corresponding model curve determined using the Hermia equation for $n = 2$.

Analysis of the graphs presented in Fig. 7 reveals significant differences in the quality of the Hermia model fit for $n = 2$ depending on the filtration variant. In variant Fig. 7a, the model curve matches the experimental data very well, confirming that the intermediate blocking mechanism adequately describes the observed mild fouling behaviour. However, a different situation occurs in variants in Fig. 7b and Fig. 7c. Although for both cases the value of $n = 2$ provided the best fit among the four Hermia model regimes considered, the graphs clearly show that the model's agreement with the experimental data is far from satisfactory. These differences indicate that fouling in the presence of a bacterial suspension is more complex and requires the use of extended or hybrid models that allow for a more accurate description of the process dynamics in these two filtration variants.

The literature on modelling degradation, aging, and the growth of cumulative phenomena increasingly utilizes approaches based on reliability theory, where the description of event intensity variation over time is crucial. One of the most commonly used distributions in such analysis is the Weibull distribution, traditionally used in statistics and survival analysis to model time to failure or time between events (Weibull, 1951). The model equation has the following form:

$$S(t) = e^{-\left(\frac{t}{\tau}\right)^m} \tag{2}$$

where $S(t)$ is the probability that the system survives until time t [s], τ is the time scale parameter, m is the shape parameter, which describes how the rate of events changes over time: when $m < 1$, the rate decreases and early failures dominate; $m = 1$ it remains constant, corresponding to the exponential case; and when $m > 1$, the rate increases, reflecting ageing or the accumulation of damage.

The classical Hermia model for $n = 2$ (see *Appendix*), which provided the best description for all three filtration variants considered, describes the exponential decay of flux, assuming a constant blocking intensity (a constant hazard):

$$J = J_0 e^{-kt} \tag{3}$$

where J is the permeate flux [$m^3h^{-1}m^{-2}$], J_0 is the initial permeate flux [$m^3h^{-1}m^{-2}$] and k is the fouling rate (defined earlier).

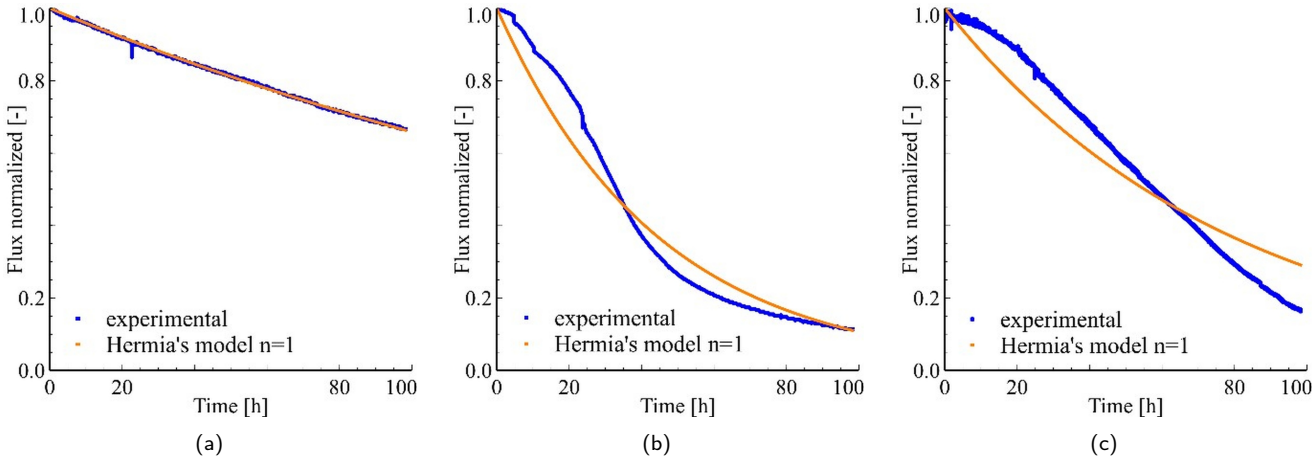


Figure 7. Normalized permeate flux: experimental (blue line) and Hermia model curve (orange line); (a) pure water filtration with PP membrane, (b) pure water with bacterial suspension filtration with PP membrane, (C) pure water with bacterial suspension filtration with PP+CuO membrane.

However, real fouling, especially biofouling, rarely occurs at a constant rate. Therefore, the Hermia model (Eq. 3) was generalized to the Weibull form:

$$J = J_0 e^{(-kt)^m} \tag{4}$$

where the shape parameter m allows the process to be described with variable intensity, i.e., with a fouling rate that changes over time rather than remains constant. In this formulation, $m < 1$ corresponds to a decreasing fouling rate, $m = 1$ represents a constant-rate process equivalent to the classical exponential model, whereas $m > 1$ indicates an increasing fouling rate during filtration. The Weibull formulation thus provides a natural extension of the Hermia's $n = 2$ model, preserving its structure while enabling a more realistic representation of fouling dynamics.

Table 4 presents the least-squares-fitted values of the parameters k and m for the three filtration variants.

Table 4. Calculated k and m coefficients and BIC values for the Weibull-generalized Hermia model fits.

	Pure water–PP membrane	Pure water + *E. coli*–PP membrane	Pure water + *E. coli*–PP+CuO membrane
k	0.0041	0.0224	0.0141
m	0.98	1.35	1.65
BIC	−67509	−38967	−54681
R^2	0.999	0.985	0.999
RMSE	0.003	0.037	0.009

When analysing the BIC (Bayesian Information Criterion) values, it should be noted that for all examined cases the data are better described by the model extended with the Weibull formulation than by the standard Hermia model (see Table 3). Similar conclusions can be drawn from the analysis of the remaining statistical parameters. Moreover, for pure-water filtration on the PP membrane, the parameter m differs only slightly from 1, meaning it deviates only marginally from the classical Hermia model for $n = 1$. In contrast, for both the filtration of water containing *E. coli* using the PP membrane and the filtration of water containing *E. coli* using the PP+CuO membrane, the exponent m takes values noticeably higher than 1. Furthermore, for the PP membrane it is lower ($m = 1.35$) than for the PP+CuO membrane, which exhibits bacteriostatic properties ($m = 1.65$).

The Weibull model makes it possible to separate the time scale of fouling development (parameter k) from the nature of the flux-decline evolution (parameter m). The lower k value obtained for the PP+CuO membrane (bacteriostatic) indicates a slower initial rate of flux reduction and an extended period of effective membrane operation. In contrast, the higher m value reflects a more strongly accelerating fouling behaviour in the later stages of filtration, likely associated with the progressive accumulation and restructuring of biological material at the membrane surface, which, after reaching a certain critical level, forms a rapidly densifying layer.

Figure 8 presents the measurement data obtained for the two filtration variants in which a bacterial suspension was used, along with the corresponding model curve determined using the Hermia model generalized to Weibull form. Since the results obtained for the generalized model in the case of filtration of pure water and a PP membrane do not differ significantly from the results obtained from the classical Hermia model, Fig. 8 only presents the model fits for those filtration variants in which pure water containing a bacterial suspension was used.

Moreover, in both the Hermia model and its extension to the Weibull model, the parameter k defines the time scale of fouling, and thus the rate of flux decay (Pereira et al., 2023).

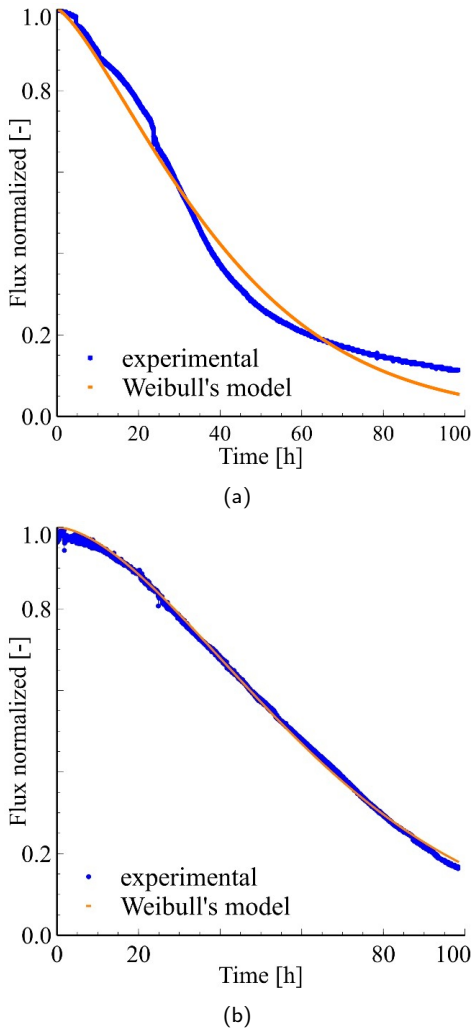


Figure 8. Normalized permeate flux: experimental (blue line) and Weibull model curve (orange line); (a) pure water with bacterial suspension filtration with PP membrane, (b) pure water with bacterial suspension filtration with PP+CuO membrane.

The characteristic time of the process can be determined from the condition

$$(kt^*)^m = 1 \tag{5}$$

which leads to (for every m value)

$$t^* = \frac{1}{k} \tag{6}$$

i.e., the moment at which the flux decreases to

$$J = \frac{J_0}{e} \tag{7}$$

For PP membrane, the characteristic time is 45 hours and for PP+CuO membrane it is 71 hours. This means that the bactericidal membrane maintains a high flux level for a much longer period and demonstrates significantly greater temporal resistance to fouling than the reference membrane.

4. CONCLUSIONS

The results of this study demonstrate that surface modification of capillary polypropylene membranes with a thin, porous polysulfone layer containing CuO nanoparticles significantly improves the long-term operational stability of membrane filtration processes conducted under constant transmembrane pressure in biologically active environments. Morphological and structural analyses (SEM, XRF, porosimetry) confirmed that the modification was successfully introduced into the near-surface region of the membrane without causing detrimental changes to its intrinsic porous structure or initial hydraulic performance.

Long-term cross-flow filtration experiments revealed that, despite similar initial permeate fluxes, membranes modified with CuO nanoparticles exhibited a substantially slower rate of hydraulic resistance buildup in the presence of E. coli. As a result, the cumulative permeate volume obtained over 96 hours of continuous operation was nearly 43% higher than that of the unmodified polypropylene membranes. From a process-engineering perspective, this improvement corresponds to a prolonged effective operating period of the membrane module and a reduced intensity of biofouling-driven flux decline under steady operating conditions.

Analysis of permeate flux decline using the Hermia model indicated that, for all filtration variants, the dominant fouling mechanism was best described by the complete blocking regime ($n = 2$). However, the limited ability of the classical Hermia model to capture the evolving dynamics of biofouling under long-term operation motivated the application of a generalized Weibull formulation. This extended approach enabled separation of the fouling time scale from the temporal evolution of fouling intensity, providing a more realistic description of resistance development in biologically active systems.

The Weibull-based analysis showed that membranes modified with CuO nanoparticles were characterized by a lower initial fouling rate and a significantly longer characteristic fouling time compared to the reference membranes. The characteristic time increased from approximately 45 hours for unmodified polypropylene membranes to 71 hours for CuO-modified membranes, indicating a delayed transition to high-resistance operating conditions. In practical terms, this behaviour suggests extended filtration cycles, delayed cleaning requirements, and improved reliability of membrane operation in continuous processes.

Overall, the presented results confirm that incorporating bacteriostatic CuO nanoparticles into the membrane surface represents an effective strategy for mitigating biofouling-induced performance deterioration without compromising membrane selectivity or hydraulic functionality. The combination of long-term experimental evaluation with time-resolved process modelling provides a framework that is directly applicable to the design, optimization, and assessment of membrane filtration systems operated under realistic process conditions.

From an application perspective, the obtained results indicate that bacteriostatic surface modification with CuO nanoparticles may represent a promising strategy for improving the long-term stability of membrane systems used in water treatment and other biologically active filtration processes. The demonstrated extension of effective operating time under constant transmembrane pressure suggests potential benefits in terms of reduced cleaning frequency, improved process continuity, and lower operational costs. Future studies should focus on verification of the observed effects under pilot- and industrial-scale operating conditions, as well as on long-term durability of the modifying layer and its performance in the presence of more complex natural microbial consortia and feed compositions.

SYMBOLS

A	membrane area, m^2
J	permeate flux, $m^3m^{-2}h^{-1}$
J_0	initial permeate flux, $m^3m^{-2}h^{-1}$
k	fouling rate constant (Hermia model), units depend on exponent n
m	Weibull shape parameter, –
n	Hermia model exponent describing fouling mechanism, –
R^2	coefficient of determination, –
SD	standard deviation, μm
S	survival probability function (Weibull model), –
t	time, s
V	permeate volume, m^3

Greek symbols

μ_{ln}	mean of log-normal pore size distribution, –
ρ_{ln}	standard deviation of log-normal pore size distribution, –
τ	characteristic time scale parameter (Weibull model), s

Abbreviations

BIC	Bayesian Information Criterion
CFU	colony forming units
CuO	copper(II) oxide
EPS	extracellular polymeric substances
LB	Luria–Bertani broth
NMP	N-methyl-2-pyrrolidone
PSf	polysulfone
RMSE	root mean square error
RLU	relative light units
SEM	scanning electron microscopy
TMP	transmembrane pressure
VBNC	viable but nonculturable
XRF	X-ray fluorescence

REFERENCES

Alnumani A., Abutaleb A., Park B., Mubashir M., 2024. Recent advancement on water filtration membranes: navigating biofouling challenges. *Environ. Res.,* 251, 118615. DOI: 10.1016/j.envres.2024.118615.

AlSawaftah N., Abuwatfa W., Darwish N., Husseini G.A., 2022. A review on membrane biofouling: prediction, characterization, and mitigation. *Membranes,* 12. DOI: 10.3390/membranes12121271.

Asamoah R.B., Annan E., Mensah B., Nbelayim P., Apalangya V., Onwona-Agyeman B., Yaya A., 2020. A comparative study of antibacterial activity of CuO/Ag and ZnO/Ag nanocomposites. *Adv. Mater. Sci. Eng.,* 2020, 7814324. DOI: 10.1155/2020/7814324.

Banerjee I., Pangule R.C., Kane R.S., 2011. Antifouling coatings: recent developments in the design of surfaces that prevent fouling by proteins, bacteria, and marine organisms. *Adv. Mater.*, 23, 690–718. DOI: 10.1002/adma.201001215.

Dadi R., Azouani R., Traore M., Mielcarek C., Kanaev A., 2019. Antibacterial activity of ZnO and CuO nanoparticles against gram positive and gram negative strains. *Mater. Sci. Eng.: C,* 104, 109968. DOI: 10.1016/j.msec.2019.109968.

Dehghani S., Peighambardoust S.H., Peighambardoust S.J., Hosseini S.V., Regenstein J.M., 2019. Improved mechanical and antibacterial properties of active LDPE films prepared with combination of Ag, ZnO and CuO nanoparticles. *Food Packag. Shelf Life,* 22, 100391. DOI: 10.1016/j.fpsl.2019.100391.

Desiriani R., Susanto H., Aryanti N., Abriyanto H., 2023. Improvement of the antifouling and antibacterial properties of polyethersulfone membrane by incorporating the natural additives collagen and green tea. *Results Eng.,* 18, 101176. DOI: 10.1016/j.rineng.2023.101176.

Di Martino P., 2018. Extracellular polymeric substances, a key element in understanding biofilm phenotype. *AIMS Microbiology,* 4, 274–288. DOI: 10.3934/microbiol.2018.2.274.

Dumitriu R.P., Sacarescu L., Macocinschi D., Filip D., Vasile C., 2016. Effect of silver nanoparticles on the dispersion, rheological properties and morphological aspect of solvent cast polyurethane/biopolymers bionanocomposite membranes. *J. Adhes. Sci. Technol.,* 30, 1716–1726. DOI: 10.1080/01694243.2015.1111287.

Gaylarde C.C., Morton L.H.G., 1999. Deteriogenic biofilms on buildings and their control: a review. *Biofouling,* 14, 59–74. DOI: 10.1080/08927019909378397.

Geng C., Zhao F., Wang Q., Zheng S., Liu Y., Niu H., Zhang J., Dong H., 2022. Anti-biofouling property and anti-leaching investigation of modifier for PVDF ultrafiltration membrane by incorporating antibacterial graphene oxide derivatives. *J. Environ. Chem. Eng.,* 10, 108558. DOI: 10.1016/j.jece.2022.108558.

Khan S.A., Shakoor A., 2023. Recent strategies and future recommendations for the fabrication of antimicrobial, antibiofilm, and antibiofouling biomaterials. *Int. J. Nanomedicine,* 18, 3377–3405. DOI: 10.2147/IJN.S406078.

Krasiński A., Stor M., Kryszczyńska K., Scalese S., 2025. Reduction of biofouling rate of water filters exposed to *Escherichia coli* by incorporating aluminosilicate-Ag composite particles into melt-blown media. *Chem. Process Eng.: New Front.,* 46, e103. DOI: %2010.24425/cpe.2025.155541.

Lee E.R., Noh H., Park B.U., 2014. Model selection via Bayesian information criterion for quantile regression models. *J. Am. Stat. Assoc.,* 109, 216–229. DOI: 10.1080/01621459.2013.836975.

Liu J., Yang L., Kjellerup B.V., Xu Z., 2023. Viable but non-culturable (VBNC) state, an underestimated and controversial microbial survival strategy. *Trends Microbiol.,* 31, 1013–1023. DOI: 10.1016/j.tim.2023.04.009.

Momba M.N.B., Kfir R., Venter S.N., Cloete T.E., 2000. An overview of biofilm formation in distribution systems and its impact on the deterioration of water quality. *Water SA,* 26, 59–66.

Niu B., Yang L., Meng S., Liang D., Liu H., Yang L., Shen L., Zhao Q., 2022. Time-dependent analysis of polysaccharide fouling by Hermia models: reveal the structure of fouling layer. *Sep. Purif. Technol.,* 302, 122093. DOI: 10.1016/j.seppur.2022.122093.

Pandey M., Singh M., Wasnik K., Gupta S., Patra S., Gupta P.S., Pareek D., Chaitanya N.S.N., Maity S., Reddy A.B.M., Tilak R., Paik P., 2021. Targeted and enhanced antimicrobial inhibition of mesoporous ZnO–Ag_2O/Ag, ZnO–CuO, and ZnO–SnO_2 composite nanoparticles. *ACS Omega,* 6, 31615–31631. DOI: 10.1021/acsomega.1c04139.

Pereira G.L.D., Cardozo-Filho L., Jegatheesan V., Guirardello R., 2023. Generalization and expansion of the Hermia model for a better understanding of membrane fouling. *Membranes,* 13, 290. DOI: 10.3390/membranes13030290.

Persson K.M., Gekas V., Trägårdh G., 1995. Study of membrane compaction and its influence on ultrafiltration water permeability. *J. Membr. Sci.,* 100, 155–162. DOI: 10.1016/0376-7388(94)00263-X.

Salama Y., Chennaoui M., Sylla A., Mountadar M., Rihani M., Assobhei O., 2016. Characterization, structure, and function of extracellular polymeric substances (EPS) of microbial biofilm in biological wastewater treatment systems: a review. *Desalin. Water Treat.*, 57, 16220–16237. DOI: 10.1080/19443994.2015.1077739.

Shams H., Alavi Moghaddam M.R., Maknoon R., Mąkinia J., Hasani Zonoozi M., 2022. Fouling mechanisms in anoxic-aerobic sequencing batch membrane bioreactor based on adapted Hermia models and main foulant characteristics. *J. Environ. Manage.,* 323, 116146. DOI: 10.1016/j.jenvman.2022.116146.

Sotto A., Boromand A., Zhang R., Luis P., Arsuaga J.M., Kim J., van der Bruggen B., 2011. Effect of nanoparticle aggregation at low concentrations of TiO_2 on the hydrophilicity, morphology, and fouling resistance of PES-TiO_2 membranes. *J. Colloid Interface Sci.,* 363, 540–550. DOI: 10.1016/j.jcis.2011.07.089.

Szwast M., Polak D., Perelshtein I., Gedanken A., Krasiński A., Stor M., Piątkiewicz W., Fabianowski W., 2023. Research on structural and process properties of polysulfone membranes modified by CuO. *Desalin. Water Treat.,* 316, 574–582. DOI: 10.5004/dwt.2023.30173.

Tian L., Zhou P., Graham N., Li G., Yu W., 2023. Long-term operation and biofouling of graphene oxide membrane in practical water treatment: insights from performance and biofilm characteristics. *J. Membr. Sci.,* 680, 121761. DOI: 10.1016/j.memsci.2023.121761.

van der Bruggen B., Braeken L., Vandecasteele C., 2002. Flux decline in nanofiltration due to adsorption of organic compounds. *Sep. Purif. Technol.,* 29, 23–31. DOI: 10.1016/S1383-5866(01)00199-X.

Vishwakarma V., 2020. Impact of environmental biofilms: industrial components and its remediation. *J. Basic Microbiol.,* 60, 198–206. DOI: 10.1002/jobm.201900569.

Weibull W., 1951. A statistical distribution function of wide applicability. *J. Appl. Mech. Sep,* 18, 293–297, DOI: 10.1115/1.4010337.

Yang Y., Bar-Zeev E., Oron G., Herzberg M., Bernstein R., 2022. Biofilm formation and biofouling development on different ultrafiltration membranes by natural anaerobes from an anaerobic membrane bioreactor. *Environ. Sci. Technol.,* 56, 10339–10348. DOI: 10.1021/acs.est.2c02007.

Younas H., Fei Y., Shao J., He Y., 2016. Developing an antibacterial super-hydrophilic barrier between bacteria and membranes to mitigate the severe impacts of biofouling. *Biofouling* 32, 1089–1102. DOI: 10.1080/08927014.2016.1229775.

Zhang H., Zhu S., Yang J., Ma A., 2022. Advancing strategies of biofouling control in water-treated polymeric membranes. *Polymers*, 14, 1167. DOI: 10.3390/polym14061167.

Zhang J., Yang Y., Ding J., 2023. Information criteria for model selection. *WIREs Comput. Stat.*, 15, e1607. DOI: 10.1002/wics.1607.

APPENDIX

Derivation of the Hermia model expressed in terms of permeate flux

The general form of the Hermia fouling model is given by

$$\frac{\mathrm{d}^2 t}{\mathrm{d}V^2} = k\left(\frac{\mathrm{d}t}{\mathrm{d}V}\right)^n \tag{A1}$$

where t is the filtration time, V is the permeate volume, k is the fouling constant, and n is an exponent defining the fouling mechanism.

The permeate flux is defined as

$$J = \frac{\mathrm{d}V}{\mathrm{d}t} \tag{A2}$$

Therefore

$$\frac{\mathrm{d}t}{\mathrm{d}V} = \frac{1}{J} \tag{A3}$$

Taking the derivative with respect to V

$$\frac{\mathrm{d}^2 t}{\mathrm{d}V^2} = \frac{\mathrm{d}}{\mathrm{d}V}\left(\frac{1}{J}\right) \tag{A4}$$

Using the chain rule and the relation between derivatives with respect to V and t

$$\frac{\mathrm{d}}{\mathrm{d}V} = \frac{\mathrm{d}}{\mathrm{d}t}\frac{\mathrm{d}t}{\mathrm{d}V} \tag{A5}$$

one obtains

$$\frac{\mathrm{d}^2 t}{\mathrm{d}V^2} = -\frac{1}{J^3}\frac{\mathrm{d}J}{\mathrm{d}t} \tag{A6}$$

Substituting this expression into the Hermia equation (Eq. A1) yields

$$-\frac{1}{J^3}\frac{\mathrm{d}J}{\mathrm{d}t} = k\left(\frac{1}{J}\right)^n \tag{A7}$$

After rearrangement, the differential equation in terms of permeate flux is obtained

$$\frac{\mathrm{d}J}{\mathrm{d}t} = -kJ^{3-n} \tag{A8}$$

For the particular case $n = 0$, Equation (A8) reduces to the form

$$\frac{dJ}{dt} = -kJ^3 \tag{A9}$$

Integration of this equation leads to

$$\frac{1}{J^2} = 2kt + \frac{1}{J_0^2} \tag{A10}$$

and finally

$$J = \frac{J_0}{\sqrt{1 + 2kJ_0^2 t}} \tag{A11}$$

For the particular case $n = 1$, Equation (A8) reduces to the form

$$\frac{dJ}{dt} = -kJ^2 \tag{A12}$$

Integration of this equation leads to

$$\frac{1}{J} = kt + \frac{1}{J_0} \tag{A13}$$

and finally

$$J = \frac{J_0}{1 + kJ_0 t} \tag{A14}$$

For the particular case $n = 1.5$, Equation (A8) reduces to the form

$$\frac{dJ}{dt} = -kJ^{1.5} \tag{A15}$$

Integration of this equation leads to

$$\frac{1}{\sqrt{J}} = 0.5kt + \frac{1}{\sqrt{J_0}} \tag{A16}$$

and finally

$$J = \frac{J_0}{\left(1 + 0.5k\sqrt{J_0}t\right)^2} \tag{A17}$$

For the particular case $n = 2$, Equation (A8) reduces to the form

$$\frac{dJ}{dt} = -kJ \tag{A18}$$

Integration of this equation leads to

$$\ln\left(\frac{J}{J_0}\right) = -kt \tag{A19}$$

and finally

$$J = J_0 e^{-kt} \tag{A20}$$

Chemical and Process Engineering: New Frontiers, 2026, 47(2), e131
DOI: 10.24425/cpe.2026.158129

Study of the photopolymerization process of luminescent-labeled photocurable compositions in liquid and gas media

Małgorzata Noworyta[1], Maciej Pilch[2,*], Dawid Kiesiewicz[2], Renata Kłaput[2], Joanna Ortyl[1]

[1] Faculty of Chemical Engineering and Technology, Cracow University of Technology, Warszawska 24, 31-155 Kraków, Poland
[2] Wind Engineering Laboratory, Faculty of Civil Engineering, Cracow University of Technology, Warszawska 24, 31-155 Kraków, Poland

*** Corresponding author, e-mail:** maciej.pilch@pk.edu.pl

Presented at
5th Seminar on Practical Aspects of Chemical Engineering PAIC 2025, 22–23 September 2025, Zaniemyśl, Poland.
Guest Editors: Andżelika Krupińska and Sylwia Włodarczak.

Article info:
Received: 07 December 2025
Revised: 28 February 2026
Accepted: 06 May 2026

Abstract
Although photocurable compositions are widely used in 3D printing, protective coatings and biomedical materials, their polymerization in oxygen-containing environments is strongly hindered by oxygen inhibition, which prolongs the reaction time and reduces the conversion rate of monomers. This study investigated the effect of the reaction environment (argon atmosphere and liquid media: distilled water and $CuSO_4$ solutions) on the kinetics of free-radical photopolymerization of four acrylic compositions (Bis-GMA with TMPTA or EBECRYL 45, 130, 3300 oligomers). The kinetics were monitored using Fluorescence Probe Technology (FPT) with a coumarin 102 fluorescence probe and photorheology under 365 nm UV-LED irradiation. The results showed that in an argon atmosphere, oxygen inhibition is eliminated, resulting in the shortest induction times. In liquid environments, induction times are longer, but initial polymerization rates are higher than in the gas phase due to multiple reflections of UV radiation and a higher effective dose. The addition of Cu^{2+} ions partially suppresses this effect by absorbing light. The work provides new data on the design of photopolymerizable systems with increased oxygen resistance, which is important for applications in VPP photopolymerization 3D printing.

Keywords
photopolymerization, luminescence, light cured

1. INTRODUCTION

Photopolymerization is a chemical process involving the initiation and progression of polymerization under the influence of electromagnetic radiation, most commonly in the UV or visible light range. The absorption of photons by photoinitiators results in the formation of reactive radicals or cations, which initiate the formation of long polymer chains from monomers (Corrigan et al., 2019; Jandt and Mills, 2013). This mechanism allows for precise control of the reaction process both in terms of time and space, making photopolymerization an energy-efficient and more environmentally friendly process than techniques based on elevated temperatures (He et al., 2023). It has found wide application in coating technology, dental materials, 3D printing, biomedicine (including the production of hydrogels that imitate tissues) and electronics, particularly in the production of flexible functional components (Chiulan et al., 2021; Fiedor et al., 2020; Lu et al., 2022; Ribas-Massonis et al., 2022; Schneider et al., 2010; Tezel et al., 2025; Topa and Ortyl, 2020; Wang et al., 2023). In recent years, there has been intensive development of photoinitiators activated by visible light and near-infrared light, which significantly increases the safety of processes carried out in biological environments, e.g., in regenerative medicine (Gao et al., 2025; Xiao et al., 2025; Xu et al., 2025). At the same time, hybrid systems combining radical and cationic mechanisms, composites reinforced with nanomaterials such as graphene and smart formulations enabling process monitoring thanks to built-in luminescent probes are also being developed (Chen et al., 2025; Hola et al., 2021; Mohd Shuhairi et al., 2025).

Photopolymerization can be carried out in various phases, which significantly affects its kinetics and efficiency. In liquid systems, such as aqueous solutions, the process is easy to carry out, but its efficiency may be limited by light absorption by the solvent and slower diffusion of molecules. In gaseous systems, especially in an atmosphere of inert gases (argon, nitrogen), these limitations are minimal, resulting in faster reactions and high monomer conversion (Bowers et al., 2022; Hsieh and Zellers, 2002; Liz-Basteiro et al., 2023; Luo et al., 2024; Yang et al., 2023).

The most serious challenge in free radical photopolymerization remains oxygen inhibition. Oxygen, which dissolves easily in many solvents, reacts with radicals to form less reactive oxyradicals that inhibit polymer chain propagation. This phenomenon leads to longer induction times, reduced polymerization rates and lower conversion rates, resulting in materials with poorer mechanical properties and the presence of residual monomers. This problem is particularly important in open-air processes such as 3D printing and in biomedical applications. Inhibition is more intense in liquid systems where oxygen solubility is higher, while in gaseous systems under an inert atmosphere, this effect practically disappears. Strategies to reduce inhibition include the use of protective atmospheres,

© 2026. The Author(s). This is an open-access article distributed under the terms of the Creative Commons Attribution (CC-BY 4.0, https://creativecommons.org/licenses/by/4.0/), which permits unrestricted use, distribution, and reproduction in any medium, provided the original author and source are credited.

oxygen scavenger additives (e.g., triphenylphosphine), enzymatic oxygen removal systems (glucose/glucose oxidase), the use of thiol-ene or cationic mechanisms and increasing light intensity (Andrzejewska, 2001; Belon et al., 2010; O'Brien and Bowman, 2006; Cai et al., 2021; Li et al., 2024; Llorente et al., 2021; Müller et al., 2022; Zhang et al., 2025).

Optimizing photopolymerization requires advanced methods for monitoring reaction kinetics. Photo-DSC enables analysis of reaction heat and determination of the rate and activation energy of the process. Real-time FT-IR spectroscopy allows direct tracking of the disappearance of characteristic bonds, such as C=C bonds. Techniques based on luminescent probes (FPT), which use dyes sensitive to changes in viscosity and polarization of the environment, are of particular importance. The intensity or wavelength of the emitted light changes as polymerization progresses, enabling non-invasive monitoring of the process with high temporal and spatial resolution (Camposeo et al., 2022; Hu et al., 1998; Jiang and Drummer, 2020; Lang et al., 2022; Li et al., 2020; Szymaszek et al., 2023).

The use of luminescently labeled photopolymerizing compositions in liquid and gaseous environments allows for an in-depth understanding of the effect of oxygen on the kinetics of the process in different phases. Comparing reactions carried out in water, where oxygen inhibition is particularly strong, with reactions in an argon atmosphere, where this effect is almost completely absent, provides mechanistic insight into oxygen-related effects and can guide the rational design of oxygen-resistant photopolymer systems. This opens up new avenues of development in the areas of 3D printing, smart coatings and advanced polymer materials, making photopolymerization a key technology for sustainable innovation in science and industry.

2. EXPERIMENTAL PART

2.1. Materials

The study used systems consisting of 2,2-bis[4(2-hydroxy-3-methacryloxypropoxy)phenylene]propane (Bis-GMA, Sigma-Aldrich), trimethylolpropane triacrylate (TMPTA, Sigma-Aldrich), four-functional acrylated oligomer EBECRYL 45 (E45, Allnex), aliphatic diacrylate EBECRYL 130 (E130, Allnex), modified bisphenol-A-based epoxy acrylate oligomer EBECRYL 3300 (E3300, Allnex) and the photoinitiator diphenyl (2,4,6-trimethylbenzoyl) phosphine oxide (TPO, Allnex). In addition, 2,3,6,7-tetrahydro-9-methyl-1H,5H-quinolizino(9,1-gh) coumarin (coumarin 102) was used as a fluorescent probe to monitor the kinetics of the photopolymerization process.

2.2. Instrumentation

2.2.1. Rheometer

A Physica MCR 302 rheometer (Anton Paar) was used to determine the viscosity of the tested composites. For photorheological measurements, the device was equipped with a special attachment enabling the samples to be exposed to UV radiation using parallel plate geometry. The attachment was fitted with a Thorlabs M365L2 UV (30 mA, 8 mW/cm²) diode with a wavelength of 365 nm. The rheometer operated under controlled temperature conditions thanks to the use of a thermostat.

2.2.2. UV-Vis apparatus (Fluorescence Probe Technology)

A set of equipment included a SILVER fiber optic spectrophotometer -Nova 200 TEC fiber optic spectrophotometer from StellarNet Inc. with a spectral range of 190–1100 nm and a Roithner Laser Technik RLT365-10E UV-LED emitting radiation with a wavelength of $\lambda_{max} = 365$ nm, with a diode power

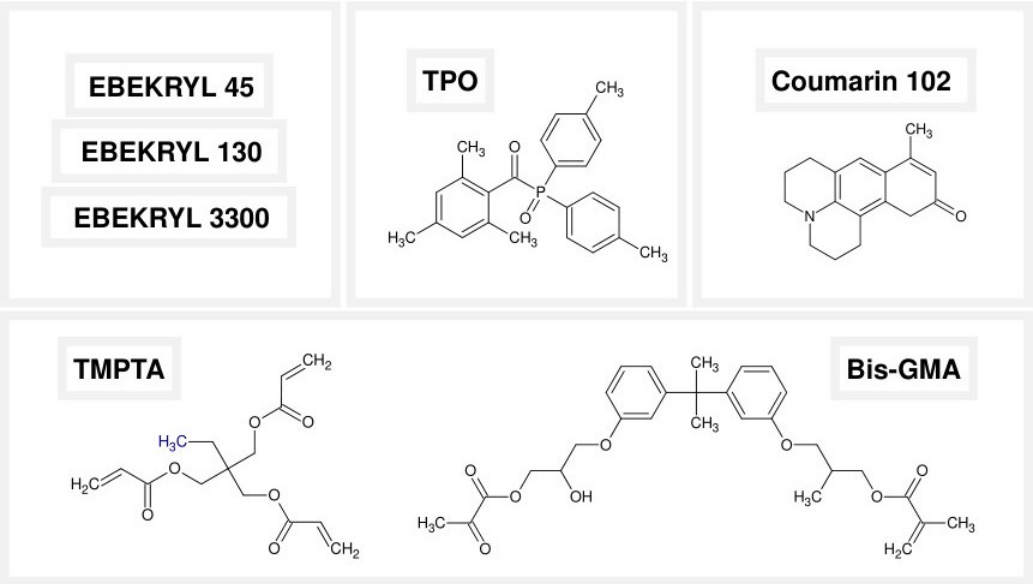


Figure 1. Compounds used for research.

of 22.5 mA (6 mW/cm^2). These components were connected using Fibrochem fiber optics and the diode was powered by a dedicated power supply controlled by a computer equipped with software enabling both UV source control and analysis of recorded data. The temperature of the system was stabilized by a Thorlabs ITC4020 thermostat working in conjunction with a Peltier module equipped with a heat sink. The sample was irradiated perpendicular to its surface using a UV-LED diode, while the optical fiber connected to the spectrophotometer was set at an angle of 30° to the diode axis.

2.3. Measurement methodology

2.3.1. Rheological and photorheological measurements

Rheological tests of photopolymerizable compositions were performed at 25 °C, setting the zero gap at 0.2 mm using a spindle with a diameter of 25.019 mm. The procedure began with applying the sample to the rheometer base and setting the appropriate distance between the spindle and the substrate. Once this was achieved, excess material was removed and the actual measurement started. The analysis was carried out at variable spindle speeds (shear rates) ranging from 1 s^{-1} to 100 s^{-1} for 550 seconds. A spindle with a diameter of 20 mm was used for photorheological tests. During photorheological measurements, after temperature stabilization, the composition was evenly spread on a UV-transmitting glass plate, the zero gap was set and the excess was removed. The total measurement time was 10 minutes and the UV source was activated simultaneously with its start. Irradiation began 10 seconds after the start of the measurement, which is reflected in the rapid increase in both mechanical moduli after this time. The total recording time was 600 seconds, but due to the rapid transition of the composition from sol to gel, the graphical analysis was limited to the first 150 seconds of the measurement.

2.3.2. Kinetic studies using the FPT technique

The composition prepared for testing was dripped onto a holder consisting of a microscope slide and a 0.1 mm thick ring glued to it. The tests were conducted in four environments: argon, distilled water, saturated copper sulphate solution and saturated copper sulphate solution with the addition of sulfuric acid at a concentration of 1 mol/dm^3. The selection of media allowed for the simultaneous assessment of the influence of oxygen content, optical properties and rheological characteristics on the course of photopolymerization. In order to conduct the tests in an aqueous environment, the prepared sample was placed on a polystyrene dish and then the dish was placed in the measuring chamber. For measurements in an argon environment, the measuring chamber was connected to an argon cylinder using a silicone hose before thermostating began. The measuring chamber was purged with argon for 2 minutes to ensure the removal of oxygen. Based on previous investigations, a purging time of 1 minute was found to be sufficient to reduce the oxygen concentration below the limit of detection. Therefore, a 2-minute purging period was applied, corresponding to an adopted safety factor of 2. For measurements in the remaining three environments, the sample was covered with the liquid before thermostating, to a depth of 5 mm below the surface. The tests were carried out in two modes: fast and slow data collection. In fast mode, the program collected the emission spectrum of the sample every 3 seconds and in the next stage, in slow mode, every 32 seconds. The program was set to 150 fast scans and 100 slow scans. The measurement of one sample in a given environment took a total of 80 minutes, of which 60 minutes were spent measuring the kinetics of photopolymerization and 20 minutes were spent thermostating the measuring chamber to stabilize the temperature at 25 °C.

The aim of the study was to determine the influence of the reaction environment on the kinetics of photopolymerization, analyzed by measuring changes in the R parameter using the FPT (Fluorescence Probe Technology) method. This technique enables real-time monitoring of the cross-linking process based on changes in the emission characteristics of a luminescent fluorescent probe placed in a photopolymerizable composition. With increasing monomer conversion and growing stiffness of the resulting polymer network, systematic modifications in the probe emission spectrum are observed (Fig. 2), reflected by the R parameter, defined as the ratio of the recorded emission spectrum at time t to the emission spectrum before polymerization. Analysis of the $R(t)$ function allows the determination of key kinetic parameters: the induction time t_{ind} and the initial polymerization rate $\left(\frac{dR}{dt}\right)_0$, which is a measure of the reaction dynamics in the early stage of crosslinked structure formation.

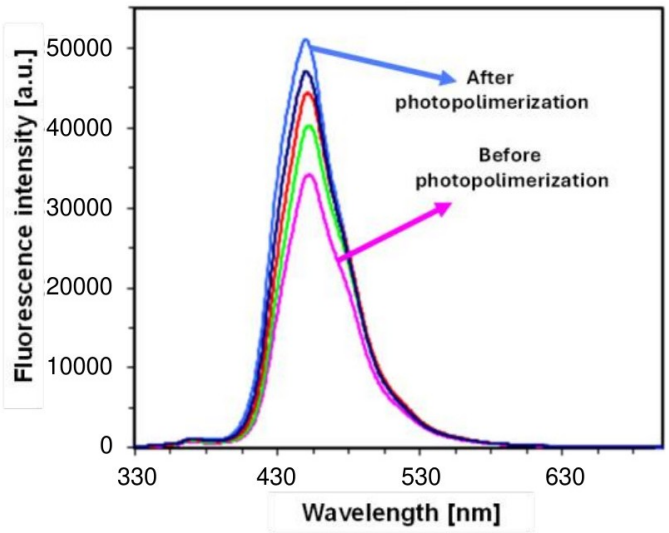


Figure 2. Changes in the emission spectrum of a fluorescent probe during the polymerization process for sample E45+BisGMA in a saturated copper(II) sulfate solution.

2.4. Sample preparation

For rheological and photorheological studies, four samples were prepared consisting of TPO photoinitiator added to the composition at a concentration of 1% by weight and E45+BisGMA, E130+BisGMA, E3300+BisGMA and TMPTA+BisGMA monomers in a 1:1 weight ratio for each composition. The compositions for testing the kinetics of photopolymerization using the FPT method were prepared with the addition of 0.1% by weight of a fluorescent probe (coumarin 102).

3. RESULTS

3.1. Rheological and photorheological studies

Figures 3–6 present the dependence of viscosity on shear rate for four compositions: E45 + BisGMA, E130 + BisGMA, E3300 + BisGMA and TMPTA + BisGMA. All tested systems exhibit shear-thinning behavior typical of non-Newtonian fluids, with viscosity decreasing as the shear rate increases. The most pronounced effect is observed in the case of the E45+BisGMA mixture, for which the viscosity initially reaches very high values, then decreases rapidly, stabilizing only at higher shear rates. This indicates a strong susceptibility of this system to liquefaction under the influence of deformation. The E130+BisGMA mixture is characterized by significantly higher rheological stability. Over the entire shear-rate range, the viscosity changes only slightly and remains close to approximately 16362 mPa·s. A similar trend, albeit with significantly higher viscosity values, is observed in the E3300+BisGMA system, in which the viscosity gradually but slightly decreases from approximately 48424 mPa·s. The lowest viscosity values were recorded for the TMPTA+BisGMA mixture, where, despite a slight decrease in viscosity with increasing shear, it remains relatively stable at around 10084 mPa·s. All graphs indicate the shear-rate ranges used to calculate the average viscosity, corresponding to regions of relatively stable viscosity behavior for each composition.

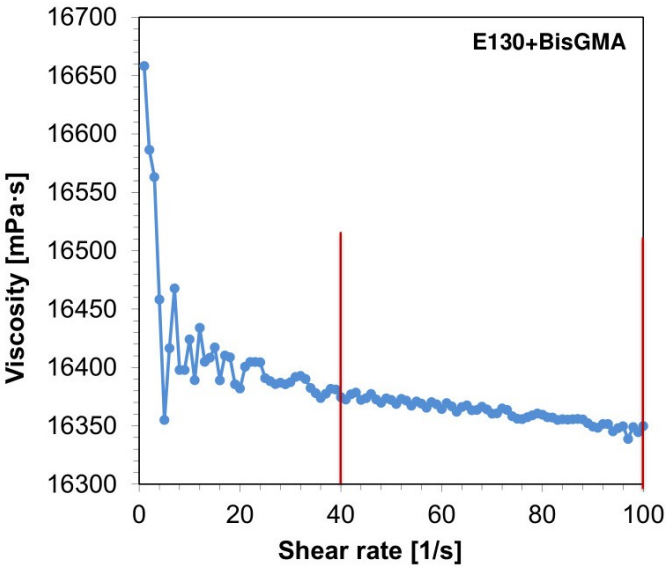


Figure 4. The dependence of viscosity on the shear rate of the E130+BisGMA sample, with the area from which the average viscosity of the composition was calculated marked.

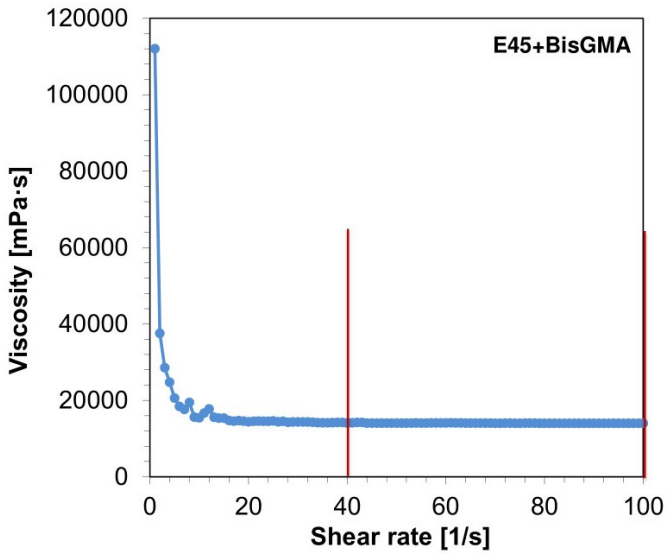


Figure 3. The dependence of viscosity on the shear rate of the E45+BisGMA sample, with the area from which the average viscosity of the composition was calculated marked.

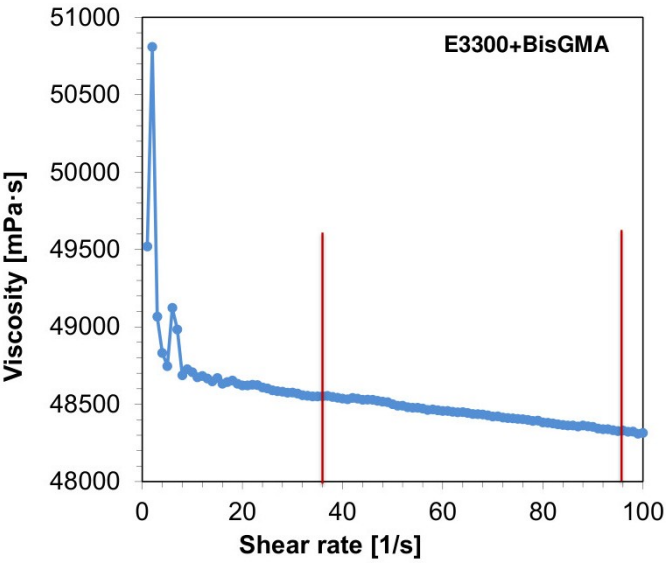


Figure 5. The dependence of viscosity on the shear rate of the E3300+BisGMA sample, with the area from which the average viscosity of the composition was calculated marked.

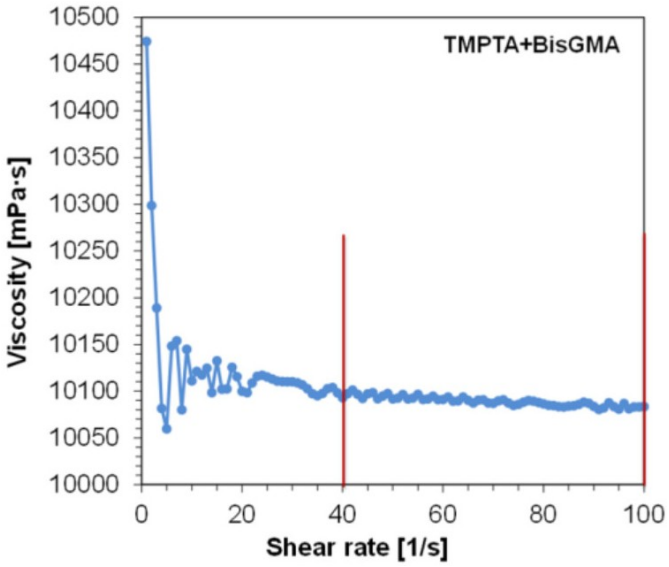


Figure 6. The dependence of viscosity on the shear rate of the TMPTA+BisGMA sample, with the area from which the average viscosity of the composition was calculated marked.

Based on rheological tests, changes in the conservative modulus, loss modulus and normal force were presented for four photopolymerizable compositions (Figs. 7–10) exposed to UV. In rheological studies, the gelation time, which corresponds to the moment of intersection of the conservative modulus and the loss modulus, was considered a key parameter. At this point, the material begins to behave like an elastic body, which indicates the formation of a three-dimensional polymer network. Analysis of the graphs and numerical data clearly shows that the individual compositions differ both in the rate of polymerization and in the amount of shrinkage accompanying the cross-linking process.

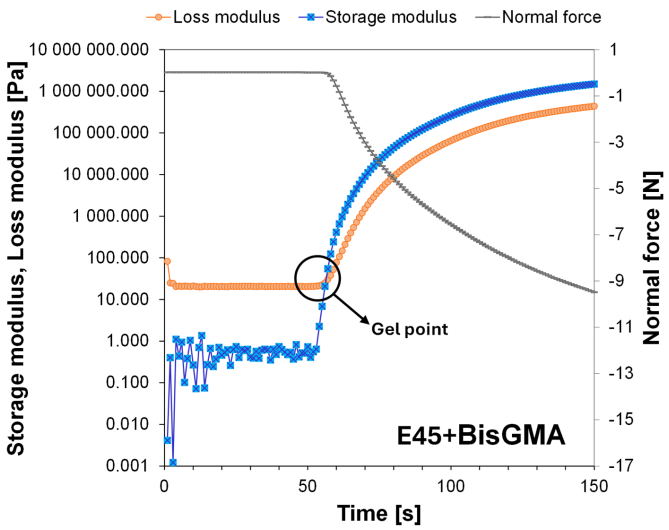


Figure 7. The relationship between the retention modulus, loss modulus and normal force over time, with the gel point marked for sample E45+BisGMA.

The E45+BisGMA sample reaches the gelation point 56 seconds after the start of the measurement, which indicates a moderate rate of network structure formation. The polymerization shrinkage calculated from Equation (1) for this composition is 1.40%, which is the highest value among all the materials tested. Analysis of the normal force curve confirms more intense shrinkage deformation after gel formation. The E130+BisGMA composition has one of the fastest polymerization processes, reaching the gel point after only 50 seconds. At the same time, the polymerization shrinkage of this sample is 1.00%, which is an intermediate value. The combination of a short gelation time and moderate shrinkage indicates a favorable balance between reactivity and dimensional stability during cross-linking.

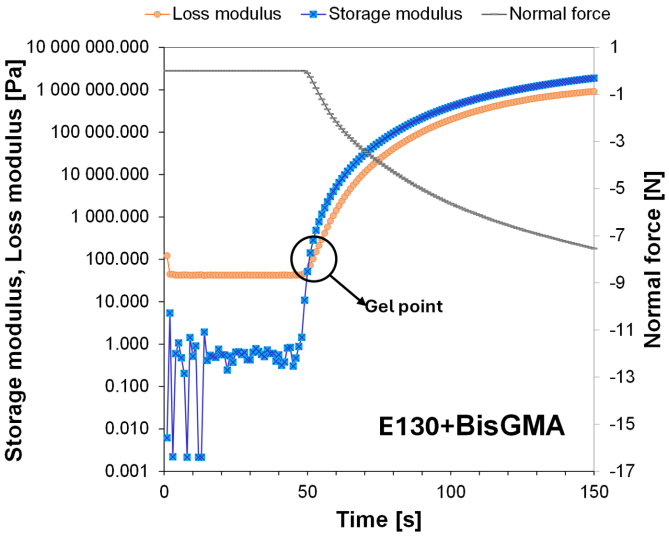


Figure 8. The relationship between the retention modulus, loss modulus and normal force over time, with the gel point marked for sample E130+BisGMA.

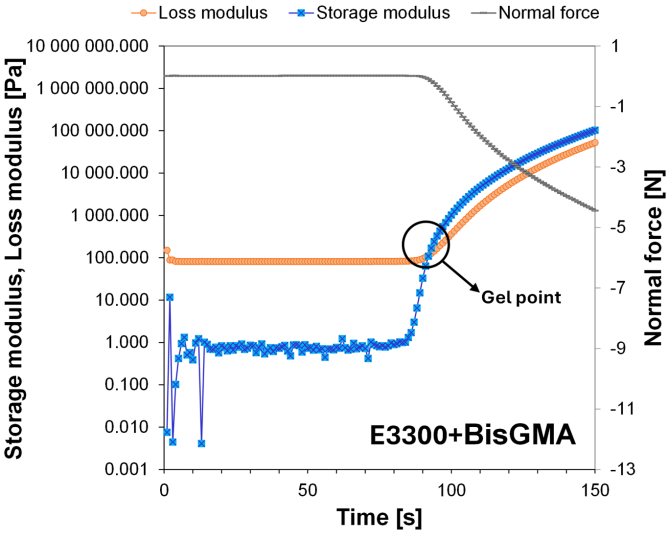


Figure 9. The relationship between the retention modulus, loss modulus and normal force over time, with the gel point marked for sample E3300+BisGMA.

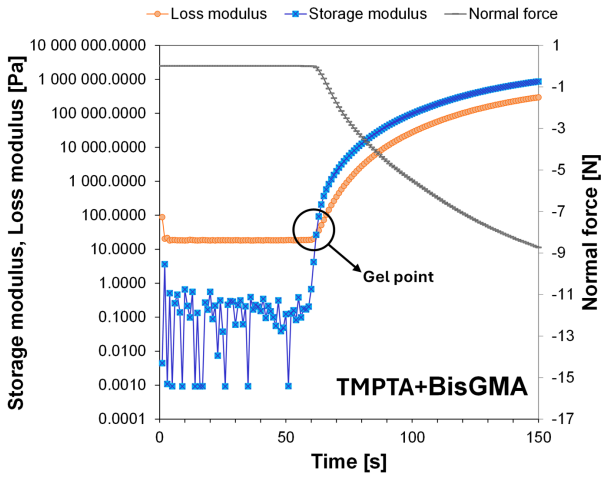


Figure 10. The relationship between the retention modulus, loss modulus and normal force over time, with the gel point marked for sample TMPTA+BisGMA.

The E3300+BisGMA composition exhibits the slowest polymerization kinetics, reaching the gel point only after 92 s — the longest gelation time among all tested samples. The slow transition from the viscous to the elastic phase is reflected in the lowest polymerization shrinkage of only 0.80%. The last of the tested compositions, TMPTA+BisGMA, reaches the gelation point after 62 seconds, which indicates a fast, but not the fastest, polymerization rate. The polymerization shrinkage value for this sample is also 1.00%. The presence of the trifunctional TMPTA monomer promotes the dynamic development of the cross-linked network, which is confirmed by the rapid increase in the conservative modulus and clear changes in normal force after reaching the gelation point. The data obtained during photorheological measurements are summarized in Table 1.

$$\text{Polymerization shrinkage [\%]} = \left(1 - \frac{d_{\text{before}}}{d_{\text{after}}}\right) \cdot 100\% \quad (1)$$

where: d_{after} – distance between the aluminum spindle and the glass base after completion of the polymerization process [mm], d_{before} – distance between the aluminum spindle and the glass base before the start of the polymerization process [mm].

Table 1. Photorheology measurement results.

Composition	Medium	Gel time [s]	Polymerization shrinkage [%]	Average viscosity [mPa·s]
E45+BisGMA	UV Light	56	1.40	–
E130+BisGMA	UV Light	50	1.00	16362
E3300+BisGMA	UV Light	92	0.80	48424
TMPTA+BisGMA	UV Light	62	1.00	10084

3.2. Kinetic measurements using the FPT method

Analysis of induction times (Table 2) showed that the shortest t_{ind} values occurred in an argon atmosphere, longer ones in water, even longer ones in a $CuSO_4$ solution and the longest ones in a $CuSO_4$–H_2SO_4 solution. This trend was fully confirmed by the $R(t)$ curves (Figs. 11–14). The mechanism behind the observed sequence is mainly due to oxygen inhibition. Under anaerobic conditions (argon), the quenching of radicals by oxygen is negligible, allowing propagation to start almost immediately. In an aqueous environment, however, dissolved oxygen is present, resulting in a short-term inhibition

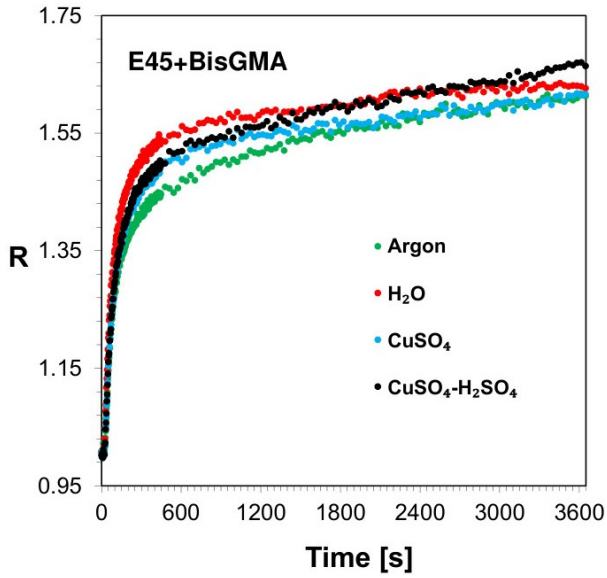


Figure 11. Graph showing the dependence of the r parameter on time for the composition named e45+bisgma in different environments.

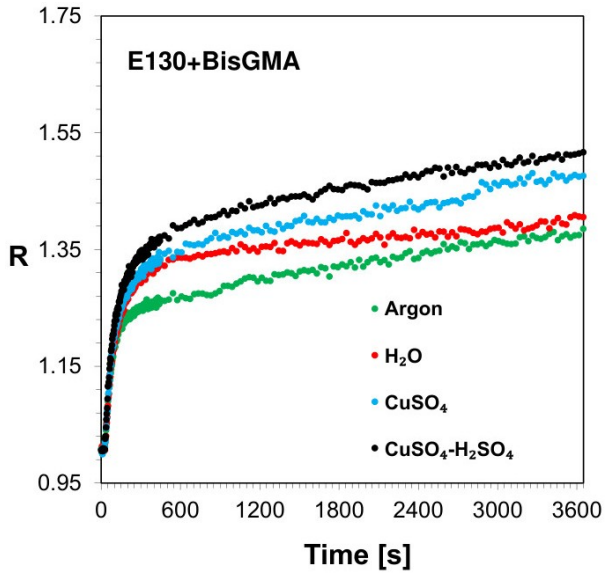


Figure 12. Graph showing the dependence of the r parameter on time for the composition named e130+bisgma in different environments.

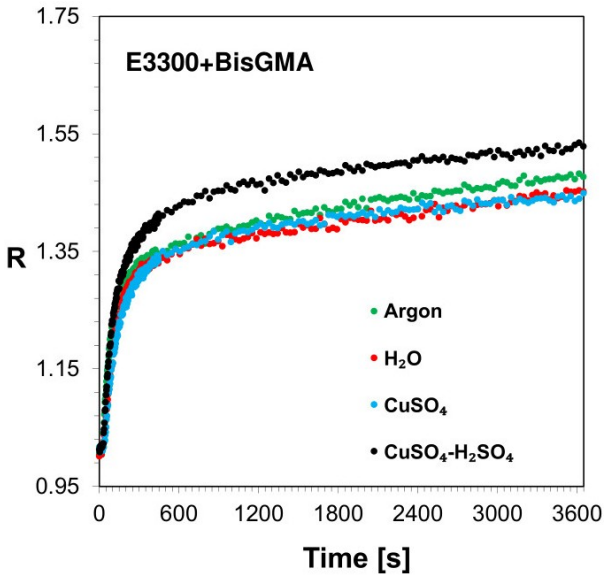


Figure 13. Graph showing the dependence of the r parameter on time for the composition named e3300+bisgma in different environments.

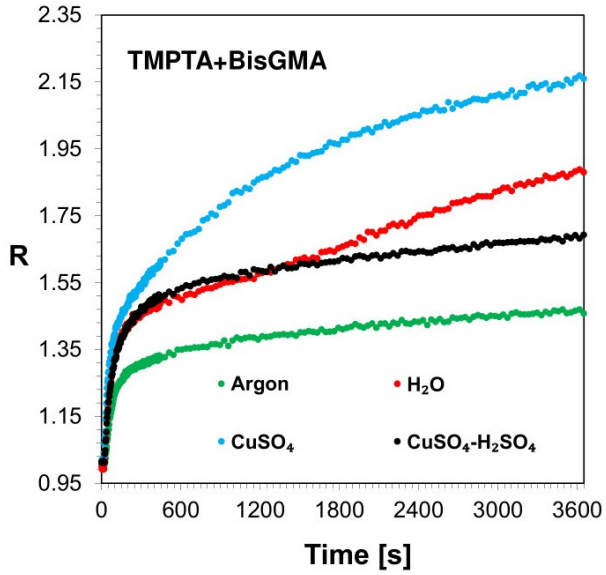


Figure 14. Graph showing the dependence of the r parameter on time for the composition named tmpta+bisgma in different environments.

of initiation. In the $CuSO_4$ solution, oxygen inhibition persists longer despite the presence of Cu^{2+} ions capable of reducing oxygen, because some oxygen remains available and, in addition, the liquid limits the diffusion of radicals. The strongest delay in initiation was observed in the $CuSO_4$–H_2SO_4 solution, where strongly hydrated copper(II) ions have a limited ability to reduce oxygen, which prolongs the time it takes to remove it from the reaction environment.

The values for the initial polymerization rates $\left(\frac{dR}{dt}\right)_0$ in liquid media, especially in water, were higher than in argon. This is due to fundamental optical differences between the gas and liquid phases. In argon, the UV beam penetrates the sample and is reflected to a minimal extent. In liquid media, however, multiple reflections occur at the phase boundary, leading to secondary irradiation of the sample and, consequently, an increase in the effective radiation dose. The higher photon flux results in more intense radical generation and a higher initial rate of increase of the R parameter.

Table 2. Results of kinetic studies using the FPT technique.

Composition	Medium	t_{ind} [s]	$\left(\frac{dR}{dt}\right)_0$
E45+BisGMA	Argon	18.15	$4.34 \cdot 10^{-3}$
	Distilled water	19.55	$6.26 \cdot 10^{-3}$
	$CuSO_4$	20.30	$4.72 \cdot 10^{-3}$
	$CuSO_4$–H_2SO_4	21.28	$4.75 \cdot 10^{-3}$
E130+BisGMA	Argon	25.09	$3.05 \cdot 10^{-3}$
	Distilled water	27.50	$3.15 \cdot 10^{-3}$
	$CuSO_4$	27.48	$3.16 \cdot 10^{-3}$
	$CuSO_4$–H_2SO_4	27.17	$4.00 \cdot 10^{-3}$
E3300+BisGMA	Argon	18.78	$3.20 \cdot 10^{-3}$
	Distilled water	24.73	$2.18 \cdot 10^{-3}$
	$CuSO_4$	27.18	$2.16 \cdot 10^{-3}$
	$CuSO_4$–H_2SO_4	27.51	$3.61 \cdot 10^{-3}$
TMPTA+BisGMA	Argon	15.07	$2.86 \cdot 10^{-3}$
	Distilled water	14.73	$5.34 \cdot 10^{-3}$
	$CuSO_4$	16.45	$7.45 \cdot 10^{-3}$
	$CuSO_4$–H_2SO_4	18.02	$4.59 \cdot 10^{-3}$

In $CuSO_4$ and $CuSO_4$–H_2SO_4 solutions, there is an additional effect of UV radiation absorption by Cu^{2+} ions, reducing the intensity of radiation reaching the interior of the sample. This has a dampening effect on the propagation rate, making $\left(\frac{dR}{dt}\right)_0$ in these media greater than in argon, but lower than in water. These trends are shown in the $R(t)$ curves (Figs. 11–14).

4. CONCLUSIONS

The investigated resin systems exhibited non-Newtonian shear-thinning behavior with viscosity and gelation characteristics strongly dependent on composition. Photorheological analysis confirmed that resin formulation governed polymerization rate and shrinkage, directly influencing network formation and dimensional stability. Kinetic studies using the FPT technique demonstrated a pronounced influence of the reaction environment on photopolymerization. The shortest induction times were observed under argon, confirming the role of oxygen inhibition, whereas aqueous and metal-ion-containing media prolonged the induction period. In contrast, the initial polymerization rate $\left(\frac{dR}{dt}\right)_0$ was higher in liquid environments, indicating the additional contribution of optical effects to the

reaction kinetics. Overall, the results highlight the combined impact of chemical and optical factors on photopolymerization and provide guidance for the development of oxygen-tolerant photopolymer systems.

ACKNOWLEDGEMENTS

The research work was conducted as part of the LIDER XII project (agreement no. LIDER/51/0270/L-12/20/NCBR/2021) titled "Multi-material 3D printer dedicated to production of solid metal and galvanic alloys parts, as well as metal-polymer hybrid elements using developed coupled technology of metal electrodeposition and photopolymerization of polymer resins" funded by the National Centre for Research and Development.

Part of the research work was conducted within the framework of PRELUDIUM project entitled "Kinetic-calorimetric studies of photopolymerization in thin porous layers using new two-component luminescent sensor systems" (contract no. UMO-2021/41/N/ST8/04127) funded by the National Science Center.

REFERENCES

Andrzejewska E., 2001. Photopolymerization kinetics of multifunctional monomers. *Prog. Polym. Sci.*, 26, 605–665. DOI: 10.1016/S0079-6700(01)00004-1.

Belon C., Allonas X., Croutxé-Barghorn C., Lalevée J., 2010. Overcoming the oxygen inhibition in the photopolymerization of acrylates: a study of the beneficial effect of triphenylphosphine. *J. Polym. Sci., Part A: Polym. Chem.*, 48, 2462–2469. DOI: 10.1002/pola.24017.

Bowers L.N., Stefaniak A.B., Knepp A.K., LeBouf R.F., Martin S.B. Jr., Ranpara A.C., Burns D.A., Virji M.A., 2022. Potential for exposure to particles and gases throughout vat photopolymerization additive manufacturing processes. *Buildings*, 12, 1222. DOI: 10.3390/buildings12081222.

Cai W.-B., Liu D.-D., Chen Y., Zhang L., Tan J.-B., 2021. Enzyme-assisted photoinitiated polymerization-induced self-assembly in continuous flow reactors with oxygen tolerance. *Chin. J. Polym. Sci.*, 39, 1127–1137. DOI: 10.1007/s10118-021-2533-z.

Camposeo A., Arkadii A., Romano L., D'Elia F., Fabbri F., Zussman E., Pisignano D., 2022. Impact of size effects on photopolymerization and its optical monitoring *in-situ*. *Addit. Manuf.*, 58, 103020. DOI: 10.1016/j.addma.2022.103020.

Chen Y., Li L., Han G., Liu R., An G., Zhu Y., 2025. Macromolecular coumarin sulfonium salt with side chain effect constructed by copolymerization strategy for free radical, cationic and hybrid photopolymerizations. *Chin. Chem. Lett.*, 36, 110458. DOI: 10.1016/j.cclet.2024.110458.

Chiulan I., Heggset E.B., Voicu Ș.I., Chinga-Carrasco G., 2021. Photopolymerization of bio-based polymers in a biomedical engineering perspective. *Biomacromolecules*, 22, 1795–1814. DOI: 10.1021/acs.biomac.0c01745.

Corrigan N., Yeow J., Judzewitsch P., Xu J., Boyer C., 2019. Seeing the light: Advancing materials chemistry through photopolymerization. *Angew. Chem. Int. Ed.*, 58, 5170–5189. DOI: 10.1002/anie.201805473.

Fiedor P., Pilch M., Szymaszek P., Chachaj-Brekiesz A., Galek M., Ortyl J., 2020. Photochemical study of a new bimolecular photoinitiating system for vat photopolymerization 3D printing techniques under visible light. *Catalysts*, 10, 284. DOI: 10.3390/catal10030284.

Gao T., Liu Z., Yin J., Feng J., Dietlin C., Morlet-Savary F., Schmitt M., Petithory T., Pieuchot L., Zhang J., Dumur F., Lalevée J., Xiao P., 2025. Novel low-cytotoxic and highly efficient type I photoinitiators for visible LED-/sunlight-induced photopolymerization and high-precision 3D printing. *Angew. Chem. Int. Ed.*, 64, e202425598. DOI: 10.1002/anie.202425598.

He X., Zang L., Xin Y., Zou Y., 2023. An overview of photopolymerization and its diverse applications. *Appl. Res.*, 2, e202300030. DOI: 10.1002/appl.202300030.

Hola E., Gruchała A., Popielarz R., Ortyl J., 2021. Non-destructive visual inspection of photocurable coatings based on fluorescent response of naked-eye visible colorimetric and fluorescent sensors. *Eur. Polym. J.*, 160, 110802. DOI: 10.1016/j.eurpolymj.2021.110802.

Hsieh M.-D., Zellers E.T., 2002. In situ UV-photopolymerization of gas-phase monomers for microanalytical system applications. *Sens. Actuators, B: Chem.*, 82, 287–296. DOI: 10.1016/S0925-4005(01)01011-5.

Hu S., Popielarz R., Neckers D.C., 1998. Fluorescence probe techniques (FPT) for measuring the relative efficiencies of free-radical photoinitiators. *Macromolecules*, 31, 4107–4113. DOI: 10.1021/ma971390l.

Jandt K.D., Mills R.W., 2013. A brief history of LED photopolymerization. *Dent. Mater.*, 29, 605–617. DOI: 10.1016/j.dental.2013.02.003.

Jiang F., Drummer D., 2020. Curing kinetic analysis of acrylate photopolymer for additive manufacturing by photo-DSC. *Polymers*, 12, 1080. DOI: 10.3390/polym12051080.

Lang M., Hirner S., Wiesbrock F., Fuchs P., 2022. A review on modeling cure kinetics and mechanisms of photopolymerization. *Polymers*, 14, 2074. DOI: 10.3390/polym14102074.

Li J., Li S., Li Y., Li R., Nie J., Zhu X., 2020. In situ monitoring of photopolymerization by photoinitiator with luminescence characteristics. *J. Photochem. Photobiol., A: Chem.*, 389, 112225. DOI: 10.1016/j.jphotochem.2019.112225.

Li X., Bian F., Huang R., Wei J., Gui X., Hu J., Li W., Lin S., 2024. Preparation of free radical/cationic hybrid UV-cured silicone materials with reducing oxygen inhibition via silyl radicals. *Eur. Polym. J.*, 221, 113582. DOI: 10.1016/j.eurpolymj.2024.113582.

Liz-Basteiro P., Sanz-Horta R., Reviriego F., Martínez-Campos E., Reinecke H., Elvira C., Rodríguez-Hernández J., Gallardo A., 2023. High resolution molds, sacrificial in aqueous media, obtained by vat photopolymerization 3D printing. *Addit. Manuf.*, 75, 103758. DOI: 10.1016/j.addma.2023.103758.

Llorente O., Agirre A., Calvo I., Olaso M., Tomovska R., Sardon H., 2021. Exploring the advantages of oxygen-tolerant thiol-ene polymerization over conventional acrylate free radical photopolymerization processes for pressure-sensitive adhesives. *Polym. J.*, 53, 1195–1204. DOI: 10.1038/s41428-021-00520-z.

Lu G., Yuan H., Zhou J., Chen F., Li C., Xue T., Shu X., Zhao Y., Nie J., Zhu X., 2022. Patterned magnetofluids via magnetic printing and photopolymerization for multifunctional flexible electronic sensors. *ACS Appl. Mater. Interfaces*, 14, 30332–30342. DOI: 10.1021/acsami.2c04755.

Luo J., Ruta V., Kwon I.S., Albertazzi J., Allasia N., Nevskyi O., Busini V., Moscatelli D., Vilé G., 2024. Fabricating a structured single-atom catalyst via high-resolution photopolymerization 3D printing. *Adv. Funct. Mater.*, 34, 2404794. DOI: 10.1002/adfm.202404794.

Mohd Shuhairi D.N., Abdul Malek N.S., Mohd Ghazali M.I., Sin N.D.M., Bonnia N.N., Yamada K., Rosman N., Hajar N., Omar H., Asli N.A., 2025. Nanofillers in vat photopolymerisation additive manufacturing: Mechanical properties of graphene and acrylate-based composites. *Prog. Addit. Manuf.*, 10, 11319–11341. DOI: 10.1007/s40964-025-01289-w.

Müller S.M., Schlögl S., Wiesner T., Haas M., Griesser T., 2022. Recent advances in type I photoinitiators for visible light induced photopolymerization. *ChemPhotoChem*, 6, e202200091. DOI: 10.1002/cptc.202200091.

O'Brien A.K., Bowman C.N., 2006. Impact of oxygen on photopolymerization kinetics and polymer structure. *Macromolecules*, 39, 2501–2506. DOI: 10.1021/ma051863l.

Ribas-Massonis A., Cicujano M., Duran J., Besalú E., Poater A., 2022. Free-radical photopolymerization for curing products for refinish coatings market. *Polymers*, 14, 2856. DOI: 10.3390/polym14142856.

Schneider O.D., Stepuk A., Mohn D., Luechinger N.A., Feldman K., Stark W.J., 2010. Light-curable polymer/calcium phosphate nanocomposite glue for bone defect treatment. *Acta Biomater.*, 6, 2704–2710. DOI: 10.1016/j.actbio.2010.01.033.

Szymaszek P., Tomal W., Świergosz T., Kamińska-Borek I., Popielarz R., Ortyl J., 2023. Review of quantitative and qualitative methods for monitoring photopolymerization reactions. *Polym. Chem.*, 14, 1690–1717. DOI: 10.1039/D2PY01538B.

Tezel Ö., Kahraman M.V., Ceylan R., Açıksarı A., Demir E., Çetinel S., 2025. Usage of 3D-printed scaffolds manufactured with bio-based photopolymer resin via 3D DLP in tissue engineering. *J. Polym. Environ.*, 33, 3013–3028. DOI: 10.1007/s10924-025-03592-7.

Topa M., Ortyl J., 2020. Moving towards a finer way of light-cured resin-based restorative dental materials: recent advances in photoinitiating systems based on iodonium salts. *Materials*, 13, 4093. DOI: 10.3390/ma13184093.

Wang P., Li J., Yang J., Wang G., He L., Zhang H., 2023. Enabling 3D multilayer electronics through the hybrid of vat photopolymerization and laser-activated selective metallization. *Addit. Manuf.*, 74, 103717. DOI: 10.1016/j.addma.2023.103717.

Xiao X., Huang Z., Duan H., Yang L., Yang Y., Lai Y., Li C., Feng L., 2025. Enhanced near-infrared light-mediated hydrogel curing using photoinitiator integrated upconversion particles as nano initiator for 3D bioprinting. *Biomacromolecules*, 26, 3364–3379. DOI: 10.1021/acs.biomac.4c01775.

Xu M., Liu M., Wang F., Chi H., 2025. Strategies to improve water solubility of photoinitiator for photopolymerization-based 3D printing in biomedical applications. *ACS Appl. Polym. Mater.*, 7, 4077–4092. DOI: 10.1021/acsapm.5c00184.

Yang S., Chen T., Bu Z., Tuo X., Gong Y., Guo J., 2023. Thermal responsive photopolymerization 3D printed shape memory polymers enhanced by heat transfer media. *J. Appl. Polym. Sci.*, 140, e53514. DOI: 10.1002/app.53514.

Zhang Y., de Haan H., Houlahan K., Sampson K.L., Webber D., Orth A., Lacelle T., Gaburici L., Lam R., Deore B., Paquet C., 2025. Impact of oxygen inhibition on (meth)acrylate photopolymerization in tomographic volumetric printing. *Addit. Manuf.*, 109, 104844. DOI: 10.1016/j.addma.2025.104844.

Chemical and Process Engineering: New Frontiers, 2026, 47(2), e132
DOI: 10.24425/cpe.2026.158130

CRITICAL REVIEW

Cathode and anode materials for alkali metal electrochemical reactions in energy storage systems – current state of the art and potential developments

Wojciech Rejmer[1], Szymon Racewicz[2,*], Sławomir Wierzbicki[2]

[1] University of Warmia and Mazury in Olsztyn, Faculty of Technical Sciences, Department of Materials and Machines Technology, Oczapowskiego 11, Olsztyn, Poland
[2] University of Warmia and Mazury in Olsztyn, Faculty of Technical Sciences, Department of Mechatronics, Oczapowskiego 11, Olsztyn, Poland

* **Corresponding author, e-mail:** szymon.racewicz@uwm.edu.pl

Article info:
Received: 15 January 2026
Revised: 21 April 2026
Accepted: 06 May 2026

Abstract
European and world economies are displaying increased use of renewable energy sources (RES). Energy sources such as wind energy, solar energy and water current energy, while clean and not emitting carbon dioxide, do not allow for stable electrical energy production due to their dependence on weather conditions. Current development trends are focused on the production of energy storage units, which will allow for stable electricity production from renewable sources. One unit investigated by researchers is flow and steady state high-capacity batteries. Ideal storage system should be characterised by high electric stability, charge-discharge reversibility, stability and low cost. The most widely used technology is ion lithium batteries. However, sources of lithium are geographically and quantitatively limited. There is an increasing interest in the application of other active metals in energy storage systems. Most active metal salts exhibit high water solubility and are available in most parts of the world. The objective of this work was to catalogue known active metals usage in energy storage, including their current and most promising applications, with a focus on the capacity of electrochemical processes and on anode and cathode materials.

Keywords
energy storage, renewable sources, active metals, cathodes, anodes

1. RENEWABLE ENERGY SOURCES

Current discussion on climate change, both in the European Union and the world, leads to increasing implementation of RES. The most common non-emissive energy sources are solar energy, wind energy, hydroelectric power, and geothermal energy (Nazarov et al., 2024). Solar power is divided into active and passive technologies, and active technologies are divided into concentrated solar power and photovoltaic technologies. Active solar power sources are those that convert heat or solar irradiation into electric energy. Their current efficiency ranges from 13 to 30% (Shahabuddin et al., 2021). To utilise solar energy technology in electrical grids, energy storage systems are paramount. The objective is to capture the excess generated electric energy and use it in times of energy generation decline.

Extensive investigations have underscored the critical role of electrochemical energy storage technologies in enhancing the overall efficiency and utilisation of photovoltaic systems. According to data published by the International Renewable Energy Agency (IRENA), the integration of energy storage systems can elevate the self-consumption rate of solar-generated electricity to approximately 50%, while concurrently mitigating dependence on the electrical grid and minimising curtailment of photovoltaic output (IRENA, 2017).

In recent years, stringent environmental legislation implemented in both the United States and the European Union has mandated reductions in anthropogenic greenhouse gas emissions in the order of 20–30%. These regulatory frameworks actively incentivise the large-scale deployment of RES, thereby driving accelerated expansion of the global battery market (Kim and Lee, 2024).

2. ENERGY STORAGE SYSTEMS

Rechargeable battery-based storage systems, such as lithium-ion batteries, are of considerable interest because of their high energy density, efficiency, and cost-effectiveness (Bustos et al., 2023; Hong et al., 2023). Rechargeable batteries, also called storage batteries or secondary cells, are electrochemical systems that use reversible redox reactions, which allow for multiple charging and recharging cycles. This is opposed to primary cells that have only one discharge cycle due to one of the reaction products being gaseous or unstable. Rechargeable systems store electrical energy employing conjugated electronation and de-electronation chemical reactions and release it in the same manner when needed (Lung et al., 2023). Evaluation research was performed considering the performance of a lithium-ion battery energy storage system

© 2026. The Author(s). This is an open-access article distributed under the terms of the Creative Commons Attribution (CC-BY 4.0, https://creativecommons.org/licenses/by/4.0/), which permits unrestricted use, distribution, and reproduction in any medium, provided the original author and source are credited.

integrated with solar PV installations. It has been found that the self-consumption of solar energy was improved by 30% and the reliance on grid electricity was reduced with the implementation of lithium-ion batteries (Vieira et al., 2017). Another research (Roberts et al., 2019) analysed the performance of a battery energy storage system (BESS) integrated with a solar PV system. In this study, it was concluded that the BESS increased the self-consumption of solar energy to over 70%, resulting in a significant reduction in grid electricity purchases. The techno-economic performance of a lithium-ion battery was evaluated in another study (Hassan et al., 2024) as an application for a solar self-consumption energy storage system. Other studies also showed improvement in self-consumption and economic efficiency of solar systems (Hasan et al., 2023). Presented research shows that integration of energy storage systems with PV installations is economically viable, underscoring the need for further development in this field. Because of this fact, it is crucial to develop storage systems based on a wider resource base. For this reason, energy storage systems based on alkali metals have been recognised by European markets due to their strong reliance on the foreign supply of both raw materials and end products, especially from Asia (Nowaczek and Kulczycka, 2020).

Although energy storage technologies have evolved in recent years, their main principles have not changed. The chemical energy storage systems are used mostly in the consumer sector and infrastructure maintenance (Komarnicki, 2016). Battery technology advancement has been revolutionised by portable electronics. This advancement has led to battery usage on demand and as a supply in fields like transportation or the electrical grid. Due to the high costs of power grid instabilities in the US, significant investments are being made (Amarapala et al., 2023). According to Jones Lang LaSalle Incorporated, utility-scale battery energy storage systems have reached the point of 16 GW in the USA by 2023, and their value worldwide can grow to 150 billion USD by the end of 2030 (JLL, 2024). The development and wide usage of lithium-ion batteries led to interest in other systems based on alkali metals such as sodium, potassium, magnesium, and calcium. Those metals are significantly close to lithium in the periodic table and are more abundant in Earth's crust. The amount of those elements is as follows (mass%): lithium is 0.002%, sodium is 2.36%, potassium is 2.09%, magnesium is 2.33% (Haynes et al., 2016; Lindagato et al., 2023) and calcium 4.15% (Royal Society of Chemistry) (Fig. 1). The main sources of lithium are places in Southeast Asia, Australia, and South America. Sodium and potassium are most abundant in North America (U.S. Geological Survey, 2020). Magnesium is most widespread but mostly produced in China and Russia (Zhang et al., 2023a). Calcium sources are most abundant in Indonesia, South America, and Central Africa (Wood et al., 2022). The new materials development for components of batteries (electrodes) is key to the improvement of battery performance and safety (Palumbo, 2023). Due to the anticipated increase in the usage of lithium-ion batteries, research on the recycling of materials from used systems is widely investigated (Barsegyan and Baghdasaryan, 2022; Huang et al., 2025; Kujawińska et al., 2022; Shim et al., 2024).

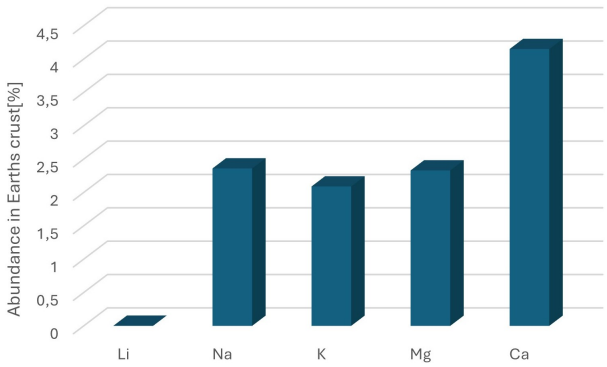


Figure 1. Abundance of lithium, sodium, potassium and magnesium in Earth's crust.

3. LITHIUM-ION BATTERIES (LIBS)

The prototype of lithium-ion batteries was introduced in 1986 by a research group of Akira Yoshino. The base principle of LIBs is the same as that of other alkali-ion batteries. Its core principle is reversible intercalation of ions, which began with research on the transport of ions in solids published in the 1960s (Lavanya et al., 2025), which was followed by investigation of reversible intercalation of lithium ions into graphite developed in the 1970s (Besenhard and Eichinger, 1976). In the same decade, the development of the first lithium metal battery occurred, thanks to the works of Whittingham, who developed the first lithium-ion rechargeable battery with titanium sulphide cathode. This set-up proved not sufficient for commercial use due to high material cost and hydrogen sulphide production during cathode decomposition (Whittingham, 1976). The end of the 70s saw the incorporation of lithium–transition metal oxides as cathodes, which proved more viable than titanium sulphide in works of Godshall (Godshall et al., 1980), Goodenough and Mizushima (Mizushima et al., 1980). A final development made by a group in the pre-commercialisation phase was the development of rechargeable batteries using ethyl carbonate as solvent, with $LiPF_6$ as electrolyte, which was Yoshino's group's prototype. Since then, the performance of lithium-ion cells has improved from a specific energy of 120 Wh/kg for the first Sony battery to 270 Wh/kg for current products (Waldmann et al., 2020). The remaining problem of LIBs is heat generation, which can be a reason for the proliferation of safety issues (fires and explosions included). Another problem is decreased performance with the lowering of temperature, which has been proven to reduce power outputs, life cycles and usable capacity (Xu et al., 2024).

The substantial annual production volumes of lithium-ion batteries, currently ranging from 1 to 10 GWh per manufacturing facility, necessitate the unequivocal demonstration of gigawatt-hour-scale production capability. Such a demonstration is

essential to satisfy the stringent qualification requirements imposed by automotive original equipment manufacturers (OEMs) and to ensure that the resulting cells achieve the cost-competitiveness required for widespread adoption (Nelson et al., 2011). Scale-up of production has precipitated a precipitous decline in specific cell costs, from approximately 5000 $/kWh in 1991 to 101 $/kWh in 2021 (Kittner et al., 2017; Ziegler and Trancik, 2021). This dramatic reduction underpinned the proliferation of portable electronic devices during the so-called "decade of the smartphone". Global demand for lithium-ion batteries expanded more than tenfold over the same period, rising from approximately 30 GWh in 2011 to 492 GWh in 2021, with projections indicating an increase to 2–3.5 TWh by 2030 (IEA, 2022). Sustained growth in demand is anticipated to drive further enhancements in electrochemical performance concomitant with additional price reductions. Advances in cell chemistry and architecture, battery-pack engineering, and manufacturing processes have collectively contributed to these improvements in energy density, cycle life, safety, and cost. At the inception of commercialisation in 1991, only cells employing lithium cobalt oxide ($LiCoO_2$, commonly abbreviated LCO) cathodes paired with graphitic carbon anodes were available on the market. In these early formulations, the active cathode material contained approximately 60 wt% of cobalt (Winter et al., 2018; Yűksel and Lale, 2024). According to the current research, the specific energy of lithium cells exceeds 270 Wh/kg (Sgourou et al., 2023). Positive electrode materials in such devices have high nickel and low cobalt content. Examples include lithium nickel manganese cobalt oxide ($LiNi_{1-a-b}Mn_aCo_bO_2$, where $a+b<1$, or $Ni_xMn_yCo_z$ where $x:y:z$ reflects the molar ratio of metals Ni:Mn:Co). Changes in positive electrode chemistry also led to improvements in both energy and cost effectiveness. Lithium iron phosphate ($LiFePO_4$, LFP)-based batteries employing a cell-to-pack (CTP) architecture have been implemented, achieving a gravimetric energy density of approximately 160 Wh/kg and a volumetric energy density of 330 Wh/l (Yang et al., 2021). These materials are safer and potentially cheaper (Wentker et al., 2019). The current generation of lithium-ion batteries, relying on intercalation-based cathodes, is approaching its theoretical performance limits. Accordingly, scientists are now directing attention towards alternative electrode materials and advanced processing techniques.

Key innovations include silicon-rich negative electrodes (Zhao et al., 2025), lithium-metal negative electrodes (Jeon et al., 2025), and solid-state electrolytes (Yun et al., 2024), negative electrode pre-lithiation strategies (Overhoff et al., 2021), and dry electrode coating processes (Park et al., 2025).

Emerging research directions in positive-electrode development focus on active materials that operate via conversion mechanisms, notably sulfur-based and oxygen-based systems. Although these chemistries offer potential advantages in raw-material cost and abundance, they typically compromise volumetric and gravimetric energy density, cycle life, and voltage stability compared with conventional intercalation hosts (Frith et al., 2023).

The fundamental energy-storage mechanism in lithium-ion batteries relies on reversible electrochemical insertion/extraction (intercalation/deintercalation) reactions. During charge, lithium ions are extracted from the crystal lattice of the cathode, migrate through the electrolyte and separator, and incorporate into the anode host structure. The reverse process occurs upon discharge. The reversible cell capacity is therefore governed by the number of lithium ions that can be accommodated per unit mass or volume within the respective electrode frameworks.

To tailor parameters such as energy density, power, safety, cost, and operating temperature range, diverse cathode and anode material pairings are employed. Widely commercialised cathode compositions include spinel lithium manganese oxide ($LiMn_2O_4$, LMO), olivine lithium iron phosphate ($LiFePO_4$, LFP), and layered nickel-cobalt-manganese oxides ($Li[Ni_xCo_yMn_{1-x-y}]O_2$, NCM or NMC). Common negative-electrode materials comprise graphite and spinel lithium titanate ($Li_4Ti_5O_{12}$, LTO).

Layered NCM cathodes are distinguished by their high theoretical specific capacity ($\approx$ 270–280 mAh/g when fully delithiated) (Ahangari et al., 2024; Hu et al., 2020), favourable rate capability, and respectable low-temperature kinetics. Performance can be further optimised by adjusting the transition-metal stoichiometry (Ni:Co:Mn ratio), wherein higher nickel content generally increases capacity at the expense of thermal stability and cycle life. In contrast, $LiFePO_4$ exhibits a lower practical specific capacity ($\approx$ 160–170 mAh/g) but offers intrinsic thermal and electrochemical stability, dramatically reducing the risk of oxygen release and thermal runaway even under abusive conditions such as overcharge (Hu et al., 2024; Lung-Hao Hu et al., 2013). Spinel LMO provides the lowest capacity among the three ($\approx$ 100–120 mAh/g practical) yet benefits from low material cost and environmental benignity (Abbas et al., 2024; Jiang et al., 2023).

On the anode side, graphite's highly ordered layered structure enables a high gravimetric capacity ($\approx$ 360–370 mAh/g via formation of LiC_6) and excellent performance rate. However, during the initial charge cycle, reductive decomposition of the electrolyte generates a solid-electrolyte interphase (SEI) layer on the graphite surface. Although this passivating film is essential for preventing continuous electrolyte degradation, it irreversibly consumes lithium and reduces overall cell capacity (Stournara and Shenoy, 2011; Xie and Lu, 2020). Lithium titanate, by contrast, operates at a higher potential ($\approx$ 1.55 V vs. Li/Li^+) outside the electrolyte reduction window, eliminating SEI formation and conferring exceptional safety and cycle life. These advantages come at the cost of substantially lower cell voltage and energy density, as well as higher material cost, restricting LTO deployment to niche applications demanding ultra-high safety and moderate energy requirements (Wang et al., 2017).

Commercially dominant cell chemistries remain limited to a few well-optimised pairings, including LFP/graphite,

LMO/graphite (or LMO-NCM blends), NCM/graphite, and LFP/LTO. Among these, NCM/graphite systems currently predominate in battery-electric passenger vehicles owing to their superior combination of gravimetric and volumetric energy density, high-rate capability, and acceptable low-temperature performance, all of which directly translate to extended driving range and dynamic vehicle performance (Yang et al., 2023).

3.1. Anodes for LIBs

The foundation of modern lithium-ion battery systems continues to rely on intercalation-based cathode and anode materials paired with non-aqueous liquid electrolytes, commonly comprising 1–1.2 M $LiPF_6$ in binary or multicomponent solvents of cyclic and chain alkyl carbonates (e.g., ethylene carbonate (EC) blended with dimethyl carbonate (DMC), diethyl carbonate (DEC), or ethyl methyl carbonate (EMC)). For more than a quarter of a century, graphite has served as the predominant anode material in commercial cells owing to its low average delithiation potential (≈ 0.1 V vs. Li/Li^+), high specific capacity of 372 mAh/g (corresponding to the stoichiometric stage-one compound LiC_6), excellent cycle life when properly passivated, and low cost (Basu, 1982; Zaghib et al., 2013). Nevertheless, graphite-based anodes are increasingly approaching their practical performance limits, particularly with respect to fast-charge capability, low-temperature operation, ultimate energy density, and safety.

The thermodynamic reduction potential of graphite lies above the lowest unoccupied molecular orbital (LUMO) of standard carbonate-based electrolytes. Consequently, during the initial formation cycles, reductive decomposition of the electrolyte generates a passivating solid-electrolyte interphase (SEI) on the graphite surface. While this SEI is crucial for long-term kinetic stability by preventing continuous electrolyte reduction, it imposes several drawbacks: irreversible lithium loss, increased impedance, sluggish Li^+ diffusion at high rates or low temperatures, and a propensity for uneven lithium plating and dendritic growth – especially under aggressive charging protocols – ultimately raising the risk of internal short circuits and thermal runaway.

In contrast, the spinel lithium titanate $Li_4Ti_5O_{12}$ (LTO) exhibits a redox potential of approximately 1.55 V versus Li/Li^+, situated well within the electrochemical stability window of conventional carbonate-based electrolytes. This positioning eliminates SEI formation entirely and enables near-zero volumetric strain ($< 1\%$) upon cycling, conferring exceptional cycle life ($> 10\,000$ cycles) and intrinsic safety. However, the elevated voltage and modest theoretical capacity (175 mAh/g, practical ≈ 160 mAh/g) substantially reduce full-cell energy density, restricting LTO to specialised applications where safety and longevity supersede energy requirements (Thackeray, 1999; Yang et al., 2023).

To overcome the limitations of both graphite and LTO, intensive research is directed toward high-capacity alloying and conversion-type anode materials. Silicon, germanium, tin, antimony, phosphorus, and their oxides, carbides (e.g., SiC, or SiO_x), as well as numerous carbon-based nanocomposites, are under active investigation (Leonova et al., 2023). Among these, tin-oxide-based anodes have demonstrated encouraging performance, achieving reversible capacities in excess of 650 mAh/g at current densities up to 1000 mA/g while retaining stable cycling over at least 100 cycles (Florez Gomez et al., 2024). Similarly, antimony–titanium-oxide composite systems have delivered specific capacities of ≈ 536 mAh/g after 100 cycles at 100 mA/g, coupled with excellent rate capability across a wide range of current densities (Gomez et al., 2024). These emerging materials offer the prospect of dramatically higher gravimetric and volumetric capacities than graphite, provided that challenges related to large volume expansion (up to 300% for Si), SEI instability, and particle pulverisation can be effectively mitigated through nanostructuring, protective coatings, advanced binders, and optimised electrolyte formulations.

3.2. Cathodes for LIBs

Three principal families of intercalation compounds currently dominate as cathode materials in commercial lithium-ion batteries, i.e. layered $LiMO_2$ (where M = Co, Ni, Mn or their combinations), spinel $LiMn_2O_4$, and olivine $LiFePO_4$ (Basu, 1982; Limachi et al., 2024; Padhi et al., 1997).

Layered oxides belonging to the $R-3m$ structure (α-$NaFeO_2$-type) offer the highest practical specific capacity of the three classes, with state-of-the-art materials now routinely achieving 180–220 mAh/g in full cells. This superiority arises from their two-dimensional Li^+ diffusion pathways and the ability to extract a large fraction of lithium before the host structure becomes unstable. However, long-term stability strongly depends on both composition and state of charge. Instability manifests in two primary forms: (i) structural degradation caused by transition-metal migration from octahedral sites in the TM layer to octahedral sites in the Li layer via intermediate tetrahedral coordination, and (ii) chemical instability linked to oxygen-anion redox activity at high degrees of delithiation (Qian et al., 2022).

Among the parent ternary end-members, Co^{3+} imparts excellent structural integrity owing to its high octahedral site stabilisation energy (OSSE), yet $Li_{1-x}CoO_2$ becomes chemically unstable when $x > 0.5$ because the $Co^{3+/4+}$: t_{2g} band overlaps the top of the O^{2-} : $2p$ band, leading to partial oxidation of lattice oxygen and irreversible O_2 release (Chebiam et al., 2001; Grey et al., 2004). Batteries equipped with cobalt-based layered oxide cathodes exhibit high voltages of around 4.4 V and are common in wearable consumer technology (Li et al., 2026).

$Mn^{4+/3+}$, conversely, provides outstanding chemical stability but is prone to cation migration and layered-to-spinel transformation owing to the low OSSE of Mn^{3+} (Sangsanit et al., 2025). $Ni^{2+/3+/4+}$ occupies an intermediate position, offering reasonable structural resilience while the pronounced Ni-O covalency enhances intrinsic electronic conductivity. Cost and toxicity also follow the order Co > Ni > Mn.

To exploit the complementary strengths of the three metals, the industry has converged on compositionally balanced materials such as $LiNi_{1/3}Mn_{1/3}Co_{1/3}O_2$ (NMC-111) and, increasingly, nickel-rich variants (NMC-622, NMC-811, etc.), which provide the optimum compromise among energy density, cycle life, intrinsic safety, and raw-material considerations (Zheng et al., 2023). The above-mentioned advantages of nickel and manganese-rich electrodes made batteries incorporating them more universal than cobalt analogues, and contributed to their wider application. Manganese and nickel-containing layered oxide cathodes have been a choice not only for portable electronics but also for electric vehicles and energy storage systems (Shahid and Agelin-Chaab, 2023).

The cubic spinel $LiMn_2O_4$ ($Fd-3m$) features a robust three-dimensional interstitial network that facilitates rapid Li^+ diffusion, endowing it with excellent power capability and structural resilience without major phase transformations during cycling. Its practical capacity is restricted to < 120 mAh/g, and long-term durability is compromised by Mn dissolution triggered by disproportionation of Mn^{3+} into Mn^{4+} and soluble Mn^{2+}. This process is catalysed by trace protons originating from hydrolysis of $LiPF_6$ in the presence of residual water (typically ppm levels). Despite these limitations, the low cost and acceptable power performance of $LiMn_2O_4$ (often blended with NMC) make it attractive for certain grid-storage applications (Koech et al., 2024).

The olivine $LiFePO_4$ ($Pnma$) is distinguished by exceptional thermal stability and intrinsic safety. Strong covalent bonding within the polyanion $(PO_4)^{3-}$ units suppresses oxygen release even under severe abuse conditions. As originally elucidated by Manthiram and Goodenough (1980s), the inductive effect of the polyanion lowers the $Fe^{2+/3+}$ redox energy relative to oxides, raising the operating voltage to ≈ 3.4 V versus lithium and thereby increasing energy density compared with earlier polyanion systems. Drawbacks include modest theoretical capacity (170 mAh/g, practical < 160 mAh/g), low average voltage, poor intrinsic electronic conductivity ($\approx 10^{-9}$–10^{-10} S cm^{-1}), and one-dimensional Li^+ diffusion. These shortcomings are routinely mitigated by nanosizing the particles and applying conductive carbon coatings, although such measures further reduce an already unfavourable volumetric energy density. The olivine $LiFePO_4$ is applied in the same areas as nickel and manganese layered oxides but provides higher cyclability and is more environmentally friendly (Yuan et al., 2011).

Among the three established intercalation cathode families, layered transition-metal oxides remain unrivalled in delivering the highest gravimetric and volumetric energy density, which explains their dominance in electric-vehicle applications where driving range is paramount (Manthiram, 2017; Nandihalli et al., 2024; Nitta et al., 2015; Zanoletti et al., 2024).

4. SODIUM-ION BATTERIES (SIBS)

The development of sodium-ion batteries has started as a possible solution for environmental issues connected with lithium mining. Sodium-ion batteries can be cheaper due to greater abundance and less costly supply charges (Nekahi et al., 2024). Sodium-ion batteries also provide functional benefits such as higher power, faster charging, and low-temperature operation (Zhao et al., 2024). The downside of this technology is lower energy, which causes a higher need for storage units to supply the same amount of energy as the corresponding LIBs. Sodium is readily available in seawater, although sodium carbonate deposits represent a more practical and concentrated industrial source and occur widely across the globe. Owing to the chemical analogies between sodium and lithium, the corresponding technologies have advanced rapidly and have already entered the stage of commercial deployment. Physicochemical differences between the first two group metals, such as redox potential, are relevant for battery construction. Lower redox potential causes less energy to be delivered to the cathode compared to LIB. The higher atomic mass of sodium relative to lithium inherently results in lower gravimetric energy density, a critical drawback when evaluating the life-cycle environmental impact of a battery system (Schirber, 2024).

4.1. Anodes for SIBs

In carbon materials, intercalation of sodium occurs especially in ester-based electrolytes. Carbonaceous anode materials can be classified into graphitic carbon, expanded graphite, and amorphous carbons, with the latter category encompassing non-graphitizable hard carbon and graphitizable soft carbon. These classes of carbon exhibit distinct sodiation and desodiation behaviours, which vary according to the electrolyte system employed (Jia et al., 2024). Lately, there is also a need for the synthesis of carbon materials from natural materials, which produce amorphous carbon (Kim et al., 2023; Wu et al., 2024). Such materials exhibit larger interlayer spacing than graphite, leading to an adsorption/intercalation mechanism in ester-based electrolytes and, unfortunately, a co-intercalation mechanism in ether-based electrolytes (Wahid et al., 2018). Larger layer spacing is also present in expanded graphite and undergoes a combined adsorption-intercalation process during charge-discharge when operated in ester-based electrolyte systems (Pan et al., 2024; Wen et al., 2014). Similar ion transfer occurs in TiO_2 and Nb_2O_5 charge-discharge (Liu et al., 2018). Interestingly, 2D carbon materials such as MXenes, which are 2D metal carbides, can act as an intercalation anode with a relatively limited capacity, also thanks to the larger interlayer spacing (Jia et al., 2023; Wang et al., 2015).

Interesting material for anodes was synthesised by embedding carbon fiber with tin oxide nanopowder, with a capacity of 1275 mAh/g at 50 mA/g (Kim et al., 2021).

Another interesting mechanism occurs in anodes with elements such as Sn, Sb, Bi, Si, Ge, and P. These kinds of electrodes exhibit alloying reactions with a universal equation written as follows (Eq. (1)) (Choi et al., 2024).

$$M + nNa^+ + ne^- \rightarrow Na_nM \quad (1)$$

Alloying-type negative electrodes react with sodium through the formation of binary intermetallic compounds Na_nM (where M = Sn, Sb, Si, Ge, Bi, P, etc.). The gravimetric capacity of the mentioned materials scales with the maximum number of sodium atoms accommodated per atom of M (i.e., the electron-transfer number n), which in turn depends on the atomic mass of the host element.

Tin forms $Na_{15}Sn_4$ upon full sodiation ($n = 3.75$), delivering a theoretical specific capacity of 847 mAh/g. However, this is accompanied by a massive volumetric expansion of approximately 420% (Darwiche et al., 2012; Passerini et al., 2024). Antimony alloys to Na_3Sb ($n = 3$), providing 660 mAh/g with a similarly severe expansion of $\approx$ 390% (Darwiche et al., 2012; Passerini et al., 2024). Germanium exhibits a more modest theoretical capacity of 396 mAh/g (NaGe), while bismuth reaches 385 mAh/g via the Na_3Bi phase ($n = 3$) (Abel et al., 2013; Su et al., 2015).

Silicon, despite its outstanding performance in lithium-ion systems, reacts only partially with sodium, forming amorphous $Na_{0.76}Si$ at room temperature. This limited sodiation nevertheless yields a respectable 725 mAh/g and, crucially, a comparatively low volume expansion of only $\approx$ 114%, making silicon one of the more mechanically tolerant high-capacity hosts for sodium (Jung et al., 2014).

Red phosphorus stands out with by far the highest theoretical capacity of any known sodium-ion anode material: 2596 mAh/g, corresponding to the formation of Na_3P ($n = 3$). Both theoretical and experimentally achievable values place phosphorus at the pinnacle of gravimetric performance among sodium-ion anode candidates.

Notwithstanding their exceptional capacities, alloying anodes universally suffer from extreme volumetric strains during sodiation/desodiation (Fig. 2). Repeated expansion and contraction induce particle fracturing, pulverisation, loss of electrical contact, and continuous reformation of the solid-electrolyte interphase, all of which culminate in rapid capacity decay and poor cycle life (Ni et al., 2018; Nowak et al., 2024). Successful commercialisation, therefore, hinges on the development of effective nanostructuring, protective coatings, composite architectures, and tailored electrolyte formulations capable of accommodating or mitigating these mechanical stresses.

The practical deployment of alloying and conversion-type anodes in sodium-ion batteries is critically limited by their poor

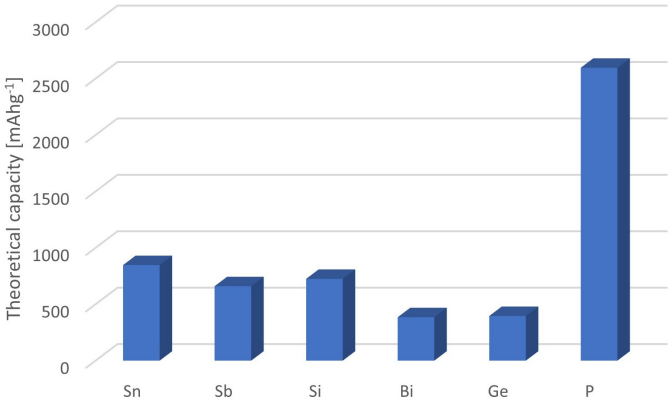


Figure 2. Theoretical capacities of sodium binary alloys vs the alloying element.

long-term stability. Substantial improvements are therefore required through deliberate nanostructural engineering, composite design, and precise control of the electrode-electrolyte interphase (Ying and Han, 2017).

A widely explored mitigation strategy involves the incorporation of conversion-type non-metallic elements (P, S, O, N, F, Se, etc.) that react reversibly with sodium to form Na_nX compounds. In practice, these elements are rarely used in pure form; instead, they are pre-combined with metallic or non-metallic hosts (both alloying and non-alloying) to yield oxides, sulphides, selenides, phosphides, nitrides, or fluorides. During the initial sodiation, these compounds undergo a displacement (conversion) reaction of the general form (2).

$$nNa^+ + ne^- + M^{n+}X \rightarrow Na_nX + M \quad (2)$$

in which the electrochemically generated metallic phase (M) subsequently serves as a conductive matrix or buffer for further alloying reactions, while the Na_nX phase contributes additional capacity.

Among conversion compounds, metal oxides, sulphides, and especially phosphides exhibit attractive specific capacities and relatively low average sodiation potentials, making them appealing candidates for high-energy sodium-ion cells. Table leg, like their pure alloying counterparts, conversion anodes suffer from pronounced volumetric changes during cycling, severe particle pulverisation, repeated fracturing and reformation of the solid-electrolyte interphase, and consequent rapid capacity fade. These interrelated degradation modes remain the principal obstacles to their commercialisation (Wei et al., 2024; Zhang et al., 2019b).

Overcoming these challenges demands multifaceted approaches, including yolk-shell or core-shell architectures, embedding active particles within porous carbon scaffolds, in situ formation of flexible buffering matrices, and the design of artificial interphases or sodium-compatible electrolyte additives that can accommodate large strain while preserving electrical continuity and ionic accessibility.

4.2. Cathodes for SIBs

Transition-metal oxides of the form Na_xMO_2 (M = Co, Mn, Fe, Ni, etc.) have gained significant attention as intercalation cathodes for sodium-ion batteries (SIBs), owing to their structural analogy with established lithium-ion counterparts. The crystallographic architecture of these oxides is highly sensitive to synthesis parameters and sodium stoichiometry, resulting in a broad spectrum of phases. Electroactive Na_xMO_2 cathodes are broadly categorised into layered and tunnel structures, both of which can be prepared via air-compatible techniques such as solid-state sintering, co-precipitation, or hydrothermal processing (Billaud et al., 2014; Delmas et al., 1980).

Layered Na_xCoO_2 has been a focal point of early research, inspired by the commercial success of $LiCoO_2$. However, the larger ionic radius of Na^+ (1.02 Å vs. 0.76 Å for Li^+) induces pronounced lattice strain, yielding suboptimal practical capacities of 70–100 mAh/g and mediocre rate capability (Kehne et al., 2019; Lei et al., 2014; Shibata et al., 2015). Phase-pure variants of Na_xCoO_2 can be selectively accessed through high-temperature solid-state methods by fine-tuning the Na:Co precursor ratio, enabling control over stacking sequences (e.g., O3, P2, P3 phases) and electrochemical properties.

In comparison, Na_xMnO_2 layered oxides offer greater promise, with a theoretical capacity of 243 mAh/g derived from the $Mn^{3+/4+}$ redox couple, alongside the economic and environmental advantages of manganese. Practical capacities in these systems span 160–219 mAh/g, yet they are plagued by structural degradation, including amorphisation and collapse under repeated Na^+ extraction/insertion, driven by Jahn-Teller distortions and cumulative lattice strain (Hidalgo et al., 2024). Layered $NaFeO_2$, leveraging abundant iron resources and the highly reversible $Fe^{4+/3+}$ couple, exhibits voltage-dependent performance. Capacities of 80–100 mAh/g are achievable when the upper cut-off is restricted to 3.4 V vs. Na/Na^+; higher voltages provoke irreversible phase transitions, loss of Na^+ diffusion pathways, and capacity fade (Zhao et al., 2013). Additional single-transition-metal oxides, such as $NaCrO_2$ (Kubota et al., 2015), $NaNiO_2$ (Han et al., 2014), and $Na_xV_yO_i$ (Dong et al., 2015), have also been evaluated as viable intercalation hosts.

Tunnel-structured Na_xMO_2 oxides adopt an orthorhombic framework, characterised by one-dimensional Na^+ diffusion channels that inherently limit rate performance compared with two- or three-dimensional counterparts (Liu et al., 2024; Sauvage et al., 2007). $Na_{0.44}MnO_2$, with its theoretical capacity of 121 mAh/g, remains the most studied tunnel cathode and can be synthesised via diverse routes, including solid-state reactions (Sauvage et al., 2007), hydrothermal treatments (Hosono et al., 2012), solution combustion (Saint et al., 2008), or sol-gel processes (Xu et al., 2014).

Notably, sol-gel-derived sub-micrometre $Na_{0.44}MnO_2$ slabs have demonstrated capacities exceeding 120 mAh/g, coupled with robust cycling stability over 100 cycles, highlighting the efficacy of morphology control in enhancing accessibility and mechanical integrity (Xu et al., 2014). Beyond oxides, polyanionic compounds represent a burgeoning class of SIB cathodes, prized for their structural versatility, thermal resilience, and elevated operating potentials arising from the inductive withdrawal of electron density by the polyanion. Prominent examples encompass phosphates (e.g., $Na_3V_2(PO_4)_3$), mixed phosphates/pyrophosphates (e.g., $Na_2FeP_2O_7$), fluorophosphates (e.g., $NaVPO_4F$), and sulphates (e.g., $NaFeSO_4F$), which collectively deliver high voltages (> 3.5 V) and exceptional cycle life, albeit often at the expense of gravimetric capacity. Polyanionic compounds can also possess other transition metals in their structure, such as manganese, nickel, cobalt, molybdenum, titanium and tungsten. Addition of nickel, manganese and titanium improves voltages and energy densities, while cobalt, molybdenum and tungsten improve structural stability of electrodes during charge/discharge cycles (Dacek et al., 2016; Xu et al., 2023). Another class of polyanionic compounds are fluorophosphates $Na_3M_2(PO_4)_2F_3$. In SIB cathodes, their derivates with iron, vanadium and vanadium oxide are of high interest. Iron derivate is mostly used for its cost-effectiveness. Vanadium derivate possesses a high capacity of around 243 mAh/g and a high voltage of around 4.1 V, vanadium oxide derivates provide additional stability for high power applications (Dacek et al., 2016; Hwang et al., 2025). Alluaudites are another class of polyanionic compounds with $Na_2Fe_2(SO_4)_3$ being an exemplary material exhibiting 3.8 V potential and 405 Wh/kg energy density (Liu and Palmore, 2017).

Prussian blue analogues – metal hexacyanometallates – constitute another promising framework family, wherein transition-metal cations are octahedrally bridged by cyanide ligands to form an open cubic lattice with spacious interstitial sites for reversible Na^+ occupancy. Early studies in aqueous electrolytes (e.g., with Ag/AgCl references) revealed commendable cycling durability and rate capability, though limited by modest discharge voltages (< 1.5 V). These constraints, attributable to the aqueous medium and reference electrode, have spurred investigations into non-aqueous SIB configurations, where hexacyanometallates such as $Na_2MnFe(CN)_6$ exhibit voltages approaching 3.5 V and capacities > 100 mAh/g (Wessells et al., 2011a).

Organic materials offer a sustainable alternative for SIB cathodes, with ongoing efforts centred on organosulphur, radical, carbonyl, and polymeric systems. Aromatic carbonyl derivatives, in particular, function via reversible Na^+ coordination to the C=O redox centre, typically at ≈ 2.2 V vs. Na/Na^+, affording capacities of 140–250 mAh/g and retention over 40–200 cycles, modulated by molecular weight and conjugation (Sakaushi et al., 2013). Pteridine-based organics and conjugated polymers further expand this palette.

Anion-insertion cathodes, predominantly polymeric or doped variants, enable operation at higher potentials (> 3.0 V) through the accommodation of large anions (e.g., PF_6^-, ClO_4^-). For instance, a poly(aniline-co-nitroaniline) copolymer (P(AN-NA)) in $NaPF_6$/EC-DEC-DMC delivers 180 mAh/g at 3.2 V, with 96% retention after 50 cycles via

reversible $[PF_6]^-$ shuttling. Poly(triphenylamine) (PTPAn) in $NaPF_6$/DME-DOL exhibits 98 mAh/g at ≈ 3.6 V, while amorphous oligopyrene (AOL) in ClO_4^-/PC achieves 121 mAh/g at 3.5 V through ClO_4^- insertion. Polypyrrole variants doped with $[Fe(CN)_6]^{4-}$ (PPy-Fe) or diphenylamine-4-sulphonate (PPy-Ds) yield 100–135 mAh/g at ≈ 3.0 V. Intriguingly, Sakaushi and co-workers demonstrated that aromatic porous honeycomb (APH) electrodes can toggle between anion-insertion (4.1–2.8 V) and cation-insertion (2.8–1.3 V) regimes, attaining a specific power of 10 W/g and energy of 500 Wh/kg (Xiang et al., 2015).

A comparative summary of electrochemical metrics for these diverse SIB cathode classes is illustrated in Fig. 3 (Iyer et al., 2024).

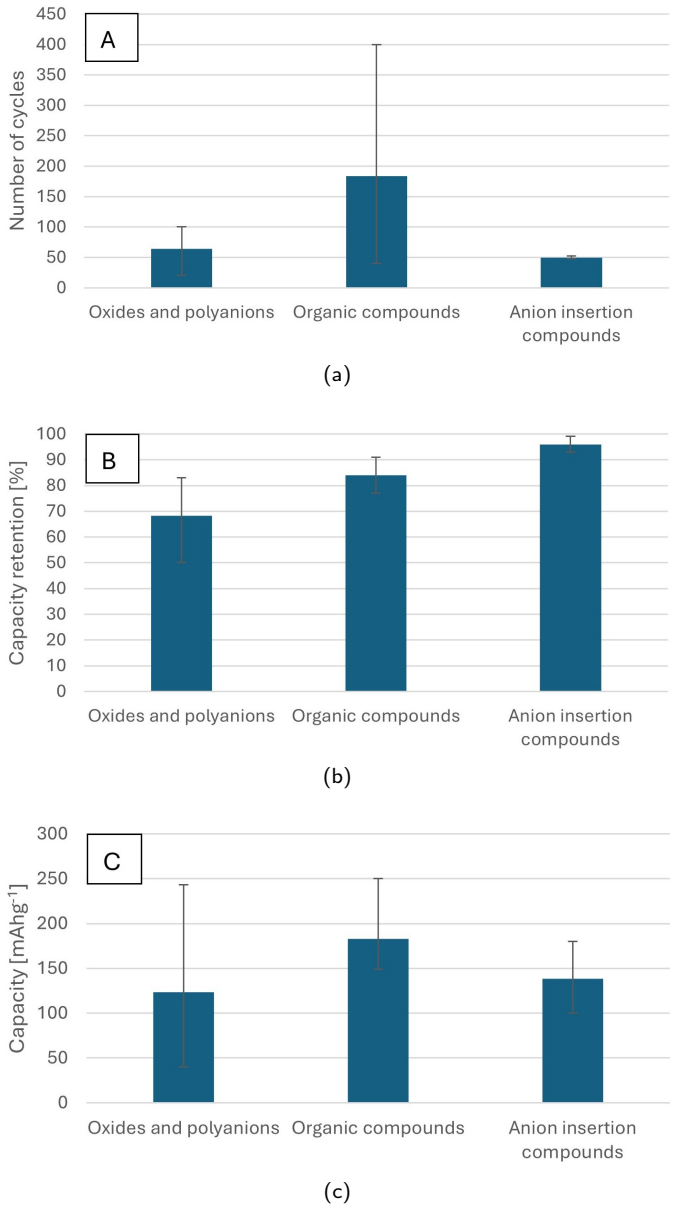


Figure 3. Performance of SIBs cathodes: (a) number of cycles, (b) capacity retention, (c) capacity.

5. POTASSIUM ION BATTERIES (KIBS)

The first functional potassium-ion battery (KIB) prototype was disclosed in 2004, employing Prussian blue as the cathode and metallic potassium as the anode. This milestone triggered a rapidly expanding body of research focused on novel electrode materials, optimised binders, and tailored electrolytes.

Potassium belongs to the same group (Group 1) of the periodic table as lithium and sodium and is far more earth-abundant than lithium (17000 ppm vs. 20 ppm in the Earth's crust), conferring a substantial raw-material cost advantage. Although metallic potassium is currently more expensive than sodium metal, the key precursor for cathode synthesis – potassium carbonate (K_2CO_3) – is priced comparably to sodium carbonate (Na_2CO_3). Consequently, assuming equivalent processing and supply-chain maturity, any mature KIB technology is projected to undercut the cost of present-day lithium-ion systems.

A distinctive electrochemical feature of KIBs is their potential for high operating voltage and energy density. In aqueous standard conditions, the K^+/K couple exhibits a redox potential of −2.936 V vs. SHE, comparable to that of Li^+/Li (−3.040 V) and considerably lower than Na^+/Na (−2.714 V) (Zhang et al., 2019a). More importantly, this trend is amplified in non-aqueous media. Solvated-ion theoretical calculations and experimental measurements in carbonate esters consistently show that the standard electrode potential of K^+/K is the most negative among alkali metals in common battery electrolytes.

In propylene carbonate (PC), for example, the computed potentials are approximately −2.79 V (Li), −2.56 V (Na), −2.88 V (K), −2.95 V (Rb), and −3.10 V (Cs) versus the respective alkali-metal reference (Anoopkumar et al., 2020).

Similar rankings hold across ethylene carbonate, dimethyl carbonate, and ether-based solvents. The anomalously low desolvation energy and weak solvation shell of K^+ in organic electrolytes are responsible for this counterintuitive behaviour, effectively positioning the K^+/K couple below Li^+/Li on the electrochemical scale under practical battery conditions.

As a direct consequence, full KIB cells can in principle deliver higher average discharge voltages than their lithium-ion counterparts when paired with identical cathode materials, translating into superior gravimetric and volumetric energy density – provided suitable high-capacity, K^+-compatible electrodes and stable electrolytes can be developed. This intrinsic thermodynamic advantage, combined with resource abundance, underpins the growing academic and industrial interest in potassium-ion batteries as a credible post-lithium technology.

Due to economic reasons, potassium is a viable material because of its abundance and even geographical distribution. Potassium ion has many advantages over sodium and lithium, but as it has a larger molecular weight, KIBs did not attract substantial interest in the early stages of research. However, when comparing two analogous systems employing Prussian

blue cathodes and carbon-based anodes, the potassium-ion configuration is only 7.85% heavier than its competing sodium-ion counterpart (Ge et al., 2022). Therefore, potassium ion batteries do not have to exhibit lower energy density than those based on lighter metals.

A further practical benefit of potassium chemistry is its negligible alloying reactivity with aluminium at potentials relevant to anode operation. Unlike lithium, which readily forms Li-Al alloys below ≈ 0.3 V vs. Li/Li^+ and therefore mandates the use of costlier copper foil as the negative-side current collector, potassium shows no thermodynamically favourable alloying with aluminium across the entire operating window of typical KIB anodes. Conclusionally, lightweight and inexpensive aluminium foil can be employed on both electrodes without risk of degradation, offering a meaningful reduction in cell-level materials cost and overall stack weight – advantages that are not similarly realised in lithium-ion technology.

The solvation behaviour of K^+ ions in non-aqueous electrolytes also confers distinct kinetic benefits. Owing to its large bare ionic radius (1.38 Å) and comparatively low charge density, K^+ exhibits the weakest Lewis acidity among the alkali-metal cations. This results in the loosest solvation sheath and the lowest cation-solvent interaction energy in common carbonate and ether solvents, as corroborated by both ab initio calculations and spectroscopic measurements. The primary solvation number for K^+ is typically 4–5, markedly lower than the 6–7 observed for Li^+ and Na^+, yielding the smallest effective solvated radius and the highest ionic mobility.

Experimental ionic conductivities of potassium-based electrolytes routinely exceed those of analogous lithium or sodium salts at equivalent concentrations, while maintaining high cation transference numbers. These attributes underpin the outstanding rate performance routinely observed in KIB prototypes, even with relatively thick electrodes and conventional separator materials.

Finally, potassium readily intercalates into graphite to form the stage-I compound KC_8, delivering a reversible specific capacity of 273 mAh/g (the theoretical value is 279 mAh/g for the reaction $8C + K^+ + e^- \rightleftharpoons KC_8$).

This capacity is substantially higher than the ≈ 35 mAh/g achievable with sodium under comparable conditions and eliminates the need for the complex hard-carbon anodes required in sodium-ion systems. The ability to utilise inexpensive, widely available graphite as a high-performance anode, coupled with aluminium current collectors and a high-voltage cathode, positions potassium-ion technology as a uniquely cost-effective and energy-dense complement to existing lithium-ion platforms (Anoopkumar et al., 2020).

5.1. Cathodes for KIBs

The inaugural potassium-ion battery prototype utilised Prussian blue (PB) as the cathode material. Since that demonstration, PB and its analogues have been the subject of intensive investigation as cathodes for KIBs (Xiang et al., 2015). Additional classes of cathode materials under active exploration include layered transition-metal oxides (Nathan et al., 2022), polyanionic compounds, and organic crystalline frameworks (Hosaka et al., 2019). Prussian blue, chemically ferric(III) hexacyanoferrate(II), $Fe_4[Fe(CN)_6]_3$, exhibits an open-framework structure that enables highly reversible K^+ intercalation. Studies have shown that PB thin films can withstand millions of potassiation/depotassiation cycles with negligible structural deterioration and minimal capacity loss.

Analysis of electrochemical tests leads to the assessment that K^+ ions are intercalating in PB crystals. The reactions that occur on Prussian blue films are the oxidation of Prussian blue to Berlin green and its reduction to Prussian white.

Early studies on KIB cathodes focused on K_xCoO_2-type layered potassium metal oxide, which gave specific capacities of around 60 mAh/g at voltages in the range of 2–3.9 V. A further advance toward high-capacity materials has led to the development of iron- and manganese-based potassium oxide cathodes. The studied compounds delivered reversible capacities of 136–178 mAh/g with cycle life extending to 200 cycles. Regrettably, their average discharge potentials are notably lower than those of the corresponding sodium-based analogues (Nathan et al., 2022).

Manganese-based cathode systems tend to exhibit low cost and non-toxicity. However, the presence of Mn^{3+} ions can adversely influence the electrochemical performance of these materials. In other research, it was shown that this can be decreased through metal doping methods. The drawback of these cathodes is vulnerability towards water intercalation and oxidation. This leads to the need for the use of inert gases during cell assembly (Jian et al., 2015).

5.2. Anode materials for KIBs

Carbon-based materials, predominantly graphite, are widely employed as negative electrodes in alkali-metal-ion batteries. Theoretical investigations have established that K^+ intercalation into graphite is thermodynamically more favourable than that of other alkali-metal cations (Chen et al., 2019). The primary challenge hindering KIB development remains the identification of a robust anode capable of reversibly hosting the large K^+ ion over repeated insertion/extraction cycles without significant structural degradation. In parallel with trends observed in sodium-ion systems, considerable effort is currently devoted to deriving carbon anodes from abundant natural precursors (Ma et al., 2024).

Potassium graphite complexes can be obtained by pyrolysis of a potassium metal and graphite mixture. Research has demonstrated that potassium ions intercalate into graphite by occupying the interlayer galleries, leading to graphite expansion and exfoliation (Li et al., 2019). Other studies were performed on non-graphitic carbon nanofibers (CNF). However,

low-capacity retention was observed with a 73% reduction after 20 cycles. It was suggested that disordered carbon can hold a larger number of ions smaller layer expansion during intercalation (Li et al., 2024). Researchers released a paper showing that potassium ions (K^+) can be reversibly inserted into and extracted from a graphite electrode using a non-aqueous electrolyte, achieving a reversible capacity of 273 mAh/g. The addition of low-density soft carbon was shown to enhance both cycle life and rate performance (Komaba et al., 2015). In separate work, scientists developed a hollow carbon material derived from melamine-formaldehyde resin, which was transformed through pyrolysis into a neuron-inspired architecture and tested as an anode for potassium-ion batteries. Thanks to its inherent structural flexibility and good electrical conductivity, this material could serve directly as the anode without requiring a current collector, binder, or conductive additives. The nanostructured electrode delivered a reversible capacity of 340 mAh/g at 0.1 C, outstanding cycling stability with nearly full capacity retention ($\approx$ 100%) after 150 cycles at 0.5 C, and high Coulombic efficiency (72.1% in the initial cycle and exceeding 99% in subsequent cycles) (Wang et al., 2018a). Commercial hard carbon, Carbotron P(J) supplied by Kureha Co., exhibited a reversible specific capacity of approximately 215 mAh/g while displaying exceptionally low sensitivity to air and moisture – an essential characteristic for the practical deployment of potassium-ion batteries (Kubota et al., 2018). Among non-carbon intercalation hosts, molybdenum disulfide (MoS_2), a representative transition-metal dichalcogenide (TMD), has attracted considerable interest as a KIB anode owing to its natural abundance, low cost, and layered crystal structure that provides two-dimensional diffusion pathways for K^+ ions. Nevertheless, the intrinsic poor electronic conductivity of MoS_2 continues to restrict its rate capability and long-term electrochemical stability (Wang et al., 2024).

6. MAGNESIUM BATTERIES (RMBS)

Rechargeable magnesium batteries (RMBs) employ metallic magnesium as the negative electrode, which offers a high volumetric capacity of 3833 mAh/cm^3 (Mousavian and Bautin, 2025) and a markedly reduced propensity for dendrite formation compared with alkali metals. The low standard redox potential of the Mg^{2+}/Mg couple (−2.37 V vs. SHE) (Atkins et al., 2017) combined with its divalent charge carrier, it promises substantially higher theoretical energy densities than monovalent systems. Nevertheless, established design principles and materials developed for alkali-metal batteries cannot be directly transferred to magnesium chemistries owing to fundamental differences in ion solvation, interfacial passivation behaviour, and electrolyte compatibility.

6.1. Cathodes for RMBs

In contrast to monovalent alkali-metal systems, rechargeable magnesium batteries suffer from a scarcity of suitable high-capacity intercalation cathodes capable of reversibly hosting the divalent Mg^{2+} ion.

Particle nanosizing remains a proven strategy to minimise solid-state diffusion limitations by reducing ion-transport path lengths and increasing reactive surface area (Mao et al., 2020). For instance, non-stoichiometric anatase TiO_2 deliberately engineered with titanium vacancies via fluorine doping has been shown to enhance Mg^{2+} diffusion kinetics and provide additional charge-storage sites (Levi et al., 2008).

A noteworthy advance is the demonstration of dual-cation co-intercalation in the Chevrel phase Mo_6S_8 using Mg-Li hybrid electrolytes, whereby both Li^+ and Mg^{2+} contribute to charge compensation and enable dendrite-free magnesium deposition. Although highly effective in Mo_6S_8, this co-intercalation approach has only rarely been extended to other host lattices (Richard et al., 2017).

Transition-metal oxides are widely investigated as RMB cathodes because their strong metal-oxygen bonds confer high redox potentials and reasonable oxidative stability. Prominent candidates include V_2O_5, MnO_2, MoO_3, and various TiO_2 polymorphs (Masese and Kanyolo, 2023).

Layered α-V_2O_5 permits room-temperature Mg^{2+} insertion accompanied by a phase transition to δ-$Mg_xV_2O_5$; the expanded interlayer gallery in the δ-phase facilitates faster Mg^{2+} mobility and yields a higher operating voltage. Performance is further improved by particle downsizing, structural or electrolytic water incorporation, pillar pre-intercalation, expanded interlayer spacing, and carbon compositing. Bilayered V_2O_5 nanoribbons supported on carbon nanofoam, for example, achieved an initial discharge capacity of 240 mAh/g, albeit with rapid subsequent fading (Tepavcevic et al., 2015; Zhang et al., 2023b).

Orthorhombic α-MoO_3 is another attractive intercalation host, but structural rearrangements during cycling typically cause steep capacity decay. Nanostructured α-MoO_3 electrodes have delivered $\approx$ 220 mAh/g at $\sim$ 1.8 V vs. Mg/Mg^{2+}. Mild fluorination to form $MoO_{2.8}F_{0.2}$ lowers lattice energy, boosts electronic conductivity, markedly accelerates Mg^{2+} diffusion, and improves cycling stability (Gershinsky et al., 2013; Wan et al., 2016).

Polymorphic TiO_2, particularly anatase and TiO_2(B), also functions as an RMB cathode, although strong electrostatic Mg^{2+}–lattice interactions severely hamper reversible insertion. Defect engineering, especially fluorine doping, generates active intercalation sites and significantly enhances performance. Optimised F-doped TiO_2 electrodes have demonstrated reversible capacities of $\sim$ 150 mAh/g with excellent retention over 300 cycles at 300 mA/g (Koketsu et al., 2017).

MnO_2 stands out as a very attractive cathode material thanks to its straightforward preparation, rich variety of crystal structures, and the ease with which its electrochemical properties can be adjusted. Nano-sized α-MnO_2 featuring the

(2 × 2) tunnel structure delivered an impressive initial discharge capacity of approximately 280 mAh/g. Nevertheless, the material suffered from fast capacity fading in the following cycles. Investigation of the Mg^{2+} insertion process in α-MnO_2 suggests a progressive transformation to MnO occurring at the surface/interface, ultimately leading to the creation of a K-αMnO_2@(Mg,Mn)O core-shell structure after complete discharge. Birnessite-type MnO_2, when cycled in water-containing magnesium electrolytes, delivers a high discharge capacity of 227.6 mAh/g at an average potential of 2.8 V vs. Mg^{2+}/Mg, primarily through a reversible Mg^{2+} intercalation mechanism. In contrast, the same material in conventional non-aqueous electrolytes undergoes a conversion-type reaction pathway, as reported by Sun and co-workers (Sun et al., 2016; Tolstoy et al., 2019). Both nanosizing the primary particles and expanding the interlayer gallery have been confirmed as powerful strategies for enhancing rate capability and reversible capacity in MnO_2-based cathodes (Koketsu et al., 2017). A comparison of the specific capacities achieved with various oxide cathodes in rechargeable magnesium batteries is shown in Fig. 4.

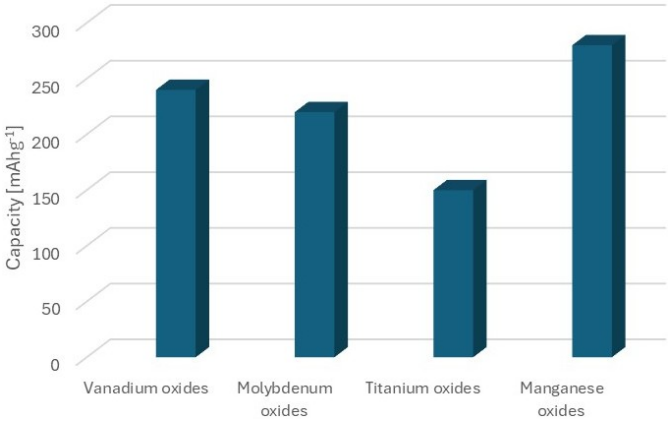


Figure 4. Capacities of metal oxide cathodes for RMBs.

6.2. Anode materials for RMBs

The relatively low reactivity of magnesium metal permits its direct use as a negative electrode in RMBs. Mg electrodeposition typically produces smooth, uniform layers and exhibits a markedly lower dendrite propensity than alkali metals, conferring intrinsic safety – though dendrite-free plating is not guaranteed under all electrolyte conditions. However, in conventional polar aprotic electrolytes, the Mg surface rapidly develops an ionically blocking passivation film, prompting intense research into three main anode strategies: surface-modified Mg metal, low-potential intercalation hosts, and alloying/conversion-type materials (Ling and Zhang, 2017).

Intercalation-type anodes compatible with standard Mg^{2+}-conducting electrolytes avoid passivation issues but suffer from sluggish Mg^{2+} diffusion, large volume changes, and particle fragmentation. Theoretical studies predict that defective graphene (e.g., 25% divacancy concentration) could achieve capacities up to 1042 mAh/g, while nanostructured carbons (nanotubes, nanocones, nanosheets, C_{60} cages) also show promise (Bella et al., 2021). Experimentally, graphite delivers ≈ 180 mAh/g in conventional electrolytes. Spinel $Li_4Ti_5O_{12}$ exhibits strongly size-dependent Mg^{2+} insertion, with 7–8 nm particles yielding 175 mAh/g and excellent stability (> 500 cycles). $Na_2Ti_6O_{13}$ and hollow Li_3VO_4/carbon spheres provide 166–318 mAh/g with enhanced structural robustness (Luo et al., 2020). Ultrathin TiO_2-B nanowires expose highly reactive (110) facets, enabling surface-dominated Mg^{2+} coordination and delivering 110 mAh/g with only 0.08% capacity loss per cycle (Zeng et al., 2017).

Alloying anodes offers far higher theoretical capacities and operates at low potentials. Bismuth (385 mAh/g, ≈ 0.23/0.32 V vs. Mg^{2+}/Mg), $Bi_{0.88}Sb_{0.12}$ (Wang et al., 2018b; Niu et al., 2020), Bi nanotubes (350 mAh/g, 92% retention after 200 cycles) (Shao et al., 2014), and BiOF nanosheets (335 mAh/g via in situ conversion to 2D Bi) (Tan et al., 2018) demonstrate excellent reversibility and rate performance. Tin (903 mAh/g, ≈ 0.15/0.20 V) and Sn-Sb nanoparticulate alloys reach 420 mAh/g with good rate capability and 74% retention after 200 cycles (Cheng et al., 2015). Bi-Sn alloys outperform their pure constituents owing to accelerated Mg^{2+} transport along phase boundaries and self-supporting nanoporous architectures. A breakthrough Ga-based liquid-solid interconversion anode ($Mg_2Ga_5 \leftrightarrow Ga$) recently achieved > 1000 cycles at 922.5 mA/g, marking a milestone toward practical high-power RMB anodes (Wang et al., 2019).

Although intercalation anodes eliminate passivation and enable conventional high-voltage electrolytes, the strong Mg^{2+}–host electrostatic interaction results in sluggish kinetics, elevated operating potentials, and reduced full-cell energy density compared with Mg-metal configurations. Alloying and conversion systems currently offer the most attractive combination of capacity, voltage, and cycle life for next-generation rechargeable magnesium batteries.

7. CALCIUM ION BATTERIES

Calcium ranks as the fifth most abundant element within the Earth's crust. It is also nontoxic, which allows for cleaner, more ecologically friendly products. Calcium ions also exhibit favourable electrochemical properties, showing only slightly lower deposition potential than that of lithium and higher than that of magnesium (Yin et al., 2025). The size of calcium ions is similar to that of sodium but larger than magnesium and lithium. Reversible electrochemical processes of calcium cations in electrolytes were first presented in 2016 (Ponrouch et al., 2016). Because of that fact, the research on calcium-ion batteries remains in its infancy. Currently, no working prototypes exist, and available data are of experimental and laboratory nature.

7.1. Cathode materials for CIBs

Various types of materials are investigated as cathodes for calcium-ion batteries.

The first type is polyanionic compounds based on transition metal oxide and a tetrahedral anion. Transition metal oxides include iron and vanadium. The iron polyanionic cathodes have reached a capacity of 80 mAh/g, for vanadium 88–103 mAh/g. The stability of such materials reached 400 cycles for iron polyanionic cathodes, and vanadium materials show capacity retention after 200 cycles.

Another class of cathode materials comprises organic compounds, including conducting polymers, organosulfur compounds, and carbonyl-based materials, which are distinguished by their low cost, wide availability, and environmental compatibility. These materials can be categorised into three primary groups: n-type (cations storage), p-type (anions storage), and bipolar-type (capable of storing both cations and anions). The capacity of organic compounds cathodes is between 100 and 150 mAh/g, but their capacity retention is between 50 and 79% after 5000 cycles.

Another kind of cathode materials studied for CIBs applications are metal oxides of special consideration, such as vanadium, molybdenum, manganese, and cobalt oxides.

Vanadium-based oxides include a series of compounds due to their many oxidation levels. They are of low-cost due to high abundance in the Earth's crust, and intercalation reactions between calcium cations were investigated from 2003. Several forms of V_2O_5 were investigated, both crystalline and amorphous. Research indicated that amorphous materials exhibited larger amounts of calcium cation reactions (Wu et al., 2021; Zhou et al., 2021). In recent years vanadium oxides mixed with active metals or ammonia were developed as a new kind of cathodes for CIBs. One of such popular options is calcium vanadium oxides hydrates (Jeon et al., 2022; Wang et al., 2022). Calcium modified oxides can deliver reversible capacity after 200 cycles of magnitude 141 mAh/g. In a similar fashion, magnesium-modified vanadium oxides were synthesised (Xu et al., 2019). Capacity retention 1 reached 86.9% after 500 cycles with columbic efficiency of over 98.4%. Electrochemical experiments demonstrated that the structure changed only slightly with the insertion/extraction of calcium ions. Mixed magnesium ions were stable in the interlayer during electrochemical reactions. Another element that is present in vanadium oxide cathodes is iron.

Prussian Blue Analogues (PBAs): These three-dimensional open-framework structures are considered potential candidates for calcium-ion storage due to their ability to facilitate rapid Ca^{2+} diffusion, though their low conductivity can limit performance. Similar to potassium and sodium ions, Prussian blue is used as a cathode material. Cui's group (Wang et al., 2013) demonstrated the reversible insertion of calcium ions into nickel hexacyanoferrate. Cycling voltages ranged between 0.22 and 0.92 V, and capacity retention after 2000 cycles was 53% (Wessells et al., 2011b; Mu et al., 2022). Another Prussian blue analogue that was reported was barium hexacyanoferrate. This material was used to build a working battery with a coulumbic efficiency of 90%, and a capacity of 70 mAh/g. The capacity retention of this cathode was 93% after 2000 cycles. Due to high potentials versus silver chloride copper hexacyanoferrate electrode was used. The electrochemical reaction of Ca^{2+} ion insertion is coupled with iron cation change of charge. The cathode retained much of its structural stability during cycling, resulting in 88% of capacity retention after 2000 cycles. The capacity of this copper-based Prussian blue analogue cathode was 65 mAh/g (Gheytani et al., 2017). In non-aqueous solutions, manganese-based Prussian blue analogues can be used. Lipson et al. (2015) performed research on this subject and reported a capacity of intercalation in the range of 80 mAh/g. The mechanism of insertion was investigated at 60 °C. It was assumed that high temperatures and ionic solvents accelerated the calcium ion exchange process.

7.2. Anode materials for CIBs

Anode materials for calcium-ion batteries include calcium metal, carbon-based materials (like graphite and silicon carbide), organic compounds (such as anthracene and pentacene), and metal alloys (including alloys of silicon, tin, and antimony. The most important point of investigation is their potential to store and release calcium ions reversibly. Research focuses on the improvement of their capacity, cycle life, and overall performance (Guo et al., 2025; Maltsev et al., 2024; Zhang and Guo, 2025).

The simplest approach is to use calcium metal as an anode. The benefit is achieving high current densities, but such electrodes decompose quickly during the process and give only satisfactory performances. Another problem is the dendrite growth of calcium metal.

Another investigated anode material is graphite, which has the benefit of not forming a protective insoluble layer around the electrode. The capacities reached are between 60–80 mAh/g, being stable for 500 cycles.

Another group of materials are organic compounds. Polyaromatic hydrocarbons (PAHs), including anthracene and pentacene, have emerged as promising anode materials for rechargeable batteries. They are considered prototypical carbonaceous materials. Calcium intercalants are inserted between crystalline structures bonded by van der Waals forces. Research has shown that such anodes can reach capacities up to 1000 mAh/g.

Metal alloys anodes that have been investigated are Zn, Li, Na, Al, and Si. Except for Na, they can mix with calcium and form intermetallic compositions. Examples of the alloy anodes

are Ca_3Zn, Ca_2Sn, and $CaLi_2$. These materials exhibit theoretical capacities of 1366, 903, and 3860 mAh/g, respectively (Tinker et al., 2023).

8. CONCLUSIONS

All energy storage systems presented in this article are perspectives for future applications in electrical energy grids and electric vehicles. The main argument for the development of sodium, potassium and magnesium systems is their higher abundance in Earth's crust, which is significantly higher than that of lithium. Every system faces its challenges. In the case of sodium and potassium batteries, these are safety and full temperature adaptability (Bai et al., 2024).

SIBs are considered frontrunners for addressing the demands of the grid storage market (Hirsh et al., 2020). Key challenges impeding their commercialisation include the optimisation of electrolyte composition, anode performance, stability at the electrode-electrolyte interface, safety concerns, and sustainable recyclability. These issues have been analysed in detail, alongside potential strategies for their mitigation (Zhao et al., 2023). Potassium-ion batteries (KIBs) hold considerable promise as a scalable solution for grid-level energy storage. This optimism stems from the low cost of potassium precursors and auxiliary components, which contrasts sharply with the escalating prices of lithium-based materials. Moreover, the established manufacturing infrastructure, electrode architectures, and electrolyte formulations from mature lithium-ion technology provide a robust foundation for accelerating KIB research, prototyping, and eventual commercial deployment (He et al., 2024). Magnesium batteries are still in their beginning stage (Shah et al., 2021). The construction of the prototype is challenged by various factors like diffusion kinetics and the formation of passive layers (Medina et al., 2021). However, there is a large drive to improve those drawbacks in the scientific community, and more innovative materials are being developed.

Calcium-ion batteries are still being investigated for most effective processes and electrode materials. Lithium is still being investigated, especially to make it more recyclable. There is a growing interest in recovering as many materials as possible (Fan et al., 2020; Roy et al., 2024). Contemporary lithium-ion batteries are well-suited to high-value applications such as frequency regulation, short-duration storage, and microgrids. However, their high cost and long-term concerns over the availability of critical minerals (lithium, cobalt, nickel) continue to restrict their widespread deployment for large-scale, long-duration grid storage. Among the numerous emerging alternatives, sodium-ion and potassium-ion chemistries currently represent the most actively developed and promising post-lithium options (Grey and Hall, 2020).

REFERENCES

Wang S., Quan W., Zhu Z., Yang Y., Liu Q., Ren Y., Zhang X., Xu R., Hong Y., Zhang Z., Amine K., Tang Z., Lu J., Li J., 2017. Lithium titanate hydrates with superfast and stable cycling in lithium ion batteries. *Nat. Commun.*, 8, 627. DOI: 10.1038/s41467-017-00574-9.

Abbas S.M., Fayed M.G., El-Tawil R.S., Mohamed S.G., Abdel-Ghany A.E., Hashem A.M., Mauger A., Julien C.M., 2024. Lithium-rich spinel cathode with higher energy density for sustainable Li-ion batteries operating in extended potential range. *Intell. Sustainable Manuf.*, 1, 10014. DOI: 10.70322/ism.2024.10014.

Abel P.R., Lin Y.-M., de Souza T., Chou C.-Y., Gupta A., Goodenough J.B., Hwang G.S., Heller A., Mullins C.B., 2013. Nanocolumnar germanium thin films as a high-rate sodium-ion battery anode material. *J. Phys. Chem. C*, 117, 18885–18890. DOI: 10.1021/jp407322k.

Ahangari M., Szalai B., Lujan J., Zhou M., Luo H., 2024. Advancements and challenges in high-capacity Ni-rich cathode materials for lithium-ion batteries. *Materials*, 17, 801. DOI: 10.3390/ma17040801.

Amarapala V., Darwish A.S.K., Farrell P., 2023. Storage of wind power energy: main facts and feasibility – hydrogen as an option. *Renewable Energy Environ. Sustainability*, 8, 16. DOI: 10.1051/rees/2023013.

Anoopkumar V., John B., Mercy T.D., 2020. Potassium-ion batteries: Key to future large-scale energy storage? *ACS Appl. Energy Mater.*, 3, 9478–9492. DOI: 10.1021/acsaem.0c01574.

Atkins P., de Paula J., Keeler J., 2017. Atkins' Physical Chemistry. 11th edition. Oxford University Press, Oxford.

Bai Z., Yao Q., Wang M., Meng W., Dou S., Liu H.K., Wang N., 2024. Low-temperature sodium-ion batteries: challenges and progress. *Adv. Energy Mater.*, 14, 2303788. DOI: 10.1002/aenm.202303788.

Barsegyan A.A., Baghdasaryan I.R., 2022. Prospects for the use of energy storage devices in the process of solar energy production. *Polityka Energetyczna – Energy Policy J.*, 25, 135–148. DOI: 10.33223/EPJ/155789.

Basu S., 1982. *Ambient temperature rechargeable battery*. US Patent, US4423125A.

Bella F., De Luca S., Fagiolari L., Versaci D., Amici J., Francia C., Bodoardo S., 2021. An overview on anodes for magnesium batteries: challenges towards a promising storage solution for renewables. *Nanomaterials*, 11, 810. DOI: 10.3390/nano11030810.

Besenhard J.O., Eichinger G., 1976. High energy density lithium cells: Part I. Electrolytes and anodes. *J. Electroanal. Chem. Interfacial Electrochem.*, 68, 1–18. DOI: 10.1016/S0022-0728(76)80298-7.

Billaud J., Clément R.J., Armstrong A.R., Canales-Vázquez J., Rozier P., Grey C.P., Bruce P.G., 2014. β-$NaMnO_2$: a high-performance cathode for sodium-ion batteries. *J. Am. Chem. Soc.*, 136, 17243–17248. DOI: 10.1021/ja509704t.

Bustos R., Gadsden S.A., Al-Shabi M., Mahmud S., 2023. Lithium-ion battery health estimation using an adaptive dual interacting model algorithm for electric vehicles. *Appl. Sci.*, 13, 1132. DOI: 10.3390/app13021132.

Chebiam R.V., Prado F., Manthiram A., 2001. Structural instability of delithiated $Li_{1-x}Ni_{1-y}Co_yO_2$ cathodes. *J. Electrochem. Soc.*, 148, A49. DOI: 10.1149/1.1339029.

Chen M., Wang E., Liu Q., Guo X., Chen W., Chou S.-L., Dou S.-X., 2019. Recent progress on iron- and manganese-based anodes for sodium-ion and potassium-ion batteries. *Energy Storage Mater.*, 163–178. DOI: 10.1016/j.ensm.2019.03.030.

Cheng Y., Shao Y., Parent L.R., Sushko M.L., Li G., Sushko P.V., Browning N.D., Wang C., Liu J., 2015. Interface promoted reversible Mg insertion in nanostructured tin-antimony alloys. *Adv. Mater.*, 27, 6598–6605. DOI: 10.1002/adma.201502378.

Choi I., Ha S., Kim K.-H., 2024. Review and recent advances in metal compounds as potential high-performance anodes for sodium ion batteries. *Energies*, 17, 2646. DOI: 10.3390/en17112646.

Dacek S.T., Richards W.D., Kitchaev D.A., Ceder G., 2016. Structure and dynamics of fluorophosphate Na-ion battery cathodes. *Chem. Mater.*, 28, 5450–5460. DOI: 10.1021/acs.chemmater.6b01989.

Darwiche A., Marino C., Sougrati M.T., Fraisse B., Stievano L., Monconduit L., 2012. Better cycling performances of bulk Sb in Na-ion batteries compared to Li-ion systems: an unexpected electrochemical mechanism. *J. Am. Chem. Soc.*, 134, 20805–20811. DOI: 10.1021/ja310347x.

Delmas C., Fouassier C., Hagenmuller P., 1980. Structural classification and properties of the layered oxides. *Physica B+C*, 99, 81–85. DOI: 10.1016/0378-4363(80)90214-4.

Dong Y., Li S., Zhao K., Han C., Chen W., Wang B., Wang L., Xu B., Wei Q., Zhang L., Xu X., Mai L., 2015. Hierarchical zigzag $Na_{1.25}V_3O_8$ nanowires with topotactically encoded superior performance for sodium-ion battery cathodes. *Energy Environ. Sci.*, 8, 1267–1275. DOI: 10.1039/c5ee00036j.

Fan E., Li L., Wang Z., Lin J., Huang Y., Yao Y., Chen R., Wu F., 2020. Sustainable recycling technology for Li-ion batteries and beyond: challenges and future prospects. *Chem. Rev.*, 120, 7020–7063. DOI: 10.1021/acs.chemrev.9b00535.

Florez Gomez J.F., Domenech F.C., Chang S., Dorvilien V., Oli N., Weiner B.R., Morell G., Wu X., 2024. Enhancing tin dioxide anode performance by narrowing the potential range and optimizing electrolytes. *Batteries*, 10, 334. DOI: 10.3390/batteries10090334.

Frith J.T., Lacey M.J., Ulissi U., 2023. A non-academic perspective on the future of lithium-based batteries. *Nat. Commun.*, 14, 420. DOI: 10.1038/s41467-023-35933-2.

Ge J., Fan L., Rao A.M., Zhou J., Lu B., 2022. Surface-substituted Prussian blue analogue cathode for sustainable potassium-ion batteries. *Nat. Sustainability*, 5, 225–234. DOI: 10.1038/s41893-021-00810-7.

Gershinsky G., Yoo H.D., Gofer Y., Aurbach D., 2013. Electrochemical and spectroscopic analysis of Mg^{2+} intercalation into thin film electrodes of layered oxides: V_2O_5 and MoO_3. *Langmuir*, 29, 10964–10972. DOI: 10.1021/la402391f.

Gheytani S., Liang Y., Jing Y., Dong H., Chi X., Yao Y., 2017. An Aqueous Ca-Ion Battery. *Adv. Sci.*, 4, 1700465. DOI: 10.1002/ADVS.201700465.

Godshall N.A., Raistrick I.D., Huggins R.A., 1980. Thermodynamic investigations of ternary lithium-transition metal-oxygen cathode materials. *Mater. Res. Bull.*, 15, 561–570. DOI: 10.1016/0025-5408(80)90135-X.

Gomez K., Fletes E., Parsons J.G., Alcoutlabi M., 2024. The effect of TiO_2 on the electrochemical performance of Sb_2O_3 anodes for Li-ion batteries. *Appl. Sci.*, 14, 6598. DOI: 10.3390/app14156598.

Grey C.P., Hall D.S., 2020. Prospects for lithium-ion batteries and beyond – a 2030 vision. *Nat. Commun.*, 11, 6279. DOI: 10.1038/s41467-020-19991-4.

Grey C.P., Yoon W.-S., Reed J., Ceder G., 2004. Electrochemical activity of Li in the transition-metal sites of O3 $Li[Li_{(1-2x)/3}Mn_{(2-x)/3}Ni_x]$ O_2. *Electrochem. Solid-State Lett.*, 7, A290. DOI: 10.1149/1.1783113.

Guo Y., Wang C., Tan C., Zhang D., 2025. A comprehensive review of anode materials in rechargeable calcium-ion batteries. *Chem. Eur. J.*, 31, e202500071. DOI: 10.1002/CHEM.202500071.

Han M.H., Gonzalo E., Casas-Cabanas M., Rojo T., 2014. Structural evolution and electrochemistry of monoclinic $NaNiO_2$ upon the first cycling process. *J. Power Sources*, 258, 266–271. DOI: 10.1016/j.jpowsour.2014.02.048.

Hasan M.M., Hossain S., Mofijur M., Kabir Z., Badrudd I.A., Yunus Khan T.M., Jassim E., 2023. Harnessing solar power: a review of photovoltaic innovations, solar thermal systems, and the dawn of energy storage solutions. *Energies*, 16, 6456. DOI: 10.3390/en16186456.

Hassan Q., Abbas M.K., Tabar V.S., Tohidi S., Sameen A.Z., Salman H.M., 2024. Techno-economic assessment of battery storage with photovoltaics for maximum self-consumption. *Energy Harvesting Syst.*, 11, 1–15. DOI: 10.1515/ehs-2022-0050.

Haynes W.M., Lide D.R., Bruno T.J. (Eds.), 2016. *CRC Handbook of Chemistry and Physics*. 97th edition, CRC Press.

He X., Iqbal N., Ghani U., Li T., 2024. Potassium ion batteries: recent advancements in anodic, cathodic, and electrolytic materials. *J. Alloys Compd.*, 981, 173680. DOI: 10.1016/j.jallcom.2024.173680.

Hidalgo M.Á., Lavela P., Tirado J.L., Aranda M., 2024. Modification of layered cathodes of sodium-ion batteries with conducting polymers. *Batteries*, 10, 93. DOI: 10.3390/batteries10030093.

Hirsh H.S., Li Y., Tan D.H.S., Zhang M., Zhao E., Meng Y.S., 2020. Sodium-ion batteries paving the way for grid energy storage. *Adv. Energy Mater.*, 10, 2001274. DOI: 10.1002/aenm.202001274.

Hong S., Lee H., Yu Y.-S., Park J., Kim C., 2023. Development of a rock-salt structure for high energy density lithium-ion batteries. *Electron. Mater. Lett.*, 19, 359–366. DOI: 10.1007/s13391-022-00397-x.

Hosaka T., Shimamura T., Kubota K., Komaba S., 2019. Polyanionic compounds for potassium-ion batteries. *Chem. Rec.*, 19, 735–745. DOI: 10.1002/tcr.201800143.

Hosono E., Saito T., Hoshino J., Okubo M., Saito Y., Nishio-Hamane D., Kudo T., Zhou H., 2012. High power Na-ion rechargeable battery with single-crystalline $Na_{0.44}MnO_2$ nanowire electrode. *J. Power Sources*, 217, 43–46. DOI: 10.1016/j.jpowsour.2012.05.100.

Hu C., Geng M., Yang H., Fan M., Sun Z., Yu R., Wei B., 2024. A review of capacity fade mechanism and promotion strategies for lithium iron phosphate batteries. *Coatings*, 14, 832. DOI: 10.3390/coatings14070832.

Hu J.-P., Sheng H., Deng Q., Ma Q., Liu J., Wu X.-W., Liu J.-J., Wu Y.-P., 2020. High-rate layered cathode of lithium-ion batteries through regulating three-dimensional agglomerated structure. *Energies*, 13, 1602. DOI: 10.3390/en13071602.

Huang Y.-R., Lee C.-H., Popuri S.R., Lee L.-C., 2025. Optimization of hydrometallurgical recovery of lithium, aluminum, iron, and copper from lithium-iron batteries. *Arch. Environ. Prot.*, 51, 75–82. DOI: 10.24425/AEP.2025.153751.

Hwang M., Kim R., Hwang J., Jang G., Kim W.I, Min W., Kwon D., Kim D., Park H.S., 2025. Modulating chemical state of cation site for fast and reversible Na ion storage of fluorophosphate cathodes. *ACS Energy Lett.*, 10, 6297–6306. DOI: 10.1021/acsenergylett.5c02540.

IEA, 2022. Global EV Outlook 2022 – Analysis. International Energy Agency. Available at: https://www.iea.org/reports/global-ev-outlook-2022.

IRENA, 2017. *Electricity storage and renewables: Costs and markets to 2030*. International Renewable Energy Agency, Abu Dhabi. Available at: https://www.irena.org/-/media/Files/IRENA/Agency/Publication/2017/Oct/IRENA_Electricity_Storage_Costs_2017.pdf.

Iyer V., Petersen J., Geier S., Wierach P., 2024. Design and characterization of poly(ethylene oxide)-based multifunctional composites with succinonitrile fillers for ambient-temperature structural sodium-ion batteries. *Polymers*, 16, 2806. DOI: 10.3390/polym16192806.

Jeon B., Kwak H.H., Hong S.-T., 2022. Bilayered $Ca_{0.28}V_2O_5{\cdot}H_2O$: high-capacity cathode material for rechargeable Ca-ion batteries and its charge storage mechanism. *Chem. Mater.*, 34, 1491–1498. DOI: 10.1021/ACS.CHEMMATER.1C02774.

Jeon Y., Lee D.J., Zheng H., Behara S.S., Lee J-P., Wu J., Li F., Tang W., Zhang L., Chen Y.-T., Xu D., Kim J., Song M.-S., der Ven A.V., He K., Chen Z., 2025. Lithium diffusion-controlled Li-Al alloy negative electrode for all-solid-state battery. *Nat. Commun.*, 16, 9629. DOI: 10.1038/s41467-025-64386-y.

Jia M., Zhang L., Yuan Q., 2023. Application of new COF materials in secondary battery anode materials. *Molecules*, 28, 5953. DOI: 10.3390/molecules28165953.

Jia Q., Li Z., Ruan H., Luo D., Wang J., Ding Z., Chen L., 2024. A review of carbon anode materials for sodium-ion batteries: key materials, sodium-storage mechanisms, applications, and large-scale design principles. *Molecules*, 29, 4331. DOI: 10.3390/molecules29184331.

Jian Z., Luo W., Ji X., 2015. Carbon electrodes for K-ion batteries. *J. Am. Chem. Soc.*, 137, 11566–11569. DOI: 10.1021/jacs.5b06809.

Jiang Y., Li K., Alhassan S.I., Cao Y., Deng H., Tan S. Wang H., Tang C., Chai L., 2023. Spinel $LiMn_2O_4$ as a capacitive deionization electrode material with high desalination capacity: experiment and simulation. *Int. J. Environ. Res. Public Health*, 20, 517. DOI: 10.3390/ijerph20010517.

JLL, 2024. Utility-scale battery storage opens up for investors. Available at: https://www.jll.com/en-us/insights/utility-scale-battery-storage-opens-up-for-investors.

Jung S.C., Jung D.S., Choi J.W., Han Y.-K., 2014. Atom-level understanding of the sodiation process in silicon anode material. *J. Phys. Chem. Lett.*, 5, 1283–1288. DOI: 10.1021/jz5002743.

Kehne P., Guhl C., Ma Q., Tietz F., Alff L., Hausbrand R., Komissinskiy P., 2019. Electrochemical performance of all-solid-state sodium-ion model cells with crystalline Na_xCoO_2 thin-film cathodes. *J. Electrochem. Soc.*, 166, A5328. DOI: 10.1149/2.0491903jes.

Kim H., Sadan M.K., Kim C., Choi G.-I., Seong M., Cho K.-K., Kim K.-W., Ahn J.-H., Ahn H.-J., 2021. Electrochemical properties of flexible anode with SnO_2 nanopowder for sodium-ion batteries. *Arch. Metall. Mater.*, 66, 931–934. DOI: 10.24425/AMM.2021.136399.

Kim J., Han S.-D., Koo B., Lee S.-H., Yang J., 2023. Structure dependent electrochemical behaviors of hard carbon anode materials derived from natural polymer for next-generation sodium ion battery. *Polymers*, 15, 4373. DOI: 10.3390/polym15224373.

Kim S.-B., Lee S.-H., 2024. Application of deep learning techniques for the state of charge prediction of lithium-ion batteries. *Appl. Sci.*, 14, 8077. DOI: 10.3390/app14178077.

Kittner N., Lill F., Kammen D.M., 2017. Energy storage deployment and innovation for the clean energy transition. *Nat. Energy*, 2, 17125. DOI: 10.1038/nenergy.2017.125.

Koech A.K., Mwandila G., Mulolani F., Mwaanga P., 2024. Lithium-ion battery fundamentals and exploration of cathode materials: a review. *S. Afr. J. Chem. Eng.*, 50, 321–339. DOI: 10.1016/j.sajce.2024.09.008.

Koketsu T., Ma J., Morgan B.J., Body M., Legein C., Dachraoui W., Giannini M., Demortière A., Salanne M., Dardoize F., Groult H., Borkiewicz O.J., Chapman K.W., Strasser P., Dambournet D., 2017. Reversible magnesium and aluminium ions insertion in cation-deficient anatase TiO_2. *Nat. Mater.*, 16, 1142–1148. DOI: 10.1038/NMAT4976.

Komaba S., Hasegawa T., Dahbi M., Kubota K., 2015. Potassium intercalation into graphite to realize high-voltage/high-power potassium-ion batteries and potassium-ion capacitors. *Electrochem. Commun.*, 60, 172–175. DOI: 10.1016/j.elecom.2015.09.002.

Komarnicki P., 2016. Energy storage systems: power grid and energy market use cases. *Arch. Electr. Eng.*, 65, 495–511. DOI: 10.1515/AEE-2016-0036.

Kubota K., Dahbi M., Hosaka T., Kumakura S., Komaba S., 2018. Towards K-ion and Na-ion batteries as 'beyond Li-ion'. *Chem. Rec.*, 18, 459–479. DOI: 10.1002/tcr.201700057.

Kubota K., Ikeuchi I., Nakayama T., Takei C., Yabuuchi N., Shiiba H., Nakayama M., Komaba S., 2015. New insight into structural evolution in layered $NaCrO_2$ during electrochemical sodium extraction. *J. Phys. Chem. C*, 119, 166–175. DOI: 10.1021/jp5105888.

Kujawińska A., Hamrol A., Brzozowski K., 2022. Minimizing the emission of material waste in the production process of batteries. *Bull. Pol. Acad. Sci. Tech. Sci.*, 70, e144049. DOI: 10.24425/BPASTS.2022.144049.

Lavanya N., Sahaya Dennish Babu G., Judith Jayarani A., Prithivirajan P., Ayeshamariam A., 2025. Chapter 1 - Introduction and history of lithium-ion batteries, In: Thomas S., Gueye A.B., Savadogo O., Maria H.J. (Eds.), *Nanostructured lithium-ion battery materials: Synthesis, characterization, and applications*. Elsevier, 3–20. DOI: 10.1016/B978-0-443-13338-1.00016-2.

Lei Y., Li X., Liu L., Ceder G., 2014. Synthesis and stoichiometry of different layered sodium cobalt oxides. *Chem. Mater.*, 26, 5288–5296. DOI: 10.1021/cm5021788.

Leonova A.M., Bashirov O.A., Leonova N.M., Lebedev A.S., Trofimov A.A., Suzdaltsev A.V, 2023. Synthesis of C/SiC mixtures for composite anodes of lithium-ion power sources. *Appl. Sci.*, 13, 901. DOI: 10.3390/app13020901.

Levi E., Mitelman A., Isnard O., Brunelli M., Aurbach D., 2008. Phase diagram of Mg insertion into Chevrel phases, $Mg_xMo_6T_8$ (T = S, Se). 3. The crystal structure of triclinic $Mg_2Mo_6Se_8$. *Inorg. Chem.*, 47, 1975–1983. DOI: 10.1021/ic702311f.

Li C., Jiang W.-J., Liu Z.-Y., 2024. Carbon nanofibers-based anodes for potassium-ion battery. *ChemistryOpen*, 13, e202300286. DOI: 10.1002/open.202300286.

Li Y., Lu Y., Adelhelm P., Titirici M.-M., Hu Y.-S., 2019. Intercalation chemistry of graphite: alkali metal ions and beyond. *Chem. Soc. Rev.*, 48, 4655–4687. DOI: 10.1039/c9cs00162j.

Li Y., Ma J., Yin J., Xu J., Wei X., Hu Z., Chen W., Hu F., Yue C., 2026. Flexible lithium-ion batteries with LCO cathodes: recent advances and perspectives. *Nano Energy*, 148, 111644. DOI: 10.1016/j.nanoen.2025.111644.

Limachi C., Rogala K., Broszkiewicz M., Cabello M., Niedzicki L., Armand M., Wieczorek W., 2024. Development of fluorine-free electrolytes for aqueous-processed olivine-type phosphate cathodes. *Molecules*, 29, 4698. DOI: 10.3390/molecules29194698.

Lindagato P., Li Y., Macháček J., Yang G., Mungwarakarama I., Ndahimana A., Kanimba Ntwali H.P., 2023. Lithium metal: the key to green transportation. *Appl. Sci.*, 13, 405. DOI: 10.3390/app13010405.

Ling C., Zhang R., 2017. Manganese dioxide as rechargeable magnesium battery cathode. *Front. Energy Res.,* 5, 30. DOI: 10.3389/fenrg.2017.00030.

Lipson A.L., Pan B., Lapidus S.H., Liao C., Vaughey J.T., Ingram B.J., 2015. Rechargeable Ca-ion batteries: a new energy storage system. *Chem. Mater.*, 27, 8442–8447. DOI: 10.1021/ACS.CHEMMATER.5B04027.

Liu D., Palmore G.T.R., 2017. Synthesis, crystal structure, and electrochemical properties of alluaudite $Na_{1.702}Fe_3(PO_4)_3$ as a sodium-ion battery cathode. *ACS Sustainable Chem. Eng.*, 5, 5766–5771. DOI: 10.1021/acssuschemeng.7b00371.

Liu F., Cheng X., Xu R., Wu Y., Jiang Y., Yu Y., 2018. Binding sulfur-doped Nb_2O_5 hollow nanospheres on sulfur-doped graphene networks for highly reversible sodium storage. *Adv. Funct. Mater.*, 28, 1800394. DOI: 10.1002/adfm.201800394.

Liu S.-W., Niu B.-T., Lin B.-L., Lin Y.-T., Chen X.-P., Guo H.-X., Chen Y.-X., Lin X.-M., 2024. Investigating the electrochemical performance of $MnFe_2O_4$@xC nanocomposites as anode materials for sodium-ion batteries. *Molecules*, 29, 3912. DOI: 10.3390/molecules29163912.

Lung L.-Y., Chou T.-Y., Chang W.-C., Kuo C.-C., 2023. Development of energy storage systems for high penetration of renewable energy grids. *Appl. Sci.*, 13, 11978. DOI: 10.3390/app132111978.

Lung-Hao Hu B., Wu F.-Y., Lin C.-T., Khlobystov A.N., Li L.-J., 2013. Graphene-modified $LiFePO_4$ cathode for lithium ion battery beyond theoretical capacity. *Nat. Commun.*, 4, 1687. DOI: 10.1038/ncomms2705.

Luo L., Zhen Y., Lu Y., Zhou K., Huang J., Huang Z., Mathur S., Hong Z., 2020. Structural evolution from layered $Na_2Ti_3O_7$ to $Na_2Ti_6O_{13}$ nanowires enabling a highly reversible anode for Mg-ion batteries. *Nanoscale*, 12, 230–238. DOI: 10.1039/c9nr08003a.

Ma Y., Liu W., Liu W., Zhang G., Wang Y., Wang H., Chen W., Huang M., Wang X., 2024. Coconut-solid-waste-derived hard-carbon anode materials for fast potassium ion storage. *Coatings*, 14, 208. DOI: 10.3390/coatings14020208.

Maltsev A.P., Chepkasov I.V., Oganov A.R., 2024. New promising class of anode materials for Ca-ion battery: polyaromatic hydrocarbons. *Mater. Today Energy*, 39, 101467. DOI: 10.1016/J.MTENER.2023.101467.

Manthiram A., 2017. An outlook on lithium ion battery technology. *ACS Cent. Sci.*, 3, 1063–1069. DOI: 10.1021/acscentsci.7b00288.

Mao M., Lin Z., Tong Y., Yue J., Zhao C., Lu J., Zhang Q., Gu L., Suo L., Hu Y.-S., Li H., Huang X., Chen L., 2020. Iodine vapor transport-triggered preferential growth of Chevrel Mo_6S_8 nanosheets for advanced multivalent batteries. *ACS Nano*, 14, 1102–1110. DOI: 10.1021/acsnano.9b08848.

Masese T., Kanyolo G.M., 2023. Advancements in cathode materials for potassium-ion batteries: current landscape, obstacles, and prospects. *Energy Adv.*, 3, 60–107. DOI: 10.1039/d3ya00406f.

Medina A., Pérez-Vicente C., Alcántara R., 2021. Advancing towards a practical magnesium ion battery. *Materials*, 14, 7488. DOI: 10.3390/ma14237488.

Mizushima K., Jones P.C., Wiseman P.J., Goodenough J.B., 1980. Li_xCoO_2 ($0 < x < 1$): a new cathode material for batteries of high energy density. *Mater. Res. Bull.*, 15, 783–789. DOI: 10.1016/0025-5408(80)90012-4.

Mousavian S.M.H., Bautin V.A., 2025. Rechargeable magnesium batteries: overcoming challenges for high-efficiency energy applications. *J. Energy Storage*, 126, 117079. DOI: 10.1016/j.est.2025.117079.

Mu K., Mu Y., Wang X., Wu X., Pang C., Huang Y.-T., Feng S.-P., 2022. Direct thermal charging cell using nickel hexacyanoferrate (II) anode for green recycling of low-grade heat. *ACS Energy Lett.*, 7, 1146–1153. DOI: 10.1021/acsenergylett.2c00057.

Nandihalli N., Chouhan R.K., Kuchi R., Hlova I.Z., 2024. Aspects of spodumene lithium extraction techniques. *Sustainability*, 16, 8513. DOI: 10.3390/su16198513.

Nathan M.G.T., Yu H., Kim G.T., Kim J.H., Cho J.S., Kim J., Kim J.K., 2022. Recent advances in layered metal-oxide cathodes for application in potassium-ion batteries. *Adv. Sci.*, 9, 2105882. DOI: 10.1002/advs.202105882.

Nazarov A., Sulimin V., Shvedov V., 2024. Renewable energy sources: global implementation experience. *E3S Web Conf.*, 474, 01030. DOI: 10.1051/e3sconf/202447401030.

Nekahi A., Dorri M., Rezaei M., Bouguern M.D., Madikere Raghunatha Reddy A.K., Li X., Deng S., Zaghib K., 2024. Comparative issues of metal-ion batteries toward sustainable energy storage: lithium vs. sodium. *Batteries*, 10, 279. DOI: 10.3390/batteries10080279.

Nelson P.A., Gallagher K.G., Bloom I., Dees D.W., 2011. Modeling the performance and cost of lithium-ion batteries for electric-drive vehicles. Argonne National Laboratory. Avaiable at: https://publications.anl.gov/anlpubs/2011/10/71302.pdf.

Ni J., Li L., Lu J., 2018. Phosphorus: an anode of choice for sodium-ion batteries. *ACS Energy Lett.*, 3, 1137–1144. DOI: 10.1021/acsenergylett.8b00312.

Nitta N., Wu F., Lee J.T., Yushin G., 2015. Li-ion battery materials: present and future. *Mater. Today*, 18, 252–264. DOI: 10.1016/j.mattod.2014.10.040.

Niu J., Zhang Z., Aurbach D., 2020. Alloy Anode Materials for Rechargeable Mg Ion Batteries. *Adv. Energy Mater.*, 2000697. DOI: 10.1002/aenm.202000697.

Nowaczek A., Kulczycka J., 2020. Overview of funding sources and technologies for the recovery of raw materials from spent batteries and rechargeable batteries in Poland. *Gospod. Surowcami Miner. – Miner. Resour. Manage.*, 36, 153–172. DOI: 10.24425/gsm.2020.132564.

Nowak A.P., Rutecki P., Szkoda M., Trzciński K., 2024. Determination of sodium ion diffusion coefficient in tin sulfide@carbon anode material using GITT and EIS techniques. *Energies*, 17, 3233. DOI: 10.3390/en17133233.

Overhoff G.M., Nölle R., Siozios V., Winter M., Placke T., 2021. A thorough analysis of two different pre-lithiation techniques for silicon/carbon negative electrodes in lithium ion batteries. *Batteries Supercaps*, 4, 1163–1174. DOI: 10.1002/batt.202100024.

Padhi A.K., Nanjundaswamy K.S., Goodenough J.B., 1997. Phospho-olivines as positive-electrode materials for rechargeable lithium batteries. *J. Electrochem. Soc.*, 144, 1188. DOI: 10.1149/1.1837571.

Palumbo O., 2023. Innovative materials for batteries. *Appl. Sci.*, 13, 7595. DOI: 10.3390/app13137595.

Pan H., Zheng K., Chen Z., Wang Y., Tan Y., Wang J., Yao L., Wang L., Sun C., Yang J., 2024. Tuning the electronic structures of Mo-based sulfides/selenides with biomass-derived carbon for hydrogen evolution reaction and sodium-ion batteries. *Catalysts*, 14, 627. DOI: 10.3390/catal14090627.

Park J., Kim J., Kim J., Kim M., Song T., Paik U., 2025. Sustainable and cost-effective electrode manufacturing for advanced lithium batteries: the roll-to-roll dry coating process. *Chem. Sci.*, 16, 6598–6619. DOI: 10.1039/d5sc00059a.

Passerini S., Barelli L., Baumann M.J., Peters J.F., 2024. *Emerging battery technologies to boost the clean energy transition: cost, sustainability, and performance analysis*. Springer Cham. DOI: 10.1007/978-3-031-48359-2.

Ponrouch A., Frontera C., Bardé F., Palacín M.R., 2016. Towards a calcium-based rechargeable battery. *Nat. Mater.*, 15, 169–172. DOI: 10.1038/nmat4462.

Qian G., Wang J., Li H., Ma Z.-F., Pianetta P., Li L., Yu X., Liu Y., 2022. Structural and chemical evolution in layered oxide cathodes of lithium-ion batteries revealed by synchrotron techniques. *Natl. Sci. Rev.*, 9, nwab146. DOI: 10.1093/nsr/nwab146.

Richard J., Benayad A., Colin J.-F., Martinet S., 2017. Charge transfer mechanism into the Chevrel phase Mo_6S_8 during Mg intercalation. *J. Phys. Chem. C*, 121, 17096–17103. DOI: 10.1021/acs.jpcc.7b03979.

Roberts M.B., Bruce A., MacGill I., 2019. Impact of shared battery energy storage systems on photovoltaic self-consumption and electricity bills in apartment buildings. *Appl. Energy*, 245, 78–95. DOI: 10.1016/j.apenergy.2019.04.001.

Roy J.J., Phuong D.M., Verma V., Chaudhary R., Carboni M., Meyer D., Cao B., Srinivasan M., 2024. Direct recycling of Li-ion batteries from cell to pack level: challenges and prospects on technology, scalability, sustainability, and economics. *Carbon Energy*, 6, e492. DOI: 10.1002/cey2.492.

Royal Society of Chemistry. *Calcium*. RSC Periodic Table. Available at: https://periodic-table.rsc.org/element/20/calcium.

Saint J.A., Doeff M.M., Wilcox J., 2008. Electrode materials with the $Na_{0.44}MnO_2$ structure: effect of titanium substitution on physical and electrochemical properties. *Chem. Mater.*, 20, 3404–3411. DOI: 10.1021/cm800247u.

Sakaushi K., Hosono E., Nickerl G., Gemming T., Zhou H., Kaskel S., Eckert J., 2013. Aromatic porous-honeycomb electrodes for a sodium-organic energy storage device. *Nat. Commun.*, 4, 1485. DOI: 10.1038/ncomms2481.

Sangsanit T., Matkhaw N., Benwannamas N., Songthan R., Tejangkura W., Sawangphruk M., 2025. Layered lithium- and manganese-rich oxide cathode cells in large-scale cylindrical configuration: optimized electrolyte formulations with LiDFOB and $LiBF_4$ Co-additives for enhanced stability. *J. Power Sources*, 632, 236337. DOI: 10.1016/j.jpowsour.2025.236337.

Sauvage F., Laffont L., Tarascon J.-M., Baudrin E., 2007. Study of the insertion/deinsertion mechanism of sodium into $Na_{0.44}MnO_2$. *Inorg. Chem.*, 46, 3289–3294. DOI: 10.1021/ic0700250.

Schirber M., 2024. Sodium as a green substitute for lithium in batteries. *Physics*, 17, 73. DOI: 10.1103/physics.17.73.

Sgourou E.N., Daskalopulu A., Tsoukalas L.H., Goulatis I.L., Vovk R.V., Chroneos A., 2023. Kinetics of ions in post-lithium batteries. *Appl. Sci.*, 13, 9619. DOI: 10.3390/app13179619.

Shah R., Mittal V., Matsil E., Rosenkranz A., 2021. Magnesium-ion batteries for electric vehicles: current trends and future perspectives. *Adv. Mech. Eng.* 13, 1–9 DOI: 10.1177/16878140211003398.

Shahabuddin M., Alim M.A., Alam T., Mofijur M., Ahmed S.F., Perkins G., 2021. A critical review on the development and challenges of concentrated solar power technologies. *Sustainable Energy Technol. Assess.*, 47, 101434. DOI: 10.1016/j.seta.2021.101434.

Shahid S., Agelin-Chaab M., 2023. Chapter 10 – Battery thermal management through simulation and experiment: Air cooling and enhancement, In: Aloui F., Varuvel E.G., Sonthalia A. (Eds.), Handbook of Thermal Management Systems. Elsevier, 221–254. DOI: 10.1016/B978-0-443-19017-9.00008-8.

Shao Y., Gu M., Li X., Nie Z., Zuo P., Li G., Liu T., Xiao J., Cheng Y., Wang C., Zhang J.-G., Liu J., 2014. Highly reversible Mg insertion in nanostructured Bi for Mg ion batteries. *Nano Lett.*, 14, 255–260. DOI: 10.1021/nl403874y.

Shibata T., Fukuzumi Y., Kobayashi W., Moritomo Y., 2015. Fast discharge process of layered cobalt oxides due to high Na^+ diffusion. *Sci. Rep.*, 5, 9006. DOI: 10.1038/srep09006.

Shim H.-W., Im B., Joo S., Kim D.-G., 2024. Facile synthesis and Li-electroactivity of cobalt oxide based on resources recovered from waste lithium-ion batteries. *Arch. Metall. Mater.*, 69, 67–72. DOI: 10.24425/AMM.2024.147787.

Stournara M.E., Shenoy V.B., 2011. Enhanced Li capacity at high lithiation potentials in graphene oxide. *J. Power Sources*, 196, 5697–5703. DOI: 10.1016/j.jpowsour.2011.02.024.

Su D., Dou S., Wang G., 2015. Bismuth: a new anode for the Na-ion battery. *Nano Energy*, 12, 88–95. DOI: 10.1016/j.nanoen.2014.12.012.

Sun X., Duffort V., Mehdi B.L., Browning N.D., Nazar L.F., 2016. Investigation of the mechanism of Mg insertion in birnessite in nonaqueous and aqueous rechargeable Mg-ion batteries. *Chem. Mater.*, 28, 534–542. DOI: 10.1021/acs.chemmater.5b03983.

Tan Y.-H., Yao W.-T., Zhang T., Ma T., Lu L.-L., Zhou F., Yao H.-B., Yu S.-H., 2018. High voltage magnesium-ion battery enabled by nanocluster Mg*3*Bi*2* alloy anode in noncorrosive electrolyte. *ACS Nano*, 12, 5856–5865. DOI: 10.1021/acsnano.8b01847.

Tepavcevic S., Liu Y., Zhou D., Lai B., Maser J., Zuo X., Chan H., Král P., Johnson C.S., Stamenkovic V., Markovic N.M., Rajh T., 2015. Nanostructured layered cathode for rechargeable Mg-ion batteries. *ACS Nano*, 9, 8194–8205. DOI: 10.1021/acsnano.5b02450.

Thackeray M.M., 1999. Spinel electrodes for lithium batteries. *J. Am. Ceram. Soc.*, 82, 3347–3354. DOI: 10.1111/j.1151-2916.1999.tb02250.x.

Tinker H.R., Howard C.A., Zhou M., Xu Y., 2023. Exploring anodes for calcium-ion batteries. *Mater. Adv.*, 4, 2028–2041. DOI: 10.1039/D2MA01034H.

Tolstoy V.P., Vladimirova N.I., Gulina L.B., 2019. Formation of ordered honeycomb-like structures of manganese oxide 2D nanocrystals with the birnessite-like structure and their electrocatalytic properties during oxygen evolution reaction upon water splitting in an alkaline medium. *ACS Omega*, 4, 22203–22208. DOI: 10.1021/acsomega.9b03499.

U.S. Geological Survey, 2020. Mineral Commodity Summaries 2020. U.S. Geological Survey, Reston, Virginia. DOI: https://doi.org/10.3133/mcs2020.

Vieira F.M., Moura P.S., de Almeida A.T., 2017. Energy storage system for self-consumption of photovoltaic energy in residential zero energy buildings. *Renewable Energy*, 103, 308–320. DOI: 10.1016/j.renene.2016.11.048.

Wahid M., Puthusseri D., Gawli Y., Sharma N., Ogale S., 2018. Hard carbons for sodium-ion battery anodes: synthetic strategies, material properties, and storage mechanisms. *ChemSusChem*, 11, 506–526. DOI: 10.1002/cssc.201701664.

Waldmann T., Scurtu R.-G., Richter K., Wohlfahrt-Mehrens M., 2020. 18650 vs. 21700 Li-ion cells – a direct comparison of electrochemical, thermal, and geometrical properties. *J. Power Sources*, 472, 228614. DOI: 10.1016/j.jpowsour.2020.228614.

Wan L.F., Incorvati J.T., Poeppelmeier K.R., Prendergast D., 2016. Building a fast lane for Mg diffusion in α-MoO_3 by fluorine doping. *Chem. Mater.*, 28, 6900–6908. DOI: 10.1021/acs.chemmater.6b02223.

Wang B., Deng T., Liu J., Sun B., Su Y., Ti R., Shangguan L., Zhang C., Tang Y., Cheng N., Xu Y., Guo J., 2024. Scaly MoS_2/rGO composite as an anode material for high-performance potassium-ion battery. *Molecules*, 29, 2977. DOI: 10.3390/molecules29132977.

Wang G., Xiong X., Xie D., Lin Z., Zheng J., Zheng F., Li Y., Liu Y., Yang C., Liu M., 2018a. Chemically activated hollow carbon nanospheres as a high-performance anode material for potassium ion batteries. *J. Mater. Chem. A*, 6, 24317–24323. DOI: 10.1039/c8ta09751h.

Wang J., Wang J., Jiang Y., Xiong F., Tan S., Qiao F., Chen J., An Q., Mai L., 2022. $CaV_6O_{16}{\cdot}2.8H_2O$ with Ca^{2+} pillar and water lubrication as a high-rate and long-life cathode material for Ca-ion batteries. *Adv. Funct. Mater.*, 32, 2113030. DOI: 10.1002/ADFM.202113030.

Wang L., Welborn S.S., Kumar H., Li M., Wang Z., Shenoy V.B., Detsi E., 2019. High-rate and long cycle-life alloy-type magnesium-ion battery anode enabled through (de)magnesiation-induced near-room-temperature solid–liquid phase transformation. *Adv. Energy Mater.*, 9, 1902086. DOI: 10.1002/aenm.201902086.

Wang R.Y., Wessells C.D., Huggins R.A., Cui Y., 2013. Highly reversible open framework nanoscale electrodes for divalent ion batteries. *Nano Lett.*, 13, 5748–5752. DOI: 10.1021/NL403669A.

Wang W., Liu L., Wang P.-F., Zuo T.-T., Yin Y.-X., Wu N., Zhou J.-M., Wei Y., Guo Y.-G., 2018b. A novel bismuth-based anode material with a stable alloying process by the space confinement of an in situ conversion reaction for a rechargeable magnesium ion battery. *Chem. Commun.*, 54, 1714–1717. DOI: 10.1039/c7cc08206a.

Wang X., Kajiyama S., Iinuma H., Hosono E., Oro S., Moriguchi I., Okubo M., Yamada A., 2015. Pseudocapacitance of MXene nanosheets for high-power sodium-ion hybrid capacitors. *Nat. Commun.*, 6, 6544. DOI: 10.1038/ncomms7544.

Wei L., Ji D., Zhao F., Tian X., Guo Y., Yan J., 2024. A review of carbon nanofiber materials for dendrite-free lithium-metal anodes. *Molecules*, 29, 4096. DOI: 10.3390/molecules29174096.

Wen Y., He K., Zhu Y., Han F., Xu Y., Matsuda I., Ishii Y., Cumings J., Wang C., 2014. Expanded graphite as superior anode for sodium-ion batteries. *Nat. Commun.*, 5, 4033. DOI: 10.1038/ncomms5033.

Wentker M., Greenwood M., Leker J., 2019. A bottom-up approach to lithium-ion battery cost modeling with a focus on cathode active materials. *Energies*, 12, 504. DOI: 10.3390/en12030504.

Wessells C.D., Huggins R.A., Cui Y., 2011a. Copper hexacyanoferrate battery electrodes with long cycle life and high power. *Nat. Commun.*, 2, 550. DOI: 10.1038/ncomms1563.

Wessells C.D., Peddada S.V., Huggins R.A., Cui Y., 2011b. Nickel hexacyanoferrate nanoparticle electrodes for aqueous sodium and potassium ion batteries. *Nano Lett.*, 11, 5421–5425. DOI: 10.1021/NL203193Q.

Whittingham M.S., 1976. Electrical energy storage and intercalation chemistry. *Science*, 192, 1126–1127. DOI: 10.1126/science.192.4244.1126.

Winter M., Barnett B., Xu K., 2018. Before Li ion batteries. *Chem. Rev.*, 118, 11433–11456. DOI: 10.1021/acs.chemrev.8b00422.

Wood W.W., Smedley P.L., Lindsey B.D., Wood W.T., Kirchheim R.E., Cherry J.A., 2022. Global groundwater solute composition and concentrations. *Groundwater*, 60, 714–720. DOI: 10.1111/GWAT.13205.

Wu Q., Shu K., Zhao L., Zhang J., 2024. Pomegranate peel-derived hard carbons as anode materials for sodium-ion batteries. *Molecules*, 29, 4639. DOI: 10.3390/molecules29194639.

Wu Y., Song T.-Y., Chen L.-N., 2021. A review on recent developments of vanadium-based cathode for rechargeable zinc-ion batteries. *Tungsten*, 3, 289–304. DOI: 10.1007/s42864-021-00091-9.

Xiang X., Zhang K., Chen J., 2015. Recent advances and prospects of cathode materials for sodium-ion batteries. *Adv. Mater.*, 27, 5343–5364. DOI: 10.1002/adma.201501527.

Xie J., Lu Y.-C., 2020. A retrospective on lithium-ion batteries. *Nat. Commun.*, 11, 2499. DOI: 10.1038/s41467-020-16259-9.

Xu L., Wang S., Xi L., Li Y., Gao J., 2024. A review of thermal management and heat transfer of lithium-ion batteries. *Energies*, 17, 3873. DOI: 10.3390/en17163873.

Xu M., Niu Y., Chen C., Song J., Bao S., Li C.M., 2014. Synthesis and application of ultra-long $Na_{0.44}MnO_2$ submicron slabs as a cathode material for Na-ion batteries. *RSC Adv.*, 4, 38140–38143. DOI: 10.1039/c4ra07355j.

Xu S., Dong H., Yang D., Wu C., Yao Y., Rui X., Chou S.-L., Yu Y., 2023. Promising cathode materials for sodium-ion batteries from lab to application. *ACS Cent. Sci.*, 9, 2012–2035. DOI: 10.1021/acscentsci.3c01022.

Xu X., Duan M., Yue Y., Li Q., Zhang X., Wu L., Wu P., Song, B., Mai L., 2019. Bilayered $Mg_{0.25}V_2O_5{\cdot}H_2O$ as a stable cathode for rechargeable Ca-ion batteries. *ACS Energy Lett.*, 4, 1328–1335. DOI: 10.1021/ACSENERGYLETT.9B00830.

Yang X.-G., Liu T., Wang C.-Y., 2021. Thermally modulated lithium iron phosphate batteries for mass-market electric vehicles. *Nat. Energy*, 6, 176–185. DOI: 10.1038/s41560-020-00757-7.

Yang Y., Wang R., Shen Z., Yu Q., Xiong R., Shen W., 2023. Towards a safer lithium-ion batteries: a critical review on cause, characteristics, warning and disposal strategy for thermal runaway. *Adv. Appl. Energy*, 11, 100146. DOI: 10.1016/j.adapen.2023.100146.

Yin Z., Wu J., Tian Y., Yuan Y., Gu M., Cheng L., Wang Y., Kim Y., 2025. High-performance quasi-solid-state calcium-ion batteries from redox-active covalent organic framework electrolytes. *Adv. Sci.*, 13, e12328. DOI: 10.1002/advs.202512328.

Ying H., Han W.-Q., 2017. Metallic Sn-based anode materials: application in high-performance lithium-ion and sodium-ion batteries. *Adv. Sci.*, 4, 1700298. DOI: 10.1002/advs.201700298.

Yuan L.-X., Wang Z.-H., Zhang W.-X., Hu X.-L., Chen J.-T., Huang Y.-H., Goodenough J.B., 2011. Development and challenges of LiFePO*4* cathode material for lithium-ion batteries. *Energy Environ. Sci.*, 4, 269–284. DOI: 10.1039/c0ee00029a.

Yüksek G., Lale T., 2024. Improved thermal management of lithium-based batteries employing genetic algorithm optimization. *Bull. Pol. Acad. Sci. Tech. Sci.*, 72, e151378. DOI: 10.24425/BPASTS.2024.151378.

Yun S., Liang X., Xi J., Liao L., Cui S., Chen L., Li S., Hu Q., 2024. Electrolytes for high-safety lithium-ion batteries at low temperature: a review. *Polymers*, 16, 2661. DOI: 10.3390/polym16182661.

Zaghib K., Mauger A., Goult H., Goodenough J.B., Julien C.M., 2013. Advanced electrodes for high power Li-ion batteries. *Materials*, 6, 1028–1049. DOI: 10.3390/ma6031028.

Zanoletti A., Carena E., Ferrara C., Bontempi E., 2024. A review of lithium-ion battery recycling: technologies, sustainability, and open issues. *Batteries*, 10, 38. DOI: 10.3390/batteries10010038.

Zeng J., Yang Y., Li C., Li J., Huang J., Wang J., Zhao J., 2017. Li_3VO_4: an insertion anode material for magnesium ion batteries with high specific capacity. *Electrochim. Acta*, 247, 265–270. DOI: 10.1016/j.electacta.2017.06.143.

Zhang J., Miao J., Balasubramani N., Cho D.H., Avey T., Chang C.-Y., Luo A.A., 2023a. Magnesium research and applications: past, present and future. *J. Magnesium Alloys*, 11, 3867–3895. DOI: 10.1016/j.jma.2023.11.007.

Zhang Q., Guo Y., 2025. $MoSe_2$ as a potential anode material for calcium ion batteries: first-principles study. *Mol. Phys.,* 123, e2482680. DOI: 10.1080/00268976.2025.2482680.

Zhang W., Liu Y., Guo Z., 2019a. Approaching high-performance potassium-ion batteries via advanced design strategies and engineering. *Sci. Adv.*, 5, eaav7412. DOI: 10.1126/sciadv.aav7412.

Zhang W., Zhang F., Ming F., Alshareef H.N., 2019b. Sodium-ion battery anodes: status and future trends. *EnergyChem*, 1, 100012. DOI: 10.1016/j.enchem.2019.100012.

Zhang X., Li D., Ruan Q., Liu L., Wang B., Xiong F., Huang C., Chu P.K., 2023b. Vanadium-based cathode materials for rechargeable magnesium batteries. *Mater. Today Energy*, 32, 101232. DOI: 10.1016/j.mtener.2022.101232.

Zhao J., Zhao L., Dimov N., Okada S., Nishida T., 2013. Electrochemical and thermal properties of α-$NaFeO_2$ cathode for Na-ion batteries. *J. Electrochem. Soc.*, 160, A3077. DOI: 10.1149/2.007305jes.

Zhao P.-Y., Zhang S., Choy K.-L., Song Y., Zhang S., Guo D., Yang C., 2025. Silicon negative electrodes for lithium-ion batteries: challenges, advances, and future prospects. *Mater. Horiz.*, 12, 6440–6484. DOI: 10.1039/d5mh00504c.

Zhao Y., Kang Y., Wozny J., Lu J., Du H., Li C., Li T., Kang F., Tavajohi N., Li, B., 2023. Recycling of sodium-ion batteries. *Nat. Rev. Mater.*, 8, 623–634. DOI: 10.1038/s41578-023-00574-w.

Zhao Y., Zhang Z., Zheng Y., Luo Y., Jiang X., Wang Y., Wang Z., Wu Y., Zhang Y., Liu X., Fang B., 2024. Sodium-ion battery at low temperature: challenges and strategies. *Nanomaterials*, 14, 1604. DOI: 10.3390/nano14191604.

Zheng X., Cai Z., Sun J., He J., Rao W., Wang J., Zhang Y., Gao Q., Han B., Xia K., Sun R., Zhou C., 2023. Nickel-rich layered oxide cathodes for lithium-ion batteries: failure mechanisms and modification strategies. *J. Energy Storage*, 58, 106405. DOI: 10.1016/j.est.2022.106405.

Zhou Y.-Y., Zhang Z.-Y., Zhang H.-Z., Li Y., Weng Y., 2021. Progress and perspective of vanadium-based cathode materials for lithium ion batteries. *Tungsten*, 3, 279–288. DOI: 10.1007/S42864-021-00101-W.

Ziegler M.S., Trancik J.E., 2021. Re-examining rates of lithium-ion battery technology improvement and cost decline. *Energy Environ. Sci.*, 14, 1635–1651. DOI: 10.1039/d0ee02681f.

Chemical and Process Engineering: New Frontiers, 2026, 47(2), e133
DOI: 10.24425/cpe.2026.158131

Photocurable resins for 3D printing: chemical and materials engineering aspects

Jakub Pietraszewski[1], Monika Topa-Skwarczyńska[1], Małgorzata Noworyta[1,2], Joanna Ortyl[1,2,4]

[1] Cracow University of Technology, Faculty of Chemical Engineering and Technology, Department of Biotechnology and Physical Chemistry, Warszawska 24, 31-155 Cracow, Poland
[2] Cracow University of Technology, CUT Doctoral School, Faculty of Chemical Engineering and Technology, Department of Biotechnology and Physical Chemistry, Warszawska 24, 31-155 Cracow, Poland
[3] Photo HiTech Ltd., Bobrzyńskiego 14, 30-348 Cracow, Poland
[4] Photo4Chem Ltd., Lea 114, 30-133 Cracow, Poland

*** Corresponding author, e-mail:**
monika.topa@pk.edu.pl

Article info:
Received: 06 January 2026
Revised: 9 April 2026
Accepted: 06 May 2026

Abstract
The development of functional photopolymer resins for additive manufacturing requires a combined materials and chemical engineering approach that addresses both resin formulation and the interactions between photocurable systems and 3D printing technologies. Herein, a series of investigations was conducted to rigorously delineate the influence of titanium dioxide (TiO_2) as an additive on the kinetics of the photopolymerization process and on the resulting quality parameters of photocurable resin prints. TiO_2 was incorporated at concentrations of 0.1–30 wt.%, and the resins were studied using Real-Time FT-IR, photo-DSC, photo-rheology and Jacobs curves. Low-to-medium additive concentrations accelerated early polymerization due to enhanced light scattering, whereas higher concentrations reduced light penetration and delayed curing. In addition to material performance, the chemical engineering aspects of additive manufacturing were examined by fabricating printouts on two 3D printers employing different technologies. Printouts from two 3D printers with different technologies, LCD and DLP, revealed a strong dependence on printer technology: the LCD system successfully printed only the base and 0.1 wt.% TiO_2 formulations, but with higher quality, while the higher-intensity DLP system processed all formulations. These results demonstrate that both titanium dioxide content and printing technology influence curing efficiency and final print quality, which are critical for the development of photopolymer resins.

Keywords
titanium dioxide (TiO_2), photopolymer materials, additive manufacturing, photopolymerization kinetics

1. INTRODUCTION

Additive manufacturing, also known as 3D printing, has rapidly evolved into a widely used technology in fields like engineering (Iftekar et al., 2023; Jayakrishna et al., 2023; Sharma et al., 2025), medicine (Aimar et al., 2019; Hellman et al., 2023; Paul et al., 2018), and dentistry (Jeong et al., 2023; Tian et al., 2021), as a way to create 3D objects. Among the diverse techniques, photochemical resin 3D printing is especially interesting as a topic of research because of its material versatility, high object resolution, fast fabrication time and relatively low cost of the materials, as well as the 3D printers (Gauci et al., 2024; Hobich et al., 2023; Petko et al., 2023; Topa-Skwarczyńska et al., 2025). Techniques such as Stereolithography (SLA), Liquid Crystal Display (LCD), and Digital Light Processing (DLP) are among the most prominent (Chaudhary et al., 2023; Dilberoglu et al., 2017). To expand the functionality of photocurable materials, significant research efforts are now focused on incorporating various inorganic additives into the printing matrices (Chopra et al., 2025; Maher et al., 2021; Martins de Sousa et al., 2023; Zhong et al., 2025). They can enhance mechanical, optical, thermal or biological properties of the final printout. In the vast group of the studied fillers, titanium dioxide, TiO_2, stands out as a promising one, especially for biomedical and dental photopolymers (Anselmo and Mitragotri, 2015; Bayda et al., 2020; Bobo et al., 2016; Mohammadi et al., 2025; Priyadarsini et al., 2019; Puckett et al., 2007; Tan and Lyu, 2023; Veljović and Miletic, 2023).

TiO_2 is an inorganic metal oxide, white in color, widely used as a pigment and a filler in polymer materials. It occurs in 2 common crystal structures, anatase and rutile, which differ in the spatial orientation of molecules within the crystal lattice (Stanford Advanced Materials, 2026). Because of its high refractive index, about 2.5 for both forms, it exhibits strong scattering of UV and visible light, making it valuable in applications requiring light propagation, such as photochemical 3D printing (Kaur et al., 2025). TiO_2 is inert under typical conditions and is not biodegradable. It exhibits high chemical stability, resistance to corrosion and hardness (O'Byrne et al., 2024).

In the context of resin-based additive manufacturing, TiO_2 can significantly influence the curing behavior of resins (Bao et al., 2022). It can improve it by enhancing layer formation and the uniformity of the photopolymerization process, mainly due to its scattering properties, which help distribute light

© 2026. The Author(s). This is an open-access article distributed under the terms of the Creative Commons Attribution (CC-BY 4.0, https://creativecommons.org/licenses/by/4.0/), which permits unrestricted use, distribution, and reproduction in any medium, provided the original author and source are credited.

energy. At the same time, TiO_2 particles can absorb or reflect light, altering the overall kinetics of photopolymerization and making it less favourable. These effects have been shown to influence mechanical performance and print resolution (Abd Elhamid Abo Salh et al., 2025; Aktas et al., 2024; Al Rashid et al., 2021; Ijaz and Zafar, 2021; Pai et al., 2023).

Extensive literature confirms the biocompatibility and mechanical effects of TiO_2 as an additive in 3D printing, supporting its use in biomedical contexts. When incorporated into pigment form at the macro or micro scale, TiO_2 is generally regarded as safe and non-toxic. TiO_2 has been reported to exhibit antibacterial properties under light irradiation due to its photocatalytic activity and the generation of reactive oxygen species. It is also characterized by high chemical stability and corrosion resistance in physiological environments, which further supports its suitability for biomedical applications, although such effects were not investigated in the present study (Almeshari et al., 2024; Altarazi et al., 2023; Altarazi et al., 2024; Billings et al., 2021; Mansoor et al., 2022; Noworyta et al., 2023; Remaggi et al., 2023; Serov et al., 2024; Sztorch et al., 2022; Wang et al., 2025; Wu et al., 2024; Yilmaz and Kapusuz Yavuz, 2025).

Two main factors determine the impact of TiO_2 as an additive in a photocurable resin: filler concentration and the printing technology used. What fundamentally differentiates these printing methods is the way they deliver light to the resin. Intensity, distribution and uniformity are crucial. SLA systems provide localised point exposure via a laser; DLP printers utilise high-intensity light from digital micromirrors in a single projector; and LCD printers rely on masked UV emission from multiple LEDs simultaneously (Taormina et al., 2018).

Therefore, understanding the interaction between resins and TiO_2 as an additive, as well as the specific light sources in 3D printers, is essential for designing functional composites. In this study, for the first time, the influence of TiO_2 additions at concentrations of 0.1, 1, 5, 10, and 30 wt.% on a methacrylate UDMA/TEGDMA resin system was investigated. The modified resins were evaluated on two representative 3D printers, a commercial-grade LCD Anycubic Photon Mono M7 PRO and the lab-grade DLP Lumen X^{TM} Gen 3 to assess how printer type and additive concentration affect curing behavior and overall quality of the enhanced photopolymer material.

2. EXPERIMENTAL

2.1. Materials

In this study, the monomer mixture that was the basis of the resin matrix consisted of urethane dimethacrylate (UDMA, Sigma Aldrich) combined with triethylene glycol dimethacrylate (TEGDMA, Sigma Aldrich) in a 7 : 3 proportion. Titanium dioxide was used in the form of powder with 99.8% purity, in the anatase form, with an average particle size of 25 nm, as stated by the manufacturer (TiO_2, Sigma Aldrich) (Table A2). The resin underwent radical photopolymerization, where exposure to light generated reactive free radicals, initiating a chain reaction that converted the monomers into a solid polymer network. The photoinitiator used was an iodonium salt, (7-methoxy-4-methylcoumarin-3-yl)phenyliodonium hexafluorophosphate (Sylanto 7MP), in combination with ethyl 4-(dimethylamino)benzoate (EDB, Sigma Aldrich) as an amine co-initiator. The Sylanto 7MP/EDB system has been previously described and characterized in detail in the literature (Jankowska et al., 2025). It was chosen in this study because of its absorbance near 405 nm (Fig. 1), which is the standard range for commercial 3D printers.

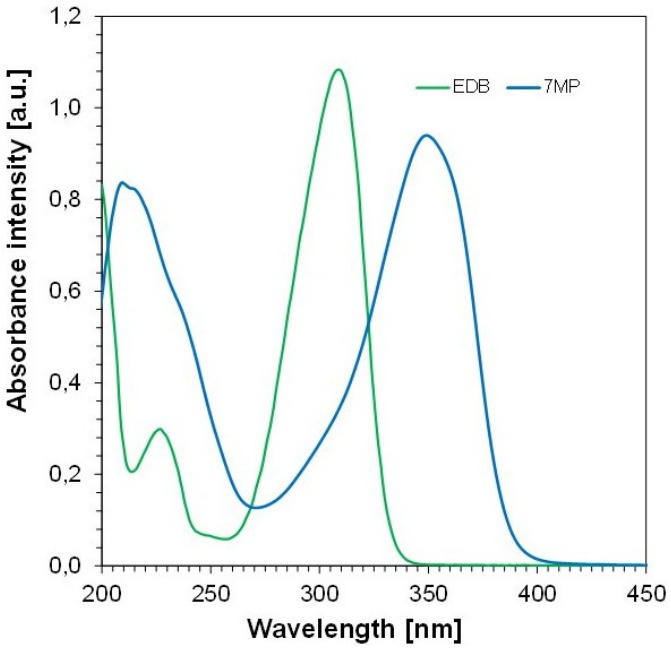


Figure 1. Absorbance of the photoinitiating system (EBD amine co-initiator and initiator Sylanto 7MP).

The dispersion protocol for titanium dioxide nanoparticles in the resin matrix was designed to ensure homogeneous distribution prior to experimental use. The required mass of nanopowder was directly added to the prepared resin mixture, after which the suspension was sealed in a glass vial containing a magnetic stir bar. The mixture was subjected to continuous magnetic stirring at 500 rpm for 12 hours at room temperature in a dark box to promote deagglomeration of the nanoparticles within the medium. Immediately before use, the suspension was sonicated for 15 seconds to re-disperse any agglomerates. This short sonication time was sufficient due to the relatively small resin volume employed. It was observed that sedimentation occurred after approximately 4 hours for nanoparticle loadings above 5 wt% and it was observed in the form of phase separation of the clear resin and the TiO_2-packed resin.

2.2. Real-time-FT-IR analysis

Photopolymerization kinetics were examined for mixtures containing photoinitiating systems dissolved in UDMA/TEGDMA monomers with a specific wt% of titanium dioxide. Real-time infrared spectra were collected using a Nicolet i10 FT-IR spectrometer (Thermo Scientific, Waltham, MA, USA) (Fig. A1). For each measurement, a small droplet of the resin mixture was deposited onto a 25 µm polypropylene (PP) film using a glass pipette. A second PP film of identical thickness was placed on top to form a thin laminate. Gentle pressure was applied to ensure a reproducible sample layer of 25 µm (±10 %). All prepared laminates were placed into a metal sample holder mounted horizontally in the FT-IR spectrometer. Measurements were conducted for up to 600 s in a dark environment illuminated only with red light ($\lambda_{max} \approx 650$ nm) to prevent premature photoinitiation. Sample exposure was carried out using UV/Vis LEDs from Thorlabs (USA) with an emission wavelength of 405 nm. The LEDs were powered by a Thorlabs DC2200 supply and positioned 2.1 cm from the sample surface. Illumination began 10 s after spectral acquisition commenced. The progress of curing was tracked by monitoring the reduction of the characteristic absorbance band of the reactive double bonds, around 1634 cm^{-1} for UDMA/TEGDMA methacrylate systems. Because the decrease in peak area corresponds to the consumption of functional groups, the degree of conversion was calculated from the ratio of initial and final absorbance values, using Eq. (1).

$$C_{\text{FT-IR}}[\%] = \left(1 - \frac{A_{\text{After}}}{A_{\text{Before}}}\right) \cdot 100\% \tag{1}$$

where: A_{Before} – area of the absorbance peak characteristic for appropriate monomer and type of photopolymerization before curing; A_{After} – area of the same absorbance peak after the polymerization process.

2.3. Photo-DSC analysis

Photo-DSC experiments were carried out using a Photo-DSC 204 F1 Phoenix ® instrument (Netzsch Gerätebau GmbH, Germany). The calorimeter was equipped with a Bluepoint LED eco light-curing system (Hönle UV Technology, Germany) using LEDs with a peak emission at 405 nm (Fig. A2). The light intensity at the sample position was adjusted to approximately 18.67 $mW \cdot cm^{-2}$ and verified with an Omni-Cure R2000 radiometer (Excelitas Technologies ®, Ontario, Canada). All measurements were performed isothermally at 25 °C under an inert gas atmosphere.

Each sample (2 ± 0.5 mg) was placed inside an aluminum crucible, covered with a thin quartz plate, and preconditioned isothermally for 10 s before irradiation. A reference crucible containing only the base monomers was used to establish baseline heat flow.

Heat evolution during polymerization was recorded continuously. Since the released heat is directly proportional to the number of reacted double bonds, both polymerization rate (R_p in Eq. (2) and functional-group conversion ($C_{\text{photo-DSC}}$ in Eq. (3)) were derived from the integrated exotherm and the known thermochemical parameters of the monomers (molar mass, functionality, enthalpy per mole of reactive groups, and compositional ratios). These calculations followed standard procedures commonly applied in photo-DSC kinetic analysis.

$$R_p \approx 1000 d_m \left(\frac{H}{m_p}\right) \frac{\sum\left(f_i \frac{w_i}{M_i}\right)}{\sum\left(f_i \frac{w_i}{M_i} \Delta H_0\right)} \tag{2}$$

where: d_m – density of monomer composition [$g \cdot cm^{-3}$]; ΔH_0 – enthalpy of polymerization the used monomers [$J \cdot mol^{-1}$] (per one functional group); H – heat flow [W]; M_i – molecular mass of i-monomer [$g \cdot mol^{-1}$]; f_i – functionality of i-monomer; w_i – percentage of i-monomer; m_p – sample mass [g].

$$C_{\text{photo-DSC}} = \frac{1}{\sum\left(f_i \frac{w_i}{M_i} \Delta H_0\right)} \int_{t_0}^{t} \frac{H(t)}{m_p} \mathrm{d}t \tag{3}$$

where: M_i – molecular mass of i-monomer [$g \cdot mol^{-1}$]; f_i – functionality of i-monomer; w_i – percentage of i-monomer; ΔH_0 – enthalpy of polymerization of used monomers [$J \cdot mol^{-1}$] (per functional group); H – heat flow [W] and m_p – sample mass [g].

2.4. Photo-rheological studies

Photo-rheological measurements were performed to characterize the kinetics of photocuring by tracking changes in viscosity during UV exposure. Experiments were carried out on an MCR302e rotational rheometer (Anton Paar, Poland) equipped with a dedicated optical module for in-situ photorheology (Fig. A3). All measurements were conducted at 25 °C with temperature control provided by an integrated thermostat.

Samples were irradiated using LEDs operating at 405 nm, with an incident intensity of approximately 19.82 $mW \cdot cm^{-2}$. LED output was supplied and regulated via a DC2200 current controller (Thorlabs Inc., Tampa, FL, USA). To allow the system to stabilize before polymerization began, illumination was triggered 10 s after the start of each rheological test.

Polymerization shrinkage was quantified by comparing the gap between the upper glass plate and the lower aluminium plate before and after curing. The percentage change in this distance was used to calculate volumetric shrinkage using the standard relationship between the initial and final gap thicknesses (Eq. (4)).

$$\text{Shrinkage } [\%] = \left(1 - \frac{d_{\text{After}}}{d_{\text{Before}}}\right) \cdot 100\% \tag{4}$$

where: d_{After} – the distance between the glass plate and the aluminum plate after the photopolymerization [mm]; d_{Before} – the distance between the glass plate and the aluminum plate before the photopolymerization [mm].

2.5. 3D printing experiments

Two photopolymer 3D printers, representing different printing technologies, were used to evaluate the printability of a resin modified with TiO_2 at 0.1, 1, 5, 10, and 30 wt.%. The LCD Anycubic Photon Mono M7 Pro (Anycubic, China) and the DLP Lumen X™ Gen 3 (CellInk Inc., USA) served as the fabrication platforms. Both systems operated with UV irradiation at 405 nm, but differed in how light was delivered to the resin vat. The LCD printer employed pixel masking in the print matrix to form the printed layers, whereas the DLP printer projected patterned illumination, which enabled assessment of how printer build influences curing behavior and print resolution. The digital model in Fig. 2 was designed in Autodesk Fusion 360. The same resin formulations were used on both printers to enable direct comparison between the two technologies. Printing parameters such as exposure time and light intensity were adjusted to the specific needs of the resin composites (Table A3), to achieve printing with the highest possible accuracy (Fig. 2).

3. RESULTS AND DISCUSSION

3.1. Kinetic studies using Real-Time FT-IR

Real-Time FT-IR spectroscopy was used to evaluate the photopolymerization kinetics of UDMA/TEGDMA resin containing different concentrations of TiO_2. The progress of radical photopolymerization was tracked by monitoring the decrease of absorbance at approximately 1634 cm^{-1}, which is the characteristic C=C bond band of the methacrylate compounds (Figs. A5–A10). Kinetic curves for the conversion rates obtained in Fig. 3 illustrate how the presence of the additive influences the rate of curing. In Table 1, the slope of the kinetic curves and the induction times were presented. From these, a clear acceleration of the early stages of polymerization were observed. As the concentration of TiO_2 increased, the resin exhibited shorter induction times and steeper initial slopes compared to the base resin, indicating faster radical polymer network formation after irradiation. It can be attributed to light scattering ability of TiO_2 particles, which promotes rapid initiation of the process in the early stages.

As the TiO_2 concentration increased, a slight decrease in the final degree of conversion was observed, due to limited light penetration into the depth of the composite. Nevertheless, in

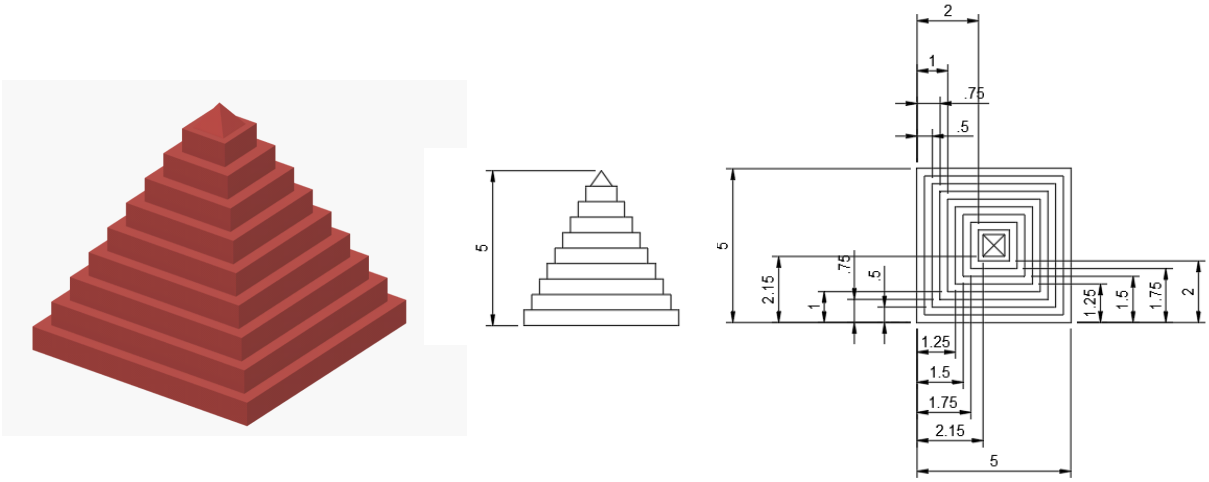


Figure 2. Printing model consisting of the 3D view of the pyramid and its dimensions (in milimeters).

Table 1. Kinetic results for the studied systems, final degree of conversion rate of acrylate monomers, slope of the polymerization process and the induction time from the Real Time FT-IR measurements.

Composition	Degree of conversion (α) [%]	$d\alpha \cdot dt^{-1}$	Induction time [s]
Base	37.7	2.99	7.48
0.1 wt.% TiO_2	34.2	3.79	5.07
1 wt.% TiO_2	34.1	4.60	2.90
5 wt.% TiO_2	29.3	3.71	2.33
10 wt.% TiO_2	31.5	4.94	2.21
30 wt.% TiO_2	41.6	2.72	2.01

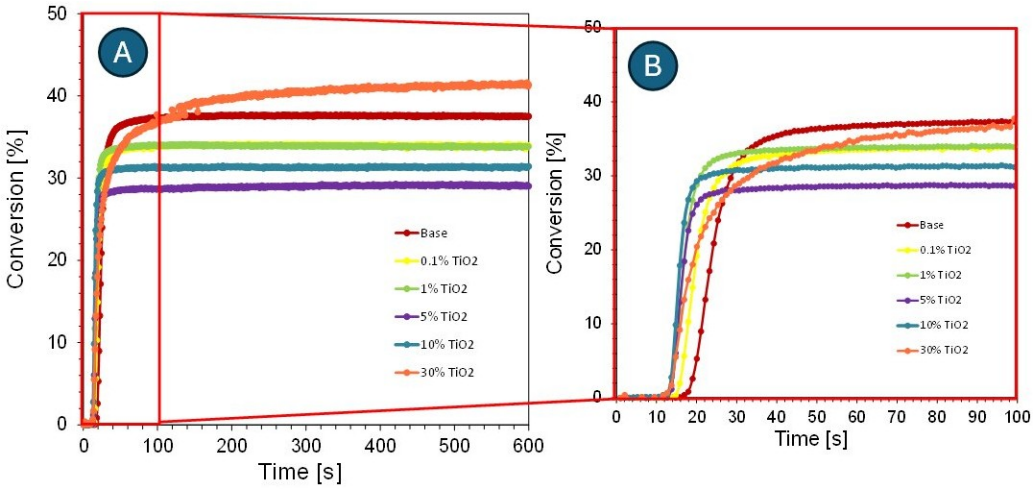


Figure 3. Kinetic profiles presenting the photopolymerization process of the UDMA/TEGDMA monomers in a 7 : 3 ratio, with a specific concentration of TiO_2 added; under LED@405 nm irradiation (and an intensity on the sample of 19.8 mW·cm^{-2}) continuously for 600 seconds. A) the whole process, B) the first 100 seconds. The sample thickness was 25 µm.

all cases, the degree of conversion levels remained acceptable for 3D printing applications. All compositions with an additive concentration of 1 wt.% or greater reached induction times below 3 s, demonstrating titanium dioxide's excellent ability to scatter light and aid the polymerisation process.

The formulation with 30 wt.% TiO_2 presented behavior distinct from the lower concentration trend. Its initial polymerization rate was lower, even below that of the base sample. It can be attributed to the very strong light scattering at such a high concentration. Although the reaction progressed slowly, requiring about 150 s to reach a plateau, compared to about 30 s in the other samples, the system achieved a higher final degree of conversion. This can be attributed to prolonged activity of the network, as the slower polymerization rate allows the systems to remain in the fluid state for longer and distribute the energy more evenly, as opposed to in the rigid solid state network, enabling continued propagation and finally yielding a higher degree of conversion.

3.2. Kinetic studies using Photo-DSC

Photo-DSC analysis was performed as an alternative and complementary method for determining photopolymerization kinetics in relation to Real Time FT-IR. Unlike the previous one, photo-DSC measured the heat released during photocuring, allowing degree of conversion to be calculated from the total reaction enthalpy. Despite the differences in the methodology of those two techniques, the same general trends were observed. Increasing TiO_2 concentration altered the rate of polymerization (Fig. 4).

At the lower TiO_2 loadings ($\leq$ 5 wt%), the resin exhibited a lower induction time of the heat-flow and its intensity decreased, indicating a faster initialization of the polymer network formation but to a lesser extent. This behavior can be attributed to the strong light scattering ability of TiO_2, which increases the effective optical path length within the resin and enhances light absorption, thus promoting radical

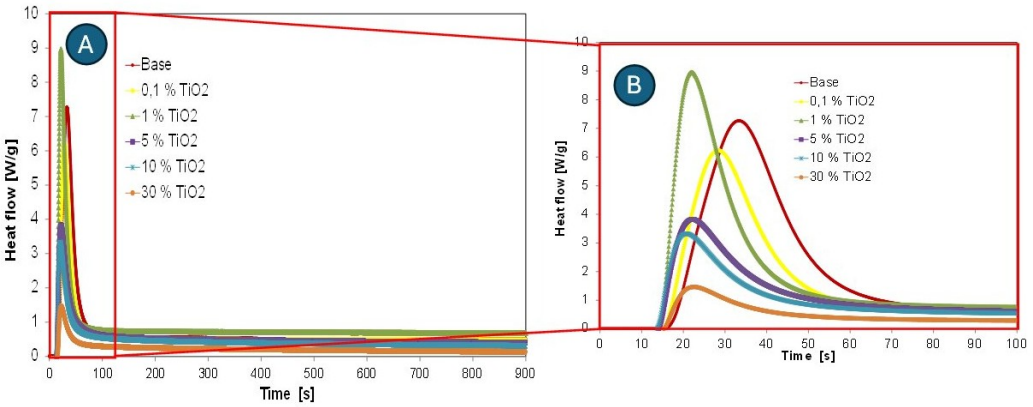


Figure 4. Photo-DSC results obtained when monitoring samples based on UDMA/TEDGMA for 900 s with an LED@405 nm light source with a sample light intensity of 18.67 mW·cm^{-2}. Heat flow results A) for the whole experiment's time, B) for the first 100 s.

generation. Similar acceleration effects were also detected in the photo-rheological measurements, confirming the consistency of these observations across techniques. However, for the 10 and 30 wt.% filler contents, the dominant filter and shadowing effects became increasingly pronounced, leading to reduced light penetration into the material. As a result, the overall heat flow intensity decreased, and the polymerization process was prolonged. Although curing still occurred, it was less efficient. These observations demonstrate that photo-DSC is an effective tool for capturing the influence of TiO_2 concentration on photopolymerization of the resin.

3.3. Rheological studies

Photo-rheological measurements provided complementary insights into the viscoelastic evolution of the resin during curing, allowing assessment of gelation behavior, the mechanical development of the polymer network, and polymerization-induced shrinkage. Monitoring the increase in storage modulus (G') as well as the loss modulus (G'') under UV exposure revealed how TiO_2 concentration influenced the transition from liquid to solid (Figs. A11–A16). Gelling time was found to be the time at which the storage and loss moduli reached the same value and their graphs crossed (Fig. 5).

Polymerization shrinkage, estimated from Eq. (4), decreased with higher additive content. This behavior is expected, as inorganic particles limit contraction during network formation. Reduced shrinkage is advantageous for dimensional accuracy in 3D printing, as it may enhance interlayer adhesion during fabrication. Formulations with low to medium TiO_2 concentrations (from 0.1 to 5 wt.%) exhibited earlier gel points compared to the reference base, reflecting the initially accelerated polymerization observed in both Real Time FT-IR and photo-DSC. However, increasing the concentration of TiO_2 in the samples to 10 and 30 wt% led to longer gelling times, which can be explained by restricted polymer network formation due to diminished light penetration. The 30 wt.% concentration displayed the longest gel point, which aligned with its delayed polymerization profile in Real Time FT-IR.

3.4. 3D printing

To assess the practical applicability of the resin with added TiO_2, all resin variants were subjected to 3D printing using two different 3D printers, a commercial-grade LCD Anycubic Photon Mono M7 PRO and the lab-grade DLP Lumen X™ Gen 3. Evaluating both made it possible to determine how the method of light projection influences the printability of resins containing increasing TiO_2 concentrations. Each print was printed out in a 50 µm layer thickness, with irradiation times and light exposure power specific to the studied resin composition (Table A3). All specimens were printed in identical geometry and orientation, such that the base face of the pyramid was directly attached to the printing platform to ensure consistent fabrication conditions. After printing, the samples were rinsed in an isopropanol bath for 10 minutes to remove uncured resin, followed by post-curing under 405 nm irradiation for 5 minutes to ensure complete polymerization.

In the LCD printer, only formulations containing up to 0.1 wt% TiO_2 could be printed successfully (Fig. 7). At higher concentrations, curing was incomplete even with extended exposure times, preventing proper layer formation. However, prints obtained from the 0.1 wt% formulation exhibited excellent surface quality, sharp feature definition, and smooth layers. The high resolution of the LCD screen and its uniform light distribution likely contributed to this precision. Nevertheless, the LCD system provided lower irradiance per pixel compared to DLP projector that provided higher power. When TiO_2 concentration increased, pronounced light scattering occurred, preventing sufficient energy from reaching deeper regions of each layer, ultimately exceeding the curing capacity of the LCD system.

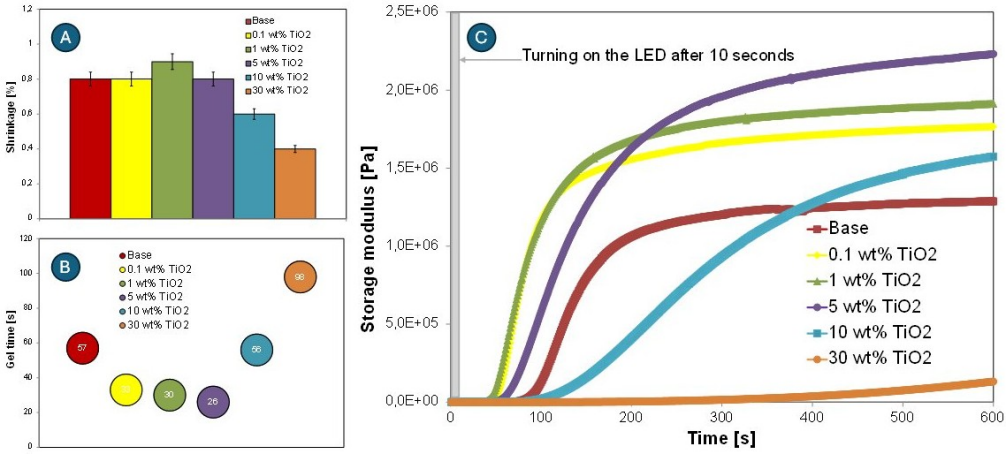


Figure 5. Photo-rheology results obtained for photo-curable compositions based on UDMA/TEGDMA and TiO_2 in various concentrations during sample monitoring for 600 s and LED@405 nm irradiation with a light intensity on the sample of 19.8 $mW \cdot cm^{-2}$. In A) photopolymerization shrinkage, B) gelling times, C) storage modulus.

In contrast, the DLP printer was able to successfully polymerize all resin variants, including the highly filled 30 wt% TiO_2 formulation (Fig. 6). At additive contents above 5 wt%, however, it was necessary to first print a thin base platform layer using the base resin to ensure adequate adhesion of the subsequent layers. DLP projector emitted a more concentrated light beam, with significantly higher irradiance than LCD panels (3 to 4 times higher). This provided a stronger curing capability that could overcome scattering losses caused by dense TiO_2 particles. As a result, complete layer formation and solidification were achieved across the entire concentration range. However, the overall print resolution and surface finish were slightly inferior to those obtained with the LCD system. This likely results from differences in optical configuration and pixel size between the systems, as DLP projector discretized light into larger pixels, which may yield more noticeable edges or curing failures compared to high-resolution monochrome LCD screens. Both printers were operated at a 50 µm layer height, however, the LCD printer offers a finer XY plane resolution of 17 µm per pixel, compared to 35 µm in the DLP system. Additionally, at high TiO_2 loadings, increased scattering likely blurred projected pixels, reducing feature definition. As a result, the LCD system provided superior surface resolution, whereas the DLP system offered greater curing capability at high filler loadings.

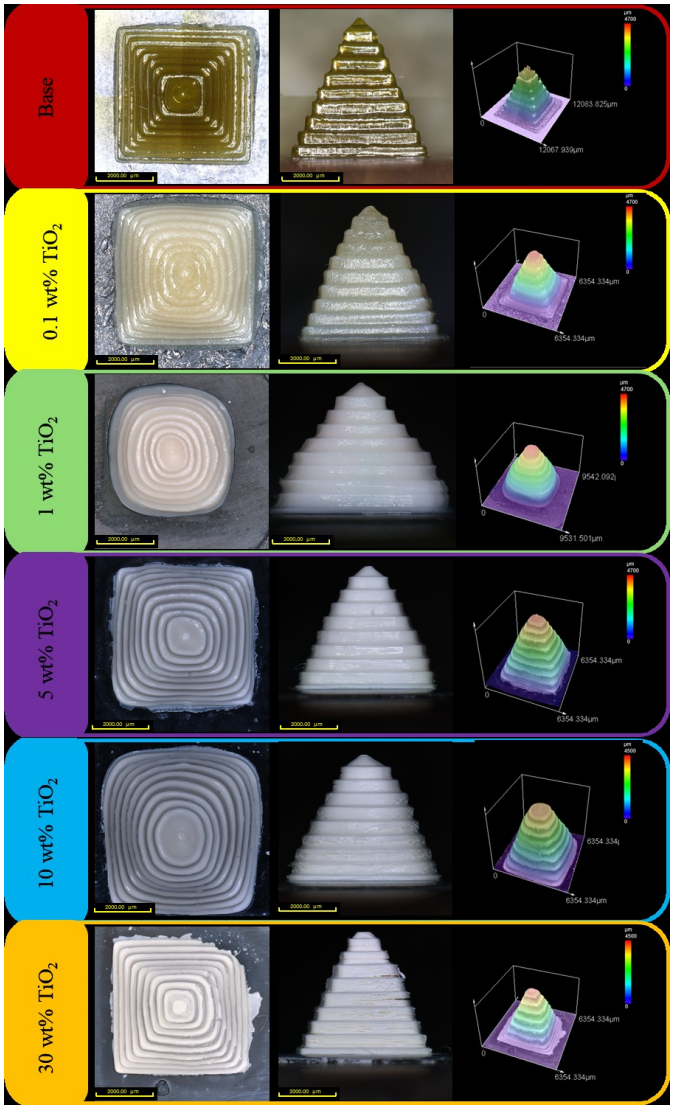


Figure 6. Optical microscope photos of the model printed from a composition consisting of UDMA/TEGDMA and various amount of TiO_2 wt% on a DLP LumenX^{TM} Gen 3 printer using different curing parameters.

The dimensions of the printouts in both LCD (Fig. 7) and DLP (Fig. 6) systems matched those of the CAD model (Fig. 2). However, they were slightly reduced due to photopolymerization shrinkage. The magnitude of this change in dimensions correlated well with the shrinkage behavior observed in the rheological measurements.

Scanning electron microscopy (SEM) was performed to evaluate the surface morphology and microstructural fidelity of the printed specimens. For the base resin and low filler concentration, LCD samples (Fig. 9) exhibited relatively smooth and homogeneous surfaces, with well-defined edges corresponding to the designed geometry, while the DLP ones (Fig. 8) retained the original outline of the finer details. With increasing TiO_2 content, however, a progressive increase in surface roughness was observed. The surface became more irregular, with visible micro protrusions that can be attributed to the presence of dispersed TiO_2 particles and their partial agglomeration. At higher magnifications, distinct clusters of TiO_2 were present, confirming that the inorganic powder was not exclusively embedded within the polymer bulk but was at least partially exposed at the surface. This observation supports the assumption that TiO_2 is present on the surface, which may be relevant for potential uses.

Despite increased roughness at higher filler loadings, the reproduction of smaller structural details remained consistent with DLP technology; however, geometric deformation

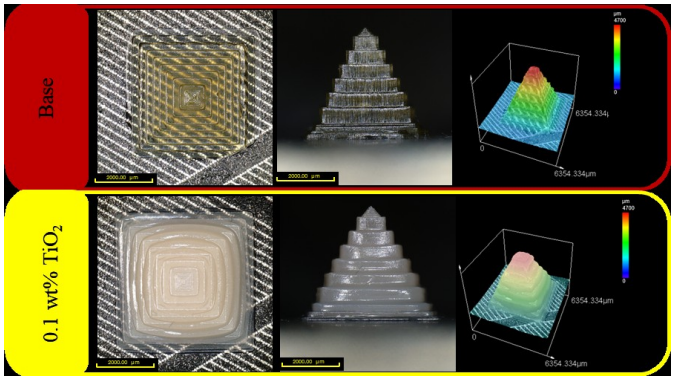


Figure 7. Optical microscope photos of the model printed from a composition consisting of UDMA/TEGDMA, and various amount of TiO_2 wt% on an LCD Anycubic Photon Mono M7 PRO printer using different curing parameters.

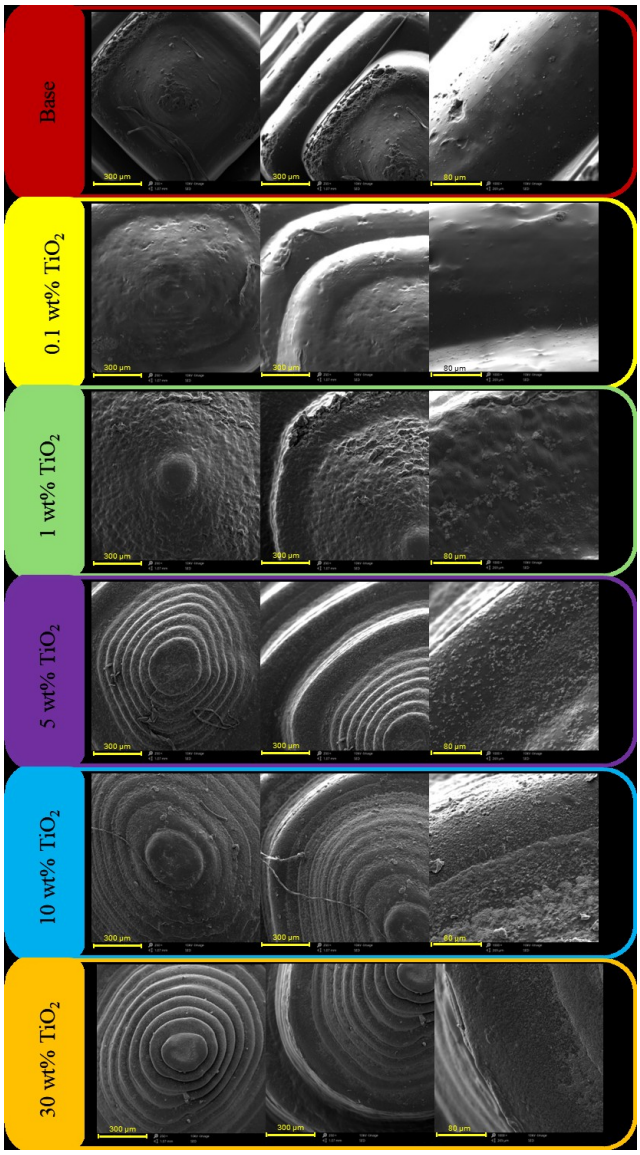


Figure 8. SEM photos of the model printed from a composition consisting of UDMA/TEGDMA and various amount of TiO_2 wt% on a DLP LumenX^{TM} Gen 3 printer using different curing parameters.

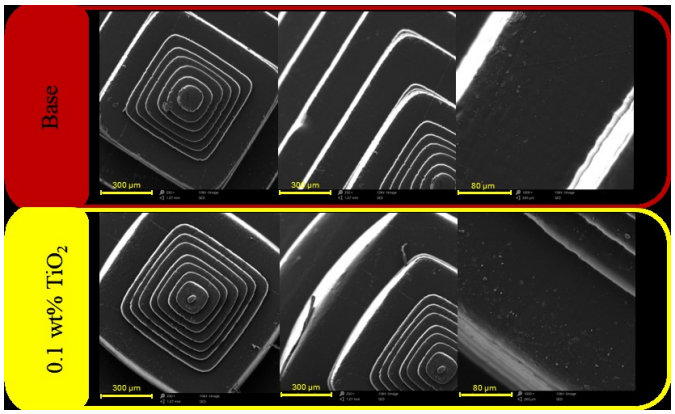


Figure 9. SEM photos of the model printed from a composition consisting of UDMA/TEGDMA, and various amount of TiO_2 wt.% on an LCD Anycubic Photon Mono M7 PRO printer using different curing parameters.

became more pronounced. In particular, at high TiO_2 concentrations (5 wt% and above), DLP-printed objects exhibited noticeable distortion from the designed square shape toward a more oval or rounded shape. This effect likely results from enhanced light scattering within the highly filled composite, leading to overcuring and partial blurring of projected pixel boundaries. In contrast, samples fabricated using the LCD system retained a more square-like geometry, although minor edge rounding was still detectable. The difference between the two systems may be attributed to their distinct optical systems. Overall, SEM analysis confirms that increasing TiO_2 concentration affects surface quality and dimensional accuracy rather than eliminating fine structural features altogether, with deformation effects being more pronounced in the DLP system at elevated loadings.

3.5. Jacobs working curves

The light penetration behavior of the investigated systems was further analyzed using the Jacobs working curve approach, which correlates the cured layer thickness, C_d, with the applied exposure dose, E_0. Experimentally, the working curves were obtained by exposing the resin directly on the vat film without the build platform attached, to avoid influencing the cured thickness. After exposure at different controlled energy doses, the isolated polymerized layers were carefully removed and their thickness measured using micrometer screw gauge. Plotting the measured layer height as a function of exposure dose enabled determination of the penetration depth (D_p) from the slope of the linear fit and the critical exposure (E_c) from the intercept.

For the DLP Lumen X^{TM} Gen 3 system, the base resin exhibited a steep working curve, indicating a high penetration depth and efficient energy transfer through the resin (Fig. 10). Interestingly, the addition of 0.1 wt.% TiO_2 initially resulted in a slight increase in cured layer thickness at comparable exposure doses, suggesting enhanced light energy utilization. However, at higher TiO_2 concentrations, both the slope of the working curve and the maximum achievable layer thickness decreased. The reduced steepness indicates a lower effective penetration depth, while the overall downward shift reflects a decrease in critical exposure, consistent with intensified light scattering caused by the nanoparticles. In parallel, the measured cured thickness increased from the base formulation to 0.1 wt.% TiO_2 but progressively declined at higher loadings in the DLP system, confirming the detrimental effect of excessive filler on curing efficiency. A comparable trend was observed for the LCD Anycubic Photon Mono M7 PRO with the base resin and the 0.1 wt% TiO_2 formulation, where sufficient cured thickness was still achieved. At higher concentrations, the printer either failed to produce a photopolymer or produced a severely undercured polymer, making it impossible to measure its thickness. Thus, the Jacobs working

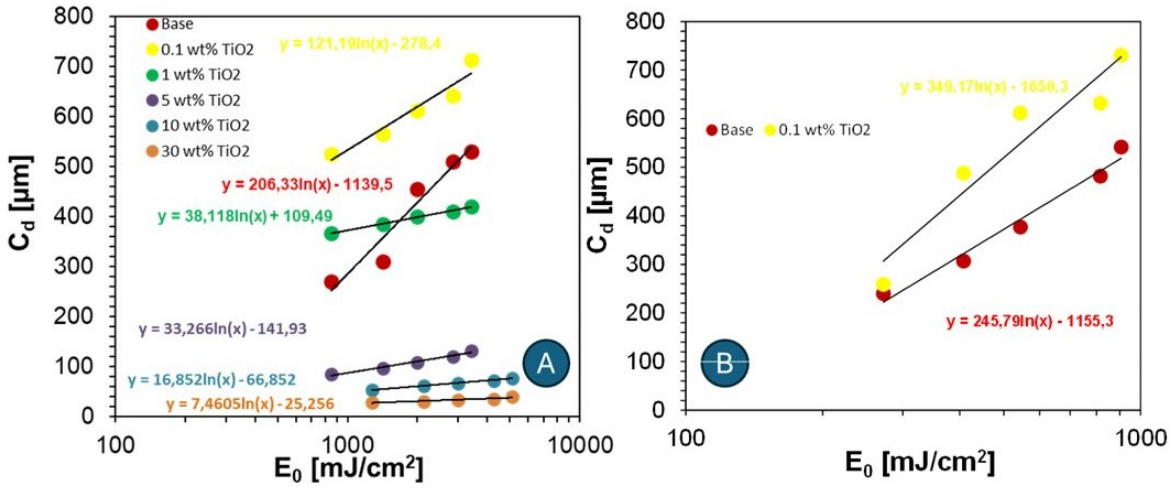


Figure 10. Jacobs working curves for the used resin formulations. Done on the A) DLP LumenX^{TM} Gen 3; B) LCD Anycubic M7 PRO.

curve analysis provides quantitative support for the observed printability limits and further concludes that the DLP system maintains superior curing power under optical hurdles.

4. CONCLUSIONS

This study provides a comprehensive evaluation of methacrylate UDMA/TEGDMA photocurable resins with added TiO_2 in various concentrations. It examined photopolymerization behavior and printability across two different 3D printing technologies. By combining Real-Time FT-IR, photo-DSC, photo-rheology, and practical printing tests, the influence of TiO_2 concentration and printer type on curing efficiency and final material quality was clearly demonstrated.

Kinetic analyses revealed that low and medium TiO_2 concentrations (≤ 5 wt%) accelerate the early stages of photopolymerization due to enhanced scattering and redistribution of light, leading to shorter induction times and steeper polymerization slopes. However, increasing the additive level reduced light penetration, resulting in gradually lower final degrees of conversion. The 30 wt% formulation behaved differently, its high opacity caused a slower initiation rate, but the delayed polymerization allowed the network to continue reacting longer, ultimately reaching the highest overall degree of conversion. Photo-DSC confirmed these trends, demonstrating that both methods lead to consistent conclusions regarding the role of TiO_2 in curing kinetics. Photo-rheology further showed that higher filler contents delayed gelation and reduced polymerization shrinkage, suggesting improved dimensional stability for highly filled formulations.

The 3D printing experiments demonstrated that TiO_2 concentration and printer build greatly influence printability. The LCD printer, characterized by high pixel resolution but lower irradiance, could successfully process only the 0.1 wt% formulation. These prints exhibited excellent surface quality but were limited by insufficient curing power at higher titanium dioxide loadings. In contrast, the DLP printer with its significantly greater light intensity could print all TiO_2 concentrations, including the 30 wt% formulation. For above 5 wt% TiO_2, a base platform layer of base resin was required for reliable adhesion. Although the DLP prints showed slightly lower quality, the ability to fabricate highly filled, optically demanding materials highlights the robustness of high intensity projection DLP curing.

Jacobs working curve analysis further quantified these differences, showing a decrease in penetration depth and in critical exposure with increasing additive loading. The steep working curves observed for the base and 0.1 wt% formulations explain why only these compositions could be reliably processed on the LCD printer.

SEM and microscope analysis revealed progressive surface roughening and partial exposure of TiO_2 particles at higher loadings, confirming that the inorganic nanoparticles influenced not only curing behavior but also surface topography and dimensional fidelity. The more pronounced geometric deformation observed in DLP prints at elevated concentrations supports the hypothesis of intensified light scattering and pixel blurring in highly filled systems.

Overall, this work demonstrates that TiO_2 can be used to tailor the photopolymerization behavior and functional properties of radical resins, but its successful application in 3D printing depends strongly on printer technology and concentration. These findings provide practical guidelines for designing composite resins and selecting appropriate printing conditions for advanced biomedical, dental, and engineering applications.

ACKNOWLEDGMENTS

This research was funded by National Centre for Research and Development in Poland under the Lider Program, grant number LIDER13/0156/2022.

SYMBOLS

A_{After}	Area of the same absorbance peak after the polymerization process, cm^{-1}
A_{Before}	Area of the absorbance peak characteristic for appropriate monomer and type of photopolymerization before curing, cm^{-1}
C_d	Cured layer thickness, μm
$C_{FT\text{-}IR}$	Degree of conversion, %
$C_{photo\text{-}DSC}$	Functional-group conversion, %
d_{After}	The distance between the glass plate and the aluminum plate after the photopolymerization, mm
d_{Before}	The distance between the glass plate and the aluminum plate before the photopolymerization, mm
d_m	Density of monomer composition, $g{\cdot}cm^{-3}$
$d\alpha \cdot dt^{-1}$	Slope of polymerization process
E_0	Applied exposure dose, $mJ{\cdot}cm^{-2}$
f_i	Functionality of *i*-monomer
H	Heat flow, W
M_i	Molecular mass of *i*-monomer, $g{\cdot}mol^{-1}$
m_p	Sample mass, g
R_p	Polymerization rate
w_i	Percentage of *i*-monomer, %
ΔH_0	Enthalpy of polymerization the used monomers, $J{\cdot}mol^{-1}$ (per one functional group)
λ_{max}	Maximum absorption, nm

REFERENCES

Abd Elhamid Abo Salh I.B., Add El-Salam E.B., Ezzat A.A., Aboshama M., Elhagali A.F., 2025. Antimicrobial effect of three different nanoparticles-modified 3D-printed denture resin: An *in vitro* study. *J. Int. Soc. Preventative Community Dent.*, 15, 42–49. 10.4103/JISPCD.JISPCD_53_24

Aimar A., Palermo A., Innocenti B., 2019. The role of 3D printing in medical applications: a state of the art. *J. Healthcare Eng.*, 2019, 5340616. 10.1155/2019/5340616

Aktas B., Das R., Acikgoz A., Demircan G., Yalcin S., Gumushan Aktas H., Balak M.V., 2024. DLP 3D printing of TiO_2-doped Al_2O_3 bioceramics: manufacturing, mechanical properties, and biological evaluation. *Mater. Today Commun.*, 38, 107872. 10.1016/j.mtcomm.2023.107872

Almeshari B., Junaedi H., Baig M., Almajid A., 2024. Effect of titanium dioxide on the mechanical properties of 3D printed short carbon-fibers composite. *J. Mater. Res. Technol.*, 33, 8590–8597. 10.1016/j.jmrt.2024.11.209

Altarazi A., Haider J., Alhotan A., Silikas N., Devlin H., 2023. 3D printed denture base material: the effect of incorporating TiO_2 nanoparticles and artificial ageing on the physical and mechanical properties. *Dent. Mater.*, 39, 1122–1136. 10.1016/j.dental.2023.10.005

Altarazi A., Jadaan L., McBain A.J., Haider J., Kushnerev E., Yates J.M., Alhotan A., Silikas N., Devlin H., 2024. 3D-printed nanocomposite denture base resin: the effect of incorporating TiO_2 nanoparticles on the growth of *Candida albicans*. *J. Prosthodont.*, 33, 25–34. 10.1111/jopr.13784

Anselmo A.C., Mitragotri S., 2015. A review of clinical translation of inorganic nanoparticles. *AAPS J.*, 17, 1041–1054. 10.1208/s12248-015-9780-2

Bao Y., Paunović N., Leroux J.-C., 2022. Challenges and opportunities in 3D printing of biodegradable medical devices by emerging photopolymerization techniques. *Adv. Funct. Mater.*, 32, 2109864. 10.1002/adfm.202109864

Bayda S., Adeel M., Tuccinardi T., Cordani M., Rizzolio F., 2020. The history of nanoscience and nanotechnology: from chemical-physical applications to nanomedicine. *Molecules*, 25, 112. 10.3390/molecules25010112

Billings C., Cai C., Liu Y., 2021. Utilization of antibacterial nanoparticles in photocurable additive manufacturing of advanced composites for improved public health. *Polymers*, 13, 2616. 10.3390/polym13162616

Bobo D., Robinson K.J., Islam J., Thurecht K.J., Corrie S.R., 2016. Nanoparticle-based medicines: a review of FDA-approved materials and clinical trials to date. *Pharm. Res.*, 33, 2373–2387. 10.1007/s11095-016-1958-5

Chaudhary R., Fabbri P., Leoni E., Mazzanti F., Akbari R., Antonini C., 2023. Additive manufacturing by digital light processing: a review. *Prog. Addit. Manuf.*, 8, 331–351. 10.1007/s40964-022-00336-0

Chopra D., Jayasree A., Guo T., Verron E., Ivanovski S., Gulati K., 2025. *Micro, nano and gallium*: bioactive and bactericidal gallium-eluting nano-engineered zirconia implants. *Chem. Eng. J.*, 523, 168628. 10.1016/j.cej.2025.168628

Dilberoglu U.M., Gharehpapagh B., Yaman U., Dolen M., 2017. The role of additive manufacturing in the era of industry 4.0. *Procedia Manuf.*, 11, 545–554. 10.1016/j.promfg.2017.07.148

Gauci S.C., Vranic A., Blasco E., Bräse S., Wegener M., Barner-Kowollik C., 2024. Photochemically activated 3D printing inks: current status, challenges, and opportunities. *Adv. Mater.*, 36, 2306468. 10.1002/adma.202306468

Hellman S., Frisch P., Platzman A., Booth P., 2023. 3D printing in a hospital: centralized clinical implementation and applications for comprehensive care. *Digital Health*, 9, 1–12. 10.1177/20552076231221899

Hobich J., Blasco E., Wegener M., Mutlu H., Barner-Kowollik C., 2023. Synergistic, orthogonal, and antagonistic photochemistry for light-induced 3D printing. *Macromol. Chem. Phys.*, 224, 2200318. 10.1002/macp.202200318

Iftekar S.F., Aabid A., Amir A., Baig M., 2023. Advancements and limitations in 3D printing materials and technologies: a critical review. *Polymers*, 15, 2519. 10.3390/polym15112519

Ijaz M., Zafar M., 2021. Titanium dioxide nanostructures as efficient photocatalyst: progress, challenges and perspective. *Int. J. Energy Res.*, 45, 3569–3589. 10.1002/er.6079

Jankowska M., Ozukanar O., Çakmakçi E., Ortyl J., 2025. A thiol-functional amine synergist as a co-initiator for DLP 3D printing applications. *Polym. Chem.*, 16, 3895–3915. 10.1039/D5PY00603A

Jayakrishna M., Vijay M., Khan B., 2023. An overview of extensive analysis of 3D printing applications in the manufacturing sector. *J. Eng.*, 2023, 7465737. 10.1155/2023/7465737

Jeong M., Radomski K., Lopez D., Liu J.T., Lee J.D., Lee S.J., 2023. Materials and applications of 3D printing technology in dentistry: an overview. *Dent. J.*, 12, 1. 10.3390/dj12010001

Kaur B., Singh P., Thakur S., Singh A., Chaudhary V., Kumar N., Khan A.A.P., Rub M.A., Azum N., Raizada P., 2025. Harnessing 3D printing for tailored TiO_2 structures redefining organic pollutant degradation. *J. Environ. Chem. Eng.*, 13, 116042. 10.1016/j.jece.2025.116042

Maher S., Linklater D., Rastin H., Liao S.T.-Y., Martins de Sousa K., Lima-Marques L., Kingshott P., Thissen H., Ivanova E.P., Losic D., 2021. Advancing of 3D-printed titanium implants with combined antibacterial protection using ultrasharp nanostructured surface and gallium-releasing agents. *ACS Biomater. Sci. Eng.*, 8, 314–327. 10.1021/acsbiomaterials.1c01030

Mansoor A., Khurshid Z., Khan M.T., Mansoor E., Butt F.A., Jamal A., Palma P.J., 2022. Medical and dental applications of titania nanoparticles: an overview. *Nanomaterials*, 12, 3670. 10.3390/nano12203670

Martins de Sousa K., Linklater D.P., Murdoch B.J., Al Kobaisi M., Crawford R.J., Judge R., Dashper S., Sloan A.J., Losic D., Ivanova E.P., 2023. Modulation of MG-63 osteogenic response on mechano-bactericidal micronanostructured titanium surfaces. *ACS Appl. Bio Mater.*, 6, 1054–1070. 10.1021/acsabm.2c00952

Mohammadi H., Moradpoor H., Beddu S., Mozaffari H.R., Sharifi R., Rezaei R., Fallahnia N., Ebadi M., Mazlan S.A., Safaei M., 2025. Current trends and research advances on the application of TiO_2 nanoparticles in dentistry: how far are we from clinical translation? *Heliyon*, 11, e42169. 10.1016/j.heliyon.2025.e42169

Noworyta M., Topa-Skwarczyńska M., Jamróz P., Oksiuta D., Tyszka-Czochara M., Trembecka-Wójciga K., Ortyl J., 2023. Influence of the type of nanofillers on the properties of composites used in dentistry and 3D printing. *Int. J. Mol. Sci.*, 24, 10549. 10.3390/ijms241310549

O'Byrne M., Kerzabi B., Abbarchi M., Lifschitz A., Zamora T., Malgras V., Gourdin A., Modaresialam M., Grosso D., Putero M., 2024. Investigation of the anatase-to-rutile transition for TiO_2 sol-gel coatings with refractive index up to 2.7. *Thin Solid Films,* 790, 140193. 10.1016/j.tsf.2023.140193

Pai E., Nayak A., Hallikerimath R.B., Ruttonji Z., Astagi P., Pokale S., 2023. Comparison of titanium dioxide nanoparticles and silver nanoparticles for flexural strength once incorporated in heat-cure acrylic denture base resin: an *in vitro* study. *J. Indian Prosthodont. Soc.*, 23, 127–334. 10.4103/jips.jips_354_22

Paul G.M., Rezaienia A., Wen P., Condoor S., Parkar N., King W., Korakianitis T., 2018. Medical applications for 3D printing: recent developments. *Mo Med.*, 115, 75–81.

Petko F., Hola E., Jankowska M., Gruchała-Hałat A., Ortyl J., 2023. 3D-VAT printing of nanocomposites by photopolymerisation processes using amino-meta-terphenyls as visible light-absorbing photoinitiators. *Virtual Phys. Prototyping*, 18, e2244936. 10.1080/17452759.2023.2244936

Priyadarsini S., Mukherjee S., Bag J., Nayak N., Mishra M., 2019. Application of nanoparticles in dentistry: current trends. In: Shukla A. (Ed.), *Nanoparticles in medicine*. Springer, Singapore, 55–98. 10.1007/978-981-13-8954-2_3

Puckett A.D., Fitchie J.G., Kirk P.C., Gamblin J., 2007. Direct composite restorative materials. *Dent. Clin. N. Am.*, 51, 659–675. 10.1016/j.cden.2007.04.003

Al Rashid A., Khan S.A., Al-Ghamdi S.G., Koç M., 2021. Additive manufacturing of polymer nanocomposites: Needs and challenges in materials, processes, and applications. *J. Mater. Res. Technol.*, 14, 910–941. 10.1016/j.jmrt.2021.07.016

Remaggi G., Bergamonti L., Graiff C., Ossiprandi M.C., Elviri L., 2023. Rapid prototyping of 3D-printed AgNPs- and nano-TiO_2-embedded hydrogels as novel devices with multiresponsive antimicrobial capability in wound healing. *Antibiotics*, 12, 1104. 10.3390/antibiotics12071104

Serov D.A., Gritsaeva A.V., Yanbaev F.M., Simakin A.V., Gudkov S.V., 2024. Review of antimicrobial properties of titanium dioxide nanoparticles. *Int. J. Mol. Sci.*, 25, 10519. 10.3390/ijms251910519

Sharma G., Singh Chundawat G., Suthar B., Dangi A., 2025. Reviewing research studies in the evaluation of 3D-printing technology in civil engineering (past, present and future). *IARJSET*, 12, 120–126. 10.17148/iarjset/integrate.2025.12227

Stanford Advanced Materials, 2026. *Titanium dioxide polymorphs: Rutile vs. anatase*, 2026. Available at: https://www.samaterials.co.uk/titanium-dioxide-polymorphs-rutile-vs-anatase.html.

Sztorch B., Głowacka J., Hanuszewska A., Romańczuk-Ruszuk E., Konieczna R., Przekop R., 2022. Chapter 13 – Modified titanium dioxide for 3D printing applications, In: Pauk J., Dardzińska-Głębocka A., Mrozek P., Oksiuta Z. (Eds.), *Advances in biomedical engineering*. Oficyna Wydawnicza Politechniki Białostockiej, Białystok, 165–179. 10.24427/978-83-67185-49-3_13

Tan Y., Lyu J., 2023. Nanocomposites and other restorative materials, In: Thomas S., Baiju R.M. (Eds.), *Nanomaterials in Dental Medicine. Materials Horizons: From Nature to Nanomaterials*. Springer, Singapore, 75–91. 10.1007/978-981-19-8718-2_4

Taormina G., Sciancalepore C., Messori M., Bondioli F., 2018. 3D printing processes for photocurable polymeric materials: technologies, materials, and future trends. *J. Appl. Biomater. Funct. Mater.*, 16, 151–160. 10.1177/2280800018764770

Tian Y., Chen C.X., Xu X., Wang J., Hou X., Li K., Lu X., Shi H.Y., Lee E.-S., Jiang H.B., 2021. A review of 3D printing in dentistry: technologies, affecting factors, and applications. *Scanning*, 2021, 9950131. 10.1155/2021/9950131

Topa-Skwarczyńska M., Starzak K., Galek M., Mirek I., Świeży A., Tyszka-Czochara M., Lukes J., Ortyl J., 2025. Less is more: innovative cationic initiators effective in visible light for 3D printing. *Chem. Eng. J.*, 519, 165033. 10.1016/j.cej.2025.165033

Veljović D., Miletic V., 2023. Bioceramic dental inserts based on calcium phosphate nano-particles, In: Thomas S., Baiju R.M. (Eds.), *Nanomaterials in Dental Medicine. Materials Horizons: From Nature to Nanomaterials*. Springer, Singapore, 215–238. 10.1007/978-981-19-8718-2_12

Wang M.-K., Xiao F., Xu X., 2025. Antibacterial properties and biological activity of 3D-printed titanium alloy implants with a near-infrared photoresponsive surface. *Int. J. Implant Dent.*, 11, 3. 10.1186/s40729-024-00587-2

Wu J., Yang M., Huang Y., Zhang Y., Wu B., Qiu S., Hong F., Gao Y., Wang Z., Wang G., 2024. Enhancing the biological performance of titanium alloy through in situ modulation of the surface nanostructure: near-infrared-responsive antibacterial function and osteoinductivity. *ACS Appl. Bio Mater.*, 7, 3900–3914. 10.1021/acsabm.4c00244

Yilmaz M., Kapusuz Yavuz D., 2025. Bioactivity, mineralization, and mechanical properties of 3D-printed nano-TiO_2-reinforced polymer composite immersed in SBF. *Bioprinting*, 49, e00420. 10.1016/j.bprint.2025.e00420

Zhong Y., Li Y., Fu Y., Zhang Z., Lin H., Li H., Chen X.-B., Ma T., Jia B., 2025. Advancing mechano-bactericidal surfaces: mechanisms, fabrication, and synergistic antimicrobial strategies. *Adv. Mater. Interfaces.*, 12, e00792. 10.1002/admi.202500792

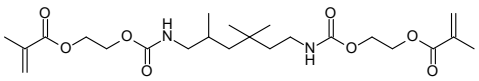
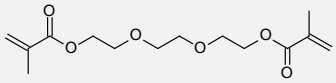
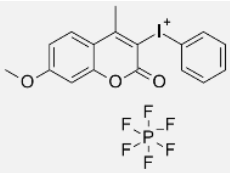
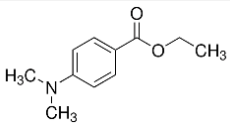
APPENDICES

A1. Materials used for testing

Table A1. Quantities of compounds and measurement conditions used in this article.

Initiating system	Number of moles	Percentage by moles	Monomer	Measurement conditions
Sylanto 7MP EDB	$2.9 \cdot 10^{-5}$ $5.2 \cdot 10^{-5}$	1.1 mol% 2.0 mol%	UDMA/TEGDMA in weight ratio 7 : 3	405 nm 19.8 mW·cm^{-2} 25 µm
Sylanto 7MP EDB Titanium (IV) oxide (TiO_2)	$2.9 \cdot 10^{-5}$ $5.2 \cdot 10^{-5}$ $1.3 \cdot 10^{-5}$	1.1 mol% 2.0 mol% 0.51 mol%	UDMA/TEGDMA in weight ratio 7 : 3	405 nm 19.8 mW·cm^{-2} 25 µm
Sylanto 7MP EDB Titanium (IV) oxide (TiO_2)	$2.9 \cdot 10^{-5}$ $5.2 \cdot 10^{-5}$ $1.3 \cdot 10^{-4}$	1.1 mol% 2.0 mol% 4.9 mol%	UDMA/TEGDMA in weight ratio 7 : 3	405 nm 19.8 mW·cm^{-2} 25 µm
Sylanto 7MP EDB Titanium (IV) oxide (TiO_2)	$2.9 \cdot 10^{-5}$ $5.2 \cdot 10^{-5}$ $6.3 \cdot 10^{-5}$	1.1 mol% 2.0 mol% 20 mol%	UDMA/TEGDMA in weight ratio 7 : 3	405 nm 19.8 mW·cm^{-2} 25 µm
Sylanto 7MP EDB Titanium (IV) oxide (TiO_2)	$2.9 \cdot 10^{-5}$ $5.2 \cdot 10^{-5}$ $1.3 \cdot 10^{-3}$	1.1 mol% 2.0 mol% 34 mol%	UDMA/TEGDMA in weight ratio 7 : 3	405 nm 19.8 mW·cm^{-2} 25 µm
Sylanto 7MP EDB Titanium (IV) oxide (TiO_2)	$2.9 \cdot 10^{-5}$ $5.2 \cdot 10^{-5}$ $3.8 \cdot 10^{-3}$	1.1 mol% 2.0 mol% 60 mol%	UDMA/TEGDMA in weight ratio 7 : 3	405 nm 19.8 mW·cm^{-2} 25 µm

Table A2. Formulas, names, CAS, acronyms and manufacturers of reagents used.

Name/Acronym	Structural formula	CAS	Manufacturers
Urethane dimethacrylate / UDMA		72869-86-4	Sigma Aldrich
Triethylene glycol dimethacrylate / TEGDMA		109-16-0	Sigma Aldrich
Titanium (IV) oxide / TiO_2	–	1317-70-0	Sigma Aldrich
(7-methoxy-4-methylcoumarin-3-yl) phenyliodonium hexafluorophosphate / Sylanto 7MP		Sylanto 7MP was obtained following the recently published procedure Pol. Pat. Appl. P-393 501 2010, Pol. Pat. Appl. P-395 515 2011.	
Ethyl 4-(dimethylamino)benzoate / EDB		10287-53-3	Sigma Aldrich

A2. Measurement setups

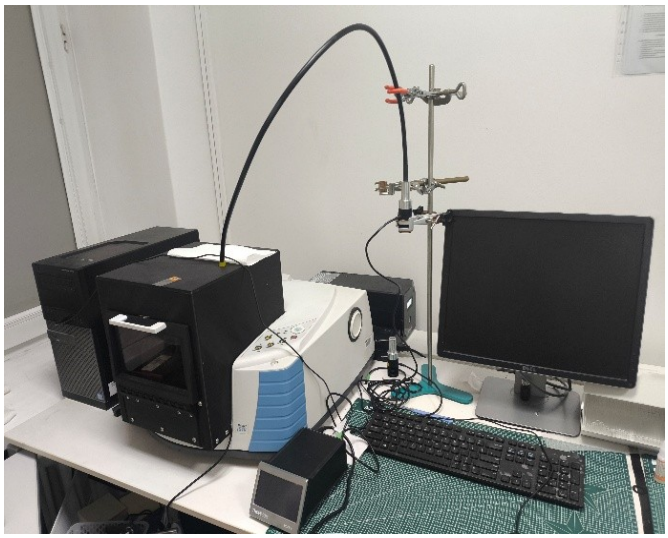


Figure A1. Nicolet i10 FT-IR spectrometer with a horizontal sample mount; samples irradiated with 405 nm Thorlabs LED ($\approx$ 19.8 mW·cm^{-2}) positioned 2.1 cm from the sample and powered by a DC2200 controller.

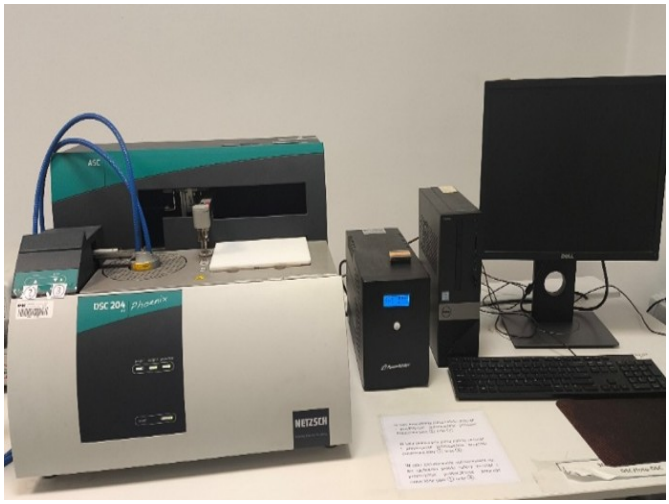


Figure A2. Photo-DSC 204 F1 Phoenix® system with Bluepoint LED eco light source at 405 nm ($\approx$ 18.67 mW·cm^{-2}), calibrated using an OmniCure R2000 radiometer; samples sealed in aluminum crucibles with quartz covers and measured isothermally at 25 °C.



Figure A3. MCR302e rheometer equipped with an optical curing module; samples irradiated with 405 nm LEDs ($\approx$ 19.8 mW·cm^{-2}) controlled by a DC2200 supply; temperature maintained at 25 °C.



Figure A4. Thermo Scientific Phenom XL G3 Desktop SEM; accelerating voltage 5–20 kV; CeB_6 source; max. magnification 200000×.

A3. Kinetic studies using the FT-IR method

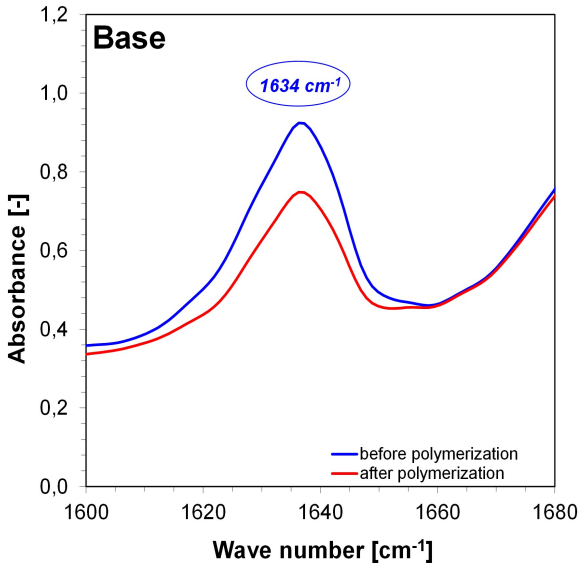


Figure A5. Before and After irradiation absorbance spectra obtained for photo-curable compositions based on UDMA/TEGDMA monomers in weight ratio 7 : 3 and one component photoinitiating systems (only photoinitiator ∼ 1 wt%) during sample monitoring for 600 s and LED@405 nm irradiation with a light intensity on the sample of 19.8 mW·cm^{-2}.

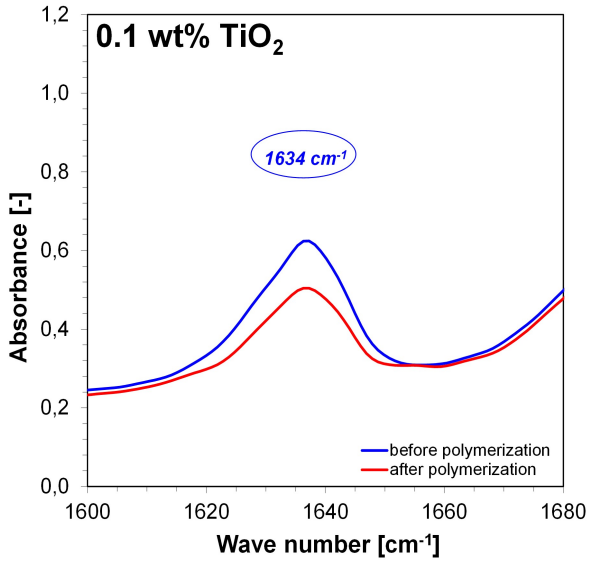


Figure A6. Before and After irradiation absorbance spectra obtained for photo-curable compositions based on UDMA/TEGDMA monomers in weight ratio 7 : 3 and one component photoinitiating systems (only photoinitiator ∼ 1 wt%) and **0.1 wt% TiO_2** during sample monitoring for 600 s and LED@405 nm irradiation with a light intensity on the sample of 19.8 mW·cm^{-2}.

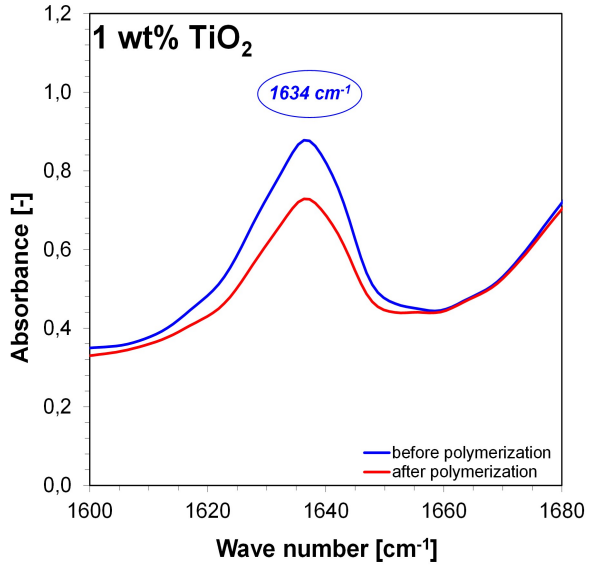


Figure A7. Before and After irradiation absorbance spectra obtained for photo-curable compositions based on UDMA/TEGDMA monomers in weight ratio 7 : 3 and one component photoinitiating systems (only photoinitiator ∼ 1 wt%) and **1 wt% TiO_2** during sample monitoring for 600 s and LED@405 nm irradiation with a light intensity on the sample of 19.8 mW·cm^{-2}.

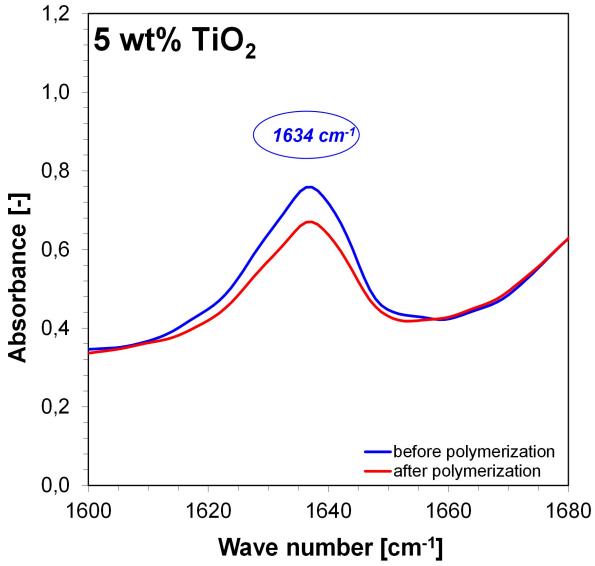


Figure A8. Before and After irradiation absorbance spectra obtained for photo-curable compositions based on UDMA/TEGDMA monomers in weight ratio 7 : 3 and one component photoinitiating systems (only photoinitiator ∼ 1 wt%) and **5 wt% TiO_2** during sample monitoring for 600 s and LED@405 nm irradiation with a light intensity on the sample of 19.8 mW·cm^{-2}.

A4. Kinetic studies using the Photo-DSC method

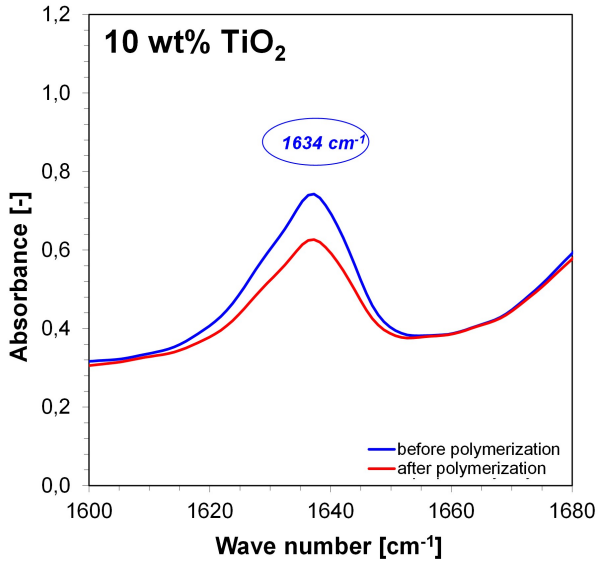


Figure A9. Before and After irradiation absorbance spectra obtained for photo- curable compositions based on UDMA/TEGDMA monomers in weight ratio 7:3 and one component photoinitiating systems (only photoinitiator $\sim$ 1 wt-%) and **10 wt% TiO_2** during sample monitoring for light intensity on the sample of 19.8 mW·cm^{-2}.

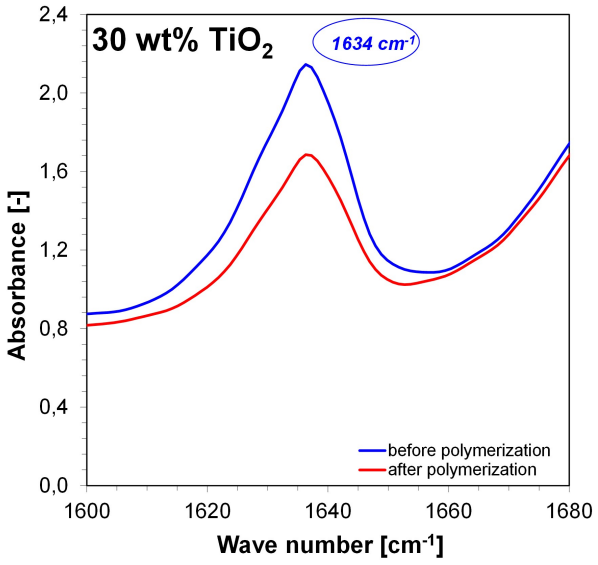


Figure A10. Before and After irradiation absorbance spectra obtained for photo- curable compositions based on UDMA/TEGDMA monomers in weight ratio 7:3 and one component photoinitiating systems (only photoinitiator $\sim$ 1wt%) and **30 wt% TiO_2** during sample monitoring for 600 s and LED@405 nm irradiation with a 19.8 mW·cm^{-2}.

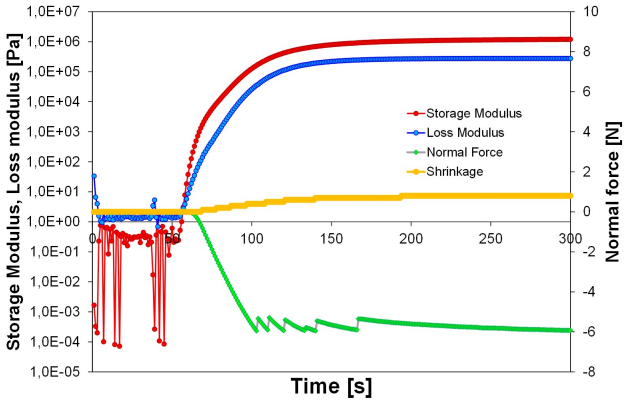


Figure A11. Photo-rheology profiles obtained for photo-curable compositions based on UDMA/TEGDMA monomers in weight ratio 7:3 and one component photoinitiating systems (only photoinitiator $\sim$ 1 wt%)) during sample monitoring for 590 s and LED@405 nm irradiation with a light intensity on the sample of 19.8 mW·cm^{-2}, the dark period was 10 s before the process of photopolymerization.

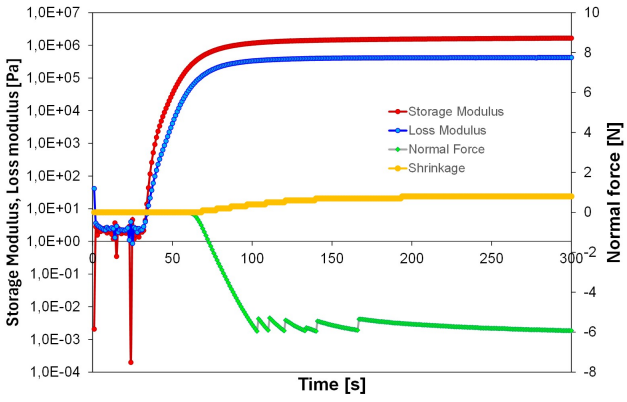


Figure A12. Photo-rheology profiles obtained for photo-curable compositions based on UDMA/TEGDMA monomers in weight ratio 7:3 and one component photoinitiating systems (only photoinitiator $\sim$ 1 wt%) and **0.1 wt% TiO_2** during sample monitoring for 600 s and LED@405 nm irradiation with a light intensity on the sample of 19.8 mW·cm^{-2}, the dark period was 10 s before the process of photopolymerization.

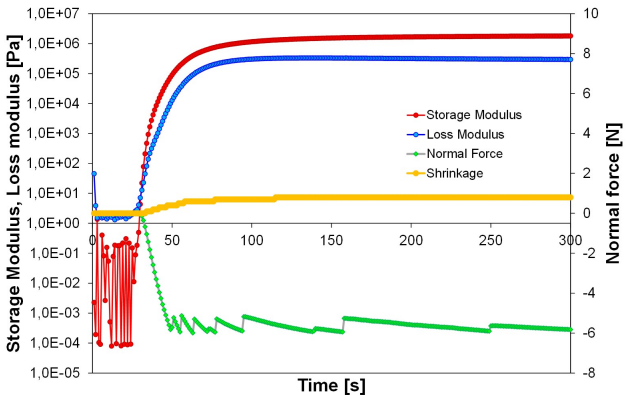


Figure A13. Photo-rheology profiles obtained for photo-curable compositions based on UDMA/TEGDMA monomers in weight ratio 7:3 and one component photoinitiating systems (only photoinitiator ~ 1 wt%) and **1 wt% TiO_2** during sample monitoring for 600 s and LED@405 nm irradiation with a light intensity on the sample of 19.8 mW·cm^{-2}, the dark period was 10 s before the process of photopolymerization.

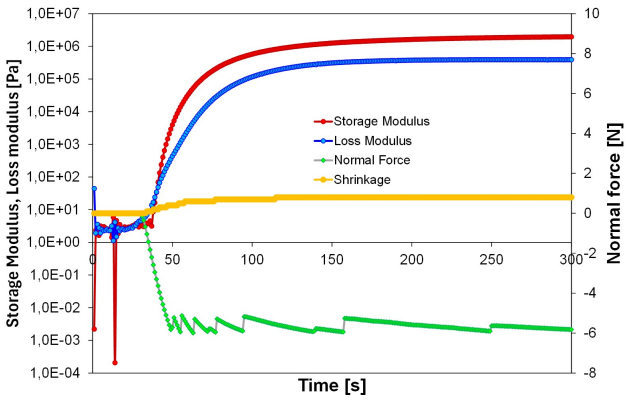


Figure A14. Photo-rheology profiles obtained for photo-curable compositions based on UDMA/TEGDMA monomers in weight ratio 7:3 and one component photoinitiating systems (only photoinitiator ~ 1 wt%)) and **5 wt%) TiO_2** during sample monitoring for 600 s and LED@405 nm irradiation with a light intensity on the sample of 19.8 mW·cm^{-2}, the dark period was 10 s before the process of photopolymerization.

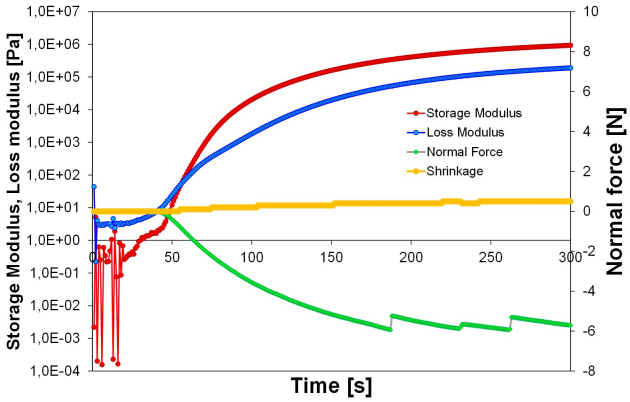


Figure A15. Photo-rheology profiles obtained for photo-curable compositions based on UDMA/TEGDMA monomers in weight ratio 7 : 3 and one component photoinitiating systems (only photoinitiator ~ 1 wt%) and **10 wt% TiO_2** during sample monitoring for 600 s and LED@405 nm irradiation with a light intensity on the sample of 19.8 mW·cm^{-2}, the dark period was 10 s before the process of photopolymerization.

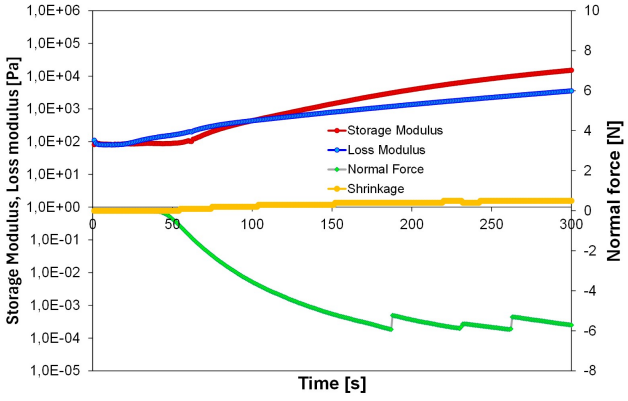


Figure A16. Photo-rheology profiles obtained for photo-curable compositions based on UDMA/TEGDMA monomers in weight ratio 7 : 3 and one component photoinitiating systems (only photoinitiator ~ 1 wt%) and **30 wt% TiO_2** during sample monitoring for 600 s and LED@405 nm irradiation with a light intensity on the sample of 19.8 mW·cm^{-2}, the dark period was 10 s before the process of photopolymerization.

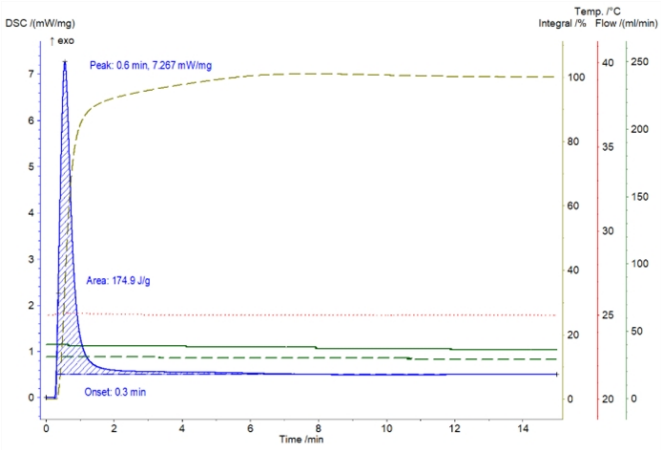


Figure A17. Photo-DSC heat profiles obtained for photo-curable compositions based on UDMA/TEGDMA monomers in weight ratio 7 : 3 and one component photoinitiating systems (only photoinitiator ~ 1 wt%) during sample monitoring for 900 s and LED@405 nm irradiation with a light intensity on the sample of 18.67 mW·cm^{-2}.

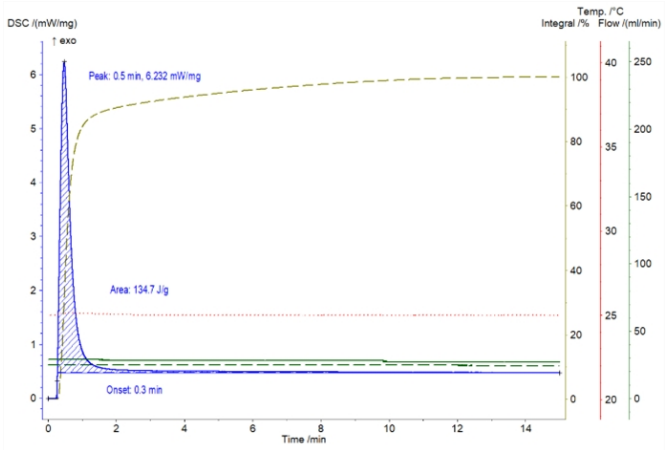


Figure A18. Photo-DSC heat profiles obtained for photo-curable compositions based on UDMA/TEGDMA monomers in weight ratio 7 : 3 and one component photoinitiating systems (only photoinitiator ~ 1 wt%) and **0.1 wt% TiO_2** during sample monitoring for 900 s and LED@405 nm irradiation with a light intensity on the sample of 18.67 mW·cm^{-2}.

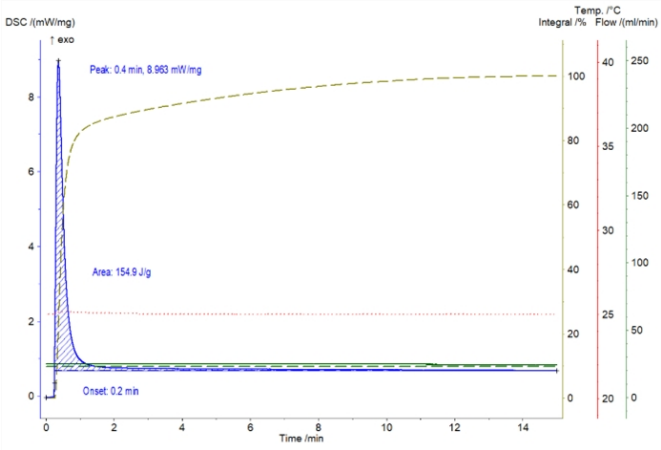


Figure A19. Photo-DSC heat profiles obtained for photo-curable compositions based on UDMA/TEGDMA monomers in weight ratio 7 : 3 and one component photoinitiating systems (only photoinitiator ~ 1 wt%) and **1 wt% TiO_2** during sample monitoring for 900 s and LED@405 nm irradiation with a light intensity on the sample of 18.67 mW·cm^{-2}.

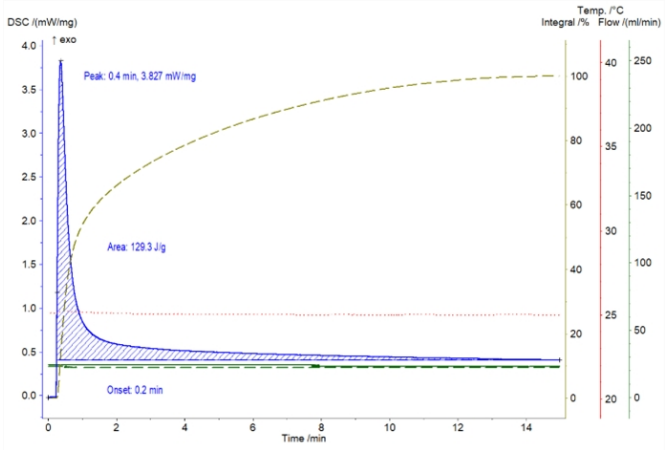


Figure A20. Photo-DSC heat profiles obtained for photo-curable compositions based on UDMA/TEGDMA monomers in weight ratio 7 : 3 and one component photoinitiating systems (only photoinitiator ~ 1 wt%) and **5 wt% TiO_2** during sample monitoring for 900 s and LED@405 nm irradiation with a light intensity on the sample of 18.67 mW·cm^{-2}.

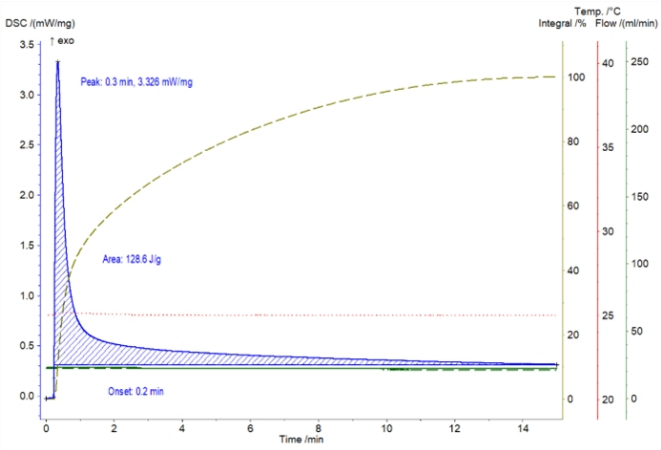


Figure A21. Photo-DSC heat profiles obtained for photo-curable compositions based on UDMA/TEGDMA monomers in weight ratio 7 : 3 and one component photoinitiating systems (only photoinitiator ∼ 1 wt%) and **10 wt% TiO_2** during sample monitoring for 900 s and LED@405 nm irradiation with a light intensity on the sample of 18.67 mW·cm^{-2}.

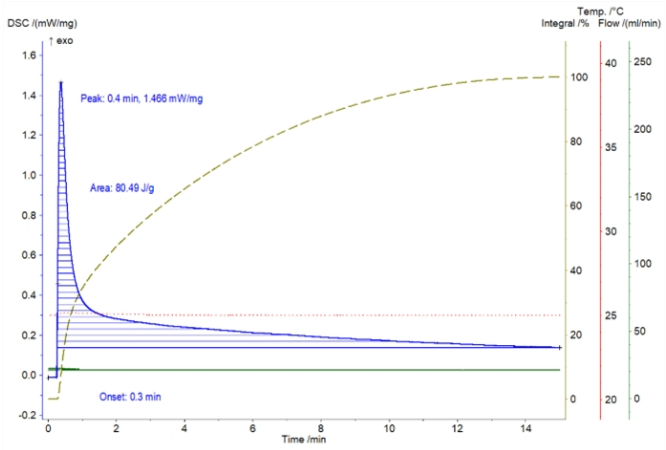


Figure A22. Photo-DSC heat profiles obtained for photo-curable compositions based on UDMA/TEGDMA monomers in weight ratio 7 : 3 and one component photoinitiating systems (only photoinitiator ∼ 1 wt%) and **30 wt% TiO_2** during sample monitoring for 900 s and LED@405 nm irradiation with a light intensity on the sample of 18.67 mW·cm^{-2}.

Table A3. Printing parameters for the 3D printers used.

DLP LumenX™ Gen 3 (UDMA/TEGDMA 7:3, One component photoinitiating system)					
Sample	Irradiation power [mW·cm^{-2}]	Energy dose [mJ·cm^{-2}]	Exposure time [s]	Base exposure time [s]	Layer height [µm]
Base	20.5	513	25	75	50
0.1 wt% TiO_2	20.5	513	25	75	50
1 wt% TiO_2	25.9	777	30	80	50
5 wt% TiO_2	25.2	907	35	75	50
10 wt% TiO_2	29.6	1480	50	85	50
30 wt% TiO_2	28.9	1387	48	90	50

LCD Anycubic Photon Mono M7 PRO (UDMA/TEGDMA 7:3, One component photoinitiating system)					
Sample	Irradiation power [mW·cm^{-2}]	Energy dose [mJ·cm^{-2}]	Exposure time [s]	Base exposure time [s]	Layer height [µm]
Base	7	490	70	120	50
0.1 wt% TiO_2	7	525	75	130	50

Chemical and Process Engineering: New Frontiers, 2026, 47(2), e134
DOI: 10.24425/cpe.2026.158132

Process parameter optimization for 3D printing of photocurable resins in hydrogel media

Mateusz Rociński, Maciej Pilch

Cracow University of Technology, Faculty of Civil Engineering, Wind Engineering Laboratory, Warszawska 24, 31-155 Cracow, Poland

*** Corresponding author, e-mail:** maciej.pilch@pk.edu.pl

Presented at
5th Seminar on Practical Aspects of Chemical Engineering PAIC 2025, 22–23 September 2025, Zaniemyśl, Poland.
Guest Editors: Andżelika Krupińska and Sylwia Włodarczak.

Article info:
Received: 07 December 2025
Revised: 16 March 2026
Accepted: 07 May 2026

Abstract
The aim of this work was to develop a low-cost 3D printing method operating in hydrogel environment and to find suitable process parameters and input materials. The proposed approach enables inexpensive fabrication of geometrically complex structures, including overhangs, without conventional support materials. A prototype device was created by modifying an FDM 3D printer with a syringe-based extrusion system, UV-curing module and dedicated vessel defining the printing workspace. Printing parameters were then optimized to achieve satisfactory resolution both in air & hydrogels. Preliminary experiments demonstrated that commercial photopolymer resins and hydrogels were inadequate for gel-based printing due to inappropriate rheological characteristics of both. Multiple 3D printing pastes and polymer gels of varied composition were prepared and examined through rheological and photorheological analyses, enabling selection of candidates for application testing.
Using the optimized materials, beam specimens were printed and mechanically tested, with results compared to analogous samples produced via commercial DLP 3D printer. Among the hydrogel media, a guar-gum-based hydrogel containing 3% solids provided the most favorable support and rheology for DIW printing. The highest promise was shown by a paste formulated from a commercial ANYCUBIC resin with 5% amorphous silica, yielding prints of superior resolution, viscosity, adhesion and strength. Notably, beams printed in the guar-gum hydrogel showed significantly higher strength than DLP counterparts. Overall, the developed budget DIW technology in liquid media enables fabrication of simple, high-resolution, mechanically robust parts, with potential applications in bioprinting, delicate-material processing and complex-geometry fabrication.

Keywords
3D printing, photocurable resin, hydrogel media

1. INTRODUCTION

The dynamic development of 3D printing technology is today inseparably linked to advances in the field of polymers. Owing to their unique properties and broad possibilities for modification, polymers form the foundation of numerous innovations in the automotive, construction, electronics, medical and packaging industries (Alghamdi et al., 2021; Murr, 2016; Namazi, 2017). Increasing attention, however, is being paid not only to their functionality but also to issues related to production, recycling and environmental impact, which aligns with the sustainability priorities of the European Union (Warner et al., 2004).

Polymer technology – combining elements of chemistry, engineering and materials science – focuses on the development of new materials, the improvement of processing techniques and the reduction of costs and emissions (Pielichowski, 2003; Szlezyngier, 2012). Progress in this area is driven by advanced methods of catalysis, controlled synthesis and modern processing technologies (Fiedor et al., 2020; Hola et al., 2020; Petko et al., 2022; Topa et al., 2020).

One of the most promising directions is 3D printing in liquid environments. This approach enables more precise shaping of polymer structures, reduces defects and broadens potential applications (Bhattacharjee et al., 2016; Wu et al., 2022; Zhao and He, 2020; Zhou et al., 2022). A key challenge remains the selection of suitable materials and process parameters.

The presented research focuses on the development of polymers printed in a hydrogel environment, with particular emphasis on process optimization and the analysis of the resulting material properties. This approach integrates knowledge from polymer chemistry, rheology, engineering and is consistent with current trends in the use of support baths and yield-stress fluids in embedded 3D printing (Compaan et al., 2019; Shiwarski et al., 2021; Zeng et al., 2022).

2. OPTIMIZATION OF THE 3D PRINTING PROCESS IN HYDROGEL ENVIRONMENTS

Fabrication in hydrogel medium was carried out using a custom-built Direct Ink Writing (DIW) 3D printing system. The device was constructed on a mechanical frame conceptually similar to that used in conventional fused deposition modeling (FDM) printers. The printing system consisted of a motion platform enabling controlled movement of the printhead in the horizontal plane and a syringe-based extru-

© 2026. The Author(s). This is an open-access article distributed under the terms of the Creative Commons Attribution (CC-BY 4.0, https://creativecommons.org/licenses/by/4.0/), which permits unrestricted use, distribution, and reproduction in any medium, provided the original author and source are credited.

sion unit designed for deposition of photocurable composite materials. Material extrusion was performed using a DIW printhead equipped with a syringe filled with the prepared photocurable composite. The extrusion process was controlled mechanically by a piston acting on the syringe plunger. The piston was driven by a carriage translating the rotational motion of a trapezoidal lead screw into linear displacement. The lead screw was powered by a stepper motor, enabling precise control of the plunger movement and consequently, the extrusion rate of the material. The extrusion speed was therefore regulated analogously to classical FDM printers by adjusting the rotational speed of the stepper motor driving the lead screw. The extrusion rate (E_{steps}), defined as the number of stepper motor steps required to extrude 1 mm of a resin track, was determined experimentally to be 98.5. This value ensured that the printed resin track did not spread laterally and did not exhibit discontinuities. The printhead was fitted with a nozzle with an internal diameter of 0.2 mm. The layer height during printing was set to 0.2 mm. This value was selected as an optimal compromise between reliable extrusion and shape retention of the deposited resin track. The use of smaller layer heights frequently led to clogging of the nozzle due to the high viscosity of the photocurable composite, whereas larger layer heights resulted in partial spreading of the uncured material before photopolymerization, which caused deformation of the printed structures. The movement speed of the printhead during deposition was set to 20 mm/s. This value was established during preliminary optimization experiments carried out prior to the present study. Higher printing speeds resulted in a noticeable deterioration in the quality and dimensional accuracy of the printed structures obtained using this system.

The printer was additionally adapted for fabrication in hydrogel environment. For this purpose, a flat-bottom vessel filled with a selected hydrogel was placed on the printing platform and served as the surrounding medium during the printing process. Before printing, the syringe installed in the extrusion unit was filled with the photocurable composite. The printing container was then filled with the hydrogel, forming a layer approximately 1 cm thick above the printed structures. During printing, the photocurable material was extruded from the syringe through the nozzle while the printhead moved according to the predefined toolpath. Simultaneously, the deposited material was exposed to ultraviolet radiation generated by a 405 nm UV-LED panel positioned beneath the printing vessel. This irradiation initiated rapid photopolymerization of the extruded resin, allowing the printed structures to be cured directly on the bottom surface of the hydrogel-filled container. The light intensity (UV irradiance) was 35 mW/cm^2 at a wavelength of 405 nm. The optimal light intensity was determined experimentally (by adjusting the supply voltage of the UV-LED diode panel) for a selected printing head movement speed of 20 mm/s, so that after passing through a hydrogel layer of approximately 1 cm thickness it provided preliminary curing of the resin, maintaining the desired shape/geometry while avoiding nozzle clogging caused by prematurely cured resin. The entire 3D printing process followed an operational scheme comparable to that used in conventional FDM 3D printing systems, with the main difference being the syringe-based extrusion mechanism and the simultaneous UV curing of the deposited photocurable composite in a hydrogel-based aqueous environment. After the 3D printing process, the sample was placed in an ultrasonic bath filled with isopropanol for 5 minutes at a temperature of approximately 20 °C. It was then dried under a laboratory fume hood for 20 minutes at approximately 20 °C. Finally, the printed object underwent UV post-curing (final curing) for 15 minutes in a custom-built post-processing chamber, equipped with UV light of 405 nm wavelength and an intensity of 20 mW/cm^2, at a temperature of approximately 30 °C. The temperature inside the chamber increased during operation of the UV LEDs despite the fact that they were actively cooled by fans.

Application tests showed that among the 10 formulations differing solely in silica content (from 0% wt to 10% wt, in increments of 1%), the best results were obtained for the composition containing 5% wt silica. In this case, the printed structures exhibited the highest quality and good detail resolution. For silica contents above 5% wt, however, frequent clogging of the 0.2 mm nozzle was observed, which significantly deteriorated print quality or prevented the printing process from starting. Attempts were made to use nozzles of larger diameter, but in every case the resulting prints exhibited poorer quality compared to those produced with the 0.2 mm nozzle, making this approach impractical. An additional challenge arose from the fact that the printer – still at the prototype stage – did not include a nozzle-clog detection system. As a result, leaving the process unattended could lead to damage of the extrusion system and in extreme cases, even to the destruction of the entire prototype.

As shown in Figure 1, both the extrusion rate and the printing speed have a significant impact on the quality of the printed structures (Dudek, 2013; Hikmat et al., 2021; Shahrubudin et al., 2019). Excessive material flow leads to rounded geometries

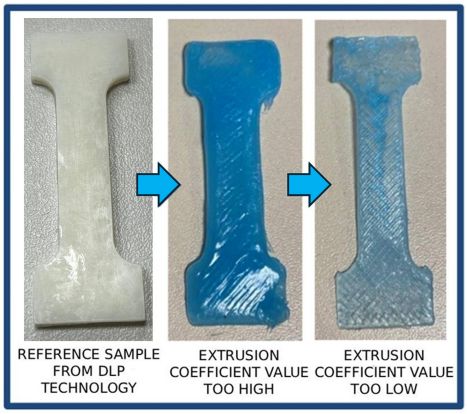


Figure 1. Comparison of models with different extrusion coefficient values.

and dimensions exceeding the intended values. Conversely, too low values of these parameters also result in prints that deviate from the target dimensions.

The conducted research showed that the most suitable medium for printing in agar-based hydrogel environment is agar-based hydrogel with a 3% concentration of the active substance (Fig. 2). Above this value, the hydrogel became excessively brittle – at concentrations of 4% and 5% the structures underwent complete degradation during the process – making printing in a hydrogel environment impossible. In contrast, hydrogels with lower concentrations (1% and 2%) exhibited a consistency similar to water and therefore did not provide the required support properties necessary for proper printing, which is consistent with observations reported for other yield-stress support baths (Compaan et al., 2019; Zhou et al., 2022).

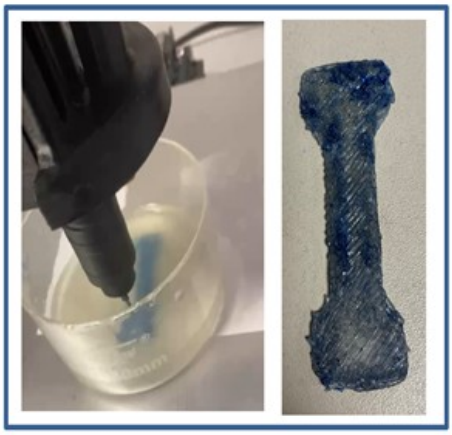


Figure 2. Images from the printing process in an agar-based hydrogel environment.

Further investigations involving agar, PVA and HEA hydrogels were discontinued due to their limited application potential. In the case of agar, the hydrogel structure was destroyed by the syringe–nozzle extrusion system. Hydrogels based on HEA and PVA were rejected because of insufficient support properties (Wu et al., 2022; Zhao and He, 2020).

The analysis of the measurement results demonstrated that prints produced in guar gum hydrogel exhibited significantly higher quality compared to those obtained in agar-based hydrogels, indicating favorable rheological properties of this system (Fig. 3). This is further supported by the dimensional measurements of the printed test samples relative to the model dimensions.

The guar gum hydrogel showed a stable viscosity profile – the viscosity curve as a function of shear rate progressed smoothly, without disruptions such as sudden spikes. This indicates good structural coherence of the material and the absence of effects such as agglomeration or coagulation confirms its homogeneity. Such stability also suggests the presence of thixotropic behavior, which facilitates the deposition of successive layers in 3D printing, similarly to other hydrogel-based support

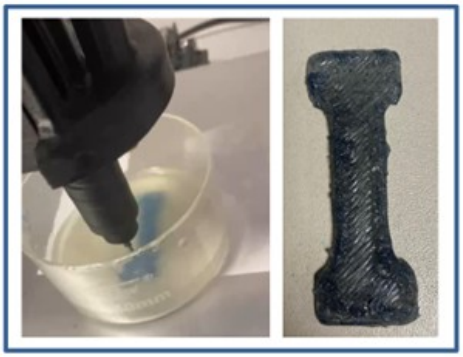


Figure 3. Images from the printing process in a guar gum hydrogel environment.

media used in embedded bioprinting (Ouyang et al., 2020; Shiwarski et al., 2021; Zhou et al., 2022). Based on these findings, the guar hydrogel can be considered to exhibit near-optimal parameters for applications in hydrogel-supported printing environments. For comparison, the agar hydrogel displayed greater instability at medium and high shear rates. The observed fluctuations suggest that although agar can form a rigid matrix, its structure is less resistant to dynamic loading. Additionally, the need for high temperature during preparation and its rapid solidification may introduce structural inhomogeneities, which further deteriorate the rheological stability of the material. The poly(vinyl alcohol)-based hydrogel exhibited moderate viscosity and a distinctly nonlinear shear profile. This indicates the presence of a weakly crosslinked structure, despite the application of a triple freeze–thaw cycle. The disturbances in the curve may stem from insufficient physical crosslinking or structural heterogeneity arising from local variations in solvent content. Although the viscosity values were acceptable, the material did not achieve the level of stability comparable to guar gum. The least stable system was the hydrogel based on hydroxylated acrylates, synthesized via photopolymerization of an HEA solution with TPO photoinitiator. The resulting gel was prone to deformation and exhibited an irregular crosslinking process. Despite its elasticity and transparency, the lack of structural integrity and pronounced rheological variability disqualified it from further printing tests. The fluctuations visible on the viscosity curve may result from both its low initial viscosity and insufficient structural densification, making the material highly sensitive to shear forces.

3. RHEOLOGY AND PHOTORHEOLOGY

Rheological measurements were performed using a Physica MCR 302 rheometer (Anton Paar). Rheological measurements clearly confirmed that the properties of the hydrogels have a direct impact on print quality (Wu et al., 2022; Zhao and He, 2020; Zhou et al., 2022). Among all analyzed samples, only the guar hydrogel (3% wt) exhibited a smooth, continuous viscosity curve without irregularities or sudden directional changes (Fig. 4). In contrast to the remaining

materials, which showed pronounced fluctuations and jagged profiles, this indicates high stability and measurement repeatability – features that are particularly desirable when assessing rheological quality (Figs. 5–7).

Application tests demonstrated that the 3% wt guar gum hydrogel provided the best supportive properties required for 3D printing processes. The remaining hydrogels (PVA and HEA) did not meet the application criteria. In the case of HEA-based hydrogels in particular, despite their transparency and high degree of hydration, a clear lack of mechanical cohesion and difficulties in maintaining geometric integrity were observed. These structures quickly deformed under their own weight and due to additional water absorption, which completely disqualified them from being used as a support medium or printable material. Due to insufficient rheological performance, they were not subjected to further additive manufacturing trials.

Hydrogels whose rheological curves exhibit a similar profile and comparable parameter values can be considered materials with properties close to the optimum for 3D printing processes carried out in a hydrogel environment (Compaan et al., 2019; Shiwarski et al., 2021; Zhou et al., 2022). Systems with sig-

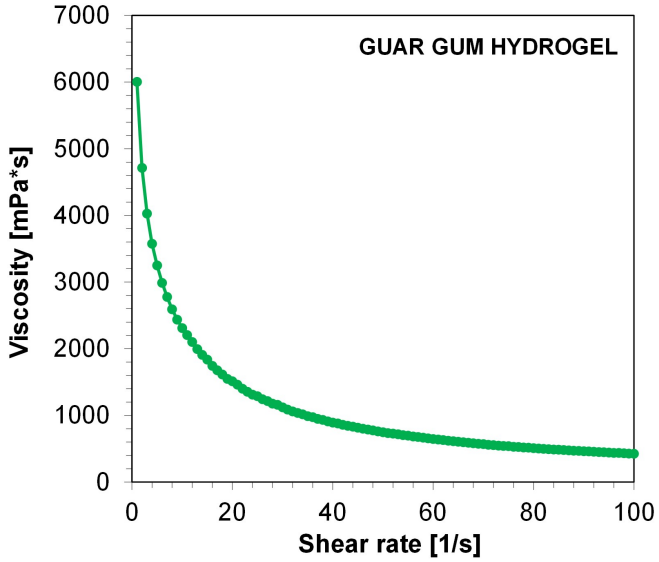


Figure 4. Graph of the viscosity–shear rate relationship for the guar gum–based hydrogel sample (3%).

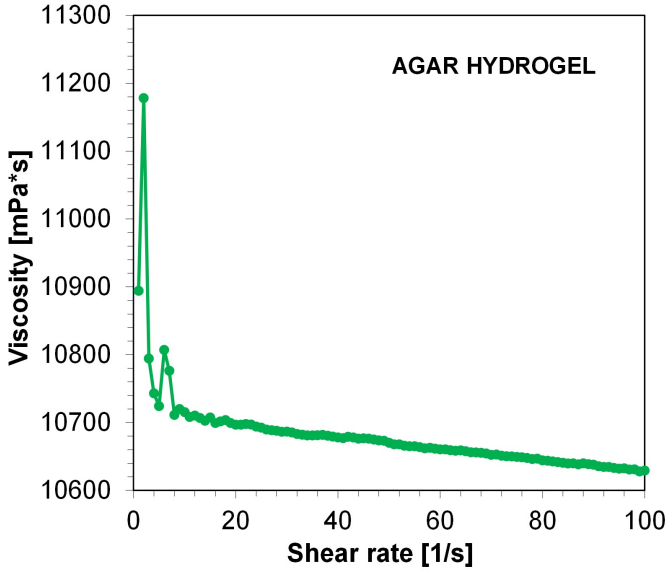


Figure 5. Graph of the viscosity–shear rate relationship for the 3% wt agar-based hydrogel sample.

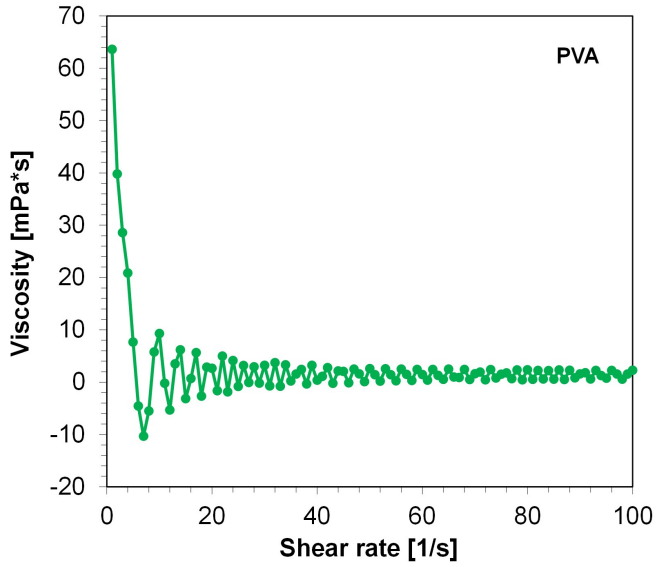


Figure 6. Graph of the viscosity–shear rate relationship for the 3% wt poly(vinyl alcohol)–based hydrogel.

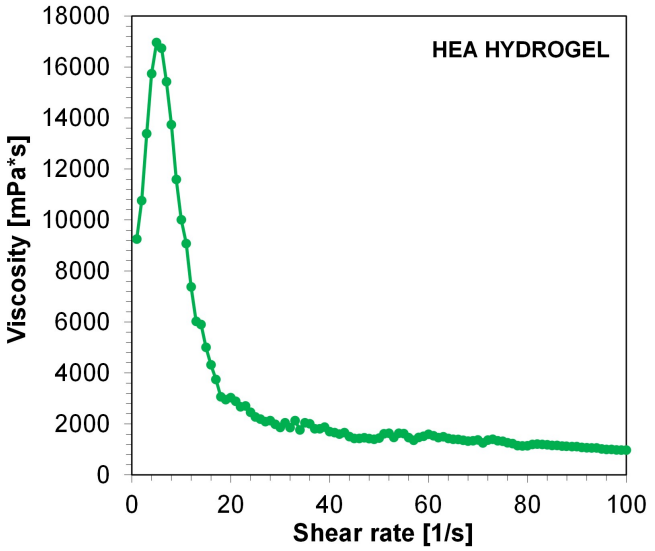


Figure 7. Graph of the viscosity–shear rate relationship for the hydrogel based on hydroxylated acrylates in a 1(HEA) : 4(H_2O) ratio.

nificantly lower or higher rheological parameters show limited suitability for shaping and stabilizing printed structures, which further confirms the applicability of the analyzed hydrogel in additive manufacturing.

After completing a detailed analysis of the hydrogel properties, the next stage of the study involved evaluating the rheology of resin pastes, including both commercial photopolymer resins and their modifications obtained through the incorporation of fillers (Figs. 8–9).

The analysis of the results confirmed that increasing the silica content leads to a noticeable rise in material viscosity, accompanied by an increase in shear resistance. The composition containing 2% wt silica exhibited the most stable rheological curve, suggesting improved dispersion of the filler particles within the resin matrix. In the case of the sample containing 1% wt silica, a rapid spike in viscosity was observed at the initial stage of the measurement, likely resulting from insufficient particle dispersion or the presence of agglomerates that disrupt uniform flow under shear forces (Padhi et al., 2015; Prabhakar et al., 2015).

The study clearly demonstrated that viscosity and shear stability are crucial for the applicability of materials in 3D printing technologies, especially within a hydrogel-supported environment (Maines et al., 2021; Melchels et al., 2010). Among all analyzed samples, only the 3% wt guar hydrogel exhibited a rheological profile considered optimal – characterized by a smooth, consistent curve and high repeatability of results. Materials exhibiting either excessively high or too low viscosity failed to provide adequate structural stability during shaping, which disqualified them from further application trials. The findings also showed that proper selection and modification of resin compositions using functional additives, such as silica, can significantly enhance their rheological properties and broaden their potential applications (Aredla et al., 2024; Yadav et al., 2023).

However, ensuring a homogeneous dispersion of the filler phase remains a necessary condition, which requires optimization of the composite preparation methods. Rheological measurements of the commercial resins showed that the base materials, without functional additives, exhibited low viscosity – approximately 195 mPa · s for the ABS-Like PRO2 resin (Anycubic) and about 235 mPa · s for the TOUGH resin (Anycubic). With increasing silica content, a systematic rise in viscosity was observed, dependent on the applied shear rate. The sudden viscosity spike in the 1% wt paste can be explained by insufficient mixing of the sample, which led to particle agglomeration and local flow disturbances.

Considering that photopolymerization processes play a crucial role in additive manufacturing of structures from light-curable resins, photorheological measurements were also performed to analyze the mechanical properties in real time during UV exposure. The experiments were conducted using a photorheology module integrated with an Anton Paar rheometer, enabling dynamic measurements while simultaneously irradiating the sample with UV light at a wavelength of 405 nm. This parameter corresponds to the standard used in most commercial 3D printing systems operating via photopolymerization (e.g., SLA) (Maines et al., 2021; Melchels et al., 2010; Stansbury and Idacavage, 2016).

The characteristic intersection of the orange and blue curves, visible in the presented graphs, corresponds to the gelation point (Figs. 10–13). The sudden increase leading to the crossover of the moduli was associated with the activation of the UV-LED 405 nm diode, which initiated the photopoly-

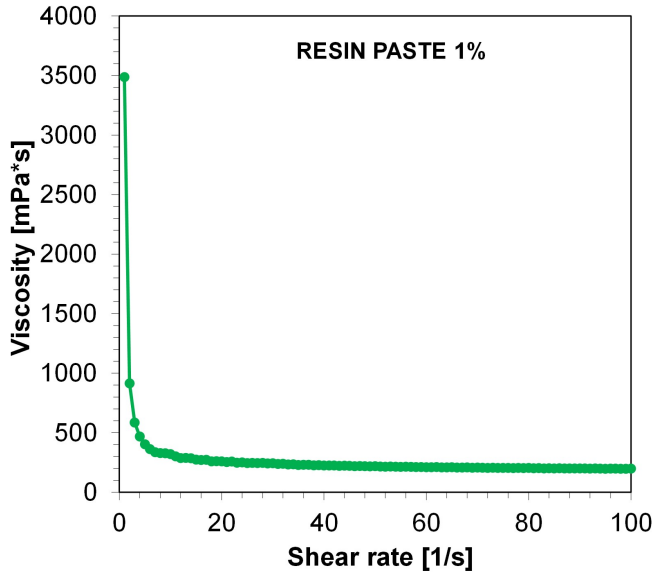


Figure 8. Graph of the viscosity–shear rate relationship for the resin paste sample containing 1% wt silica.

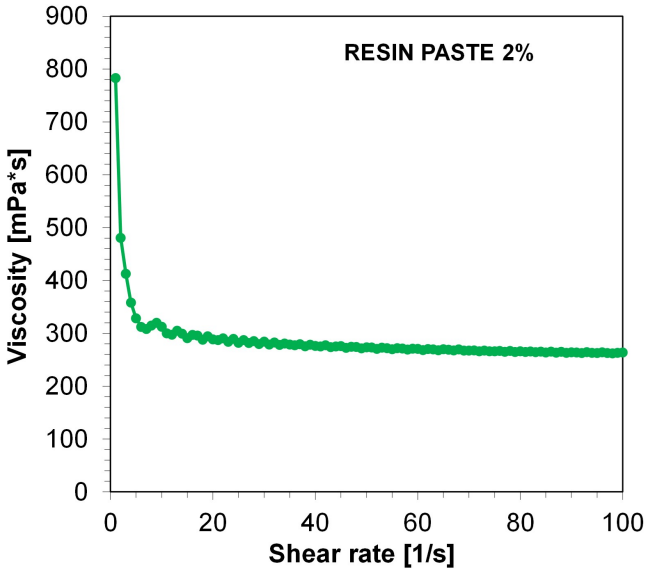


Figure 9. Graph of the viscosity–shear rate relationship for the resin paste sample containing 2% wt silica.

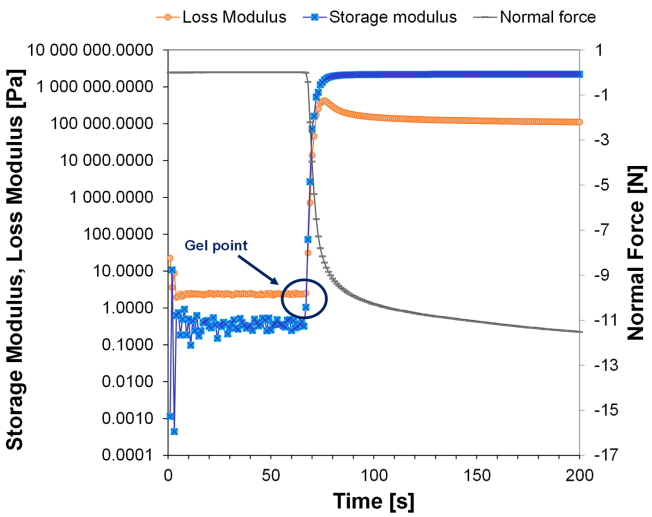


Figure 10. Graph of the dependence of normal force on the two moduli for the ABS-Like PRO2 resin.

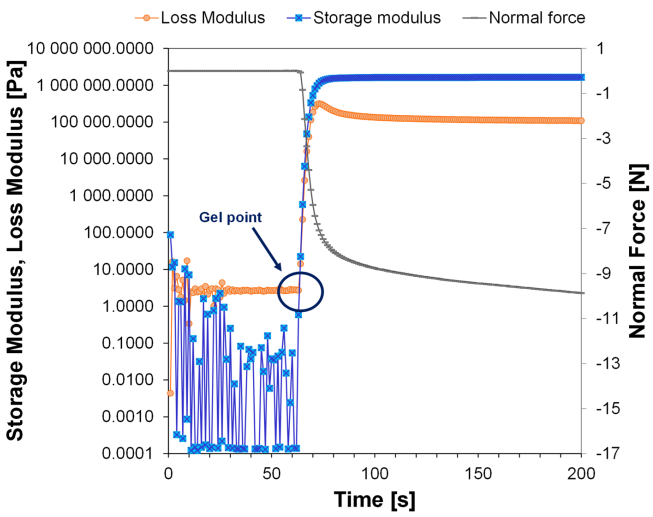


Figure 11. Graph of the dependence of normal force on the two moduli for the TOUGH resin.

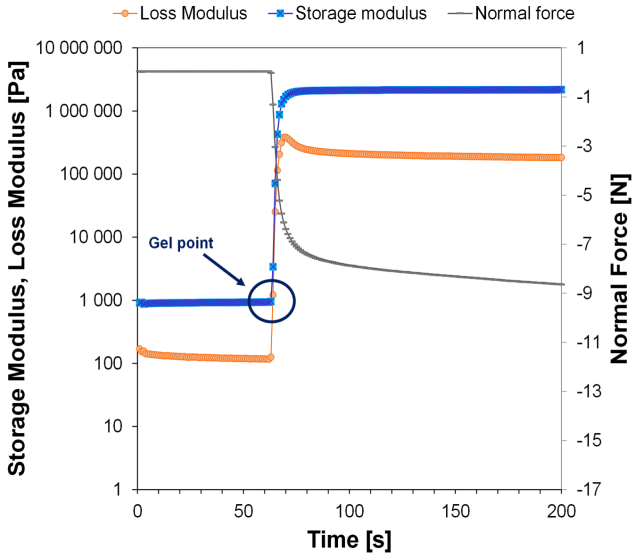


Figure 12. Graph of the dependence of normal force on the two moduli for the resin paste containing 1% wt silica.

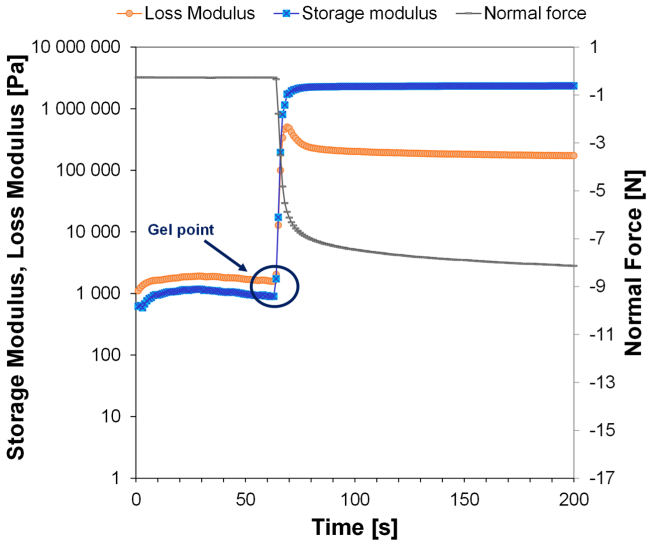


Figure 13. Graph of the dependence of normal force on the two moduli for the resin paste containing 2% wt silica.

merization of the sample placed in a 0.1 mm gap between the working plate and the vertically positioned spindle. This resulted in a rapid increase in the viscosity of the system. An important indicator of structural changes occurring during crosslinking was also the behavior of the normal force. For samples with higher filler content, the final value of this parameter was lower, which may indicate incomplete crosslinking or the presence of insufficiently cured regions, a phenomenon also discussed in studies on photopolymer networks and dental resins (Jandt and Sigusch, 2009; Stansbury and Idacavage, 2016).

The results clearly confirmed significant differences in the curing behavior between the unmodified base resins (ABS-Like PRO2 and TOUGH) and the composites containing silica. For the ABS-Like PRO2 resin, the curing process proceeded relatively smoothly and the crossover of G' and G'' occurred approximately 75 s after the start of the measurement (i.e., 15 s after UV initiation). The crossover point marks the transition of the material from the liquid state to the gel phase. The normal force changed in a linear and stable manner, suggesting uniform and gradual formation of the polymer network.

In the case of the TOUGH resin, the gelation point was recorded slightly earlier, around the 70-s mark. However, the G' and G'' curves exhibited a more unstable trajectory while visible fluctuations indicated structural heterogeneity and the potential occurrence of microscopic swelling or phase separation phenomena.

A different crosslinking behavior was observed for the silica-modified resin pastes. In the composition containing 1% wt filler, the gelation point occurred later, approximately 85 s

after the start of the measurement. The G' and G'' curves showed a smoother course than in the base resins, suggesting that the presence of the solid phase restricts the mobility of polymer segments and delays the crosslinking process. At the same time, the resulting network exhibited greater stability, as evidenced by the smooth dynamics of the G' increase.

In the sample containing 2% wt silica, the crossover of the moduli occurred more quickly (around the 80-s mark) and the growth of G' was markedly more rapid. Such behavior indicates that a higher filler concentration promotes the formation of nucleation sites for the crosslinking reaction, accelerating the spatial polymerization process. Simultaneously, the normal force showed a tendency to increase sharply in the final phase of the measurement, which may be associated with stress accumulation within the crosslinked structure, a typical effect in materials with higher particle packing density.

In summary, the photorheological analysis demonstrated that the presence of silica in resin pastes affected not only the mechanical properties after curing but also significantly modified the course of the polymerization process itself. Lower filler concentrations delay gelation, whereas higher concentrations accelerate it while increasing the risk of internal stress development. Therefore, proper optimization of resin formulations with respect to photorheological behavior is crucial for ensuring a balance between processing performance and the final quality of additively manufactured structures (Maines et al., 2021; Ouyang et al., 2020).

The obtained results confirm that photorheology is an effective tool for analyzing the curing kinetics of photosensitive formulations and for assessing the influence of composition on material behavior during UV exposure. This is particularly important in 3D printing technologies, where gelation time, curing rate and mechanical properties of individual layers directly translate into dimensional accuracy, durability and the quality of final components. From a materials engineering perspective, these data can be used to optimize photopolymer formulations in terms of reactivity and processing parameters. This enables better adjustment of printing conditions (exposure time, UV intensity, layer thickness) to the characteristics of a given composition, thereby minimizing defects such as excessive shrinkage, delamination or insufficient curing of deeper layers.

4. MECHANICAL TESTING OF COMPOSITE MATERIALS

To complement the rheological results and to obtain a more comprehensive understanding of material behavior during the 3D printing process, mechanical tests of the fabricated structures were also performed. As a reference point, an identical model was used – printed from the same base resin that served as the matrix for the resin pastes (Fig. 14). However, in this case, the printing was carried out using a DLP printer rather than the custom DIW-based device (Maines et al., 2021, Melchels et al., 2010). An ELEGOO Mars 4 DLP 3D printer was used. The standard layer exposure time was 2 s, the bottom layer exposure time was 30 s, the number of bottom layers was 5 and the layer thickness was 0.03 mm. The light intensity was 4 mW/cm^2 at a wavelength of 405 nm. Additionally, after the 3D printing process, the samples were subjected to post-processing according to a procedure analogous to that used for the samples printed using the DIW technique.



Figure 14. Reference model printed using DLP technology.

The thickness (a_0) and width (b_0) of the specimens were measured using a digital caliper with a resolution of 0.01 mm (Fig. 15). For each specimen, measurements were performed at three different locations within the gauge section. The average value was taken as the specimen dimension and used to determine the nominal cross-sectional area (S_0). The reported values represented the mean ± standard deviation for three specimens. The measurement uncertainty associated with the caliper was ±0.02 mm.

The thickness (a_0) and width (b_0) of the specimens were measured using a digital caliper with a resolution of 0.01 mm (Fig. 15). For each specimen, measurements were performed at three different locations within the gauge section. The average value was taken as the specimen dimension and used to determine the nominal cross-sectional area (S_0). The reported values represented the mean ± standard deviation for three specimens. The measurement uncertainty associated with the caliper was ±0.02 mm.

A universal testing machine MTS Insight 50 (MTS Insight™, Eden Prairie, Minnesota, USA) equipped with a ±50 kN load cell, was used for the mechanical tests. Tensile tests were performed in accordance with ISO 527, using mechanical clamping grips and anti-slip inserts to prevent specimen slippage. The crosshead speed was 10 mm/min and the initial gauge length was set to 35 mm.

Table 1 presents the results of static tensile tests performed on polymer samples fabricated under different environmental conditions. The key mechanical parameters determined include the yield strength $R_{p0.2}$ and the ultimate tensile strength R_m, along with geometric characteristics of the specimens such as thickness and cross-sectional area.

Table 1. Summary of experimental mechanical strength test data for the samples (mean ± SD).

Sample type	$R_{p0.2}$ [MPa]	R_m [MPa]	a_0 [mm]	b_0 [mm]	S_0 [mm^2]
Reference sample	1.19 ± 0.08	15.2 ± 0.36	2.89 ± 0.06	11.05 ± 0.10	31.93 ± 0.72
PVA	3.90 ± 0.28	8.4 ± 0.36	2.95 ± 0.18	11.90 ± 0.75	35.11 ± 2.96
HEA	0.60 ± 0.09	2.8 ± 0.26	1.80 ± 0.24	13.60 ± 0.75	24.48 ± 3.34
Guar gum 3%	9.70 ± 0.55	23.6 ± 0.85	2.10 ± 0.08	10.90 ± 0.20	22.89 ± 0.96
Agar 3%	0.40 ± 0.08	1.8 ± 0.20	2.07 ± 0.20	12.10 ± 0.50	25.05 ± 2.50
Air	1.30 ± 0.18	5.6 ± 0.40	1.50 ± 0.08	11.00 ± 0.20	16.50 ± 0.92

The comparison of the mechanical results with the observed morphology of the specimens indicates a clear relationship between print quality and the values of ultimate tensile strength (R_m) and yield strength ($R_{p0.2}$). The highest values of both tensile strength R_m and yield strength $R_{p0.2}$ were obtained for the specimen printed in 3% guar gum hydrogel ($R_m = 23.6 \pm 0.85$ MPa, $R_{p0.2} = 9.70 \pm 0.55$ MPa). These values exceed the R_m and $R_{p0.2}$ values obtained for the reference model produced by the DLP technique, which may indicate that the applied manufacturing approach ensures a stable and repeatable fabrication process (Padhi et al., 2015; Yadav et al., 2023). In the image, the specimen printed in 3% guar gum hydrogel exhibits a relatively compact structure and clearly preserved printing paths (Fig. 15b). Despite small material accumulations along the edges, the core structure of the specimen remains uniform, which facilitates efficient stress transfer.

The reference specimen exhibited moderate values ($R_m = 15.2 \pm 0.36$ MPa). Its surface appears relatively smooth. However, small pores and material heterogeneities are visible, which may initiate local stress concentrations and limit the maximum strength (Fig. 14).

The lowest mechanical properties were observed for specimens printed in 3% agar hydrogel ($R_m = 1.8 \pm 0.20$ MPa, $R_{p0.2} = 0.40 \pm 0.08$ MPa) and HEA hydrogel ($R_m = 2.8 \pm 0.26$ MPa, $R_{p0.2} = 0.60 \pm 0.09$ MPa). The images show a more irregular geometry and significant material accumulation along the edges, indicating lower stability of the printing process in these hydrogels. Such defects lead to increased porosity and structural heterogeneity, which in turn reduces resistance to mechanical loading (Figs. 15c and 15d).

The specimen printed in PVA hydrogel exhibited intermediate values ($R_m = 8.4 \pm 0.36$ MPa, $R_{p0.2} = 3.90 \pm 0.28$ MPa). The deformation of the edges and partial material flow observed in the image suggest reduced stability of the printing paths, which may result in local structural weakening (Fig. 15e).

In summary, the highest mechanical parameters were observed for specimens printed in guar gum hydrogel, which correlates with the most compact and homogeneous printed morphology. In contrast, the lowest values were recorded for agar and HEA, where the observed geometric irregularities and surface defects indicate less stable structural formation conditions during the printing process.



(a) (b) (c) (d) (e)

Figure 15. Model printed in: a) ambient atmosphere, b) 3% guar gum hydrogel, c) 3% agar hydrogel, d) an HEA hydrogel, e) a PVA hydrogel.

For each experimental condition, three independent specimens were tested and the results are presented as mean ± standard deviation (SD). In general, the obtained standard deviations are relatively small compared with the corresponding mean values, indicating good repeatability of the measurements within each experimental group. The lowest variability of the ultimate tensile strength R_m was observed for the agar-based and HEA-based groups, suggesting relatively consistent mechanical response of the specimens prepared in these environments. In contrast, slightly higher dispersion of results was observed for the guar gum and air conditions, although the magnitude of the standard deviations remained moderate relative to the measured mean values.

To evaluate the statistical significance of differences between the investigated printing environments, a one-way analysis of variance (ANOVA) was performed for both mechanical parameters: the yield strength $R_{p0.2}$ and the ultimate tensile strength R_m. The ANOVA analysis confirmed statistically significant differences between the investigated groups for both parameters. For the ultimate tensile strength R_m, the analysis yielded $F(5, 12) = 1013.96$ with $p < 0.001$. Similarly, statistically significant differences were observed for the yield strength $R_{p0.2}$, with $F(5, 12) = 532.6$ and $p < 0.001$. These results indicate that the printing environment significantly affects the mechanical performance of the fabricated structures.

In particular, the guar gum environment produced the highest average R_m value, while the agar and HEA environments resulted in the lowest strength levels. A similar tendency can also be observed for the yield strength $R_{p0.2}$, where the guar gum condition again exhibits the highest average values, whereas the HEA and agar environments show considerably lower values. This indicates that the surrounding medium may significantly affect both the elastic–plastic transition and the ultimate strength of the material.

The geometric parameters of the specimens (a_0, b_0 and S_0) were internally consistent, as the reported cross-sectional areas agree with the measured dimensions and their propagated standard deviations. However, some groups, particularly HEA, agar and PVA, exhibited moderate dimensional scatter, indicating that geometric variability may also contribute to the dispersion of the mechanical results. Although the measured standard deviations of the geometric parameters are relatively small, the visual inspection of the specimens reveals local surface irregularities and edge roughness typical for extrusion-based printing in hydrogel environments. Therefore, the dimensional variability reported here should be interpreted as an approximation of the nominal specimen dimensions rather than a full description of local geometric irregularities. Due to the limited number of specimens tested in each group ($n = 3$), the statistical analysis should be interpreted as indicative rather than fully conclusive. Nevertheless, the observed differences between the investigated printing environments are considerably larger than the within-group variability, suggesting that the reported trends are robust and reflect the influence of the printing medium on the mechanical performance of the printed structures.

5. SUMMARY AND CONCLUSIONS

The objective of the research work presented in this paper was to develop a low-cost 3D printing method implemented in a hydrogel environment and to identify the optimal process parameters and materials enabling stable 3D printing under such conditions.

The conducted studies demonstrated that successful implementation of the printing process in a hydrogel medium requires an appropriate adjustment of the rheological properties of both supporting and printing material. Among the analyzed systems, only guar gum hydrogel at a concentration of 3% wt exhibited a stable viscosity profile and shear-thinning behavior, providing adequate support for the extruded material and enabling the fabrication of structures with good geometric accuracy.

Modification of commercial photopolymer resins through the addition of silica resulted in an increase in viscosity and significant changes in the photopolymerization kinetics. Rheological and photorheological analyses indicated that formulations containing approximately 2–5% wt silica provided the most stable flow properties and a favorable crosslinking process. At the same time, it was confirmed that insufficient dispersion of filler particles may lead to local rheological disturbances and deterioration of print quality.

Mechanical testing revealed that samples produced in guar gum hydrogel achieved the highest tensile strength values, even exceeding those of reference samples fabricated using the DLP method. This result indicates that the hydrogel environment may positively influence the stability of the forming process and the homogeneity of the material structure.

The obtained results confirm that the combination of an appropriately selected hydrogel with modified photocurable resins constitutes a promising platform for 3D printing technologies based on photocurable materials in a supporting medium. The developed method may find applications, among others, in bioprinting, fabrication of structures with complex geometries, processing of materials sensitive to gravity or requiring support during forming, as well as in advanced multi-material 3D printing systems. Future work in this area should focus on scaling the developed method to enable its application in the fabrication of structures with more complex geometries.

ACKNOWLEDGMENTS

The research work was conducted as part of the LIDER XII project (agreement no. LIDER/51/0270/L-12/20/NCBR/2021) titled "Multi-material 3D printer dedicated to production of solid metal and galvanic alloys parts, as well as metal-polymer hybrid elements using developed coupled technology of metal electrodeposition and photopolymerization of polymer resins" funded by the National Centre for Research and Development.

Part of the research work was conducted within the framework of PRELUDIUM project entitled "Kinetic-calorimetric studies of photopolymerization in thin porous layers using new two-component luminescent sensor systems" (contract no. UMO-2021/41/N/ST8/04127) funded by the National Science Center.

SYMBOLS

a_0	initial thickness of the specimen, mm
b_0	initial width of the specimen, mm
E_{steps}	extrusion rate (stepper motor steps per millimeter), –
F	F-statistic value from the analysis of variance (ANOVA), –
G'	storage modulus (elastic behavior of the material), Pa
G''	loss modulus (viscous behavior of the material), Pa
n	number of tested specimens within an experimental group, –
p	probability value for statistical significance assessment, –
R_m	ultimate tensile strength of the polymer specimen, MPa
$R_{p0.2}$	offset yield strength (0.2% plastic strain criteria), MPa
S_0	nominal cross-sectional area of the specimen, mm^2

Abbreviations

DLP	Digital Light Processing
FDM	Fused Deposition Modeling
SLA	Stereolithography
TPO	Diphenyl(2,4,6-trimethylbenzoyl)phosphine oxide

REFERENCES

Alghamdi S.S., John S., Choudhury N.R., Dutta N.K., 2021. Additive manufacturing of polymer materials: progress, promise and challenges. *Polymers*, 13, 753. DOI: 10.3390/polym13050753.

Aredla R., Dasari H.C., Kumar S.S., Pati P.R., 2024. Mechanical properties of natural fiber reinforced natural and ceramic fillers for various engineering applications. *Interactions*, 245, 249. DOI: 10.1007/s10751-024-02109-3.

Bhattacharjee N., Urrios A., Kang S., Folch A., 2016. The upcoming 3D-printing revolution in microfluidics. *Lab Chip*, 16, 1720–1742. DOI: 10.1039/C6LC00163G.

Compaan A.M., Song K., Huang Y., 2019. Gellan fluid gel as a versatile support bath material for fluid extrusion bioprinting. *ACS Appl. Mater. Interfaces*, 11, 5714–5726. DOI: 10.1021/acsami.8b13792.

Dudek P., 2013. FDM 3D printing technology in manufacturing composite elements. *Arch. Metall. Mater.*, 58, 1415–1418. DOI: 10.2478/amm-2013-0186.

Fiedor P., Pilch M., Szymaszek P., Chachaj-Brekiesz A., Galek M., Ortyl J., 2020. Photochemical study of a new bimolecular photoinitiating system for vat photopolymerization 3D printing techniques under visible light. *Catalysts*, 10, 284. DOI: 10.3390/catal10030284.

Hikmat M., Rostam S., Ahmed Y.M., 2021. Investigation of tensile property-based Taguchi method of PLA parts fabricated by FDM 3D printing technology. *Results Eng.*, 11, 100264. DOI: 10.1016/j.rineng.2021.100264.

Hola E., Pilch M., Ortyl J., 2020. Thioxanthone derivatives as a new class of organic photocatalysts for photopolymerisation processes and the 3D printing of photocurable resins under visible light. *Catalysts*, 10, 903. DOI: 10.3390/catal10080903.

Jandt K.D., Sigusch B.W., 2009. Future perspectives of resin-based dental materials. *Dent. Mater.*, 25, 1001–1006. DOI: 10.1016/j.dental.2009.02.009.

Maines E.M., Porwal M.K., Ellison C.J., Reineke T.M., 2021. Sustainable advances in SLA/DLP 3D printing materials and processes. *Green Chem.*, 23, 6863–6897. DOI: 10.1039/D1GC01489G.

Melchels F.P.W., Feijen J., Grijpma D.W., 2010. A review on stereolithography and its applications in biomedical engineering. *Biomaterials*, 31, 6121–6130. DOI: 10.1016/j.biomaterials.2010.04.050.

Murr L.E., 2016. Frontiers of 3D printing/additive manufacturing: from human organs to aircraft fabrication. *J. Mater. Sci. Technol.*, 32, 987–995. DOI: 10.1016/j.jmst.2016.08.011.

Namazi H., 2017. Polymers in our daily life. *BioImpacts*, 7, 73–74. DOI: 10.15171/bi.2017.09.

Ouyang L., Armstrong J.P.K., Lin Y., Wojciechowski J.P., Lee-Reeves C., Hachim D., Zhou K., Burdick J.A., Stevens M.M., 2020. Expanding and optimizing 3D bioprinting capabilities using complementary network bioinks. *Sci. Adv.*, 6, eabc5529. DOI: 10.1126/sciadv.abc5529.

Padhi P.K., Satapathy A., Nakka A.M., 2015. Processing, characterization and wear analysis of short glass fiber-reinforced polypropylene composites filled with blast furnace slag. *J. Thermoplast. Compos. Mater.*, 28, 656–671. DOI: 10.1177/0892705713486142.

Petko F., Galek M., Hola E., Topa-Skwarczyńska M., Tomal W., Jankowska M., Pilch M., Popielarz R., Graff B., Morlet-Savary F., Lalevee J., Ortyl J., 2022. Symmetric iodonium salts based on benzylidene as one-component photoinitiators for applications in 3D printing. *Chem. Mater.*, 34, 10077–10092. DOI: 10.1021/acs.chemmater.2c02796.

Pielichowski J., Puszyński A., 2003. *Technologia tworzyw sztucznych*. Wydawnictwa Naukowo-Techniczne, Warszawa.

Prabhakar M.N., Shah A.U.R., Rao K.C., Song J.-I., 2015. Mechanical and thermal properties of epoxy composites reinforced with waste peanut shell powder as a bio-filler. *Fibers Polym.*, 16, 1119–1124. DOI: 10.1007/s12221-015-1119-1.

Shahrubudin N., Lee T.C., Ramlan R., 2019. An overview on 3D printing technology: technological, materials and applications. *Procedia Manuf.*, 35, 1286–1296. DOI: 10.1016/j.promfg.2019.06.089.

Shiwarski D.J., Hudson A.R., Tashman J.W., Feinberg A.W., 2021. Emergence of FRESH 3D printing as a platform for advanced tissue biofabrication. *APL Bioeng.*, 5, 010904. DOI: 10.1063/5.0032777.

Stansbury J.W., Idacavage M.J., 2016. 3D printing with polymers: challenges among expanding options and opportunities. *Dent.*

Mater., 32, 54–64. DOI: 10.1016/j.dental.2015.09.018.

Szlezyngier W., Brzozowski Z.K., 2012. *Tworzywa sztuczne. Tom 1: Tworzywa ogólnego zastosowania*. Wydawnictwo Oświatowe FOSZE, Rzeszów.

Topa M., Hola E., Galek M., Petko F., Pilch M., Popielarz R., Morlet-Savary F., Graff B., Lalevée J., Ortyl J., 2020. One-component cationic photoinitiators based on coumarin scaffold iodonium salts as highly sensitive photoacid generators for 3D printing IPN photopolymers under visible LED sources. *Polym. Chem.*, 11, 5261–5278. DOI: 10.1039/D0PY00677G.

Warner J.C., Cannon A.S., Dye K.M., 2004. Green chemistry. *Environ. Impact Assess. Rev.*, 24, 775–799. DOI: 10.1016/j.eiar.2004.06.006.

Wu Q., Song K., Zhang D., Ren B., Sole-Gras M., Huang Y., Yin J., 2022. Embedded extrusion printing in yield-stress-fluid baths. *Matter*, 5, 3775–3806. DOI: 10.1016/j.matt.2022.09.003.

Yadav R., Singh M., Shekhawat D., Lee S.-Y., Park S.-J., 2023. The role of fillers to enhance the mechanical, thermal and wear characteristics of polymer composite materials: a review. *Compos. Part A: Appl. Sci. Manuf.*, 175, 107775. DOI: 10.1016/j.compositesa.2023.107775.

Zeng X., Meng Z., He J., Mao M., Li X., Chen P., Fan J., Li D., 2022. Embedded bioprinting for designer 3D tissue constructs with complex structural organization. *Acta Biomater.*, 140, 1–22. DOI: 10.1016/j.actbio.2021.11.048.

Zhao J., He N., 2020. A mini-review of embedded 3D printing: supporting media and strategies. *J. Mater. Chem. B*, 8, 10474–10486. DOI: 10.1039/D0TB01819H.

Zhou K., Sun Y., Yang J., Mao H., Gu Z., 2022. Hydrogels for 3D embedded bioprinting: A focused review on bioinks and support baths. *J. Mater. Chem. B*, 10, 1897–1907. DOI: 10.1039/D1TB02554F.

Chemical and Process Engineering: New Frontiers, 2026, 47(2), e135
DOI: 10.24425/cpe.2026.158133

PERSPECTIVE ARTICLE

Hydrogen and syngas production from methane via thermochemical conversion: a mini review of artificial neural network applications

Robert Cherbański*, Tomasz Kotkowski, Eugeniusz Molga

Warsaw University of Technology, Faculty of Chemical and Process Engineering, Waryńskiego 1, Warsaw, Poland

*** Corresponding author, e-mail:** robert.cherbanski@pw.edu.pl

Chemical Engineering Horizons and Perspectives Article series endorsed by the Scientific Committee on Chemical and Process Engineering of the Polish Academy of Sciences, 2024–2027.

Article info:
Received: 02 April 2026
Revised: 06 May 2026
Accepted: 14 May 2026

Abstract
This mini-review examines the application of artificial neural networks (ANNs) in hydrogen and syngas production from methane via thermochemical conversion processes, including steam methane reforming, dry reforming, methane pyrolysis and partial oxidation of methane. These processes involve complex interactions between thermodynamics, reaction kinetics and transport phenomena. In particular, gaps in the understanding of reaction kinetics limit the effectiveness of conventional modelling approaches. This review highlights how ANNs, particularly multilayer perceptron (MLP) and radial basis function (RBF) networks, provide efficient data-driven alternatives for modelling thermodynamic equilibrium, reaction kinetics, catalyst deactivation (coking and poisoning) and reactor performance. Reported studies demonstrate that ANNs can achieve high predictive accuracy, often outperforming simplified empirical models while significantly reducing computational cost. The influence of key operating variables, such as temperature and feed composition, is identified as critical for process performance. Recent advances emphasize hybrid approaches integrating ANNs with first-principles models, computational fluid dynamics, and microkinetic simulations, including physics-informed and physics-enhanced neural networks. Despite promising results, challenges remain related to limited datasets and model interpretability.

Keywords
artificial neural networks, methane reforming, methane pyrolysis, hydrogen, syngas

1. INTRODUCTION

Carbon dioxide (CO_2) and methane (CH_4) are the two major greenhouse gases (GHGs) emitted by human activities, accounting for approximately 76% and 16% of global emissions, respectively. Current projections based on existing policies suggest that net GHG emissions in the European Union could be reduced by about 47% by 2030 compared with 1990 levels, while additional planned measures may increase this reduction to around 54%. Nevertheless, achieving climate neutrality by 2050 will require further substantial efforts from EU Member States (European Environmental Agency, 2025).

Although methane is widely recognized as a major GHG, it also serves as an important feedstock in chemical and energy-related applications, largely because of its high hydrogen content relative to carbon. In response to the increasing demand for cleaner and hydrogen-oriented energy technologies, significant efforts have been directed toward developing improved methane conversion pathways. Steam methane reforming (SMR, Eq. 1) remains the most established industrial method for syngas generation. However, other processes, including dry reforming (DRM), methane pyrolysis (MP), and partial oxidation (POM), are being increasingly explored as alternative solutions.

$$CH_4 + H_2O \rightleftharpoons CO + 3H_2, \quad \Delta H_r = 205.9 \left[\frac{kJ}{mol}\right] \quad (1)$$

DRM (Eq. 2) offers an environmentally friendly route by consuming CO_2 and CH_4 to produce an equimolar mixture of H_2 and CO, suitable for Fischer-Tropsch synthesis (Taherian et al., 2017), long-chain hydrocarbons, oxo-alcohols (Gadalla and Bower, 1988), and dimethyl ether (DME). MP (Eq. 3) generates H_2 without CO_2 emissions, producing solid carbon as a valuable byproduct for industrial applications, making it a bridge technology toward renewable fuels (Sánchez-Bastardo et al., 2021). POM (Eq. 4) is exothermic and energy-efficient but requires pure oxygen, posing challenges such as hot-spot formation, catalyst sintering, and higher capital costs.

$$CH_4 + CO_2 \rightleftharpoons 2H_2 + 2CO, \quad \Delta H_r = 247.0 \left[\frac{kJ}{mol}\right] \quad (2)$$

$$CH_4 \rightleftharpoons C_{(s)} + 2H_2, \quad \Delta H_r = 75.0 \left[\frac{kJ}{mol}\right] \quad (3)$$

$$CH_4 + 0.5O_2 \rightleftharpoons CO + 2H_2, \quad \Delta H_r = -36.0 \left[\frac{kJ}{mol}\right] \quad (4)$$

Overall, CH_4 conversion processes are inherently complex, involving multiple simultaneous reactions as well as coupled heat, mass, and momentum transfer phenomena. Consequently, their mathematical modelling is challenging, requiring the integration of detailed kinetic mechanisms, reactor hydrodynamics, and thermodynamic constraints.

Thermodynamics, in particular, plays an important role in determining the equilibrium compositions of gas and solid phases,

© 2026. The Author(s). This is an open-access article distributed under the terms of the Creative Commons Attribution (CC-BY 4.0, https://creativecommons.org/licenses/by/4.0/), which permits unrestricted use, distribution, and reproduction in any medium, provided the original author and source are credited.

which is essential for process design, optimization, and identifying the fundamental thermodynamic limits of CH_4 conversion. Reaction kinetics, especially when detailed mechanisms are involved, is also highly demanding. Accurate modelling requires the determination of rate constants and activation energies for multiple elementary reactions, as well as careful consideration of adsorption, surface reactions, activation processes, intermediate species, and catalyst behaviour.

Additionally, kinetic models usually need to be coupled with transport phenomena, accounting for heat and mass transfer to accurately predict reactor performance under real operating conditions. Often, multiscale modelling is necessary to integrate molecular-level reaction information with reactor-scale hydrodynamics.

To the best of our knowledge, no studies have provided a comprehensive overview of ANN applications in hydrogen and syngas production from methane via thermochemical conversion. This work aims to fill that gap.

2. ARTIFICIAL NEURAL NETWORKS

To overcome the abovementioned challenges, various machine learning (ML) techniques have been applied. In particular, ANNs constitute a class of parametric nonlinear models widely used in supervised learning tasks that require approximation of complex input-output relationships (Cybenko, 1989; Hornik et al., 1989). ML methods are generally categorized into supervised, unsupervised, semi-supervised and reinforcement learning, however, supervised approaches are of primary relevance in this work because they enable predictive modelling from labelled datasets. Common supervised techniques include regression models, classification algorithms such as decision trees and support vector machines, ensemble learning methods and ANN architectures including convolutional and recurrent neural networks. It is also worth noting that recent developments in physics-informed neural networks (PINNs) offer a promising hybrid approach by embedding thermodynamic or kinetic constraints into machine-learning models. Such methods may improve interpretability, reduce data requirements, and enhance predictive robustness, particularly for complex chemical process systems.

In the feedforward ANN architecture considered here in more detail, neuron outputs are computed as weighted transformations of inputs followed by nonlinear activation functions. For a multilayer perceptron (MLP) with a single hidden layer, the network output can be expressed as

$$\begin{aligned}\text{outputs} = y_k &= \sigma_2\left(\sum_{i=0}^{K} w_{ki}^{e} v_i\right) \\ &= \sigma_2\left(\sum_{i=0}^{K} w_{ki}^{e}\sigma_1\left(\sum_{j=0}^{N} w_{ij}^{h} x_j\right)\right)\end{aligned} \tag{5}$$

where: x_j is the *j-th* input signal, w_{ij}^{h} are weights connecting the input layer to hidden neurons, w_{ki}^{e} are weights connecting hidden neurons to outputs, v_i represents hidden layer activations, σ_1 and σ_2 are activation functions (Eqs. 6–7). A schematic representation of this architecture is shown on the left in Figure 1.

The hidden layer may employ, for example, the bipolar sigmoidal activation function (Alsaffar et al., 2020; Cherbański et al., 2026a)

$$\sigma_1(S) = \tanh(S) \tag{6}$$

which introduces nonlinearity while keeping differentiability required for gradient-based optimization. The output layer uses a linear activation

$$\sigma_2(S) = S \tag{7}$$

Network parameters are estimated by minimizing a loss function, typically the mean squared error (MSE):

$$E = E\left(\vec{w}\right) = \frac{1}{P}\sum_{p=1}^{P}\sum_{k=1}^{M}\left(y_k^{(p)} - d_k^{(p)}\right)^2 \tag{8}$$

where P denotes the number of samples, M is the number of output neurons, $y_k^{(p)}$ is the network prediction, and $d_k^{(p)}$ is the corresponding target value. Optimization is generally performed using backpropagation combined with gradient-based algorithms.

Apart from MLPs, another class of feedforward ANNs, called Radial Basis Function (RBF) networks, is also often used (Figure 1). RBF networks employ a nonlinear transformation of the input data by introducing a layer of hidden neurons based on a radially varying function centred around a priori selected centres. The output of the hidden layer is calculated using the following expression:

$$v_i = \sigma_1\left(\left\|\vec{x} - \vec{c}_i\right\|\right) \tag{9}$$

where $\left\|\vec{x} - \vec{c}_i\right\|$ means the distance between input vector data $\vec{x}$ and centroid vector $\vec{c}_i$ estimated by k-mean algorithm (unsupervised learning method), σ_1 is the similarity function (kind of radial basis function), often defined as Gaussian density probability function

$$\sigma_1(S) = \frac{1}{s\sqrt{2\pi}} e^{-\frac{(S-\mu)^2}{2s^2}} \tag{10}$$

where $S \equiv \left\|\vec{x} - \vec{c}_i\right\|$, μ is the mean input vector, s represents its standard deviation. The output layer is described by (7) and the output is given by

$$\begin{aligned}\text{outputs} = y_k &= \sigma_2\left(\sum_{i=0}^{K} w_{ki}^{e} v_i\right) \\ &= \sigma_2\left(\sum_{i=0}^{K} w_{ki}^{e}\sigma_1\left(\left\|\vec{x} - \vec{c}_i\right\|\right)\right)\end{aligned} \tag{11}$$

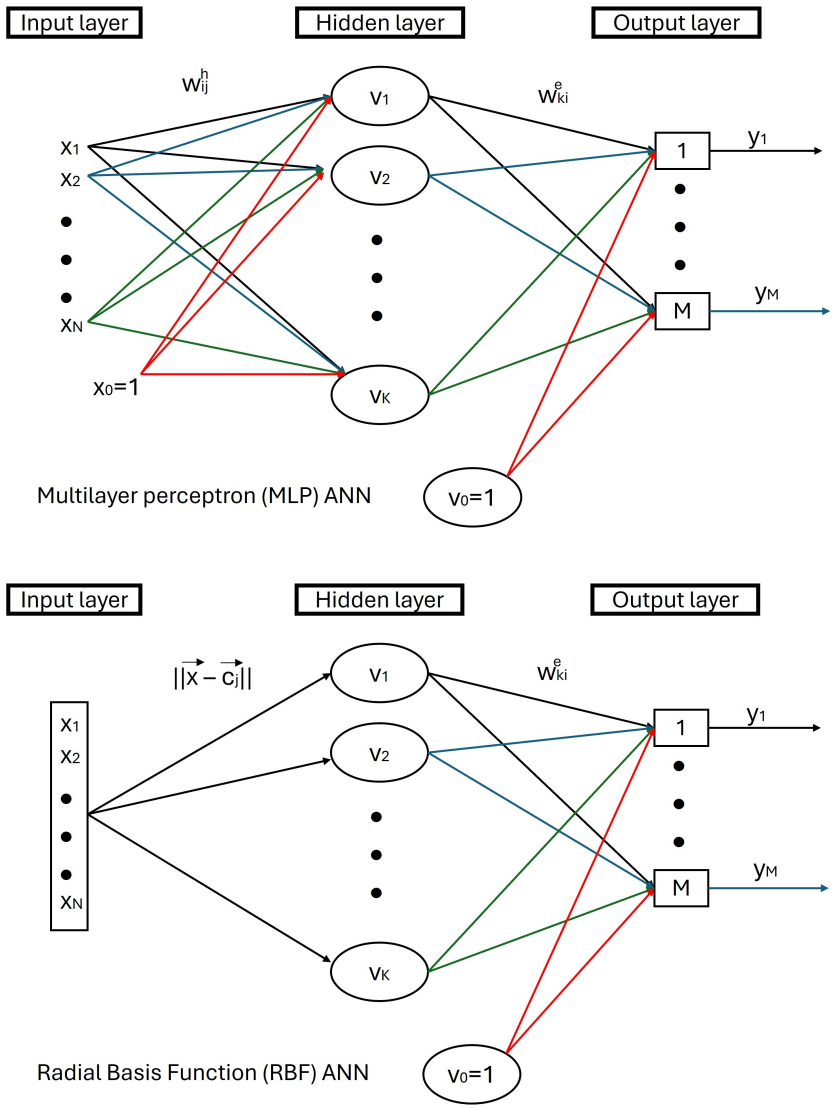


Figure 1. Structures of MLP (left) and RBF (right) ANNs.

RBF networks offer several advantages over MLPs, particularly in their ability to model nonlinear functions using a single hidden layer, whereas MLPs often require more complex architectures. In addition, RBF networks can be trained significantly faster than MLPs and may achieve higher accuracy for localized, well-clustered datasets. However, their performance tends to deteriorate when the data are sparse, scattered, or when the training set is limited in size.

From a theoretical perspective, the approximation capability of both RBF and MLP networks is supported by the universal approximation theorem (Cybenko, 1989; Hornik et al., 1989), which states that feedforward neural networks with at least one hidden layer and a non-polynomial activation function can approximate any continuous function on a compact domain to arbitrary accuracy, provided a sufficient number of hidden units is available.

Despite this strong theoretical foundation, the practical performance of ANNs depends critically on the quality and representativeness of the training data. In particular, while ANNs can interpolate complex nonlinear relationships effectively, their ability to extrapolate beyond the range of the training data is limited and may lead to unreliable predictions.

ML model performance is frequently evaluated using k-fold cross-validation (CV), a robust technique that utilizes the entire dataset to provide a reliable estimate of model generalization. This method is particularly effective at mitigating the risk of overfitting, a common challenge in training ANNs. The procedure involves splitting the dataset into k equal-sized subsets (i.e. folds). The model is then trained and validated in k iterations; in each cycle, $k-1$ folds are used for model training, while the remaining fold is used for validation. The choice of the parameter k depends on the size and nature of the dataset. For large datasets, a lower value, such as $k=3$, is often selected to minimize computational costs and the number of training iterations. For small datasets, larger values of k are typically preferred to ensure that the model is trained on a sufficiently large portion of the data

in each iteration. The strategy used for the data splitting is of equal importance, especially if the samples are sorted by class within the original dataset. To optimize the effectiveness of the method, stratification should be employed. This technique ensures that the proportion of individual classes in each validation fold remains approximately consistent with the distribution in the entire training set.

Network performance is frequently checked using the following parameters:

- Root Mean Squared Error (RMSE)

$$\mathrm{RMSE} = \sqrt{\frac{1}{PM}\sum_{p=1}^{P}\sum_{i=1}^{M}\left(y_i^{(p)} - d_i^{(p)}\right)^2} \tag{12}$$

- Mean Absolute Error (MAE)

$$\mathrm{MAE} = \frac{1}{PM}\sum_{p=1}^{P}\sum_{i=1}^{M}\left|y_i^{(p)} - d_i^{(p)}\right| \tag{13}$$

- Determination coefficient $\boldsymbol{R^2}$

$$R^2 = 1 - \frac{\sum_{p=1}^{P}\sum_{i=1}^{M}\left(y_i^{(p)} - d_i^{(p)}\right)^2}{\sum_{p=1}^{P}\sum_{i=1}^{M}\left(d_i^{(p)} - \overline{d}\right)^2} \tag{14}$$

where the mean value of destination is defined as follows

$$\overline{d} = \frac{1}{PM}\sum_{p=1}^{P}\sum_{i=1}^{M} d_i^{(p)} \tag{15}$$

- Standard Error of the Estimate (SEE)

$$\mathrm{SEE} = \sqrt{\frac{1}{(P-k)M}\sum_{p=1}^{P}\sum_{i=1}^{M}\left(y_i^{(p)} - d_i^{(p)}\right)^2} \tag{16}$$

where k is the number of estimated parameters.

- t-Student test a parametric statistical test used to compare the means of two groups (calculated output value and destination) to see whether the differences are statistically significant or due to chance.

Throughout this article, the terms *small* and *large* dataset are used. In the context of this work small datasets refer to studies containing fewer than approximately 100–200 samples, which is typical for experimental kinetic investigations with limited measurements (e.g. 27–75 patterns in several DRM studies in Table 3), while large datasets refer to datasets exceeding 1000 samples, typically derived from extensive literature databases, simulations or industrial-scale modelling (e.g. 2200+ samples in thermodynamic and process modelling studies in Table 3 and Table 4).

3. THERMODYNAMICS AND REACTION KINETICS

3.1. ANN of thermodynamic equilibrium modelling

Several studies have investigated the thermodynamic equilibrium for SMR (Ahmad et al., 2022; Ahmad et al., 2025; Demidov et al., 2011; Di Nardo et al., 2024; Jabbour, 2020), DRM (Ahmad et al., 2022; Ahmad et al., 2025; Demidov et al., 2011; Jabbour, 2020; Jensen and Duyar, 2021), POM (Ahmad et al., 2022; Ahmad et al., 2025; Zhu et al., 2001) and MP (Ahmad et al., 2022; Ahmad et al., 2025; Guéret et al., 1997) using the conventional Gibbs free energy minimization approach. In addition, equilibrium analyses have been extended to steam reforming of liquid fuels such as methanol (Di Nardo et al., 2024; Faungnawakij et al., 2006), ethanol (Di Nardo et al., 2024; Lima da Silva et al., 2009; Rossi et al., 2009), glycerol (Adhikari et al., 2007; Di Nardo et al., 2024; Ismaila et al., 2021; Rossi et al., 2009), as well as coal gasification (Ahmad et al., 2025; Shabbar and Janajreh, 2013).

While the Gibbs minimization method is well established and widely applied, data-driven approaches may offer advantages, particularly when rapid predictions or integration of equilibrium calculations into CFD simulations is required. Although ANNs have been successfully employed for modelling liquid-liquid and vapour-liquid equilibria (Carranza-Abaid et al., 2023; Del-Mazo-Alvarado and Bonilla-Petriciolet, 2022; Nguyen et al., 2007; Piotrowski et al., 2003; Reynel-Ávila et al., 2019), their application to equilibrium prediction in CH_4-based thermochemical conversion processes remains limited. For example, ANNs were used to model the steam reforming of naphthalene, using datasets generated from thermodynamic equilibrium calculations (Igwegbe et al., 2021). The models accurately captured the effects of temperature and steam-to-oil ratio on product selectivity, yielding R^2 values above 0.99 and RMSE values below 1 mol% for all datasets.

To address this gap, ANNs were applied to predict equilibrium gas composition and carbon formation in MP and various reforming processes (Cherbański et al., 2026a). In that study, equilibrium compositions for MP, DRM, SMR and POM were first calculated using Gibbs free energy minimization. The analysis considered the principal gaseous species (CH_4, CO_2, H_2, CO, H_2O, O_2 and N_2), as well as solid carbon, enabling the prediction of gas-phase compositions together with the equilibrium amount of solid carbon formed. Non-ideal gas behaviour was accounted for using the Peng-Robinson equation of state, while thermodynamic properties were obtained from standard databases and literature correlations. The minimization was performed subject to elemental mass balance constraints and non-negativity of species amounts. Model predictions were validated against literature equilibrium data for MP, showing very good agreement over a range of temperatures and pressures.

ANNs were then employed as data-driven models to predict equilibrium gas compositions and carbon yield in the above-mentioned processes. The input variables included feed composition expressed as molar ratios (CO_2/CH_4, H_2O/CH_4, O_2/CH_4), temperature, and pressure, which together define the thermodynamic state of the system (Table 1). The outputs comprised the mole fractions of the main gaseous species (CH_4, CO_2, CO, H_2, H_2O) and the carbon yield, enabling simultaneous assessment of gas-phase composition and carbon formation.

A feedforward ANN with a single hidden layer was adopted in the computations, as such architectures are generally sufficient to approximate nonlinear thermodynamic relationships while maintaining model simplicity. The network was trained using datasets generated from Gibbs free energy minimization calculations across a wide range of operating conditions. Separate validation and testing datasets were used to assess predictive accuracy and minimize overfitting.

The ANN predictions generally showed excellent agreement with equilibrium calculations, particularly for gaseous species, although slightly lower accuracy was observed for carbon yield, likely due to its stronger sensitivity to process conditions (Figure 2).

Compared with simpler data-driven approaches such as third-, fourth-, and fifth-order polynomials, ANNs provided superior predictive performance while retaining significantly lower computational cost than full thermodynamic calculations. This confirms that ANNs can be readily integrated into process optimization and control frameworks, where rapid prediction of equilibrium compositions enables dynamic adjustment of operating parameters. However, their reliability depends on the quality and representativeness of the training data, and extrapolation beyond the training domain remains a limitation.

3.2. ANN modelling of reaction kinetics

Several studies have demonstrated the effectiveness of ANNs in modelling and predicting reaction kinetics in various methane reforming processes. For example, the complex kinetics of tri-reforming of methane (TRM), integrating DRM, SMR, and POM, were investigated (de Souza et al., 2025). The developed ANN model accurately predicted CH_4 conversion across a wide range of experimental conditions, identifying reaction temperature as the most influential operational parameter. Analysis of the complete dataset showed that operational variables accounted for 68.5% of the total relative importance, with temperature being the dominant factor, whereas catalyst preparation variables contributed 31.5%. The model was trained using 6,700 experimental data points collected from the literature, involving Ni-based catalysts. Input variables included Ni content (wt.%), reaction temperature, and feed molar ratios (CO_2/CH_4, H_2O/CH_4, and O_2/CH_4), while CH_4 conversion served as the output variable. The network architecture, training strategy, and performance metrics are summarized in Table 3. Model validation using previously unseen data demonstrated strong predictive capability and generalization. The reported RMSE values for DRM, SRM, POM, and the combined TRM process were 3.44%, 2.20%, 1.61%, and 4.48%, respectively, confirming the robustness of the approach. Importantly, the study demonstrated that datasets from individual reforming reactions can be integrated to evaluate the overall TRM process, thereby facilitating catalyst formulation and targeted material screening.

The application of ANNs was explored for modelling syngas production from DRM over a $Ni/CaFe_2O_4$ catalyst (Hossain et al., 2016). The MLP and RBF network architectures were employed to model experimental data. The ANN models were

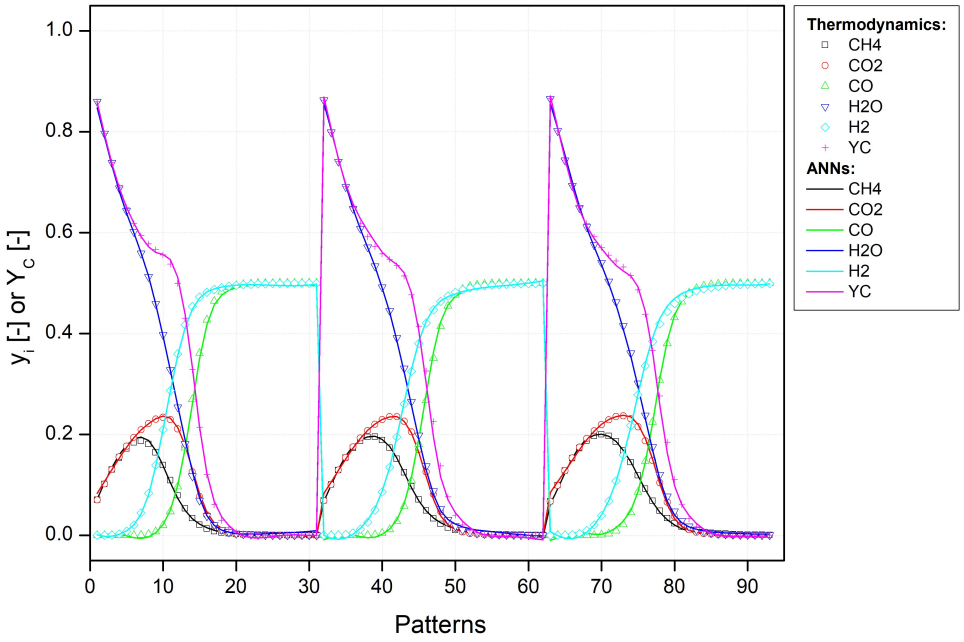


Figure 2. Comparison of the ANN predictions and targets for testing set No. 2.2 (see Table 1) (Cherbański et al., 2026a).

Table 1. List of training and test sets. Bold font indicates the interpolated domain (Cherbański et al., 2026a).

No	Training/ Testing	$\frac{n_{CO2}}{n_{CH4}}$	$\frac{n_{H2O}}{n_{CH4}}$	$\frac{n_{O2}}{n_{CH4}}$	T [°C]	P [bar]
1.	Training	0 (MP)	0	0	[0, 50, 100, . . . , 1500]	[1, 3, 5]
		0.25 (DRM)	0	0		
		0.5 (DRM)	0	0		
		0.75 (DRM)	0	0		
		1 (DRM)	0	0		
		1.25 (DRM)	0	0		
		1.5 (DRM)	0	0		
		1.75 (DRM)	0	0		
		2 (DRM)	0	0		
		0	0.25 (SMR)	0		
		0	0.5 (SMR)	0		
		0	0.75 (SMR)	0		
		0	1 (SMR)	0		
		0	1.25 (SMR)	0		
		0	1.5 (SMR)	0		
		0	1.75 (SMR)	0		
		0	2 (SMR)	0		
		0	0	0.1 (POM)		
		0	0	0.2 (POM)		
		0	0	0.3 (POM)		
		0	0	0.4 (POM)		
		0	0	0.5 (POM)		
		0	0	0.6 (POM)		
		0	0	0.7 (POM)		
2.1	Testing – interpolation	0 (MP)	0	0	[**25**, **75**, **125**, . . . , **1500**]	[1, 3, 5]
2.2		1 (DRM)	0	0		
2.3		0	1 (SMR)	0		
2.4		0	0	0.5 (POM)		
3.1	Testing – interpolation	0 (MP)	0	0	[0, 50, 100, . . . , 1500]	[**2**, **4**]
3.2		1 (DRM)	0	0		
3.3		0	1 (SMR)	0		
3.4		0	0	0.5 (POM)		
4.1	Testing – interpolation	**0.875 (DRM)**	0	0	[0, 50, 100, . . . , 1500]	[1, 3, 5]
4.2		0	**1.125 (SMR)**	0		
4.3		**0**	**0**	**0.45 (POM)**		
5.1	Testing – interpolation	**0.875 (DRM)**	0	0	[**25**, **75**, **125**, . . . , **1500**]	[**2**, **4**]
5.2		0	**1.125 (SMR)**	0		
5.3		0	0	**0.45 (POM)**		

developed using catalyst metal loading (5–15 wt.%), feed molar ratio (0.4–1.0), and reaction temperature as input variables, while the H_2 and CO yields as well as the CH_4 and CO_2 conversions were defined as output parameters. The predictive capabilities of the MLP- and RBF-based models were statistically evaluated and compared. The MLP model demonstrated superior performance, achieving higher coefficients of determination. The statistical analysis was also performed using a *t*-test on the predicted outputs, where the *t*-statistic quantified the difference between predicted and experimental mean values relative to data variability, and the resulting low *p*-values ($p < 0.005$) indicated that these differences were not due to random variation. This confirmed the higher predictive accuracy and statistical significance of the MLP model relative to the RBF approach. Overall, their findings indicated that the MLP architecture provided a more reliable tool for modelling syngas production from DRM over a $Ni/CaFe_2O_4$ catalyst, supporting its applicability in catalyst performance evaluation and process optimization.

Syngas production via DRM over a ceria-supported cobalt catalyst was investigated using a hybrid experimental-modelling approach combining ANNs with a Box-Behnken design (Ayodele and Cheng, 2015). Experimental data obtained from a fixed-bed reactor were used to evaluate the effects of reaction temperature, CH_4 partial pressure, and reactant feed ratio on CH_4 and CO_2 conversions. The ANN model was trained to capture the nonlinear relationships between operating variables and conversions, showing good agreement between predicted and experimental results. Integration of ANN with response surface methodology enabled process optimization, identifying optimal conditions at 728 °C, a CH_4 partial pressure of 46.85 kPa, and a feed ratio of 0.60, corresponding to CH_4 and CO_2 conversions of 74.84% and 76.49%, respectively. The study demonstrated that data-driven models can effectively support optimization of dry reforming systems without relying on detailed mechanistic kinetic formulations.

ANNs were further applied to model the kinetics of CO-rich hydrogen production during DRM over a Co/Pr_2O_3 catalyst (Ayodele et al., 2019). Experimental data obtained from 50 runs designed using a central composite experimental design were used to train the neural network. Reaction temperature as well as the partial pressures of CH_4 and CO_2 were considered as input variables, while the production rates of H_2 and CO were defined as the network outputs. A feedforward MLP architecture with a single hidden layer was implemented, and several training algorithms were evaluated, including the Levenberg-Marquardt, Bayesian regularization, and scaled conjugate gradient methods. The optimal network architectures were determined by minimizing MSE for hidden layers containing between 1 and 20 neurons. The developed ANN models demonstrated high predictive accuracy, with coefficients of determination exceeding 0.9 and strong correlation between predicted and experimental production rates. Among the evaluated training approaches, Bayesian regularization provided the best overall performance, yielding the lowest prediction error and improved model generalization. The study confirmed that ANN-based models can effectively capture the nonlinear relationships between reaction conditions and syngas production rates in DRM systems, providing a practical computational tool for analysing catalytic performance and supporting process optimization.

ANNs were employed to calibrate and improve the reliability of a kinetic model describing the steam reforming of naphtha compounds (hexane and heptane) over a NiMgAl catalyst synthesized from hydrotalcite-derived precursors (Morlanés et al., 2022). Multiple approaches were explored to identify the most accurate kinetic representation and to evaluate its robustness. The developed models incorporate key reactions such as hydrocarbon steam reforming, the water-gas shift reaction, and methanation. The model was validated across a broad spectrum of operating conditions using both simplified and real feedstocks, including methane, naphtha, diesel, and vegetable oil. The results demonstrate the effectiveness of ANNs in analysing complex reaction networks. Furthermore, the proposed kinetic framework can serve as a valuable tool for simulating process strategies and supporting the scale-up of reforming systems for hydrogen production.

Response Surface Methodology (RSM) and Radial Basis Function Neural Network (RBFNN) were employed to investigate and optimize the molecular dynamics of DRM over a novel Ni–Sr–Zr–Al (5Ni+3Sr/10Zr+Al) catalyst (Gendy et al., 2024). To assess how key operating parameters, namely hourly space velocity, reaction temperature, and the CO_2/CH_4 molar ratio, affect conversion efficiency and product distribution, optimal process conditions were predicted. In this context, ANN significantly outperformed RSM in terms of predictive accuracy.

3.3. ANN modelling of catalyst deactivation by coking

Predicting catalyst coking under varying operational conditions remains a significant challenge in various CH_4 conversion processes. The complex interplay of factors influencing coking mechanisms makes conventional modelling approaches inadequate. To overcome this, ANNs have emerged as powerful computational tools for forecasting catalyst performance, including coking behaviour, by learning nonlinear relationships from experimental data.

Data-driven approaches for catalyst coking are still relatively rare. Most studies focus on predicting the effect of operating conditions on the final mass of carbon deposits. For example, a full factorial experimental design was employed to systematize and evaluate the effects of the CH_4/CO_2 molar ratio, reaction temperature, and N_2 flow rate on carbon deposition (Alsaffar et al., 2020). Experimental data from 170 runs were used to develop and compare two ANN architectures: MLP and RBF. Both models were trained to predict carbon deposition per gram of catalyst. Optimization of the hidden layer

resulted in 16 and 20 neurons for the MLP and RBF models, corresponding to network architectures of 3-16-1 and 3-20-1, respectively. Statistical analysis demonstrated that the RBF provided superior predictive performance under both above- and below-stoichiometric conditions. For the MLP model, MSE values of 0.048 and 0.00285 were obtained, with corresponding R^2 values of 0.945 and 0.965. In contrast, the RBF achieved lower MSE values of 0.0073 and 0.00015, with R^2 values of 0.987 in both cases, indicating improved accuracy and robustness. Based on these results, the RBF was identified as the more reliable predictor of carbon deposition during hydrogen-rich syngas production via DRM. Furthermore, analysis of input variable importance revealed that the dominant factor influencing carbon deposition depended on the stoichiometric regime: reaction temperature was the most influential parameter under above-stoichiometric conditions, whereas the CH_4/CO_2 ratio had the greatest impact under below-stoichiometric conditions.

Both MLP and RBF ANN models were developed to predict carbon deposition during DRM under varying temperatures, N_2 flow rates, and CH_4/CO_2 molar ratios (Fang et al., 2025). The results indicated that the RBF network outperformed the MLP model in terms of predictive accuracy. To improve model reliability and reduce the risk of overfitting, k-fold cross-validation was applied for hyperparameter optimization and model selection. Their work has further highlighted the challenges associated with limited datasets, which are common in catalytic research due to experimental cost and time constraints. In one comparative study, MLP and RBF ANNs were evaluated across multiple random train-test splits to assess performance stability. The RBF architecture consistently demonstrated superior accuracy and robustness. To address the instability introduced by random data partitioning in small-sample regimes, a structured k-fold cross-validation framework was implemented, leading to the development of an optimized RBF model. The improved model achieved high predictive performance on unseen data (MSE = 0.0018, R^2 = 0.9882), with substantial reductions in prediction error and improved explanatory power relative to repeated random validations.

A more comprehensive approach to modelling catalyst deactivation was presented by Kumbhat et al. (2024), who developed ML models to predict the performance of Ni-based catalysts during both steam and dry reforming of biogas containing trace amounts of H_2S. In contrast to studies focusing solely on carbon deposition, this work addressed the combined effects of carbon formation and sulphur poisoning, which together govern catalyst deactivation under realistic reforming conditions. The authors compiled experimental datasets from several literature sources covering a wide range of operating parameters, including temperature, CH_4/CO_2 ratio, H_2O/CH_4 ratio, weight hourly space velocity, and H_2S concentration in the feed gas. In addition to operating variables, the models also incorporated catalyst properties such as BET surface area, pore volume, pore size, nickel loading, metal dispersion, and Ni crystal size. Two ML algorithms were evaluated: ANNs and random forests (RF). The models were trained to predict reactor outlet compositions and reactant conversions, including CH_4 and CO_2 conversions as well as mole fractions of H_2, CO, CH_4, and CO_2. The results demonstrated that the RF model provided superior predictive accuracy compared to the ANN, achieving a mean overall R^2 of 0.979 and significantly lower prediction errors. Furthermore, the trained RF model successfully captured transient catalyst deactivation behaviour associated with the introduction of H_2S in the feed stream and was able to generalize to new experimental conditions after limited fine-tuning using a small subset of additional data. These findings highlight the potential of ML techniques not only for predicting carbon deposition but also for modelling more complex catalyst deactivation mechanisms arising from multiple interacting processes during methane reforming.

There is growing interest in the use of Solid Oxide Fuel Cells (SOFCs) powered by hydrocarbon fuels. One of the main challenges in enhancing steam reforming processes is expanding the operational window while minimizing carbon deposition. Such improvements can be achieved through modifications to the design of conventional nickel-based catalysts. In this context, a two-layer feedforward ANN trained via the backpropagation algorithm was employed to capture the influence of process parameters on methane reforming over $LaNi_xAl_{1-x}O_3$ (x = 0.1–0.9) (Ciou et al., 2007). The developed ANN model successfully described the relationship between catalytic performance and the structural properties of the catalyst.

Syngas production via DRM over $La_{1-x}Ce_xNi_{1-y}Fe_yO_3$ (x, y = 0–0.4) perovskite catalysts has been investigated (Abedini et al., 2018). A set of catalysts with varying compositions was designed using a central composite design (CCD) approach and synthesized through a sol-gel auto-combustion method. An ANN was employed to establish the relationship between both preparation and operating parameters and the catalytic performance in the DRM process. The input variables included nickel and lanthanum molar fractions, calcination temperature, and reaction temperature, while methane conversion was treated as the output variable. The optimal ANN architecture consisted of nine neurons in the hidden layer, providing accurate predictions of methane conversion. Subsequently, a genetic algorithm (GA) was applied to identify the optimal catalyst preparation conditions aimed at maximizing methane conversion.

Recent work further demonstrates that ANNs can accurately forecast the time evolution of coking on Fe/C catalysts during MP (Cherbański et al., 2026b). Experimental data on catalyst coking evolution during MP were collected using TGA under high-purity CH_4 and N_2 flows. Measurements were conducted between 850–950 °C on ~10 mg samples of Fe/C catalyst (L'hospital et al., 2024; 2025). Each measurement included three stages: (i) heating under N_2, (ii) ramping to set temperature, and (iii) isothermal coking. Several experiments

at various temperatures were analysed, with baseline corrections applied. Thermograms of catalyst mass versus time were processed using spline interpolation with 15 s interval. The relative catalyst mass during coking was recalculated assuming 100% mass at the start of CH_4 exposure. ANNs of various architectures were trained on the thermogravimetric data to forecast coking behaviour. Input data were prepared using a sliding-window approach and normalized to $[0, 1]$ (Figure 3).

Feedforward networks with up to three hidden layers were evaluated using the Levenberg-Marquardt algorithm, with performance assessed by a weighted sum of squared errors across training, validation, and test datasets. Multi-step forecasting was performed by recursively feeding predicted outputs back into the input windows. MATLAB scripts automated preprocessing, windowing, and network training, exploring over 1,000 network architectures (Table 2).

Figure 4 shows the evolution of Fe/C catalyst coking during MP. As expected from Arrhenius-type behaviour, the coking rate increases with temperature. Note that minor deviations at the lowest temperatures after ∼25 minutes, which are likely due to experimental noise, were retained for ANN training to maintain realistic conditions.

Table 2. Tested ANN architectures and parameters for the sliding-window approach. The structure $x : y : z$ represents the initial number of neurons : the increment : the final number of neurons.

Window size	Number of nodes in the first hidden layer	Number of nodes in the second hidden layer	Number of nodes in the third hidden layer
2	1 : 1 : 10	1 : 1 : 10	0 : 1 : 10
3	1 : 1 : 10	1 : 1 : 10	0 : 1 : 10
5	1 : 1 : 15	1 : 1 : 15	0 : 1 : 15
7	1 : 1 : 15	1 : 1 : 15	0 : 1 : 15
10	1 : 1 : 25	1 : 1 : 15	0 : 1 : 15

Various feedforward ANN architectures were trained using sliding-window input data. Overall, selected networks demonstrated excellent performance across training, validation, and test datasets, accurately capturing the coking dynamics. Single-step forecasts closely matched experimental thermogravimetric profiles, highlighting the robustness and generalization capability of the ANNs. However, multi-step forecasting proved more challenging. Some architectures showed unstable predictions at lower temperatures, with small errors propagating and amplifying over time, causing oscillations

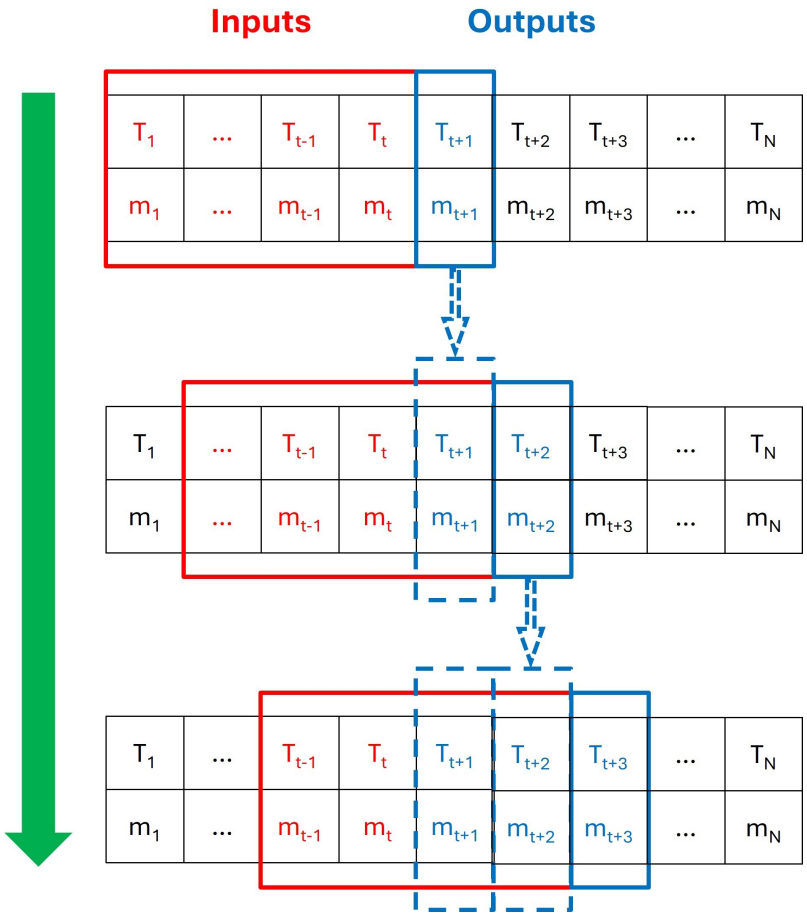


Figure 3. Illustration of a sliding window technique (solid lines) during preparation of training data (solid lines), and multi-step forecasting during predicting mode (solid and dashed lines) (Cherbański et al., 2026b).

around the experimental mass profiles. In contrast, ANN models trained with larger window sizes and optimized architectures produced reliable multi-step predictions across the full temperature range. For instance, an ANN with a window size of 10 and a 4-2-15 hidden layer structure accurately captured both training and test datasets (Figure 5), including

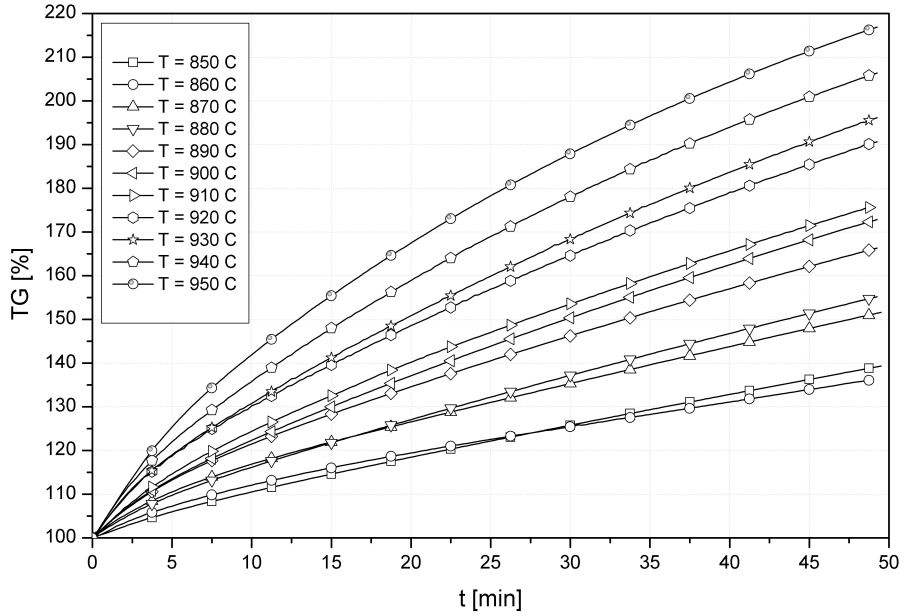


Figure 4. TGA of the Fe/C catalyst coking during methane pyrolysis at varying temperatures (Cherbański et al., 2026b).

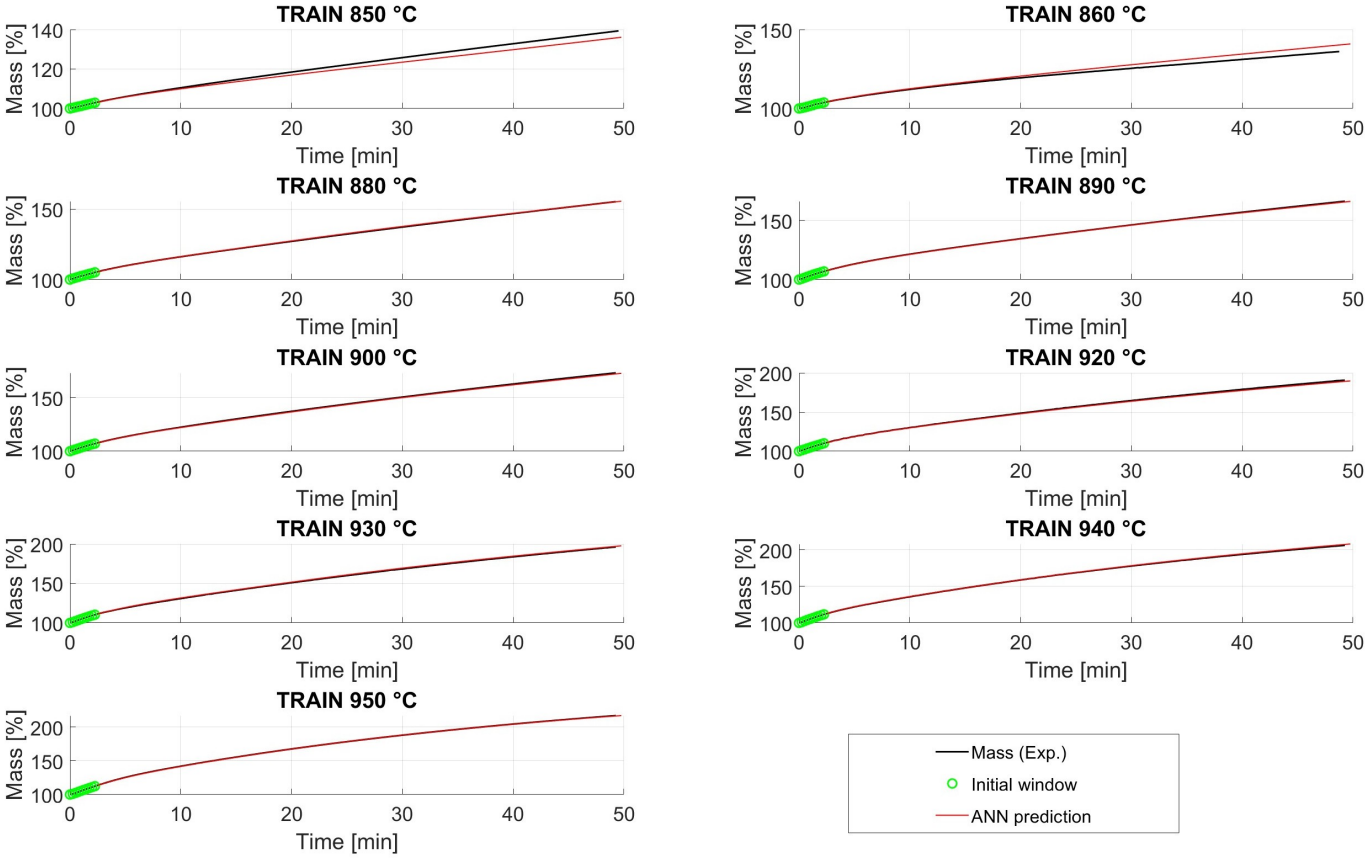


Figure 5. Results of the prediction phase using the training set: comparison between experimental relative mass profiles with those predicted by the ANN with a window size of 10 and a hidden layer structure of 4-2-15. The predictions start from the beginning (∼ 0 min) (Cherbański et al., 2026b).

temperatures not included in training, demonstrating strong generalization (Figure 6). Minor deviations at the lowest temperatures were attributed to experimental noise rather than model limitations.

These results indicate that ANN-based models can reliably forecast catalyst coking behaviour during MP, provided that appropriate network architectures and input preprocessing strategies are used. The study also highlights the importance of considering error propagation in multi-step forecasts and confirms that larger window sizes improve the stability and accuracy of long-term predictions.

The diversity of ANN approaches applied to thermodynamic and reaction kinetics modelling, including differences in data sources, network architectures and validation strategies, is summarized in Table 3.

4. REACTOR AND PROCESS PERFORMANCE MODELLING

ANNs have also been widely applied in reactor and process performance modelling. A summary of these studies, including industrial and simulation-based approaches, is presented in Table 4.

An ANN model was developed to predict the outlet gas composition in SMR (Pizoń et al., 2024a). The model was designed to estimate the molar fractions of H_2, CH_4, CO, and CO_2 as functions of five operational variables: reaction temperature, steam-to-methane ratio (H_2O/CH_4), nitrogen-to-methane ratio, inlet methane flow rate, and nickel catalyst mass. To overcome the limited availability of experimental data (72 original measurements), the authors implemented a weighted data augmentation strategy combining replicated experimental records, spline-interpolated data, and an extensive theoretical dataset generated from a kinetic model fitted via a GA.

The final training dataset consisted of 729 weighted experimental records, 305 interpolated records, and 9,441 theoretically generated samples. After normalization to the range $[0, 1]$, multiple ANN architectures were systematically evaluated. The optimal model comprised three hidden layers with a 6-8-6 neuron configuration and was trained using the BFGS Quasi-Newton backpropagation algorithm for 6,000 epochs. The selected architecture achieved a MSE of 0.00022, with a Pearson correlation coefficient of 0.97 and a Spearman correlation coefficient of 1.00, indicating excellent predictive performance.

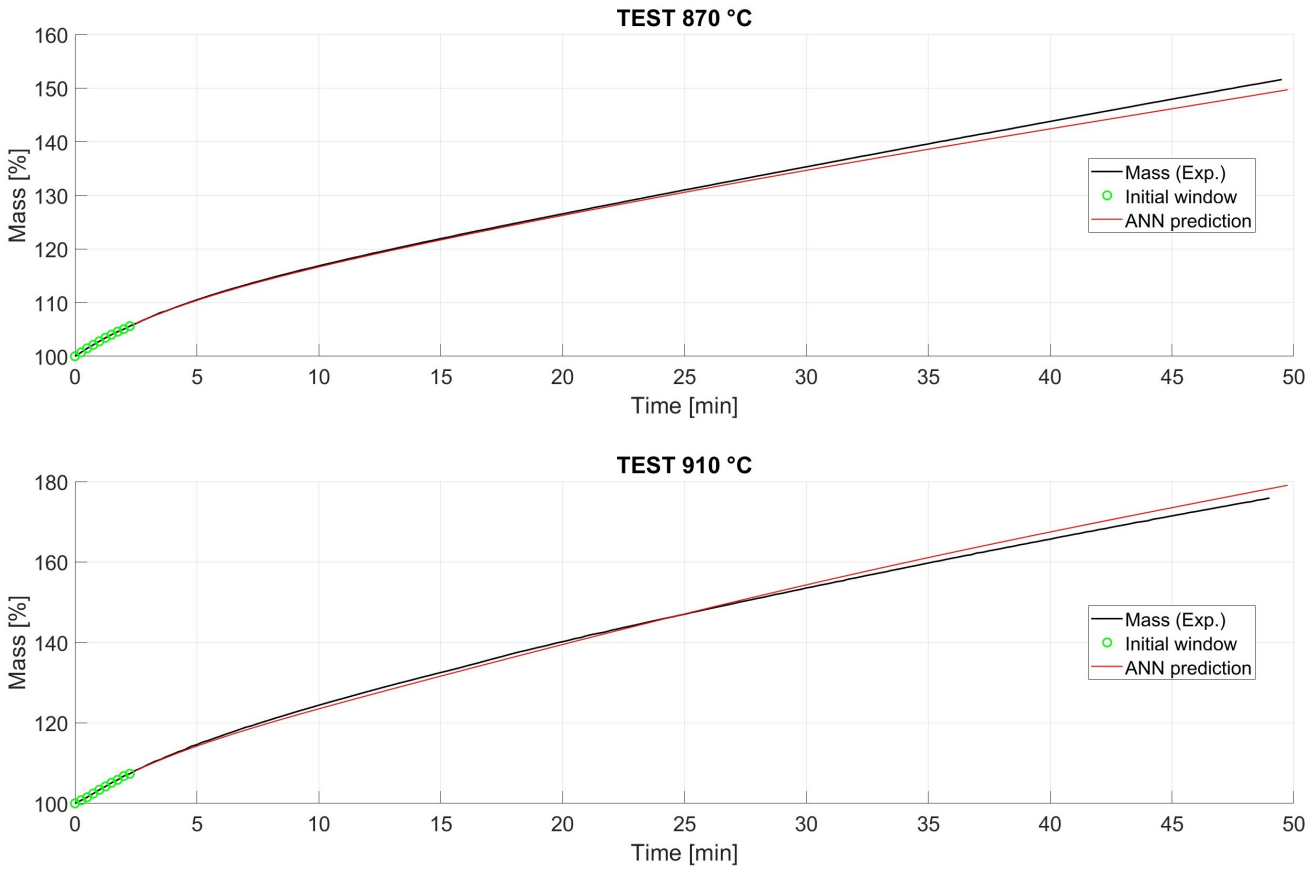


Figure 6. Results of the prediction phase using the test set: comparison between experimental relative mass profiles and those predicted by the ANN with a window size of 10 and a hidden layer structure of 4-2-15. The predictions start from the beginning (∼ 0 min) (Cherbański et al., 2026b).

Table 3. Summary of studies on ANN applications in thermodynamic and reaction kinetics modelling for hydrogen and syngas production from methane via thermochemical conversion.

Process	MP, DRM, SMR and POM (Cherbański et al., 2026a)	TRM (de Souza et al., 2025)	DRM (Hossain et al., 2016)	DRM (Ayodele and Cheng, 2015)	DRM (Ayodele et al., 2019)	DRM (Alsaffar et al., 2020)	DRM (Fang et al., 2025)
Domain	Thermodynamics	Kinetics	Kinetics	Kinetics	Kinetics	Kinetics (catalyst coking)	Kinetics (catalyst coking)
Data source (number of patterns)	Authors' calculation data (2,233)	Experimental data from literature (6,700)	Authors' experimental data (27)	Authors' experimental data (57)	Authors' experimental data obtained using central composite design (50)	Authors' experimental data (170)	Experimental data from literature (85)
Number and names of input variables	5: $\frac{CO_2}{CH_4}$, $\frac{H_2O}{CH_4}$, $\frac{O_2}{CH_4}$, T, P	5: Ni content, T, $\frac{CO_2}{CH_4}$, $\frac{H_2O}{CH_4}$, $\frac{O_2}{CH_4}$	3: metal loading, T, $\frac{CH_4}{CO_2}$	4: P_{CH4}, P_{CO2}, $\frac{CH_4}{CO_2}$, T	3: P_{CH4}, P_{CO2}, T	3: T, F_{N2}, $\frac{CH_4}{CO_2}$	3: T, F_{N2}, $\frac{CH_4}{CO_2}$
Number and names of output variable(s)	6: y_{CH4}, y_{CO2}, y_{CO}, y_{H2}, y_{H2O}, Y_C	1: X_{CH4}	4: X_{CH4}, X_{CO2}, Y_{H2}, Y_{CO}	4: r_{H2}, r_{CO}, X_{CH4}, X_{CO2}	2: r_{H2}, r_{CO}	1: C_{dep}	1: C_{dep}
Preprocessing data	Data normalization	NR	NR	NR	NR	RBF: data normalization; MLP: data standardization	NR
ANN architecture type	MLP	MLP	RBF and MLP	MLP	MLP	RBF and MLP	RBF and MLP
Best network architecture: inputs-hidden layers-outputs	5-40-6	5-4-1	RBF: 3-10-4; MLP: 3-12-4	4-16-4	RBF: 2-15-2-2; MLP: 2-13-2-2; SCG: 2-15-2-2	RBF: 3-20-1; MLP: 3-16-1	RBF: 3-max(65)-1; MLP: 3-5-1
Training	BP using LM	BP using Adam with BR and ES	RBF: not reported; MLP: BP	BP using LM	BP using LM, BR, SCG	RBF: LM; MLP: LM	RBF: NR; MLP: BP
Validation / Additional procedure	–	4-fold cross-validation	–	–	Model comparison between different training algorithms	–	5-fold cross-validation
Data split for training/ validation/ testing	70/15/15%	70/10/20%	70/15/15%	70/15/15%	70/15/15%	70/15/15%	76% (training, 5-fold CV)/ 24% (testing)
Network performance	MSE, R^2	MAE, RMSE, R^2	R^2, SEE, t-test	MSE, R^2, ARE	MSE, R^2	MSE, R	MSE, R^2

Table 3 continued

Process	Biogas SMR and DRM with H2S (Kumbhat et al., 2024)	MP (Cherbański et al., 2026b)	Steam reforming of model naphtha mixture (Morlanés et al., 2022)	DRM (Gendy et al., 2024)	SMR (SOFC) (Ciou et al., 2007)	DRM (Abedini et al., 2018)
Domain	Kinetics (catalyst deactivation: coking and sulphur poisoning)	Kinetics (catalyst coking)	Kinetics (model discrimination + kinetic modelling)	Kinetics (process optimization with RSM and ANN)	Kinetics (catalyst performance / process modelling in SOFC)	Kinetics (catalyst design and optimization using ANN + GA)
Data source (number of patterns)	Experimental data from literature ($\sim$ 300)	Authors' experimental data (2,200)	Authors' modelling and experimental data (1710 features per instance; 500 instances per model)	Authors' experimental data (28)	Authors' experimental data (not explicitly stated; generated via mass spectrometry)	Authors' experimental data (75)
Number and names of input variables	12: time, T, $\frac{CO_2}{CH_4}$, $\frac{H_2O}{CH_4}$, WHSV, c_{H2S}, BET surface area, pore size, pore volume, Ni content, Ni dispersion, Ni crystallite size	20: Sliding-window inputs (10 time steps $\times$ 2 variables: T and m_{cat})	Kinetic data (1710 features per instance: profiles of species vs. conditions – implicit inputs: T, $\frac{S}{C}$, $p_{naphtha}$, space time, compositions)	3: T, $\frac{CH_4}{CO_2}$, GHSV	6: T, time, lattice parameter, Ni molar ratio (in $LaNi_xAl_{1-x}O_3$), F_{CH4}, F_{H2O}	4: La mole fraction, Ni mole fraction, $T_{calcination}$, $T_{reaction}$
Number and names of output variable(s)	1: separate models for each output variable: X_{CH4}, X_{CO2}, y_{H2}, y_{CO}, y_{CH4}, y_{CO2}	2: T and m_{cat}	8-class classification (probability of kinetic model / rate law)	3: X_{CH4}, X_{CO2}, $\frac{H_2}{CO}$	3: F_{CH4}, F_{CO}, F_{H2O}	1: X_{CH4}
Preprocessing data	Data normalization and feature scaling	Data normalization	Data standardization (mean removal, unit variance), feature selection ($10\% < X < 90\%$)	Data normalization	Data normalization	Data normalization
ANN architecture type	MLP	MLP	MLP	RBF	MLP	MLP
Best network architecture: inputs-hidden layers-outputs	Separate ANNs for the output variables 12-24-1	20-4-2-15-2	1710-(50, 100, 200, 500)-8	3-10-1 (separate models for each output variable)	6-(optimized, not explicitly fixed)-3 (single hidden layer; number of neurons determined empirically)	4-9-1
Training	BP using Adam	BP using LM	Adam, categorical cross-entropy, ReLU + Softmax	RBFNN	BP, gradient descent (MSE minimization)	BP using LM with ES

Table 3 continued

Process	Biogas SMR and DRM with H2S (Kumbhat et al., 2024)	MP (Cherbański et al., 2026b)	Steam reforming of model naphtha mixture (Morlanés et al., 2022)	DRM (Gendy et al., 2024)	SMR (SOFC) (Ciou et al., 2007)	DRM (Abedini et al., 2018)
Validation/ Additional procedure	Model comparison with Random Forest	–	10-fold cross-validation + grid search (hyperparameter tuning)	Model comparison with RSM; performance evaluation via multiple statistical metrics (R^2, RMSE, error analysis)	CV	ES + integration with GA for optimization
Data split for training/ validation/ testing	80/20% train-test split	70/12/18%	80/20% train-validation split, CV	Not explicitly split (small dataset; full dataset used for model fitting and evaluation)	70/10/20%	70/15/15%
Network performance	RMSE, R^2	Own objective function based on SSE	Classification accuracy, confusion matrix	R^2, RMSE	MSE	R^2, ARD

Variables: C_{dep} – carbon deposition, F – flow rate, m – mass, P – pressure, r – reaction rate, T – temperature, X – conversion, y – mole fraction, Y – yield, WHSV – weight hourly space velocity; Algorithms/Training methods: Adam – adaptive moment estimation algorithm, BP – backpropagation, BR – Bayesian regularization, ES – early stopping, BFGS quasi-Newton BP – Broyden-Fletcher-Goldfarb-Shanno quasi-Newton backpropagation, GA – genetic algorithm, LM – Levenberg-Marquardt, SCG – scaled conjugate gradient; Neural network types: MLP – multilayer perceptron, RBF – radial basis function; Performance metrics/statistics: ARD – average relative deviation, ARE – average relative error, MAE – mean absolute error, MSE – mean squared error, RMSE – root mean squared error, R – Pearson correlation coefficient, R^2 – coefficient of determination, S – Spearman rank correlation coefficient, SEE – standard error of estimate, Accuracy – classification accuracy; Additional terms: CV – cross-validation, ReLU – rectified linear unit, Softmax – normalized exponential activation function, Categorical cross-entropy – loss function for classification, Feature scaling/standardization – data preprocessing to zero mean and unit variance; NR – not reported

Table 4. Summary of ANN approaches applied to reactor and process performance modelling.

Process	SMR (Arcotumapathy et al., 2012)	SMR (Zamaniyan et al., 2013)	SMR (Vo et al., 2019)	DRM (Rahman and Biswas, 2024)	SE-SMR (Nkulikiyinka et al., 2020)	SMR (Jafarizadeh et al., 2024)	SMR (Shahid et al., 2025)	SMR (Ba-Alawi et al., 2026)
Domain	Catalyst design (set A) and reactor operation (set B) optimization	Industrial hydrogen plant	Reactor performance	Catalyst performance	Process performance	Reactor performance	Reactor performance + waste heat recovery	Process performance
Data source (number of patterns)	Experimental data from literature (200)	Authors' modelling data (100)	Authors' modelling data (81)	Experimental data from literature (28)	Authors' simulation data (13,756)	Authors' modelling data (625)	Authors' experimental and simulation data (491)	Authors' simulation data (30,000)
Number and names of input variables	Set A – 14: Ni loading, support types, promoters, T, P, $\frac{S}{C}$, space time, time-on-stream, catalyst reduction temperature Set B – 14: Ni loading, support types, promoters, T, P, $\frac{S}{C}$, time-on-stream, catalyst reduction temperature	4: T, P, $\frac{S}{C}$, $\frac{CO_2}{CH_4}$	4: Reactor: F and T, $\frac{S}{C}$, Furnace: F	5: T, GHSV, surface area, pore volume, pore diameter	4: Reformer: T, P, $\frac{S}{C}$, CaO/C; Regenerator: T	4: F, $\frac{S}{C}$, heat flux, tube length	1-4 (depending on configuration): $\frac{CH_4}{H_2O}$, T, P, heat duty (for C-15)	8: Reformer: T, P, F_{CH4}, F_{H2O}; HT- and LT-WGS reactors: T_{HT}, T_{LT}, P, F_{H2O}
Number and names of output variable(s)	Both sets – 1: X_{CH4}	3: T, y_{H2}, y_{CO}	7: T, v, P, y_{CH4}, y_{CO2}, y_{H2}, y_{CO}	1: Y_{H2}	6: Reformer – X_{CH4}, y_{H2O}, y_{CO}, y_{H2}; Regenerator – y_{H2O}, y_{CO2}	7: X_{CH4}, X_{H2O}, production rates: H_2, CO_2, CO, wall temperature, product temperature	1: F_{H2}	3: UPC, NCE, EEF
Preprocessing data	Data normalization, principal component analysis (PCA); noise reduction	NR	Principal component analysis based on singular value decomposition	NR	Data randomization and normalization	Data normalization	NR	Data standardization

Table 4 continued

Process	SMR (Arcotumapathy et al., 2012)	SMR (Zamaniyan et al., 2013)	SMR (Vo et al., 2019)	DRM (Rahman and Biswas, 2024)	SE-SMR (Nkulikiyinka et al., 2020)	SMR (Jafarizadeh et al., 2024)	SMR (Shahid et al., 2025)	SMR (Ba-Alawi et al., 2026)
ANN architecture type	MLP	MLP	MLP	MLP	MLP	MLP	MLP	MLP
Best network architecture: inputs-hidden layers-outputs	Set A: in 3 hidden layers (Fibonacci-based opimization), total 83 neurons Set B: in 2 hidden layers (Fibanocci-based optimization), total 9 neurons	4-5-3	NR	LM: 5-10-1; SCG: 5-8-1	NR	4-32-16-8-8-7	4-(2-10 hidden layers, $\sim$ 10 neurons each)-1	8-64-32-16-8-6-3
Training	BP using LM with ES	BP	BP	BP using LM, SCG, BR	NR	BP using Adam	BP using LM	BP using Adam with ES (final training)
Validation/ Additional procedure	Multi-error evaluation, weighted optimal combination of ANN models	–	–	NR	–	10% validation split from training data	Testing of multiple input combinations (C-1 – C-15), hidden layers (2-10), 5-fold CV	Data normalization
Data split for training/ validation/ testing	75/12.5/12.5%	50/25/25%	72/28% train-testing split	>90% train / <10% test + validation	NR	80/(10)/20%	Variable splits (test ratios: 10%, 20%, 30%)	60/20/20%
Network performance	SSE, MSE, RMSE, MAE, MAPE	R^2	ARE	MSE, R^2	MSE, RMSE, R^2	MSE, MAE	MSE, R^2	MSE, MAE, R^2

Table 4 continued

Process	ATR (Soltanimehr et al., 2026)	SMR (Pizoń et al., 2024a)	SMR (Pizoń et al., 2024b)	SMR (Pizoń et al., 2025)	SMR (Biermann et al., 2025)*	Electrified SMR (Samris et al., 2025)	DRM (Roh et al., 2024)	Reforming processes (Yalcin et al., 2024)
Domain	Industrial auto-thermal reformer performance	Reactor performance	Reactor performance	Reactor performance	Reactor performance	Reactor performance	Kinetics (catalyst performance prediction using hybrid ANN-QNN model)	Process performance
Data source (number of patterns)	CHEMKIN-based data coupled with PFR simulations (1300)	Authors' experimental, interpolated, and calculated data (10,475)	Authors' experimental, interpolated, and calculated data (NR)	Authors' experimental, interpolated, and calculated data (NR)	Authors' modelling data (NR)	Authors' modelling data (1748)	Literature + in-house experimental data ($\sim$ 300)	Authors' simulation data (NR)
Number and names of input variables	8: y_{CH4}, y_{H2O}, y_{CO}, y_{H2}, y_{CO2}, T + 2 unspecified	5: T, $\frac{S}{C}$, $\frac{N}{C}$, m_{cat}, F_{CH4}	NR	5: T, $\frac{S}{C}$, $\frac{N}{C}$, m_{cat}, F_{CH4}	6: T, p_{CH4}, p_{CO2}, p_{H2O}, p_{CO}, p_{H2}	4: Porosity, F, y_{CH4}, y_{H2O}	$\sim$ 65 input features (catalyst composition, temperature, GHSV, gas composition, reduction conditions)	CH_4 reforming – T, P, $\frac{S}{M}$, $\frac{O_2}{M}$; 3: methanol reforming – T, $\frac{S}{methanol}$, $\frac{O_2}{methanol}$; 3: diesel reforming – T, $\frac{S}{diesel}$, $\frac{O_2}{diesel}$
Number and names of output variable(s)	6: y_{CH4}, y_{H2O}, y_{CO}, y_{H2}, y_{CO2}, T	4: y_{CH4}, y_{CO2}, y_{H2}, c_{CO}	4: y_{CH4}, y_{CO2}, y_{H2}, c_{CO}	4: y_{CH4}, y_{CO2}, y_{H2}, c_{CO}	5: $\dot{s}_{CH4}$, $\dot{s}_{CO2}$, $\dot{s}_{H2O}$, $\dot{s}_{CO}$, $\dot{s}_{H2}$ (source terms embedded in the reactor model)	2: y_{CO2}, y_{H2}	1: X_{CH4}	CH_4 reforming – Y_{H2}, y_{CO}, X_{CH4}; 2: methanol and diesel reforming – Y_{H2}, y_{CO}
Preprocessing data	NR	Data normalization and weighting	Data normalization and weighting	Data normalization and weighting	Data scaling	Data normalization, Z-score normalization, SMOTE	Dimensionality reduction via ANN layers	Data randomization and normalization
ANN architecture type	MLP	MLP	MLP	MLP	PENN	PINN	Hybrid QNN (ANN + parametrized quantum circuit, PQC)	CNN

Table 4 continued

Process	ATR (Soltanimehr et al., 2026)	SMR (Pizoń et al., 2024a)	SMR (Pizoń et al., 2024b)	SMR (Pizoń et al., 2025)	SMR (Biermann et al., 2025)*	Electrified SMR (Samris et al., 2025)	DRM (Roh et al., 2024)	Reforming processes (Yalcin et al., 2024)
Best network architecture: inputs-hidden layers-outputs	8-8-6 (number of hidden neurons not explicitly reported)	5-6-8-6-4	NR-6-8-6-4	5-15-5-15-9-8-11-4	6-60-60-60-5	4-256-256-ResBlock(256x2)-128-64-2	ANN: 65-32-16-8-4-1; Hybrid QNN: 65-32-16-4-PQC-1	CNN architecture (convolutional layers + fully connected layers)
Training	BR using LM	BP using BFGS quasi-Newton	BP using BFGS quasi-Newton	Adam + Bayesian optimization	LBFGS	Multi-phase training regimen (warm-up phase and physics-informed loss using Adam)	BP using Adam with ES	BP using Adam
Validation/ Additional procedure	–	–	–	Bayesian hyperparameter optimization	Comparison with reference microkinetic reactor model	–	30 repeated runs; ANN vs hybrid QNN comparison; validation on independent dataset	NR
Data split for training/ validation/ testing	70/15/15%	NR	NR	82.35/17.64/0.01%	25/25/50%	70/15/15%	70/14/16%	80/10/10%
Network performance	MSE, R^2, AARD	R, S	R, S	MSE, R, R^2	Agreement with mechanistic model	R^2, MAE	R^2, MAE, AE	R^2, MAPE, MAE, RMSE

Variables: T – temperature, P – pressure, v – velocity, X – conversion, Y – yield, y – mole fraction, c – concentration, F – molar flow rate, GHSV – Gas Hourly Space Velocity, m – mass, $\frac{S}{C}$ – steam-to-carbon ratio, $\frac{N}{C}$ – nitrogen-to-carbon ratio, $\frac{S}{M}$ – steam-to-methane ratio; Algorithms/Training methods: Adam – adaptive moment estimation, BP – backpropagation, BR – Bayesian regularization, BFGS quasi-Newton – Broyden-Fletcher-Goldfarb-Shanno quasi-Newton backpropagation, LBFGS – limited-memory Broyden-Fletcher-Goldfarb-Shanno, LM – Levenberg-Marquardt, SCG – scaled conjugate gradient, SMOTE – Synthetic Minority Over-sampling Technique, NSGA-II – non-dominated sorting genetic algorithm II; Neural network types: CNN – convolutional neural network, MLP – multilayer perceptron, PINN – physics-informed neural network, PENN – physics-enhanced neural network; Performance metrics/statistics: MAE – mean absolute error, MAPE – mean absolute percentage error, MSE – mean squared error, RMSE – root mean squared error, R – Pearson correlation coefficient, R^2 – coefficient of determination, S – Spearman rank correlation coefficient, AARD – average absolute relative deviation; Additional terms: CFD – computational fluid dynamics, PFR – plug flow reactor, CV – cross-validation, UPC – unit production cost, NCE – net CO2-equivalent emission, EEF – energy efficiency, SE-SMR – sorption-enhanced steam methane reforming; NR – not reported

*) Ref. (Biermann et al., 2025) employs a physics-enhanced neural network embedded within a mechanistic microkinetic reactor model rather than a standalone data-driven MLP surrogate.

Validation against independent experimental measurements and kinetic simulation data confirmed strong agreement across varying methane flow rates, catalyst masses, H_2O/CH_4 ratios, and temperatures. Minor deviations observed at elevated temperatures were attributed to the predominance of non-equilibrium data in the training set, which limited the model's ability to accurately reproduce equilibrium effects. Compared with a standalone kinetic model (MSE = 0.0032) and previously reported ANN and nonlinear response surface models, the proposed framework demonstrated superior predictive performance, demonstrating that hybrid dataset construction can significantly improve ANN-based reformer modelling.

This concept was further expanded in a subsequent study by the same authors (Pizoń et al., 2024b), which demonstrated that an ANN-based simulator can effectively model the SMR process, delivering accurate predictions based on key operating variables such as temperature, inlet gas composition, methane flow rate, and nickel catalyst mass. The training procedure incorporated experimental, interpolated, and theoretical datasets. Multiple neural network configurations were evaluated, leading to the selection of an optimal architecture with a 5-6-8-6-4 structure. The developed ANN model was then applied to predict the concentrations of components in the outlet stream as functions of varying reformer operating conditions. A comparison between the ANN predictions and validation data confirmed that the model provides a reliable and suitable representation of the studied process.

In another study by the same authors (Pizoń et al., 2025), an artificial neural network was developed to model the SMR process. Conventional models typically describe either kinetic or equilibrium regimes, which limits their broader applicability. To overcome this limitation, a unified ANN-based model capable of representing both regimes was proposed. The network was trained on a dataset comprising experimental, interpolated, and theoretical data, further enhanced using data augmentation techniques. Bayesian optimization was applied to determine the most suitable network architecture. The final model consisted of an input layer with five neurons corresponding to key operating parameters, followed by six hidden layers arranged in a 15-5-15-9-8-11 configuration, and an output layer with four neurons representing the dry gas composition of the post-reaction mixture (CH_4, H_2, CO, and CO_2). The developed ANN exhibited high predictive accuracy in estimating the composition of the outlet gas under varying operating conditions. The results indicate that the proposed model is both robust and reliable for the analysed SMR process, making it a valuable tool for reactor design and process optimization.

Similarly, a three-layer feedforward ANN was proposed to represent the performance of an industrial hydrogen production plant (Zamaniyan et al., 2013). The network predicted product temperature, pressure, and the mole fractions of H_2 and CO as functions of feed temperature, reformer pressure, steam-to-carbon ratio (S/C ratio), and CO_2/CH_4 ratio. Training data were generated from detailed process simulations covering a broad range of operating conditions. A tangent sigmoid activation function was employed in both hidden and output layers, and the network was trained using a gradient descent algorithm. The optimal number of hidden neurons was determined by minimizing the MSE. ANN predictions closely reproduced the simulation results, indicating that the network successfully captured the nonlinear behaviour of the integrated hydrogen production process. By representing all major process units within a unified framework, the approach reduced the need for complex code-based simulations and enabled computationally efficient performance analysis and process optimization within the investigated operating range.

Extending ANN-based modelling toward physically detailed reactor simulations, datasets generated using computational fluid dynamics (CFD) were utilized to train and optimize a reduced-order (surrogate) model for an industrial-scale SMR reactor (Jafarizadeh et al., 2024). The ANN predicted seven key performance indicators, including CH_4 and H_2O conversions, H_2, CO_2 and CO production rates, wall temperature, and gas outlet temperature, as functions of reformer length, feed flow rate, surface heat flux, and S/C ratio. Two-dimensional axisymmetric CFD simulations were employed to generate the training data, enabling the network to capture complex spatially resolved reactor behaviour. The optimized architecture consisted of four hidden layers with a 32-16-8-8 neuron configuration. High predictive accuracy was achieved ($R^2 > 0.98$ for all target variables), confirming the model's ability to reproduce nonlinear reactor dynamics. Coupling the trained ANN with a random search optimization algorithm yielded a computationally efficient framework for maximizing hydrogen yield while minimizing reformer dimensions, significantly reducing dependence on resource-intensive CFD simulations.

A hybrid modelling framework combining a rigorous dynamic model of a steam methane reformer with an ANN surrogate was proposed to enable rapid prediction of reactor performance (Vo et al., 2019). The mechanistic model consisted of coupled sub-models describing a multiscale catalytic reactor, reactor tube wall, and furnace, which were linked through heat transfer and transport phenomena to capture the detailed behaviour of the reforming system. The validated dynamic model was subsequently used to generate training data through deterministic and stochastic simulations covering variations in four key operating variables: the reactor inlet flow rate, reactor inlet temperature, S/C ratio, and the inlet flow rate on the furnace side. To reduce the dimensionality of the generated dataset, principal component analysis based on singular value decomposition was applied prior to ANN training. A feedforward backpropagation neural network was then trained using 81 simulation cases to map the relationship between the operating conditions and the predicted outputs at the reactor outlet, including temperature, velocity, pressure, and mole fractions of the major components. Validation against additional simulation cases showed excellent agreement between ANN predictions and the dynamic model results, with pre-

diction errors below 2% and an overall accuracy of 98.91%. Moreover, the ANN surrogate significantly reduced the computational time required for prediction from approximately 1200 s for the full dynamic simulation to about 2 s. These results demonstrate that integrating rigorous mechanistic modelling with ANN-based surrogate models provides an effective approach for real-time monitoring, process optimization, and design of industrial steam methane reformers while maintaining high predictive accuracy.

Further advancing hybrid modelling strategies, a physics-enhanced neural network (PENN) framework was introduced to accelerate microkinetics-based simulations of industrial packed-bed reactors (Biermann et al., 2025). The study addressed the high computational cost of detailed microkinetic models, which typically involve large reaction mechanisms and stiff differential equation systems that constrain their practical use in large-scale optimization studies. Rather than replacing mechanistic modelling with a purely data-driven surrogate, the authors embedded neural networks within the first-principles framework to approximate computationally demanding components of the microkinetic rate expressions. Training data were generated from accurate microkinetic simulations across a broad range of temperatures, pressures, and feed compositions representative of industrial reforming conditions. By incorporating physical constraints and thermodynamic consistency directly into the network architecture, the proposed method preserved mechanistic consistency while substantially reducing computational time. The PENN-based model exhibited strong agreement with the reference mechanistic model and demonstrated improved numerical stability and extrapolation capability compared to standard feedforward ANN surrogates. The study demonstrates that PENN models can effectively link detailed reaction kinetics with industrial-scale process simulation.

A physics-informed neural network (PINN) framework was proposed for modelling electrified SMR, integrating first-principles modelling directly into the neural network architecture (Samris et al., 2025). Unlike conventional black-box ANNs, the model incorporated mass and energy conservation constraints into the loss function, enabling physically consistent predictions across a wide operating range. The framework combined CFD simulations with deep learning, where a detailed CFD model accounting for reactor geometry, reaction kinetics, and coupled heat and mass transfer phenomena was first developed and validated. A PINN model was subsequently trained using a database generated from the CFD simulations. The network used operating parameters such as applied voltage, catalyst porosity, mass flow rate, and H_2O/CH_4 ratio as input variables, while predicting key process indicators including hydrogen production, CO_2 and CO emissions, and reactor wall temperature. The incorporation of physics-based constraints improved model accuracy and generalization compared to purely data-driven approaches. Validation against the CFD model demonstrated excellent agreement, while substantially reducing computational cost, highlighting the potential of PINN-based surrogates for rapid optimization and real-time monitoring of electrified hydrogen production systems.

An integrated artificial intelligence framework was developed for modelling and multi-objective optimization of an industrial autothermal reformer (ATR) comprising a combustion chamber and a catalytic bed (Soltanimehr et al., 2026). The combustion section was simulated in CHEMKIN using the detailed GRI-3.0 kinetic mechanism (325 elementary reactions and 53 species), while the catalytic zone was modelled as a one-dimensional heterogeneous plug-flow reactor based on the kinetic model (Xu and Froment, 1989). To overcome the lack of direct coupling between CHEMKIN and MATLAB during optimization, approximately 1,300 datasets were generated from the validated combustion simulations and used to train a MLP neural network. The trained ANN was subsequently integrated with a multi-objective NSGA-II genetic algorithm to simultaneously maximize methane conversion and hydrogen yield while minimizing net CO_2 production. The optimal operating conditions increased CH_4 conversion to 99.6% and suggested the possibility of net CO_2 consumption under specific regimes. By combining detailed kinetic combustion modelling with ANN-based modelling and evolutionary optimization, the study demonstrated a computationally efficient strategy for optimizing complex ATR systems.

ANNs were utilized to estimate hydrogen yield in SMR as a function of key operating variables, including methane and steam flow rates, reactor pressure, temperature, and heat duty (Shahid et al., 2025). The results highlight the potential of data-driven approaches for enhancing hydrogen production processes. From a practical perspective, such models can be integrated into real-time monitoring and control systems for industrial reformers, enabling improved process efficiency, reduced energy demand, and increased hydrogen output. Furthermore, combining these approaches with carbon capture and storage (CCS) technologies, as well as fostering collaboration between academia and industry, may accelerate progress toward more sustainable hydrogen production at scale. Future research may also explore the application of optimization techniques, such as genetic algorithms and gradient-based methods, to identify optimal operating conditions and further improve process performance.

A rule-based supervisory multi-objective optimization (SMOO) framework was developed to enhance the performance of the SMR process under varying biogas feed compositions (Ba-Alawi et al., 2026). The approach combines a multi-input-multi-output deep neural network (MIMO-DNN) with the non-dominated sorting genetic algorithm II (NSGA-II) to analyse different operational scenarios, including constant, moderately varying, and strongly fluctuating methane content in the feed. The effectiveness of the proposed strategy was further confirmed through implementation within a digital twin environment using real biogas data. The results indicated notable improvements, including a reduction in annual operating costs

by 30.59%, a decrease in emissions by 6.68%, and an increase in process efficiency by 22.92%. Despite these promising outcomes, the method is still being refined for full integration with industrial hydrogen production systems. Future research will focus on expanding the dataset to improve model generalization and on developing fully coupled, bidirectional frameworks applicable under real plant operating conditions.

Carbon dioxide–reduced hydrogen can be produced through several approaches, including sorption-enhanced steam methane reforming (SE-SMR), which generates separate high-purity streams of H_2 and CO_2. For this process, ANN and random forest (RF)–based soft sensor models were developed to predict hydrogen production (Nkulikiyinka et al., 2020). Both models demonstrated strong predictive capabilities for gas concentrations in the reformer and regenerator reactors, particularly for species present at high concentrations. Additionally, CH_4 conversion within the reformer was accurately predicted, providing a reliable measure of the reaction efficiency under the tested operating conditions.

ANNs were employed to address a multifactorial, multiobjective optimization problem and to analyse extensive empirical datasets (Arcotumapathy et al., 2012). The methodology involved a Fibonacci-based approach to determine the optimal number of neurons for the ANN architecture, followed by a novel weighted combination of statistically selected candidate ANN models evaluated in a multi-error framework. Data from 200 catalytic SMR cases were used to validate the accuracy and robustness of this integrated ANN modelling approach. The results not only aligned with existing qualitative knowledge but also revealed previously underappreciated factors that could guide improvements in hydrocarbon reforming reactor technology and catalyst design. Notably, the study highlighted that small additions of boron, cerium, or similar metals (below 1 wt.%) to Ni-based catalysts, as well as the use of SBA-15 as a support instead of γ-alumina, can significantly enhance catalytic performance.

A hybrid quantum neural network (QNN)-ANN model was developed to predict the performance of the DRM process (Roh et al., 2024). QNNs offer higher prediction accuracy than traditional machine learning models, including ANNs, even when limited datasets are available. Catalyst datasets for the DRM reaction, drawn from both literature and in-house experiments, were used to benchmark the hybrid QNN against conventional ANN models. The results demonstrated that the hybrid QNN achieved superior prediction accuracy and faster convergence compared to the ANN. This study not only provides a methodological framework for implementing hybrid QNN models but also offers interpretive insights into their operation. The findings underscore the potential of hybrid QNNs as powerful tools for addressing complex problems in catalysis and chemistry, particularly in areas where limited data have historically constrained the application of classical machine learning approaches.

ANNs were applied to develop empirical models for predicting hydrogen yield and providing insights for improving DRM processes over nickel-based catalysts under varying operating and physical conditions (Rahman and Biswas, 2024). The model inputs included temperature, gas velocity, and three key geometric characteristics of the nickel catalysts, enabling prediction of hydrogen production from methane. The ANN was trained using three algorithms: Levenberg-Marquardt, Bayesian regularization, and scaled conjugate gradient, with the best model performance achieved using the Levenberg-Marquardt method. Accurate hydrogen yield predictions were obtained when the network employed the optimal number of hidden neurons and appropriate learning algorithm. This approach allows precise forecasting of catalyst performance based on physical properties, promoting more consistent and reliable DRM reactor operation. However, the study did not consider the effects of catalytic support, catalyst preparation methods, or coke formation on overall activity.

An advanced convolutional neural network (CNN) framework was designed to predict hydrogen yield and carbon monoxide concentration during reforming processes involving methane, methanol, and diesel (Yalcin et al., 2024). In addition, the model was adapted to estimate methane conversion in methane reforming systems. The proposed approach integrates both 2D- and 3D-CNN architectures to improve predictive capability. The results demonstrate that this hybrid CNN model outperforms conventional CNN structures as well as other artificial intelligence methods in estimating key performance indicators of reforming processes. Furthermore, the model enables reliable prediction of critical output variables across different fuel types, highlighting its versatility. Overall, the proposed methodology enhances the accuracy of process performance estimation and provides a robust tool for analysing reforming systems involving various feedstocks.

5. CONCLUSIONS

ANNs are effective tools for modelling methane thermochemical conversion, capturing complex relationships that conventional kinetic models struggle to describe. They have been successfully applied to predict methane conversion, hydrogen yield, syngas composition, and reactor performance.

MLPs remain the most widely used architecture due to their flexibility and reliability. Other architectures, such as RBF networks, CNN and PINN models, show promise for specific tasks, including catalyst coking, dynamic reactor behaviour, and multi-output predictions, although their use is still limited. The choice of ANN depends on dataset size, dimensionality, and the modelling goal, with simpler networks sufficient for basic predictions and more complex models needed for dynamic or multi-output systems.

Data quality and availability are critical. Large experimental or simulation-generated datasets allow for deeper net-

works and better predictions, while small datasets increase the risk of overfitting. Input selection, from operating conditions to catalyst properties and time-dependent variables, is also key to capturing system dynamics accurately.

Recent trends are moving toward integrated frameworks that combine ANNs with first-principles physical knowledge and advanced simulations. Hybrid models, as well as physics-informed or physics-enhanced networks, improve predictive accuracy, enforce physical consistency, and increase interpretability. Such approaches are expected to play a central role in designing efficient reactors, optimizing catalysts, and advancing hydrogen and syngas production technologies.

ACKNOWLEDGEMENTS

This work is related to the TITAN project (No. 101069474) funded by the European Union (HORIZON EUROPE Climate, Energy and Mobility). Views and opinions expressed are however those of the authors only and do not necessarily reflect those of the European Union or the European Climate, Infrastructure and Environment Executive Agency (CINEA). Neither the European Union nor the granting authority can be held responsible for them.

REFERENCES

Abedini F., Hosseini S.A., Niaei A., Salari D., Abbasi M., Marmarshahi S., 2018. Design and optimization of new $La_{1-x}Ce_xNi_{1-y}Fe_yO_3$ (x, y = 0–0.4) nano catalysts in dry reforming of methane. *Int. J. Green Energy*, 15, 20–27. DOI: 10.1080/15435075.2017.1405813.

Adhikari S., Fernando S., Gwaltney S.R., To S.D.F., Bricka R.M., Steele P.H., Haryanto A., 2007. A thermodynamic analysis of hydrogen production by steam reforming of glycerol. *Int. J. Hydrogen Energy*, 32, 2875–2880. DOI: 10.1016/j.ijhydene.2007.03.023.

Ahmad K., Jaoude M.A., Bankole A.A., Polychronopoulou K., 2025. Hydrogen production towards carbon-free economy: a comprehensive thermodynamic analysis. *Energy Convers. Manage.*, 326, 119492. DOI: 10.1016/j.enconman.2025.119492.

Ahmad K., Polychronopoulou K., Abi Jaoude M., 2022. CH_4 valorisation reactions: a comparative thermodynamic analysis and their limitations. *Fuel*, 320, 123877. DOI: 10.1016/j.fuel.2022.123877.

Alsaffar M.A., Ayodele B.V., Mustapa S.I., 2020. Scavenging carbon deposition on alumina supported cobalt catalyst during renewable hydrogen-rich syngas production by methane dry reforming using artificial intelligence modeling technique. *J. Cleaner Prod.*, 247, 119168. DOI: 10.1016/j.jclepro.2019.119168.

Arcotumapathy V., Siahvashi A., Adesina A.A., 2012. A new weighted optimal combination of ANNs for catalyst design and reactor operation: methane steam reforming studies. *AIChE J.*, 58, 2412–2427. DOI: 10.1002/aic.12748.

Ayodele B.V., Cheng C.K., 2015. Modelling and optimization of syngas production from methane dry reforming over ceria-supported cobalt catalyst using artificial neural networks and Box–Behnken design. *J. Ind. Eng. Chem.*, 32, 246–258. DOI: 10.1016/j.jiec.2015.08.021.

Ayodele B.V., Mustapa S.I., Alsaffar M.A., Cheng C.K., 2019. Artificial intelligence modelling approach for the prediction of CO-rich hydrogen production rate from methane dry reforming. *Catalysts*, 9, 738. DOI: 10.3390/catal9090738.

Ba-Alawi A.H., Chung H., Kim J., 2026. A rule-based digital twin strategy for optimizing hydrogen production from biogas under dynamic feed conditions. *Energy*, 342, 139779. DOI: 10.1016/j.energy.2025.139779.

Biermann F., Uglietti R., Döppel F.A., Kircher T., Bracconi M., Maestri M., Votsmeier M., 2025. Enabling micro-kinetics based simulation of industrial packed-bed reactors by physics-enhanced neural networks. *Chem. Eng. J.*, 519, 163598. DOI: 10.1016/j.cej.2025.163598.

Carranza-Abaid A., Svendsen H.F., Jakobsen J.P., 2023. Thermodynamically consistent vapor-liquid equilibrium modelling with artificial neural networks. *Fluid Phase Equilib.*, 564, 113597. DOI: 10.1016/j.fluid.2022.113597.

Cherbański R., Kotkowski T., Murgrabia S., Molga E., Stankiewicz A., 2026a. ANN-based prediction of equilibrium gas composition and carbon yield in methane pyrolysis and reforming methods. *React. Chem. Eng.*, 11, 691–706. DOI: 10.1039/D5RE00322A.

Cherbański R., Murgrabia S., Molga E., Stankiewicz A., Kotkowski T., 2026b. Forecasting temporal profiles of Fe/C catalyst coking in methane pyrolysis via moving window neural networks. DOI:

Ciou S.-J., Jhang Y.-W., Lai Y.-J., Kuan-Zong F., Hung M.-H., Chiang K.-W., 2007. A neural network model in $LaNi_xAl_{1-x}O_3$ catalyst for methane reforming in SOFC. *ECS Trans.*, 7, 1929. DOI: 10.1149/1.2729305.

Cybenko G., 1989. Approximation by superpositions of a sigmoidal function. *Math. Control Signals Syst.*, 2, 303–314. DOI: 10.1007/BF02551274.

de Souza P.A.L., Afzal R.M., Camacho F.G., Mahinpey N., 2025. Catalyst development for the tri-reforming of methane (TRM) process by integrated singular machine learning models. *Can. J. Chem. Eng.*, 103, 758–770. DOI: 10.1002/cjce.25397.

Del-Mazo-Alvarado O., Bonilla-Petriciolet A., 2022. Assessment of the simultaneous regression of liquid-liquid and vapor-liquid equilibria data of binary systems using NRTL and artificial neural networks. *Fluid Phase Equilib.*, 561, 113537. DOI: 10.1016/j.fluid.2022.113537.

Demidov D.V., Mishin I.V., Mikhailov M.N., 2011. Gibbs free energy minimization as a way to optimize the combined steam and carbon dioxide reforming of methane. *Int. J. Hydrogen Energy*, 36, 5941–5950. DOI: 10.1016/j.ijhydene.2011.02.053.

Di Nardo A., Portarapillo M., Russo D., Di Benedetto A., 2024. Hydrogen production via steam reforming of different fuels: thermodynamic comparison. *Int. J. Hydrogen Energy*, 55, 1143–1160. DOI: 10.1016/j.ijhydene.2023.11.215.

European Environmental Agency, 2025. *Total net greenhouse gas emission trends and projections in Europe*. Available at: https://www.eea.europa.eu/en/analysis/indicators/total-greenhouse-gas-emission-trends.

Fang R., Zhou T., Xu Z., Hu X., Zhang M., Yang H., 2025. Energy-efficient prediction of carbon deposition in DRM processes through optimized neural network modeling. *Energies*, 18, 3172. DOI: 10.3390/en18123172.

Faungnawakij K., Kikuchi R., Eguchi K., 2006. Thermodynamic evaluation of methanol steam reforming for hydrogen production. *J. Power Sources*, 161, 87–94. DOI: 10.1016/j.jpowsour.2006.04.091.

Gadalla A.M., Bower B., 1988. The role of catalyst support on the activity of nickel for reforming methane with CO_2. *Chem. Eng. Sci.*, 43, 3049–3062. DOI: 10.1016/0009-2509(88)80058-7.

Gendy T.S., El-Salamony R.A., Alrashed M.M., Bentalib A., Osman A.I., Kumar R., Fakeeha A.H., Al-Fatesh A.S., 2024. Enhanced predictive optimization of methane dry reforming via Response Surface methodology and artificial neural network approaches: Insights using a novel nickel-strontium-zirconium-aluminum catalyst. *Mol. Catal.*, 562, 114216. DOI: 10.1016/j.mcat.2024.114216.

Guéret C., Daroux M., Billaud F., 1997. Methane pyrolysis: thermodynamics. *Chem. Eng. Sci.*, 52, 815–827. DOI: 10.1016/S0009-2509(96)00444-7.

Hornik K., Stinchcombe M., White H., 1989. Multilayer feedforward networks are universal approximators. *Neural Networks*, 2, 359–366. DOI: 10.1016/0893-6080(89)90020-8.

Hossain M.A., Ayodele B.V., Cheng C.K., Khan M.R., 2016. Artificial neural network modeling of hydrogen-rich syngas production from methane dry reforming over novel $Ni/CaFe_2O_4$ catalysts. *Int. J. Hydrogen Energy*, 41, 11119–11130. DOI: 10.1016/j.ijhydene.2016.04.034.

Igwegbe C.A., Adeniyi A.G., Ighalo J.O., 2021. ANN modelling of the steam reforming of naphthalene based on non-stoichiometric thermodynamic analysis. *Chem. Pap.*, 75, 3363–3372. DOI: 10.1007/s11696-021-01566-2.

Ismaila A., Chen X., Gao X., Fan X., 2021. Thermodynamic analysis of steam reforming of glycerol for hydrogen production at atmospheric pressure. *Front. Chem. Sci. Eng.*, 15, 60–71. DOI: 10.1007/s11705-020-1975-0.

Jabbour K., 2020. Tuning combined steam and dry reforming of methane for "metgas" production: a thermodynamic approach and state-of-the-art catalysts. *J. Energy Chem.*, 48, 54–91. DOI: 10.1016/j.jechem.2019.12.017.

Jafarizadeh A., Panjepour M., Emami M.D., 2024. Advanced modelling and optimization of steam methane reforming: from CFD simulation to machine learning – driven optimization. *Int. J. Hydrogen Energy*, 96, 1262–1280. DOI: 10.1016/j.ijhydene.2024.11.352.

Jensen C., Duyar M.S., 2021. Thermodynamic analysis of dry reforming of methane for valorization of landfill gas and natural gas. *Energy Technol.*, 9, 2100106. DOI: 10.1002/ente.202100106.

Kumbhat A., Madaan A., Goel R., Appari S., Al-Fatesh A.S., Osman A.I., 2024. Predicting nickel catalyst deactivation in biogas steam and dry reforming for hydrogen production using machine learning. *Process Saf. Environ. Prot.*, 191, 1833–1846. DOI: 10.1016/j.psep.2024.09.020.

L'hospital V., de Araujo L.G., Landrivon E., Mello A., Radoiu M., Trillaud V., Meunier J.-F., Schuurman Y., Guilhaume N., Farrusseng D., 2025. Methane pyrolysis into hydrogen and solid carbon: a comparative analysis of conventional and microwave heating approaches. *Catal. Today*, 459, 115430. DOI: 10.1016/j.cattod.2025.115430.

L'hospital V., de Araujo L.G., Schuurman Y., Guilhaume N., Farrusseng D., 2024. Direct biogas reforming to turquoise H_2 and carbon material in a catalytic fluidised-bed reactor. *New J. Chem.*, 48, 9656–9662. DOI: 10.1039/D4NJ00846D.

Lima da Silva A., Malfatti C.D.F., Müller I.L., 2009. Thermodynamic analysis of ethanol steam reforming using Gibbs energy minimization method: a detailed study of the conditions of carbon deposition. *Int. J. Hydrogen Energy*, 34, 4321–4330. DOI: 10.1016/j.ijhydene.2009.03.029.

Morlanés N., Lezcano G., Yerrayya A., Mazumder J., Castaño P., 2022. Improving robustness of kinetic models for steam reforming based on artificial neural networks and ab initio calculations. *Chem. Eng. J.*, 433, 133201. DOI: 10.1016/j.cej.2021.133201.

Nguyen V.D., Tan R.R., Brondial Y., Fuchino T., 2007. Prediction of vapor–liquid equilibrium data for ternary systems using artificial neural networks. *Fluid Phase Equilib.*, 254, 188–197. DOI: 10.1016/j.fluid.2007.03.014.

Nkulikiyinka P., Yan Y., Güleç F., Manovic V., Clough P.T., 2020. Prediction of sorption enhanced steam methane reforming products from machine learning based soft-sensor models. *Energy AI*, 2, 100037. DOI: 10.1016/j.egyai.2020.100037.

Piotrowski K., Piotrowski J., Schlesinger J., 2003. Modelling of complex liquid–vapour equilibria in the urea synthesis process with the use of artificial neural network. *Chem. Eng. Process. Process Intensif.*, 42, 285–289. DOI: 10.1016/S0255-2701(02)00060-0.

Pizoń Z., Kimijima S., Brus G., 2024a. Enhancing a deep learning model for the steam reforming process using data augmentation techniques. *Energies*, 17, 2413. DOI: 10.3390/en17102413.

Pizoń Z., Kimijima S., Brus G., 2024b. Integrating experimental and numerical data for improved steam reforming simulation with deep learning. *J. Phys. Conf. Ser.*, 2812, 012024. DOI: 10.1088/1742-6596/2812/1/012024.

Pizoń Z., Kimijima S., Brus G., 2025. Bridging equilibrium and kinetics prediction with a data-weighted neural network model of methane steam reforming. *Int. J. Hydrogen Energy*, 175, 151367. DOI: 10.1016/j.ijhydene.2025.151367.

Rahman M.H., Biswas M., 2024. Modeling of dry reforming of methane using artificial neural networks. *Hydrogen*, 5, 800–818. DOI: 10.3390/hydrogen5040042.

Reynel-Ávila H.E., Bonilla-Petriciolet A., Tapia-Picazo J.C., 2019. An artificial neural network-based NRTL model for simulating liquid-liquid equilibria of systems present in biofuels production. *Fluid Phase Equilib.*, 483, 153–164. DOI: 10.1016/j.fluid.2018.11.009.

Roh J., Oh S., Lee D., Joo C., Park J., Moon I., Ro I., Kim J., 2024. Hybrid quantum neural network model with catalyst experimental validation: application for the dry reforming of methane. *ACS Sustainable Chem. Eng.*, 12, 4121–4131. DOI: 10.1021/acssuschemeng.3c07496.

Rossi C.C.R.S., Alonso C.G., Antunes O.A.C., Guirardello R., Cardozo-Filho L., 2009. Thermodynamic analysis of steam reforming of ethanol and glycerine for hydrogen production. *Int. J. Hydrogen Energy*, 34, 323–332. DOI: 10.1016/j.ijhydene.2008.09.071.

Samris A., Naanani H., Nachtane M., Faik A., 2025. A physics-informed deep learning framework for enhanced hydrogen production via electrified steam methane reforming. *Int. J. Hydrogen Energy*, 193, 152376. DOI: 10.1016/j.ijhydene.2025.152376.

Sánchez-Bastardo N., Schlögl R., Ruland H., 2021. Methane pyrolysis for zero-emission hydrogen production: a potential bridge technology from fossil fuels to a renewable and sustainable hydrogen economy. *Ind. Eng. Chem. Res.*, 60, 11855–11881. DOI: 10.1021/acs.iecr.1c01679.

Shabbar S., Janajreh I., 2013. Thermodynamic equilibrium analysis of coal gasification using Gibbs energy minimization method. *Energy Convers. Manage.*, 65, 755–763. DOI: 10.1016/j.enconman.2012.02.032.

Shahid M.I., Farhan M., Rao A., Li W., Salam H.A., Xiao Q., Chen T., Li X., Ma F., 2025. Effect of methane/water flowrate on waste heat recovery and hydrogen production by steam methane reforming process and predicted by artificial neural network (ANN). *Energy*, 331, 136877. DOI: 10.1016/j.energy.2025.136877.

Soltanimehr S., Rahimpour M.R., Shariati A., 2026. Integrated artificial intelligence modelling and multi objective optimization to optimize an industrial auto-thermal reformer. *Energy Convers. Manage.*, 349, 120831. DOI: 10.1016/j.enconman.2025.120831.

Taherian Z., Yousefpour M., Tajally M., Khoshandam B., 2017. Catalytic performance of Samaria-promoted Ni and Co/SBA-15 catalysts for dry reforming of methane. *Int. J. Hydrogen Energy*, 42, 24811–24822. DOI: 10.1016/j.ijhydene.2017.08.080.

Vo N.D., Oh D.H., Hong S.-H., Oh M., Lee C.-H., 2019. Combined approach using mathematical modelling and artificial neural network for chemical industries: steam methane reformer. *Appl. Energy*, 255, 113809. DOI: 10.1016/j.apenergy.2019.113809.

Xu J., Froment G.F., 1989. Methane steam reforming, methanation and water-gas shift: I. Intrinsic kinetics. *AIChE J.*, 35, 88–96. DOI: 10.1002/aic.690350109.

Yalcin S., Yildirim M., Alatas B., 2024. Advanced convolutional neural network modeling for fuel cell system optimization and efficiency in methane, methanol, and diesel reforming. *PeerJ Comput. Sci.*, 10, e2113. DOI: 10.7717/peerj-cs.2113.

Zamaniyan A., Joda F., Behroozsarand A., Ebrahimi H., 2013. Application of artificial neural networks (ANN) for modeling of industrial hydrogen plant. *Int. J. Hydrogen Energy*, 38, 6289–6297. DOI: 10.1016/j.ijhydene.2013.02.136.

Zhu J., Zhang D., King K.D., 2001. Reforming of CH_4 by partial oxidation: thermodynamic and kinetic analysis. *Fuel*, 80, 899–905. DOI: 10.1016/S0016-2361(00)00165-7

Chemical Engineering Horizons and Perspectives.
Article series endorsed by the Scientific Committee on Chemical and Process Engineering
of the Polish Academy of Sciences, term 2024–2027

Chemical and Process Engineering: New Frontiers, 2026, 47(2), e136
DOI: 10.24425/cpe.2026.158134

MLP artificial neural network model for predicting natural gas composition variability

Jolanta Szoplik, Paulina Muchel

West Pomeranian University of Technology in Szczecin, Faculty of Chemical Technology and Engineering, Piastów 42, 71-065 Szczecin, Poland

Abstract

This paper proposes an artificial neural network model, MLP 17-37-5, to predict the share of five natural gas components (methane, ethane, propane, nitrogen, and carbon dioxide) in the natural gas mixture in a pipeline network, depending on selected calendar and weather factors. Natural gas composition variability in the pipeline network results from supplying it with gas of varying composition and from different suppliers. Using statistical analysis of 35,064 actual measurement data sets, factors (model input data) significantly affecting gas composition variability were selected. Models differing in structure (the MLP 17-37-5 model or five MLP 17-37-1 models) and the number of neurons in the hidden layer (from 20 to 230 neurons) were trained using sets ranging from 8,760 to 35,064 actual data points obtained using the chromatographic method. The quality of the models was assessed based on the correlation coefficient, while the quality of the forecasts was assessed based on the nRMSE error of the forecasts obtained for a new data set of 8,760 data points. The MLP 17-37-5 model was shown to predict natural gas composition with an average error of nRMSE = 0.321. The article proposes a ready-made tool, which has no equivalent in the literature, allowing for a significant reduction in the number of chromatographic tests performed to determine the composition of natural gas. This is a completely new approach to studying changes in the composition of natural gas over time, which in the proposed forecasting model depend on selected factors (not analyzed in chromatographic studies).

* **Corresponding author, e-mail:** jolanta.szoplik@zut.edu.pl

Article info:

Received: 11 April 2026
Revised: 25 May 2026
Accepted: 29 May 2026

Keywords

statistical data analysis, natural gas composition variability, MLP artificial neural network model, natural gas composition forecasting

1. INTRODUCTION AND STATE OF THE ART

Natural gas, a mixture of hydrocarbons, is transported from its point of extraction to end users (individual consumers or industry) via a suitably designed pipeline network. In reality, the pipeline network transports natural gas energy, the amount of which depends on the composition of natural gas and can be expressed as the heat of combustion value. The composition of natural gas depends, among other things, on the gas extraction location and the degree of purification of the gas fuel. Additionally, changes in the composition of natural gas in network pipelines can be influenced by supplying pipelines with gas from different suppliers, regasified LNG, or the introduction of alternative fuels (hydrogen or biomethane), mixing gases with different chemical compositions, and variability in the load on individual network pipelines resulting from uneven demand for gas from customers over time (Szoplik, 2015; Szoplik, 2016; Szoplik, 2017; Szoplik and Muchel, 2023a; Szoplik and Muchel, 2023b). In such a situation, the only way to obtain information on the composition of natural gas at a given point in the gas network is to monitor it in real time using gas chromatography method or to track changes in gas composition based on transient simulations of gas flow in the network or to forecast the composition of natural gas using artificial neural networks.

Direct measurements using gas chromatography method are conducted on an ongoing basis by gas network operators at gas stations located at multiple points in the gas network and provide information on the current composition of natural gas at a given measurement point. These measurements can be used to analyze the flow of gas of a given composition in individual gas network pipelines. Kumor and Porada (2021) analyzed the impact of the operation of the LNG terminal in the Polish gas transportation system on the quality of gaseous fuel at 16 selected points in the high-pressure gas network over a 5-year period (covering the days before and after the LNG terminal was launched). Selected results of chromatographic measurements of changes in natural gas composition recorded at selected points in the gas network of the Polish natural gas transportation system, supplied by several suppliers and the LNG terminal, were also analyzed in (Muchel, 2024; Szoplik and Muchel, 2023a).

Another method of obtaining data on natural gas composition is to track changes in natural gas composition in network pipelines based on gas flow simulation results. This method is based on solving selected model equations describing the processes occurring within pipelines and the topology of the pipeline network for known flows supplying the network and the gas flow rates received by end users. Variations in demand for gaseous fuel by customers do not affect changes in the gas composition in a pipeline if it

© 2026. The Author(s). This is an open-access article distributed under the terms of the Creative Commons Attribution (CC-BY 4.0, https://creativecommons.org/licenses/by/4.0/), which permits unrestricted use, distribution, and reproduction in any medium, provided the original author and source are credited.

is supplied by a single supplier with gas of constant composition over time. However, if streams of other gaseous fuels (hydrogen or biomethane), for example, from alternative sources, are occasionally introduced into the gas network, the uneven load on network pipelines is an additional factor influencing changes in gas composition over time. Simulation models of gas flow in the network enable tracking changes in the composition of gas mixtures with different chemical compositions both under variable gas demand conditions and under conditions of hydrogen or biomethane injection into the pipeline (Alves and Fontes, 2022; Bermúdez and Shabani, 2022; Chaczykowski and Zarodkiewicz, 2017; Chaczykowski et al., 2018; Fan et al., 2021; Osiadacz and Chaczykowski, 2020; Saedi et al., 2021; Zhang et al., 2022). Variations in gas quality over time, expressed for example by the gas's heat combustion value, caused by changes in its composition, adversely affect the maximum load of the gas transport system and the determination of its capacity. Tracking changes in gas composition or the gas's heat combustion value is essential for planning the introduction of alternative gaseous fuels into the gas network as occasional supplies and for monitoring the presence of contaminants in the gas that are corrosive or susceptible to hydrate formation during transport.

The results of simulations of the flow and mixing of gas streams extracted from onshore or offshore deposits and liquefied LNG or compressed CNG were analyzed in (Alves and Fontes, 2022). Based on the shares of the most important components of the resulting gas mixture, the heat of combustion, which is one of the parameters necessary for system balancing, was determined. The research results obtained from gas flow simulations in the Brazilian gas network allowed for a reduction in gas transportation costs by up to 22.6%.

In a paper (Bermúdez and Shabani, 2022), a multi-species model consisting of first-order partial differential equations for each pipeline and gas component was proposed to track changes in gas composition at any location and time. A characteristic feature of this model is the separate solution of momentum and mass exchange equations using two independent computational grids. Numerical calculation results, verified with real-world data, demonstrated good agreement between simulation results and actual data. According to the authors, in times of energy transformation, there is considerable interest in the introduction and transport of hydrogen or biomethane into natural gas networks, which can be analyzed, for example, using the proposed methodology.

Chaczykowski and Zarodkiewicz (2017), Chaczykowski et al. (2018) and Osiadacz and Chaczykowski (2020), taking into account the direction of changes in the natural gas transportation system and the introduction of alternative gaseous fuels, point to new challenges facing the gas industry in a multi-energy system environment. These changes are expected to cause significant fluctuations and uncertainty in the distributed supply of liquefied natural gas (LNG) or gases from renewable sources (hydrogen). Assuming non-isothermal flow conditions, the authors proposed models for tracking gas quality, assuming energy boundary conditions (energy flow rate instead of volumetric flow), for an onshore gas pipeline in the Polish transmission system and for a model of an offshore gas pipeline in the Norwegian transmission system. Differences between measured and modeled compositions and transport times were examined and it was found that both methods accurately reproduced the measured compositions and transport times. According to the authors, only a well-chosen model will provide good simulation results and facilitate the integration of the power system with the gas system.

In another paper (Fan et al., 2021), a control volume method for hydraulic simulation and a one-dimensional, non-steady-state heat transfer model for thermal simulation were proposed for tracking gas composition in real time and, based on this, calculating gas flow parameters in the network. The pipeline system in the network was represented using a special grid connecting all adjacent pipelines. The proposed model is intended to be a tool for tracking gas composition in the event of injection of new types of gas (LNG, biogas, or hydrogen), which can cause short-term and rapid fluctuations in natural gas composition. Based on a comparison of the calculation results with measurement data, the authors indicate good agreement between the gas composition simulation results and the actual data.

Saedi et al. (2021) proposed a model for tracking gas composition in an integrated power and gas system with green hydrogen injection. The model also allows for the identification of gas flow directions entering and leaving a given network node, which is important in the case of a distributed hydrogen injection system and constraints related to the size of the hydrogen flow entering the network or the share of hydrogen in the gas flow at the customer. The model was validated using two gas networks of different sizes and demonstrated that it can accurately capture gas flows entering and leaving a network node and indirectly allows for the estimation of the amount of hydrogen that can be injected into the network depending on the season, time of day, or location in the power and gas grid.

The model proposed by Zhang et al. (2022) enables tracking of gas composition, and in particular the hydrogen content of the gas stream, in a real gas network with a branched structure and multiple non-pipe elements, supplied with natural gas at multiple points, and with multiple intermittent hydrogen injection sources. The model takes into account temporal and spatial variability of gas physical properties (gas compressibility coefficient). The model was verified using a selected Belgian gas network as an example, and the effectiveness of this method in solving natural gas composition tracking problems was demonstrated. Simulation results also confirmed the impact and significance of introducing a variable gas compressibility coefficient, tracking hydrogen fraction, and varying gas demand.

Simulation methods for tracking changes in the composition of mixtures of natural gas, regasified LNG, hydrogen, or biomethane require the use of equations describing the exchange of mass, momentum, and energy within gas network pipelines. Studies of gas composition tracking have most often used a straight pipeline section, less frequently a branched network. However, in reality, the pipeline network has a more complex topology (it is branched and contains loop elements), and depending on the network pipeline load, a change in the gas flow direction is observed in some pipelines. A change in the gas flow direction in the pipeline may be caused, for example, by greater or lesser gas demand from consumers during periods of lower ambient temperatures (apartment heating) or higher ambient temperatures (apartment cooling). The variability of gas demand from consumers depending on selected weather, calendar, economic, or demographic factors was analyzed in (Bianco et al., 2014; Durmayaz et al., 2000; Geem and Roper, 2009; Kenisarin and Kenisarina, 2007; Parikh et al., 2007; Sarak and Satman, 2003; Satman and Yalcinkaya, 1999; Szoplik, 2015; Szoplik and Muchel, 2023a).

Another approach to forecasting the natural gas composition at a given point in the pipeline network is to use an artificial neural network model. In this approach, one must first identify factors that directly or indirectly influence changes in natural gas composition (using statistical analysis), and then train the artificial neural network model using a set of real data describing the natural gas composition (chromatographic methods). In studies of natural gas transportation systems, artificial neural network models have been used, among others, to forecast gas demand on a global scale (Hafezi et al., 2019), for a given country (Merkel et al., 2018), or city (Szoplik, 2015), to predict the pipeline's resistance to cracking (Wang et al., 2022) or the corrosion rate of steel pipelines (Wen et al., 2019).

However, for designers and operators of natural gas transportation systems, it is essential to know the properties of natural gas, whose changes depending on the natural gas composition, pressure, and temperature can also be predicted using artificial neural network models. Chu et al. (2021) predicted the compressibility coefficient, sound velocity, and viscosity of natural gas, while Farzaneh-Gord et al. (2018) predicted the compressibility coefficient and sound velocity. The prediction of density (Al-Quraishi and Shokir, 2011; Wood and Choubineh, 2020) and viscosity of natural gas (Al-Quraishi and Shokir, 2011; Lay et al., 2012) using an artificial neural network model was based on the dependence of these parameters on pressure, temperature, and natural gas composition. The authors considered different numbers of gas components in the forecasting model. To predict the compressibility coefficient, sound velocity, and gas viscosity, the model included 10 gas components (Chu et al., 2021), while in (Lay et al., 2012), the model for predicting gas viscosity included 12 natural gas components and 21 gas components for predicting the compressibility coefficient and gas viscosity (Farzaneh-Gord et al., 2018).

Artificial neural network models have been successfully used to predict the heat of combustion or composition of natural gas mixtures produced in gas network pipelines supplied by various suppliers (Szoplik and Muchel, 2023a; Szoplik and Muchel, 2023b), the composition of liquid-gas mixtures produced in a distillation column (Singh et al., 2007), the composition of mixtures produced in the gasification process of various types of biomass (George et al., 2018), plant biomass components (Postawa et al., 2022), and reforming gas components in diesel engine exhaust (Park et al., 2020). In the analyzed cases, an MLP model with one or two hidden layers and the number of neurons in the output layer equal to the number of predicted components was used. The quality of the trained models was assessed based on the correlation or regression coefficient, while the quality of the forecasts was assessed based on the MAPE or RMSE errors. Analysis of the literature data has revealed numerous cases of artificial neural network models being used to predict the properties and composition of process mixtures. However, only Szoplik and Muchel (2023a) attempted to predict the share of five natural gas components at a selected point in a pipeline network supplied with gas of varying quality at multiple points. Szoplik and Muchel (2023a) proposed the use of the MLP 18-65-5 model trained on a set of 8,760 actual natural gas composition measurements obtained using gas chromatography method. The quality of the forecasts was assessed based on the average component-weighted MAPE error.

The aim of the research presented in this paper is to develop an MLP model for forecasting the shares of five natural gas mixture components at a selected point in the Polish gas transportation system, taking into account the minimum number of weather or calendar factors influencing the variability of the natural gas mixture composition. The selection of factors influencing the gas composition will be based on a statistical analysis of the relationships between these factors and the forecasted components. The determined number of factors influencing the natural gas composition will be the basis for determining the number of neurons in the MLP model's input layer, while the number of neurons in the model's output layer is five, equal to the number of forecasted components. The number of neurons in the hidden layer will be selected experimentally based on the results of the correlation coefficient of the model, the quality of the representation of the relationships between the forecasted component shares, and the mean $nRMSE_{aver}$ forecast errors. Training of MLP models with different structures to select the best model quality was conducted on the basis of varying sizes of real data sets presenting the change in natural gas composition in individual hours between 2017 and 2020.

2. STATISTICAL ANALYSIS OF THE INPUT AND OUTPUT DATA OF THE MLP MODEL

Developing a high-quality artificial neural network forecasting model requires statistical analysis of the correlation between factors that influence the predicted value, as well as analysis of the correlation between factors influencing the predicted

value and the predicted values. It was assumed that there should be no correlation between factors selected as model input parameters and that there should be a correlation between the model input parameters and the values predicted by the model. Statistical analysis was performed based on a dataset of $N_4 = 35,064$ datasets representing the shares of five selected natural gas components (forecasted values, model output data) in consecutive hours over four calendar years (2017–2020) at one of the natural gas composition measurement points in the Polish gas transportation system. The following factors influencing the natural gas mixture composition (model input data) were selected: month (M), day of the month (d/M), day of the week (d/W), hour of the day (h), ambient temperature (T), and gas flow rate (Q). Correlation analysis between input data, and then between input and output data, was performed by determining the Pearson correlation coefficient at a significance level of $\alpha = 5\%$. It was assumed that the correlation between variables is statistically significant when the p-test statistic is less than the assumed significance level ($p \leq \alpha$). However, if the p-test statistic is greater than the α-significance level, it indicates a lack of significant relationship between the two features.

The selection of natural gas mixture components, whose share in natural gas depends indirectly on gas consumption by consumers and may change over time, was analyzed in Szoplik and Muchel (2023a). Based on the significance of differences between the mean shares and standard deviation, it was demonstrated that the relationships between the five natural gas components selected for forecasting (CH_4, C_2H_6, C_3H_8, N_2, and CO_2) were statistically significant. The strongest positive correlation was observed between the shares of methane and carbon dioxide, while the strongest negative correlation was found between ethane and carbon dioxide. This is also confirmed by the results of Pearson correlation coefficient calculations determined for all pairs of the five selected natural gas components, which are summarized in Table 1. Analysis of the co-occurrence of selected gas component shares in the natural gas mixture transported through the pipeline network will be one of the criteria for assessing the quality of forecasts of these natural gas components obtained using the trained MLP model.

The selection of factors significantly affecting the composition of the natural gas mixture at a given measurement point on the high-pressure pipeline was based on an analysis of correlations between six factors that could affect the composition of natural gas, followed by a correlation between these six factors and the proportion of each of the five natural gas components. The analysis resulted in the selection of factors that lack significant correlation (model input data) but that significantly influence the predicted quantities. This ensures that the MLP neural network model will only contain input variables that significantly influence the predicted proportions of natural gas composition.

The results of correlation analysis among the model input data (month, day of the month, day of the week, hour of the day, ambient temperature, and gas flow rate) are summarized in Table 2. These variables can be divided into two groups: quantitative variables expressed numerically (day of the month, hour of the day, temperature, and volumetric flow rate) and qualitative variables expressed descriptively (month and day of the week). Temperature and flow rate were shown to be moderately correlated (−0.4495), which allows for the elimination of one of these variables. Weak correlations were also observed between temperature and month (0.1992) and temperature and hour of the day (0.1728), which may be due to temperature changes depending on the season (month) and time of day (hour of the day). Taking the above into account, the model can be simplified by eliminating temperature (T) or flow rate (Q) and month (M) or hour of the day (h) from the input data.

Table 1. Pearson correlation coefficients (top row) and p-test statistics (bottom row) for the model output variables ($\alpha = 0.05$).

Component	CH_4	C_2H_6	C_3H_8	N_2	CO_2
CH_4	1.000	–0.5464	–0.2722	–0.2245	0.7570
	$p =$ —	$p = 0$	$p = 0$	$p = 0$	$p = 0$
C_2H_6	–0.5464	1.000	–0.5735	–0.6639	–0.6075
	$p = 0$	$p =$ —	$p = 0$	$p = 0$	$p = 0$
C_3H_8	–0.2722	–0.5735	1.000	–0.7791	–0.0048
	$p = 0$	$p = 0$	$p =$ —	$p = 0$	$p = 0.365$
N_2	–0.2245	–0.6639	0.7791	1.000	–0.0009
	$p = 0$	$p = 0$	$p = 0$	$p =$ —	$p = 0.0281$
CO_2	0.7570	–0.6075	–0.0048	0.0281	1.000
	$p = 0$	$p = 0$	$p = 0.365$	$p = 0$	$p =$ —

The results of the correlation coefficient analysis between the model's input and output variables are summarized in Table 3, which clearly indicate a lack of a statistically significant relationship between the time of day and the shares of natural gas components. Assuming that a correlation should be present between the input and output variables of the forecasting model, the model was simplified by eliminating the hour of day (h) parameter from the input data. Based on the correlation coefficient analysis, it was assumed that it would be reasonable to exclude the gas flow rate (Q) and hour of day (h) from the input data of the MLP forecasting model, as these parameters have too strong a correlation with ambient temperature, and additionally, there is no correlation between the hour of day and natural gas components. Based on the results of statistical analysis of the structure of the set of 35,064 results of the share of methane, ethane, propane, nitrogen and carbon dioxide in natural gas depending on calendar and weather factors and gas flow, the following input parameters were selected for the forecasting model: month M, day of the month d/M, day of the week d/W and ambient temperature T, which, among the analyzed factors, have a statistically significant impact on the shares of natural gas components at a given composition measurement point in the high-pressure pipeline.

Table 2. Pearson correlation coefficients (top row) and p-test statistics (bottom row) for model input variables ($\alpha = 0.05$).

Variable	d/W	d/M	M	h	T	Q
d/W	1.000	0.0293	–0.0257	–0.0001	0.0317	0.0756
	$p =$ —	$p = 0$	$p = 0$	$p = 0.986$	$p = 0$	$p = 0$
d/M	0.0293	1.000	0.0105	0.000	0.0204	0.0006
	$p = 0$	$p =$ —	$p = 0.049$	$p = 1.000$	$p = 0$	$p = 0.918$
M	–0.0257	0.0105	1.000	0.000	0.1992	0.0004
	$p = 0$	$p = 0.049$	$p =$ —	$p = 1.000$	$p = 0$	$p = 0.940$
h	–0.0001	0.000	0.000	1.000	0.1728	0.0691
	$p = 0.986$	$p = 1.000$	$p = 1.000$	$p =$ —	$p = 0$	$p = 0$
T	0.0317	0.0204	0.1992	0.1728	1.000	–0.4495
	$p = 0$	$p = 0$	$p = 0$	$p = 0$	$p =$ —	$p = 0$
Q	0.0756	0.0006	0.0004	0.0691	–0.4495	1.000
	$p = 0$	$p = 0.918$	$p = 0.940$	$p = 0$	$p = 0$	$p =$ —

Table 3. Pearson correlation coefficients (top row) and p-test statistics (bottom row) for model input and output variables ($\alpha = 0.05$).

Variable	CH_4	C_2H_6	C_3H_8	N_2	CO_2
d/W	0.0566	–0.0144	–0.0258	–0.0370	0.0556
	$p = 0$	$p = 0.007$	$p = 0$	$p = 0$	$p = 0$
d/M	0.0574	–0.0154	–0.0684	–0.0107	0.0466
	$p = 0$	$p = 0.004$	$p = 0$	$p = 0.046$	$p = 0$
M	0.0364	0.0141	–0.0654	–0.0374	–0.0238
	$p = 0$	$p = 0.008$	$p = 0$	$p = 0$	$p = 0$
h	0.0008	–0.0001	–0.0004	–0.0003	–0.0009
	$p = 0.882$	$p = 0.989$	$p = 0.944$	$p = 0.954$	$p = 0.866$
T	–0.0424	0.1925	–0.1514	–0.1905	–0.1352
	$p = 0$	$p = 0$	$p = 0$	$p = 0$	$p = 0$
Q	0.0182	–0.1494	0.1367	0.1554	0.0183
	$p = 0.001$	$p = 0$	$p = 0$	$p = 0$	$p = 0.001$

3. RESEARCH METHODOLOGY

To predict the composition of the natural gas mixture, an MLP artificial neural network model with a single hidden layer was selected, in which signals flow in one direction from the input layer X to the output layer Z (Fig. 1). Development of the MLP artificial neural network model involves determining the number of neurons in each of the model layers (input, hidden and output). The number of neurons in the input layer was selected based on a statistical analysis of factors influencing the change in the natural gas mixture composition. The developed model uses a total of 17 neurons in the input layer of the MLP model, containing 15 qualitative variables representing 3 types of day of the week (working D_1, holiday D_2 and weekend D_3 days) and 12 months of the year ($M_1, \ldots, M_{12}$) and 2 quantitative variables corresponding to the day of the month (d/M) and the ambient temperature (T). In the output layer of the MLP model, 5 neurons were used, corresponding to the shares of methane y_{CH_4}, ethane $y_{C_2H_6}$, propane $y_{C_3H_8}$, nitrogen y_{N_2} and carbon dioxide y_{CO_2} in natural gas.

The number of neurons in the hidden layer of the MLP model was selected experimentally based on the analysis of the correlation coefficient results and the mean errors of $nRMSE_{aver}$ forecasts performed using models trained on data sets of different sizes (8,760 – 35,064) and the analysis of the predicted co-occurrence of selected components in natural gas.

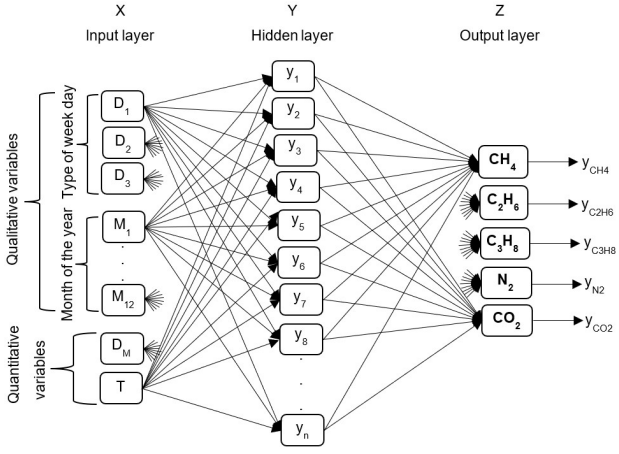


Figure 1. Schematic diagram of the MLP 17-y_n-5 model with any number of neurons in one hidden layer.

The quality of natural gas composition forecasts using MLP models was assessed based on the average $nRMSE_{aver}$ forecast error determined from Equations (1)–(3), based on the predicted and actual shares of selected natural gas components (i: y_{CH_4}, $y_{C_2H_6}$, $y_{C_3H_8}$, y_{N_2}, y_{CO_2}). The mean normalized $nRMSE_{aver}$ forecast error was used instead of the popular $MAPE_{aver}$ error due to the different values of the predicted shares of natural gas components (from 0 to 0.97).

$$nRMSE_{aver} = \frac{\sum_{i=1}^{i=5} nRMSE_i}{5} \quad (1)$$

$$nRMSE_i = \frac{RMSE_i}{y_{i,exp,max} - y_{i,exp,min}} \quad (2)$$

$$RMSE_i = \sqrt{\frac{1}{N}\sum \left(y_{i,exp} - y_{i,MLP}\right)^2} \quad (3)$$

The model was trained in Statistica using datasets of various sizes ($N_1 \div N_4$), including the shares of the five natural gas components (model output) and previously selected weather and calendar factors (model input). The data set sizes used in the model training process are summarized in Table 4.

Neural network training included: a network model training process involving modification of the weights of the hidden and output layer neurons; a validation process for ongoing monitoring of the training process; and a testing process used to assess the network's quality after training. During the neural network training process, each dataset was randomly divided into three subsets: a training subset (L) containing 70% of the data, a validation subset (V) containing 10% of the data and a test subset (T) containing 20% of the data from the entire N dataset. The training process involved selecting network neuron parameters in subsequent iterations (epochs) using the Broyden-Fletcher-Goldfarb-Shanno (BFGS) variable metric method, testing various activation functions for the hidden and output layers (linear, logistic, or hyperbolic tangent). For each dataset, differing in the number of cases, 200 MLP 17-y_n-5 models were trained for different numbers of neurons in the hidden layer in the range $y_n \in (30 \div 230)$. Models with the highest values of correlation coefficients R were selected for further analyses and comparisons (R_L, R_V, R_T).

4. RESEARCH RESULTS

The development of the MLP 17-y_n-5 model for forecasting the shares of five selected natural gas components was based on experimental selection of the number of neurons in the hidden layer of the model, trained on various size datasets. Additionally, the forecast results for the shares of the five natural gas components, obtained using the best-quality MLP 17-y_n-5 model, would be compared with the forecast results for the natural gas components obtained individually using five MLP 17-y_n-1 models. The best-quality model would be selected based on forecast results assessed based on the nRMSE forecast error. Model training and verification, as well as the forecasting of the gas component shares, were based on real data representing the natural gas composition at successive hours of the day over a five-year period, provided by the GAZ-SYSTEM S.A. – Gas Transmission Operator of the Polish natural gas network under a mutual cooperation and information exchange agreement.

4.1. Selecting the size of the training dataset and the number of neurons in the hidden layer of the MLP model

To select the number of neurons in the model's hidden layer and the size of the training dataset, a total of 16,000 MLP models were trained, differing in the number of neurons in the hidden layer ($y_n = 30 \div 230$ neurons) and the size of the training dataset (from $N_1 = 8,760$ to $N_4 = 35,064$ data). The results, in the form of correlation coefficients R_T and the prediction error nRMSE as a function of the number of neurons in the model's hidden layer, are presented in Fig. 2 and Fig. 3. Based on the analysis of the data, it was found that the size of the dataset used to train the MLP models has a greater impact on the model quality (expressed by the R coefficient) and the forecast quality (determined by the nRMSE error) than the number of neurons in the model's hidden layer.

The highest values of correlation coefficients for the training, test, and validation sets (R_L, R_T and R_V) are characteristic of the smallest data set $N_1 = 8,760$, while the lowest nRMSE forecast errors correspond to models trained on the largest data set $N_4 = 35,064$. The reduction in the correlation coefficients for models trained with the largest data set can be explained by the presence of data characterizing the COVID-19 pandemic period, which, due to unusual

Table 4. The sizes of data sets used in the MLP model training process.

Period of time	N_1 (2018)	N_2 (2017÷2018)	N_3 (2017÷2019)	N_4 (2017÷2020)	N_5 (2021)
Dataset sizes	8,760	17,520	26,280	35,064	8,760
Purpose	training	training	training	training	verification

changes in gas pipeline load and changes in flow direction in network pipelines (these values have an indirect impact on the composition of natural gas), was not representative of the pre-pandemic period.

Assuming that the best quality model should be characterized by a high correlation coefficient and low forecast error, such a model cannot be clearly identified based on the results presented in Fig. 2 and Fig. 3. Furthermore, there was no clear effect of the number of neurons in the hidden layer on the quality of the model or forecast, therefore, models with the lowest number of neurons in the hidden layer, trained on the N_1 or N_4 set, were selected to analyze the quality of the shares of gas component forecasts. Detailed results in the form of forecast errors for the shares of individual gas components, the average $nRMSE_{aver}$ error, and the correlation coefficient for the test set are summarized in Table 5.

Therefore, the selection of the data set size used to train the MLP model was based on an analysis of the interdependencies between the forecasted natural gas components. Figures 4 and 5 present the results of forecasts of the methane and ethane shares in natural gas, which were made for new data $N_5 = 8,760$ using the MLP 17-40-5 model (trained on N_1 data) and the MLP 17-37-5 model (trained on N_4 data). Analysis of the results in Figures 4 and 5 indicates that the relationships between the two forecasted natural gas components were best modeled using the MLP 17-40-5 model (N_1). The nature of the variability of the individual natural gas components in this case is similar to that observed in the real

Table 5. The summary of forecast error $nRMSE_i$ and $nRMSE_{aver}$ results.

MLP model dataset	MLP 17-40-5 ($N_1 = 8,760$)	MLP 17-37-5 ($N_4 = 35,064$)
component	$nRMSE_i$	$nRMSE_i$
CH_4	0.3135	0.2556
C_2H_6	0.4086	0.2784
C_3H_8	0.3315	0.3155
N_2	0.2986	0.2684
CO_2	0.2575	0.1805
$nRMSE_{aver}$	0.3219	0.2597
R_T	0.9700	0.5700

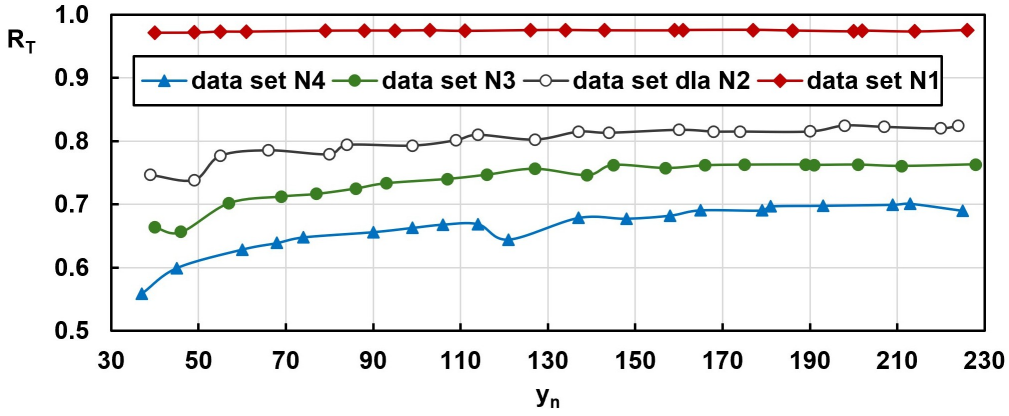


Figure 2. Values of R_T coefficient of MLP 17-y_n-5 models trained in different numbers of data ($N_1 = 8,760$, $N_2 = 17,520$, $N_3 = 26,280$, $N_4 = 35,064$).

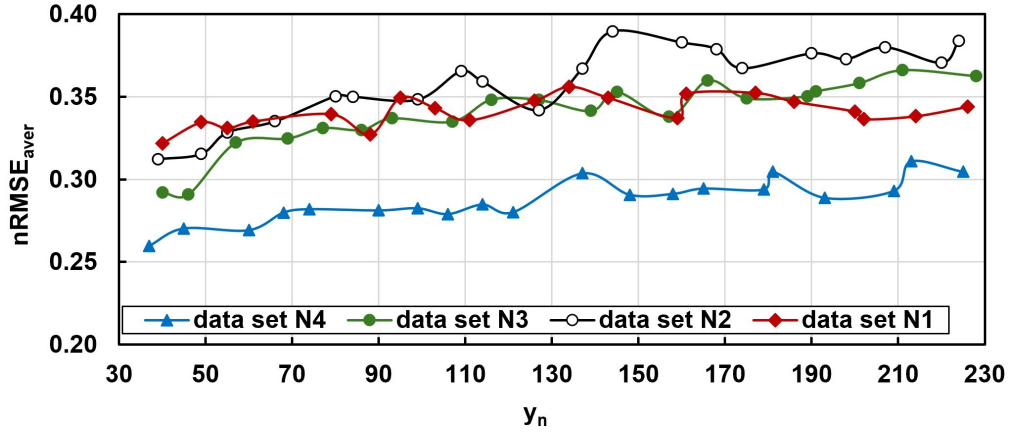


Figure 3. Values of $nRMSE_{aver}$ prediction errors of MLP 17-y_n-5 models trained on sets with different numbers of data (N_1, N_2, N_3, N_4).

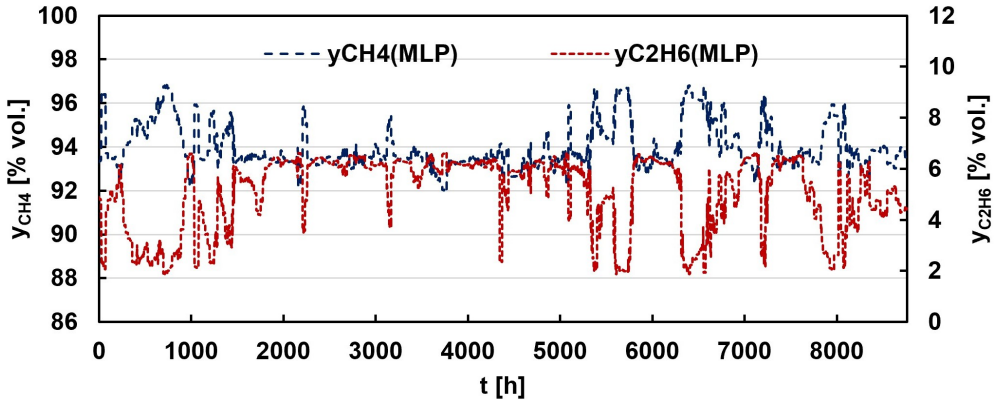


Figure 4. Variability of the predicted methane and ethane shares using the MLP 17-40-5 (N_1) model; forecast results for data set N_5.

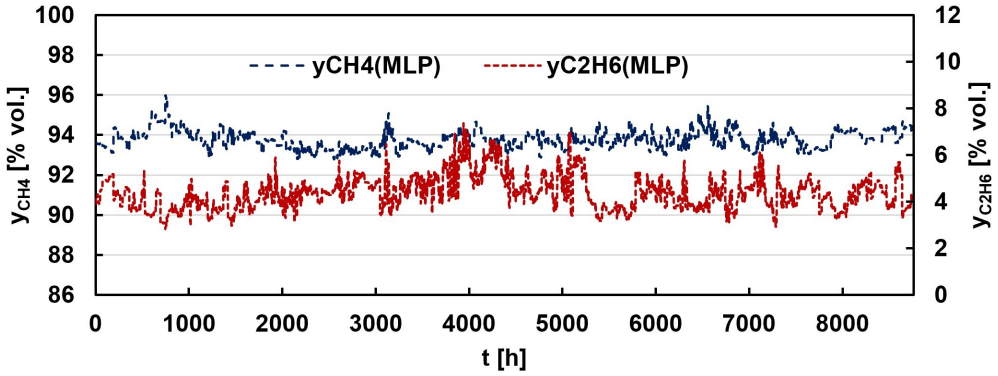


Figure 5. Variability of the predicted methane and ethane shares using the MLP 17-37-5 (N_4) model; forecast results for data set N_5.

data (an increase of methane content in natural gas causes a decrease in ethane content, and a decrease in methane content to a level of approximately 93%vol. is associated with a reduction in the carbon dioxide share to 0%).

However, increasing the data set size (N_4) for training the MLP model resulted in the relationships between the forecasted components becoming less clear and less accurate, and the forecasted values exhibiting greater variability over shorter time periods. This may be because models trained on a larger dataset recognize additional relationships or trends that were not apparent during statistical data analysis and that can complicate forecasting of natural gas components without introducing an additional input variable that significantly affects the composition of the natural gas mixture. Based on the results of the MLP model training quality, forecast errors, and the quality of the representation of relationships between the forecasted natural gas components, it was decided to train the MLP model for natural gas composition forecasting on a data of $N_1 = 8,760$.

The number of neurons in the hidden layer of the 17-y_n-5 MLP model was experimentally selected from a new set of 2,200 MLP models trained only on the $N_1 = 8,760$ dataset. The BFGS learning algorithm was applied and 200 MLP models were trained for 11 different numbers of neurons in the hidden layer of the network, narrowing the number of neurons in the hidden layer to $y_n \in \langle 35 \div 45 \rangle$. The best quality models for a given number of neurons y_n (ranging from 35 to 45) were then used to predict the natural gas composition for the new N_5 dataset.

Based on the model quality results and the natural gas composition forecast results obtained for the N_5 new data set, it was found that the MLP 17-37-5 model (logistic activation functions of neurons in the hidden and output layers) is characterized by the highest correlation coefficient $R_T = 0.9711$ and a low mean forecast error $nRMSE_{\text{aver}} = 0.321$.

4.2. Results of forecasting the shares of natural gas components using the MLP 17-37-5 or MLP 17-37-1 models

Detailed forecast results for the five natural gas components (methane, ethane, propane, nitrogen, and carbon dioxide) obtained for a new data set ($N_5 = 8,760$), which were not used in the training process of the MLP 17-37-5 model (model schematically presented in Fig. 1), compared with actual data, are presented in Fig. 6. Analysis of these results showed that the differences between the predicted and real shares of a given natural gas component can reach up to 4%, and most often, overestimating the share of one component leads to underestimating the share of another component, and vice versa.

However, the relationships between the shares of the main natural gas components are well represented (e.g., a higher share of methane reduces the share of ethane). Based on the forecast results and data on the actual shares of the five selected natural gas components, the nRMSE forecast error values for each component and the average forecast error made by the MLP 17-37-5 model were determined (results in Fig. 9). Taking into account the size of the average error nRMSE, it was found that a model with such a structure can be successfully used to simultaneously forecast five natural gas components.

To verify whether it is possible to obtain gas component forecasts with an average $nRMSE_{aver}$ error of less than 0.3210 (for the MLP 17-37-5 model), five MLP 17-37-1 models were trained to forecast each natural gas component individually. Similarly to the training of the MLP 17-37-5 model, logistic activation functions of the hidden and output layer neurons and the BFGS learning algorithm were used. The diagrams of the five MLP 17-37-1 models are presented in Fig. 7. The MLP 17-37-1 models were trained using a data set $N_1 = 8,760$ (the same set used to train the MLP 17-37-5 model).

The results of individual forecasts of the shares of five natural gas components made using the MLP 17-37-1 models for the new $N_5 = 8,760$ data set and the actual share data of these components in natural gas are presented in Fig. 8. Also in this case, regardless of the forecasted gas component, the forecast results are observed to be

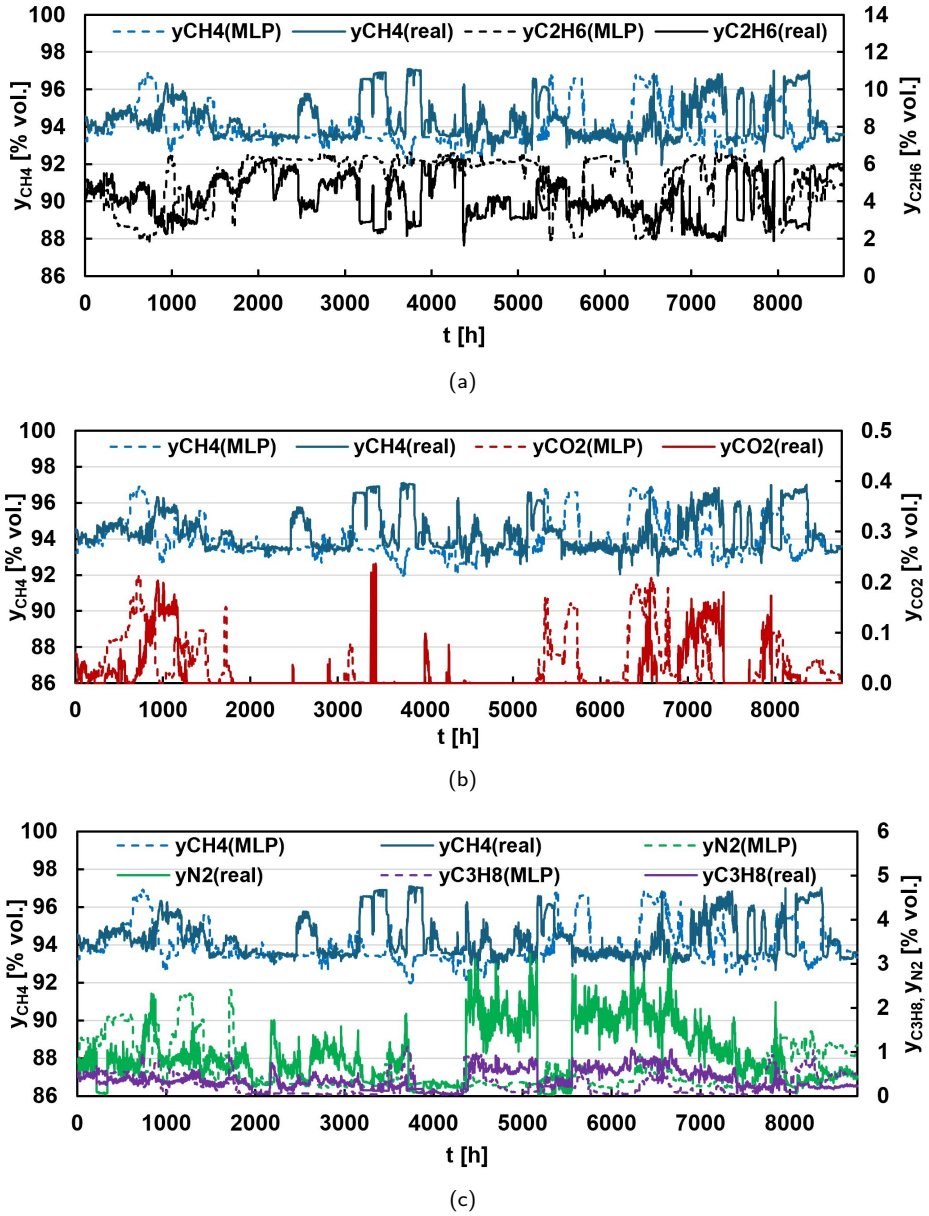


Figure 6. Variability of the actual and predicted shares of the five natural gas components using the MLP 17-37-5 model trained on a data set of $N_1 = 8,760$; a) methane and ethane, b) methane and carbon dioxide, c) methane, propane, and nitrogen; forecast results for data set $N_5 = 8,760$.

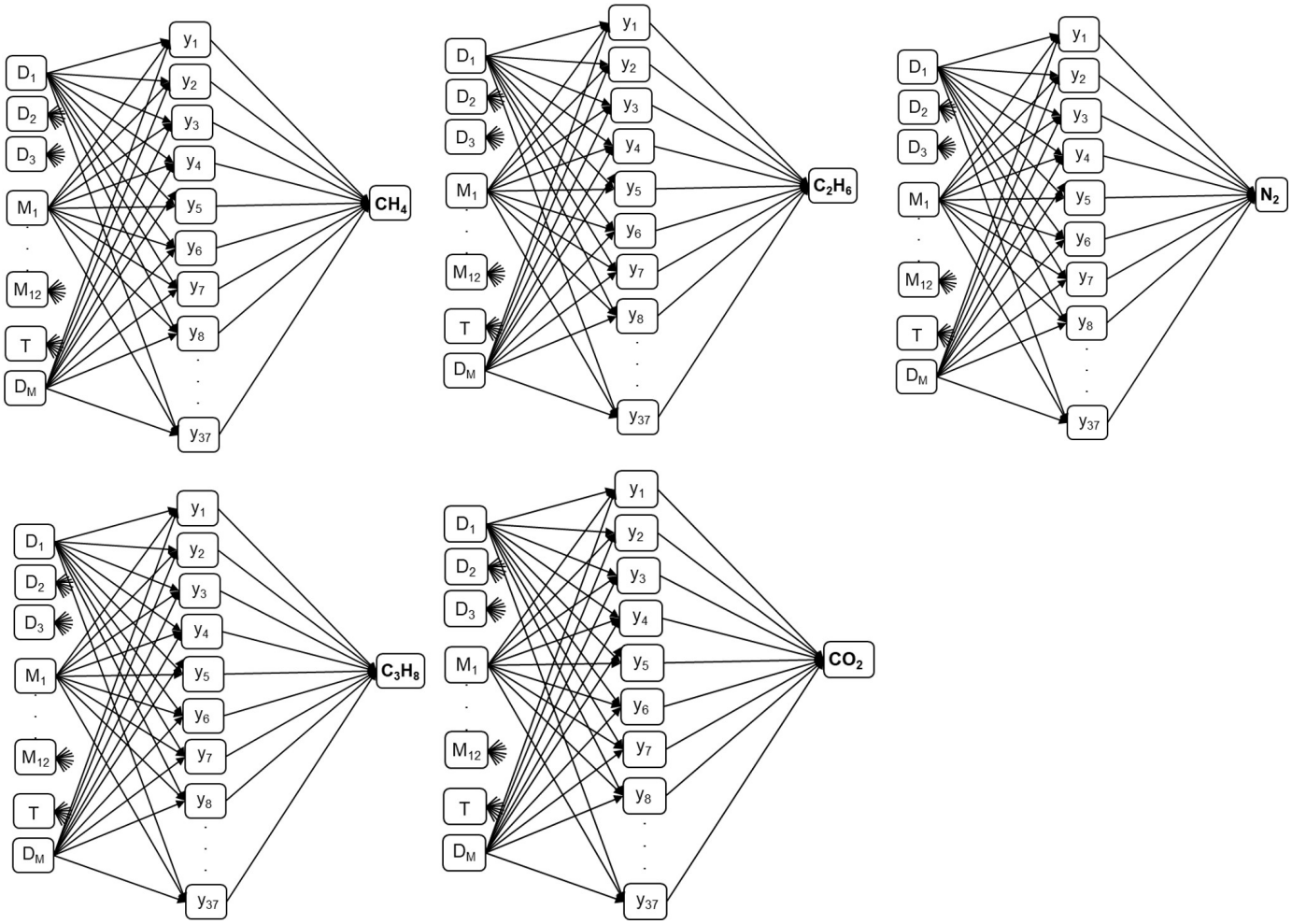


Figure 7. Schematic diagram of the MLP 17-37-1 for predicting the content of individual natural gas components: CH_4, C_2H_6, C_3H_8, N_2, CO_2.

higher or lower than the actual data by approximately 4%. Comparing the results presented in Fig. 6 and Fig. 8, it was observed that for a given natural gas component, better quality forecasts can be obtained using the MLP 17-37-5 model compared to the MLP 17-37-1 model.

Table 6 summarizes the correlation coefficients of the MLP 17-37-1 models and the MLP 17-37-5 model trained on the $N_1 = 8,760$ data set. The training results of the MLP 17-37-1 models indicate that the R_T correlation coefficient values of the models forecasting each natural gas component individually differ slightly, and the average R_T value for all MLP 17-37-1 models is only 0.37% higher compared to the R_T value obtained for the 17-37-5 model. However, based on the results of the real and forecasted (for the $N_5 = 8,760$ data set) shares of the five natural gas components, the nRMSE forecast errors were determined for each component and the averaged value for each MLP model.

Detailed results of the calculations of the average nRMSE forecast errors for each component forecasted by the MLP 17-37-5 model or the five MLP 17-37-1 models are presented in Fig. 9. Considering the results presented in Fig. 9, it can be concluded

Table 6. Parameters R_T and nRMSE of MLP 17-37-1 or MLP 17-37-5 models.

Model	Component	R_T	Algorithm	$nRMSE_{aver}$
MLP 17-37-1	CH_4	0.9663	BFGS 671	0.3383
	C_2H_6	0.9777	BFGS 750	
	C_3H_8	0.9838	BFGS 588	
	N_2	0.9805	BFGS 764	
	CO_2	0.9651	BFGS 430	
MLP 17-37-5	CH_4, C_2H_6, C_3H_8, N_2, CO_2	0.9711	BFGS 820	0.3210

that the better quality MLP model for forecasting of the five natural gas components shares was trained using five neurons in the output layer (lower forecast error $nRMSE_{aver}$). The MLP 17-37-5 model, although characterized by a slightly lower correlation coefficient compared to the mean R_T obtained for the MLP 17-37-1 models, allows for the preparation of better quality forecasts of the shares of the natural gas components.

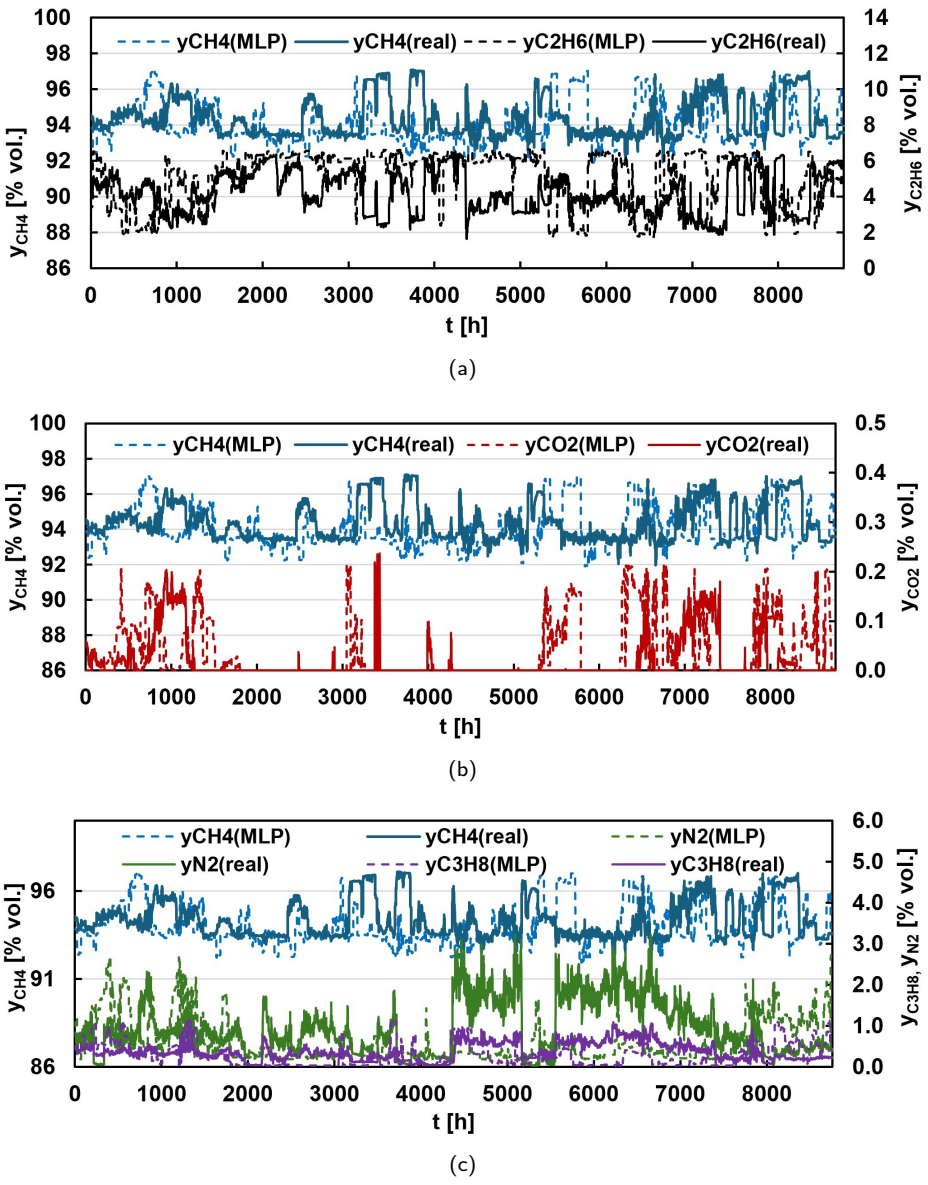


Figure 8. Variability of the actual and predicted shares of the five natural gas components using the MLP 17-37-1 models trained on a data set of $N_1 = 8,760$; a) methane and ethane, b) methane and carbon dioxide, c) methane, propane, and nitrogen; forecast results for data set $N_5 = 8,760$.

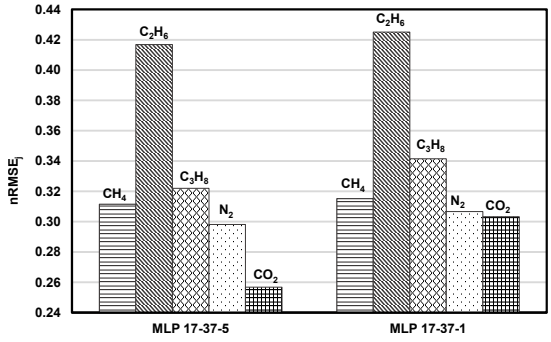


Figure 9. Forecast errors $nRMSE_j$ and $nRMSE_{aver}$ obtained with the MLP 17-37-1 and MLP 17-37-5 models; results for dataset $N_5 = 8,760$.

5. CONCLUSIONS

Based on the data set $N_1 = 8,760$ or $N_4 = 35,064$, the MLP 17-37-5 model was trained to forecast five natural gas components (methane, ethane, propane, nitrogen, and carbon dioxide) with an average prediction error nRMSE = 0.321. The input data for the MLP model were selected based on the results of statistical analysis of the correlations between input variables and between input variables and forecasted components. This allowed to reduce the number of input variables of the forecasting model to 17 neurons.

Compared to the results of the research presented in Szoplik and Muchel (2023a), the number of neurons in the model's input layer was reduced from 18 to 17, which also resulted

in a reduction of the number of neurons in the hidden layer from 65 to 37. However, such model simplification allowed to maintain good quality forecasts of the five natural gas component shares.

Based on the results of MLP forecasting models with datasets of different sizes ($N_1 = 8,760$ or $N_4 = 35,064$), it was also demonstrated that other unusual factors can indirectly influence changes in gas composition. One such unusual factor was the presence of the COVID-19 pandemic, which indirectly influenced the change in gas flow direction in some gas network pipelines due to changes in the load on the gas pipelines. In this case, an additional factor describing this unusual situation should be included among the MLP model input data.

The proposed MLP 17-37-5 model allows to forecast natural gas composition over a one-year period with a weighted average error of MAPE $\approx 3\%$, while the mean relative error of the heat of combustion calculated based on the predicted gas composition and the heat of combustion calculated based on the actual natural gas composition is 1.57%. Furthermore, no better quality forecasts of natural gas component shares were found by using five MLP 17-37-1 models to individually forecast the share of each component.

ACKNOWLEDGMENTS

The calculations presented in the paper were made on the basis of real data provided by the GAZ-SYSTEM — Gas Transmission Operator of the Polish natural gas network. The authors would like to thank the company for cooperation.

REFERENCES

Al-Quraishi A.A., Shokir E.M., 2011. Artificial neural networks modeling for hydrocarbon gas viscosity and density estimation. *J. King Saud Univ. Eng. Sci.*, 23, 123–129. DOI: 10.1016/j.jksues.2011.03.004.

Alves Jr. O., Fontes C., 2022. Modeling and optimization of natural gas distribution networks for new supplier projects. *Energy Convers. Manage., X*, 15, 100240. DOI: 10.1016/j.ecmx.2022.100240.

Bermúdez A., Shabani M., 2022. Numerical simulation of gas composition tracking in a gas transportation network. *Energy*, 247, 123459. DOI: 10.1016/j.energy.2022.123459.

Bianco V., Scarpa F., Tagliafico L.A., 2014. Scenario analysis of nonresidential natural gas consumption in Italy. *Appl. Energy*, 113, 392–403. DOI: 10.1016/j.apenergy.2013.07.054.

Chaczykowski M., Sund F., Zarodkiewicz P., Hope S.M., 2018. Gas composition tracking in transient pipeline flow. *J. Nat. Gas Sci. Eng.*, 55, 321–330. DOI: 10.1016/j.jngse.2018.03.014.

Chaczykowski M., Zarodkiewicz P., 2017. Simulation of natural gas quality distribution for pipeline systems. *Energy*, 134, 681–698. DOI: 10.1016/j.energy.2017.06.020.

Chu J., Liu X., Zhang Z., Zhang Y., He M., 2021. A novel method overcomeing overfitting of an artificial neural network for accurate prediction: application on thermophysical property of natural gas. *Case Stud. Therm. Eng.*, 28, 101406. DOI: 10.1016/j.csite.2021.101406.

Durmayaz A., Kadioğlu M., Şen Z., 2000. An application of the degree-hours method to estimate the residential heating energy requirement and fuel consumption in Istanbul. *Energy*, 25, 1245–1256. DOI: 10.1016/S0360-5442(00)00040-2.

Fan D., Gong J., Zhang S., Shi G., Kang Q., Xiao Y., Wu C., 2021. A transient composition tracking method for natural gas pipe networks. *Energy*, 215, 119131. DOI: 10.1016/j.energy.2020.119131.

Farzaneh-Gord M., Mohseni-Gharyehsafa B., Ebrahimi-Moghadam A., Jabari-Moghadam A., Toikka A., Zvereva I., 2018. Precise calculation of natural gas sound speed using neural networks: an application in flow meter calibration. *Flow Meas. Instrum.*, 64, 90–103. DOI: 10.1016/j.flowmeasinst.2018.10.013.

Geem Z.W., Roper W.E., 2009. Energy demand estimation of South Korea using artificial neural network. *Energy Policy*, 37, 4049–4054. DOI: 10.1016/j.enpol.2009.04.049.

George J., Arun P., Muraleedharan C., 2018. Assessment of producer gas composition in air gasification of biomass using artificial neural network model. *Int. J. Hydrogen Energy*, 43, 9558–9568. DOI: 10.1016/j.ijhydene.2018.04.007.

Hafezi R., Akhavan A.N., Zamani M., Pakseresht S., Shamshirband S., 2019. Developing a data mining based model to extract predictor factors in energy systems: application of global natural gas demand. *Energies*, 12, 4124. DOI: 10.3390/en12214124.

Kenisarin M., Kenisarina K., 2007. Energy saving potential in the residential sector of Uzbekistan. *Energy*, 32, 1319–1325. DOI: 10.1016/j.energy.2006.09.014.

Kumor M., Porada S., 2021. Polish LNG terminal influence on natural gas quality available in the Polish gas transmission network. *IOP Conf. Ser.: Earth Environ. Sci.*, 642, 012003. DOI: 10.1088/1755-1315/642/1/012003.

Lay E.N., Peymani M., Sanjari E., 2012. Prediction of natural gas viscosity using artificial neural network approach. *Int. J. Chem. Mol. Eng.*, 6, 577–583. DOI: 10.5281/zenodo.1333845.

Merkel G.D., Povinelli R.J., Brown R.H., 2018. Short-term load forecasting of natural gas with deep neural network regression. *Energies*, 11, 2008. DOI: 10.3390/en11082008.

Muchel P., 2024. *Modeling the variability of the composition of natural gas using the Artificial Neural Networks Method*. PhD Thesis. West Pomeranian University of Technology in Szczecin, Poland.

Osiadacz A.J., Chaczykowski M., 2020. Modeling and simulation of gas distribution networks in a multienergy system environment. Proc. IEEE, 108, 1580–1595. DOI: 10.1109/JPROC.2020.2989114.

Parikh J., Purohit P., Maitra P., 2007. Demand projections of petroleum products and natural gas in India. *Energy*, 32, 1825–1837. DOI: 10.1016/j.energy.2007.02.008.

Park J., Cho J., Choi H., Park J., 2020. Prediction of reformed gas composition for diesel engines with a reformed EGR system using an artificial neural network. *Energies*, 13, 5886. DOI: 10.3390/en13225886.

Postawa K., Fałtynowicz H., Pstrowska K., Szczygieł J., Kułażyński M., 2022. Artificial neural networks to differentiate the composition and pyrolysis kinetics of fresh and long-stored maize. *Bioresour. Technol.*, 364, 128137. DOI: 10.1016/j.biortech.2022.128137.

Saedi I., Mhanna S., Mancarella P., 2021. Integrated electricity and gas system modelling with hydrogen injections and gas composition tracking. *Appl. Energy*, 303, 117598. DOI: 10.1016/j.apenergy.2021.117598.

Sarak H., Satman A., 2003. The degree-day method to estimate the residential heating natural gas consumption in Turkey: a case study. *Energy*, 28, 929–939. DOI: 10.1016/S0360-5442(03)00035-5.

Satman A., Yalcinkaya N., 1999. Heating and cooling degree-hours for Turkey. *Energy*, 24, 833–840. DOI: 10.1016/S0360-5442(99)00035-3.

Singh V., Gupta I., Gupta H.O., 2007. ANN-based estimator for distillation using Levenberg–Marquardt approach. *Eng. Appl. Artif. Intell.*, 20, 249–259. DOI: 10.1016/j.engappai.2006.06.017.

Szoplik J., 2015. Forecasting of natural gas consumption with artificial neural networks. *Energy*, 85, 208–220. DOI: 10.1016/j.energy.2015.03.084.

Szoplik J., 2016. Improving the natural gas transporting based on the steady state simulation results. *Energy*, 109, 105–116. DOI: 10.1016/j.energy.2016.04.104.

Szoplik J., 2017. Changes in gas flow in the pipeline depending on the network foundation in the area. *J. Nat. Gas Sci. Eng.*, 43, 1–12. DOI: 10.1016/j.jngse.2017.03.020.

Szoplik J., Muchel P., 2023a. Using an artificial neural network model for natural gas heat combustion forecasting. *Chem. Process Eng.*, 44, e19. DOI: 10.24425/cpe.2023.146721.

Szoplik J., Muchel P., 2023b. Using an artificial neural network model for natural gas compositions forecasting. *Energy*, 263, 126001. DOI: 10.1016/j.energy.2022.126001.

Wang B., Guo Y., Wang D., Zhang Y., He R., Chen J., 2022. Prediction model of natural gas pipeline crack evolution based on optimized DCNN-LSTM. *Mech. Syst. Signal Process.*, 181, 109557. DOI: 10.1016/j.ymssp.2022.109557.

Wen K., He L., Liu J., Gong J., 2019. An optimization of artificial neural network modeling methodology for the reliability assessment of corroding natural gas pipelines. *J. Loss Prev. Process Ind.*, 60, 1–8. DOI: 10.1016/j.jlp.2019.03.010.

Wood D.A., Choubineh A., 2020. Transparent machine learning provides insightful estimates of natural gas density based on pressure, temperature and compositional variables. *J. Nat. Gas Geosci.*, 5, 33–43. DOI: 10.1016/j.jnggs.2019.12.003.

Zhang Z., Saedi I., Mhanna S., Wu K., Mancarella P., 2022. Modelling of gas network transient flows with multiple hydrogen injections and gas composition tracking. *Int. J. Hydrogen Energy*, 47, 2220–2233. DOI: 10.1016/j.ijhydene.2021.10.165.

Chemical and Process Engineering: New Frontiers, 2026, 47(2), e137
DOI: 10.24425/cpe.2026.158135

In situ polymerization of *p*-phenylenediamine on a bacterial cellulose matrix as a potential glucose biosensor

Tobiasz Gabryś, Dorota Biniaś

Institute of Engineering Sciences, Faculty of Materials, Civil and Environmental Engineering, University of Bielsko-Biala, Willowa 2, 43-309 Bielsko-Biala, Poland.

* **Corresponding author, e-mail:** tgabrys@ubb.edu.pl

Article info:
Received: 31 March 2026
Revised: 15 May 2026
Accepted: 29 May 2026

Abstract
Bacterial cellulose (BC) is a biopolymer distinguished by its high purity, nanofibrillar structure, large specific surface area, and excellent mechanical and biocompatible properties, making it an attractive platform for biosensing applications. In this study, we report the *in situ* polymerization of *p*-phenylenediamine (PPD) on a bacterial cellulose matrix as a novel strategy for the fabrication of a functional composite material with potential biosensor applications. The polymerization process was carried out directly within the BC network, enabling uniform deposition and strong interfacial interactions between the polymer phase and the cellulose nanofibers. The resulting BC/PPD composite was characterized using spectroscopic, structural, and morphological analyses to confirm successful polymer formation and integration within the BC matrix. The modification led to noticeable changes in the physicochemical properties of bacterial cellulose, including enhanced electrical responsiveness and altered surface chemistry, which are critical parameters for sensor performance. Owing to the combination of BC's porous architecture and the functional properties of poly(*p*-phenylenediamine), the developed composite demonstrates promising potential as a flexible, biocompatible sensing platform for future biosensor and bioelectronic applications.

Keywords
bacterial cellulose, flexible biosensor, modification, polymerization

1. Introduction

Cellulose is a ubiquitous natural polymer that plays a fundamental role in numerous industrial, biomedical, and technological applications. While plant-derived cellulose has traditionally dominated practical use, increasing attention has been directed toward BC, a structurally distinct form of cellulose biosynthesized by aerobic bacteria, primarily belonging to the genus *Komagataeibacter*. Despite its identical chemical composition to plant cellulose, bacterial cellulose exhibits a unique set of properties resulting from its biological mode of synthesis, which confers a highly ordered three-dimensional nanofibrillar architecture (Iguchi et al., 2000). The absence of lignin, hemicelluloses, and other plant-derived impurities gives bacterial cellulose exceptionally high chemical purity, uniformity, and reproducibility. It is a nanoscale fiber network that provides a large specific surface area, high crystallinity, and remarkable mechanical strength, while maintaining flexibility and excellent water retention capacity (Sozcu et al., 2025). These characteristics have driven extensive research into BC-based materials for biomedical engineering, including wound dressings, tissue scaffolds, and drug delivery systems, where biocompatibility and structural integrity are of critical importance (Gorgieva and Trček, 2019).

In recent years, the application scope of bacterial cellulose has expanded beyond passive biomedical materials toward active functional systems, particularly in the field of biosensing. The highly porous structure of BC enables efficient diffusion of analytes, while the abundance of hydroxyl groups on cellulose chains allows for chemical modification and immobilization of functional components. These features make BC an attractive matrix for the fabrication of composite materials designed to exhibit electrical, electrochemical, or stimuli-responsive behaviour (Gabryś et al., 2022). One promising approach to impart such functionality involves the incorporation of redox-active or conducting polymers into the bacterial cellulose network. Among aromatic amine monomers, PPD has gained interest due to its ability to undergo oxidative polymerization, forming poly(*p*-phenylenediamine), a conjugated polymer with redox activity and electrical conductivity. PPD is a low-molecular-weight diamine characterized by a rigid aromatic backbone and reactive amino groups, which facilitate polymer growth and strong interactions with hydroxyl-rich substrates such as cellulose. The polymerization of *p*-phenylenediamine can be achieved via chemical or electrochemical oxidation, resulting in polymer chains capable of participating in electron transfer processes (Hasan et al., 2025). Materials based on poly(*p*-phenylenediamine) have been investigated in a range of sensing-related applications, including electrochemical sensors and chemically responsive coatings, due to their sensitivity to environmental changes and their ability to mediate charge transport. When combined with biopolymer matrices, such polymers can form hybrid systems that integrate mechanical flexibility, biocompatibility, and functional electrical properties. In situ polymerization of PPD within a bacterial cellulose matrix represents a particularly effective strategy for composite fabrication (Yu et

© 2026. The Author(s). This is an open-access article distributed under the terms of the Creative Commons Attribution (CC-BY 4.0, https://creativecommons.org/licenses/by/4.0/), which permits unrestricted use, distribution, and reproduction in any medium, provided the original author and source are credited.

al., 2025). This approach enables uniform polymer deposition throughout the BC network, promotes strong interfacial interactions between the polymer phase and cellulose nanofibers, and minimizes phase separation. Similar cellulose-based composites incorporating conducting polymers such as polyaniline or polypyrrole have demonstrated enhanced sensing performance, confirming the suitability of cellulose as a scaffold for functional polymer systems.

The present study focuses on the synthesis and characterization of a bacterial cellulose–poly(*p*-phenylenediamine) (BC/PPD) composite obtained via *in situ* polymerization of PPD within the BC matrix. The work aims to evaluate the structural and physicochemical properties of the resulting material and to assess its potential as a platform for biosensor applications. By combining a natural, sustainable biopolymer with a functional aromatic polymer, this study contributes to the development of advanced bio-based materials for next-generation sensing technologies.

2. Experimental Work

2.1. Materials

The chemicals used in the experiment included: D-glucose ($\geq$ 99%), meat peptone and sodium hydroxide ($\geq$ 97%, pellets) all purchased from Sigma Aldrich (Darmstadt, Germany); yeast extract and micro agar purchased from Duchefa Biochemie (Haarlem, The Netherlands); disodium hydrogen phosphate dihydrate purchased from Merck (Darmstadt, Germany); citric acid purchased from Chempur (Piekary Śląskie, Poland); acetic acid (99.8%); and ethanol (96%) purchased from Honeywell (Charlotte, NC, USA); *p*-phenylenediamine and iron chloride ($FeCl_3$) purchased from Pol-Aura (Morąg, Poland); PBS tablets (Phosphate Buffered Saline tablets) purchased from Bionovo (Legnica, Poland).

2.2. Microorganisms

The bacterial strains used in this study were *Komagataeibacter Intermedius* (LMG 18909) purchased from Belgian Coordinated Collections of Microorganism, which were maintained and precultured in the laboratory of Faculty of Materials, Civil and Environmental Engineering, University of Bielsko-Biala.

2.3. Production of Bacterial Cellulose

The reinforced acetic ethanol culture medium (RAE) used for bacterial cellulose production was selected for the biosynthesis process. The liquid medium contained glucose (40 g/L), peptone from meat (10 g/L), yeast extract (10 g/L), disodium hydrogen phosphate dihydrate ($Na_2HPO_4 \cdot 2H_2O$, 3.38 g/L), citric acid (1.37 g/L), acetic acid (10 mL/L), and ethanol (10 mL/L). The solid medium, used for bacterial revitalization and inoculation, included the same components with the addition of agar (10 g/L). All media were sterilized by autoclaving at 121 °C for 15 minutes. Acetic acid and ethanol were added to the medium after autoclaving. The bioprocesses were carried out in 250 mL Erlenmeyer flasks equipped with membrane screw caps. Each flask, containing 50 mL of RAE medium, was inoculated with a single bacterial colony and incubated in a water bath for 7 days at 30 °C. During the first 24 hours, the flasks were shaken; after this period, shaking was stopped and the bioprocess was continued under static conditions. In this manner, bacterial cellulose samples were obtained. The prepared BC samples were subsequently washed with distilled water. Next, the purification process, which allows the removal of bacterial cell residues, was initiated using 0.5 M NaOH. The purification was carried out in a water bath at 80 °C for 1 hour with shaking. Then, they were washed again with distilled water up to neutral pH.

2.4. *In Situ* Polymerization of *p*-Phenylenediamine on a Bacterial Cellulose Matrix

The aim of the study was to carry out oxidative polymerization of PPD using the *in situ* method, i.e., directly inside the bacterial cellulose matrix to obtain BC/PPD composite. Due to the original form of bacterial cellulose as a typical hydrogel, the polymerization procedure was shown in Figure 1. In order for the polymerization process to proceed evenly throughout the entire volume of the sample, a previously prepared disc of moist and purified BC weighing 28 g was placed for 24 hours in a beaker containing 92.5 mL of a 0.1 M aqueous solution of PPD.

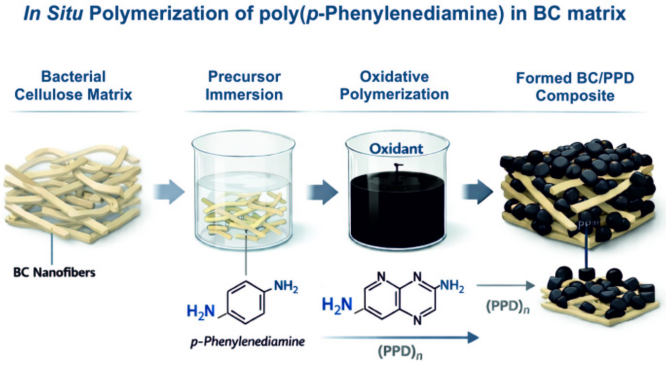


Figure 1. Scheme showing the modification process.

After this time, the beaker was placed in a water bath at a temperature of 10 °C and 185 mL of a 0.1 M iron chloride solution, which acted as an oxidizing agent, was slowly added drop by drop. Polymerization was carried out for 3 hours at a temperature of 10 °C, continuously adding the oxidizing agent and gently stirring the sample. This process allows for the gradual and equal penetration of the oxidizing agent into the BC matrix. After this time, the temperature was

increased to 30 °C, thus completing the polymerization process. The sample of BC/PPD was then rinsed several times with distilled water to remove any post-reaction residues.

The final stage was the protonation of the composite to increase its conductivity. The previously obtained composite was completely immersed for 30 minutes in 0.1 M HCl at a temperature of 21 °C. Then it was rinsed again with distilled water until the acid was neutralized. The samples prepared in this way were subjected to further testing. Figure 2 shows the experimental work.

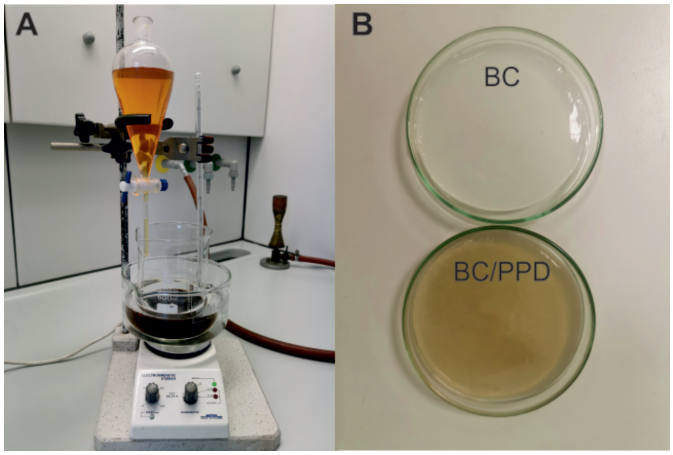


Figure 2. Experimental work (A); BC sample before and after polymerization of PPD.

2.5. Microscopy Analysis

The freeze-dried BC and BC/PPD samples were subjected to analysis using scanning electron microscopy JSM 5500 LV (Jeol, Japan), which enabled detailed observation of the surface morphology and internal structure of the materials. Prior to analysis, the samples were sputtered with gold in a low vacuum sputtering device JFC Fine Coater (Jeol, Japan).

Surface topography was examined using an optical microscope (Reichert, Vienna, Austria) equipped with an ARTCAM CCD camera (Olympus, Tokyo, Japan), controlled by the Motic Images Plus 2.0 computer program.

2.6. FTIR Analysis

Fourier Transform Infrared Spectroscopy (FTIR) measurements were taken using a Nicolet 6700 FT-IR spectrometer (Thermo Electron Corp., Madison, WI, USA) equipped with photoacoustics MTEC model 300 accessory. The following measurement parameters were used: resolution, 4 cm^{-1}; photoacoustic detector; number of scans, 128. For each sample, the spectra were collected over the range of 4000 to 500 cm^{-1}. Data collection and post-processing were performed using OMNIC software (v. 9.0, Thermo Electron Corp.).

2.7. Amperometry

The effectiveness of the developed BC/PPD composite as a biosensor for measuring glucose concentration in human body fluids was tested *in vitro* using amperometry. For this purpose, the composite obtained was placed on a graphite electrode, thus creating a working electrode with an area of 21 cm^2. The reference electrode was a platinum electrode (Eurosensor EPtP-301). The test was conducted in phosphate-buffered saline (PBS) imitating blood plasma, containing glucose in concentrations ranging from 2.5 mM to 40 mM at a temperature of 37 °C.

Measurements of changes in current intensity depending on glucose concentration, at a constant potential of 0.7 V, were performed using a Keithley 2410 Source Meter device (Tektronix, Oregon, USA). This method was used to construct a calibration curve and measure the selectivity of the biosensor.

3. Results and Discussion

3.1. Microscopy Analysis

Scanning electron microscopy revealed significant differences in the microstructure of native BC and the BC/PPD composite (Figure 3). The pristine BC exhibited a typical three-dimensional network composed of randomly oriented, interwoven nanofibers forming an open and highly porous structure. The fibrils were uniformly distributed, creating a homogeneous network, characteristic of bacterial cellulose synthesized under static culture conditions.

In contrast, the BC/PPD composite showed noticeable morphological changes after *in situ* polymerization of *p*-phenylenediamine. The fibrous network remained continuous; however, the presence of additional material deposited along the cellulose nanofibers was clearly observed. A similar effect has been described in an extensive study by other researchers (Nair et al., 2025).

As indicated by the arrows, localized thickening of fibrils and the formation of elongated, denser regions were evident throughout the matrix. These features suggest successful deposition and growth of poly(*p*-phenylenediamine) within the BC network rather than mere surface coating. The polymer phase appears to preferentially accumulate along cellulose fibers and at fiber junctions, likely due to strong interactions between amino groups of PPD and hydroxyl groups of cellulose during polymerization.

This resulted in partial reduction of pore size and increased structural anisotropy in selected regions, while preserving the overall interconnected architecture of the BC scaffold. Importantly, no evidence of large polymer agglomerates or phase separation was observed, indicating that the *in situ* polymerization approach enabled relatively uniform distribution of the polymer throughout the cellulose matrix.

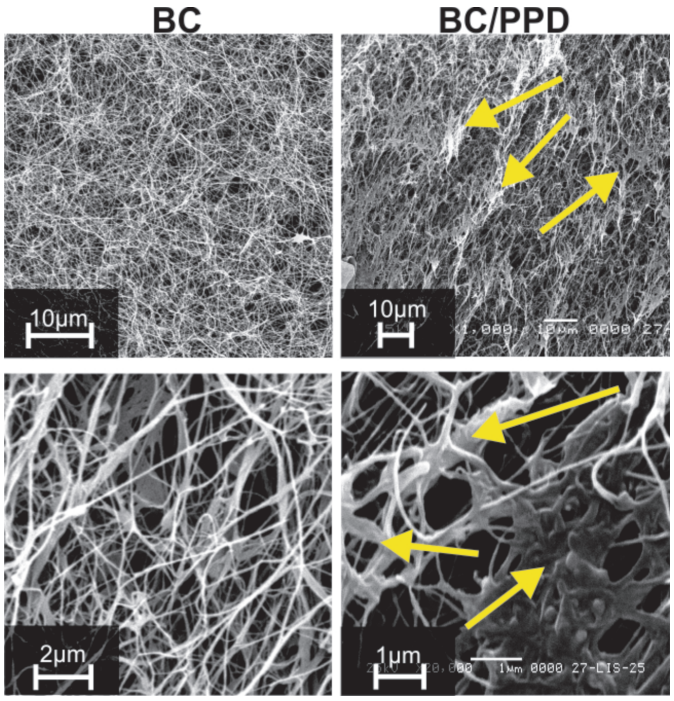


Figure 3. SEM micrographs of BC and BC/PPD at different magnifications. In the BC/PPD composite, localized polymer-rich regions are visible.

Such morphological modification is expected to enhance the functional properties of the composite, particularly with respect to electron transport pathways and interfacial area, which are critical parameters for biosensor performance. The retention of the fibrous network combined with the introduction of a conductive or redox-active polymer phase confirms the suitability of bacterial cellulose as an effective template for the fabrication of functional sensing composites.

Images of native BC and the BC/PPD composite obtained using a polarizing microscope (Figure 4) revealed differences between the morphology of pure bacterial cellulose and the morphology of cellulose after polymerization with *p*-phenylenediamine. In the case of pure BC, networks of densely arranged fibrous fibrils intertwined with each other and exhibiting a crystalline structure were observed, as indicated by the luminescence of the cellulose fibrils in the microscope's field of view.

In contrast, images obtained for the bacterial cellulose composite after polymerization with *p*-phenylenediamine (BC/PPD) showed a compact structure of the resulting material. Individual fibrillar structures, characteristic of pure bacterial cellulose, were not observed. As a result of the polymerization reaction, interactions likely occurred between the amine groups present in *p*-phenylenediamine and the hydroxyl groups of cellulose.

During the polymerization reaction, PPD penetrated deep into the cellulose fibrils, which arranged into wide, twisted ribbons, as observed in the images obtained using a polarizing microscope (Figure 4).

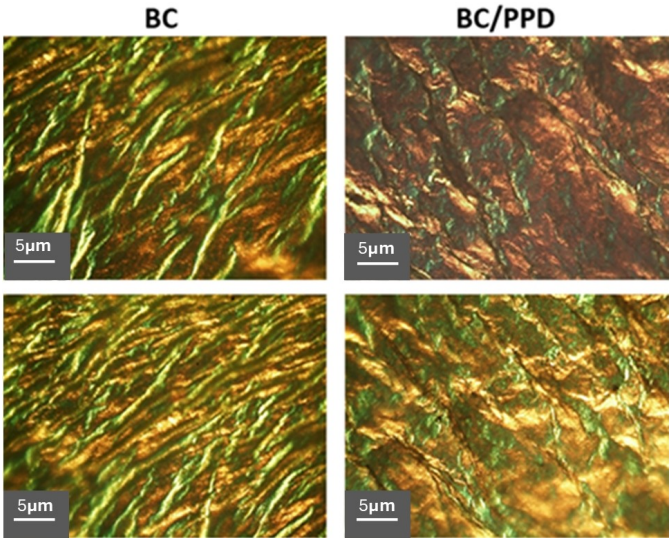


Figure 4. Micrographs of BC and BC/PPD surface morphology taken using a polarizing microscope.

3.2. FTIR Analysis

FTIR infrared spectroscopy was used to analyse the molecular structure of pure *p*-phenylenediamine (Figure 5) used in the polymerization process. The PPD spectrum features characteristic peaks at the band values of 3383 cm^{-1}, 3365 cm^{-1}, 3287 cm^{-1}, 3194 cm^{-1}, 3033 cm^{-1}, 1634 cm^{-1}, 1592 cm^{-1}, 1500 cm^{-1}, 1456 cm^{-1}, 1274 cm^{-1}, 1246 cm^{-1}, 1158 cm^{-1}, 1055 cm^{-1}, 927 cm^{-1}, 813 cm^{-1}, 750 cm^{-1}, 728 cm^{-1} and 536 cm^{-1}.

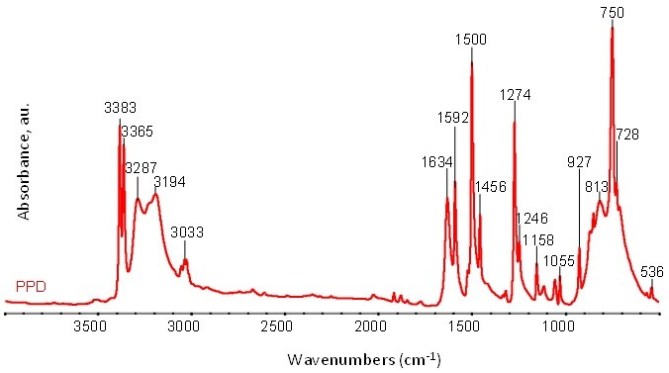


Figure 5. FTIR spectra of PPD at spectral range 4000–500 cm^{-1}.

The chemical structure of PPD contains two $-NH_2$ groups in the *para* position. In the FTIR spectrum obtained for PPD, we observe intense bands at maximum positions of 3383 cm^{-1}, 3365 cm^{-1}, 3287 cm^{-1} and 3194 cm^{-1} corresponding to the stretching vibrations of the $-N-H$ and $-NH_2$ groups (Georg, 2007; Kumar Trivedi et al., 2015).

We also observe intense bands at maximum positions of 1634 cm^{-1} and 1592 cm^{-1} corresponding to the stretching vibrations of the $-C-N-H$ functional groups. The band at a maximum of 3033 cm^{-1} is characteristic of the stretching

vibrations of the −CH group present in the aromatic ring. The bands at maxima of 1500 cm^{-1} and 1456 cm^{-1} are characteristic of the stretching vibrations of the $-C-C-$ group present in the aromatic ring.

The band with a maximum at 1274 cm^{-1} is characteristic of $-C-N-H$ bending vibrations. The bands with maxima at 1158 cm^{-1} and 1055 cm^{-1} are characteristic of $-C-H$ in-plane deformational vibrations. The band at a maximum of 750 cm^{-1} is characteristic of $-N-H$ vibrations. The band at a maximum of 728 cm^{-1} is characteristic of −C−H bending vibrations (out-of-plane) (Kumar Trivedi et al., 2015).

Spectroscopic studies were also performed on a bacterial cellulose (BC) sample and a bacterial cellulose composite following polymerization with *p*-phenylenediamine (BC/PPD) to observe differences between the tested samples (Figure 6).

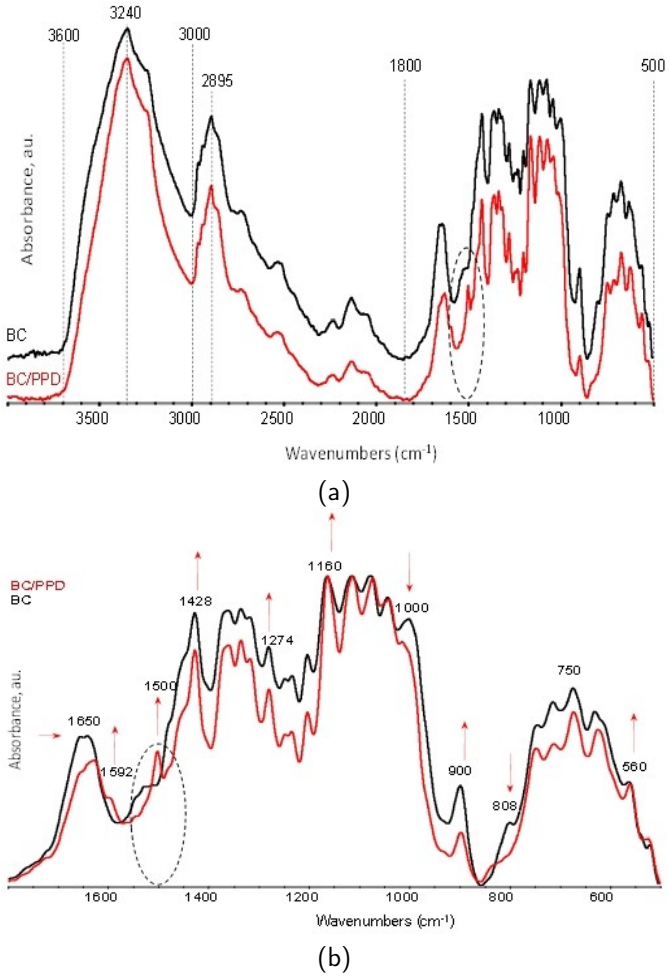


Figure 6. FTIR spectra of BC and BC/PPD beads at different spectral range: (a) 4000–500 cm^{-1}; (b) 1800–500 cm^{-1}.

In the FTIR spectra (Figure 6), it was observed that the spectra for the bacterial cellulose sample and the bacterial cellulose composite after polymerization with *p*-phenylenediamine retained all the characteristic features of the bands for pure bacterial cellulose, with the exception of the band at a maximum of 1500 cm^{-1}. This band is characteristic of the stretching vibrations of the $-C-C-H$ bonds present in the aromatic ring of *p*-phenylenediamine. This may indicate a reaction between the amine groups present in *p*-phenylenediamine and the hydroxyl groups of cellulose.

In the spectra obtained for the tested samples, a characteristic broad absorption band of the stretching vibrations of the O−H and $-N-H$ oscillators appears at wavenumbers in the range of approximately 3600–3000 cm^{-1} (Figure 6a). A characteristic band at a wavenumber of 2895 cm^{-1} is observed in the spectra, resulting from the absorption of radiation by $C-H$ oscillators.

In the 1800–500 cm^{-1} region (Figure 6b), slight shifts in the peak positions of the bands and a decrease or increase in their intensity are observed for the native BC and BC/PPD composite samples, as indicated by the red arrows. The region at 1160–500 cm^{-1} is associated with the vibrations of symmetric and asymmetric $C-O-C$ groups present in the glucopyranose ring and ether bridges (Gabryś et al., 2022).

3.3. Electrical Testing

The amperometry response of the BC/PPD composite toward glucose was investigated in PBS. Figure 7 presents the dependence of the measured current (I) on glucose concentration (C_M), demonstrating a clear and systematic increase in current with increasing analyte concentration.

The calibration curve exhibited a linear relationship over the studied concentration range, confirming the suitability of the BC/PPD composite for non-enzymatic glucose sensing. Linear regression analysis yielded an adjusted coefficient of determination ($R^2 = 0.94$), indicating good linearity and reliability of the amperometric response, which is consistent with previous reports demonstrating the applicability of BC-based materials in non-enzymatic glucose sensing systems (Yang et al., 2025).

The observed amperometric behavior can be attributed to the electrochemical oxidation of glucose occurring at the BC/PPD interface. Poly(*p*-phenylenediamine), incorporated into the bacterial cellulose network via *in situ* polymerization, provides redox-active sites that facilitate direct electron transfer between glucose molecules and the electrode surface. The possibility of modifying BC in a similar way and using it as an electrochemical sensor has been mentioned also by other scientists (Sheraz et al., 2025).

Furthermore, the intimate contact between the polymer phase and the cellulose nanofibers ensures efficient charge transport throughout the composite. The relatively low standard errors associated with the slope and intercept indicate good reproducibility and stability of the sensing response.

Unmodified BC exhibited only a negligible amperometric response toward glucose, with current values remaining close to the baseline over the investigated concentration range. Overall, the results demonstrate that the BC/PPD composite functions effectively as a non-enzymatic amperometry glucose sensor, combining the advantages of a natural, biocompatible matrix with the electrochemical activity of an aromatic amine polymer.

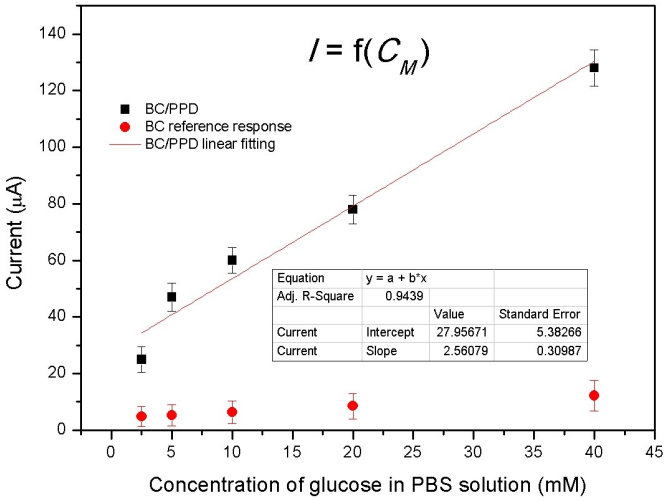


Figure 7. Amperometric response of the BC/PPD composite dependence of current on glucose concentration.

4. CONCLUSIONS

This study demonstrated the successful *in situ* polymerization of p-phenylenediamine within a bacterial cellulose matrix, resulting in a structurally integrated BC/PPD composite with enhanced functional properties. Spectroscopic and morphological analyses confirmed effective polymer incorporation and strong interactions between the polymer phase and cellulose nanofibers.

The composite exhibited a clear and reproducible amperometric response toward glucose, with good linearity, indicating its suitability for non-enzymatic sensing applications. The improved electrochemical performance is attributed to the presence of a redox-active polymer and efficient charge transport within the BC network.

Overall, the results highlight the potential of the BC/PPD composite as a flexible and biocompatible platform for biosensor development. Further work should address its long-term stability and performance in complex biological systems.

ACKNOWLEDGMENTS

The authors are grateful to the University of Bielsko-Biala, for the financial support to cover the publication fee of this research article.

REFERENCES

Gabryś T., Fryczkowska B., Fabia J., Biniaś D., 2022. Preparation of an active dressing by in situ biosynthesis of a bacterial cellulose–graphene oxide composite. *Polymers*, 14, 2864. DOI: 10.3390/polym14142864

Georg S., 2007. *Infrared and Raman Characteristic Group Frequencies: Tables and Charts*. 3rd edition. Hoboken, New Jersey, USA: John Wiley&Sons.

Gorgieva S., Trček J., 2019. Bacterial cellulose: production, modification and perspectives in biomedical applications. *Nanomaterials*, 9, 1352. DOI: 10.3390/nano9101352

Hasan M.B., Parvez M.M., Abir A.Y., Ahmad M.F., 2025. A review on conducting organic polymers: concepts, applications, and potential environmental benefits. *Heliyon*, 11, e42375. DOI: 10.1016/j.heliyon.2025.e42375

Iguchi M., Yamanaka S., Budhiono A., 2000. Bacterial cellulose — a masterpiece of nature's arts. *J. Mater. Sci.*, 35, 261–270. DOI: 10.1023/A:1004775229149

Kumar Trivedi M., Branton A., Trivedi D., Nayak G., Singh R., Jana S., 2015. Characterization of physical, thermal and spectroscopic properties of biofield energy treated p-phenylenediamine and p-toluidine. *J. Environ. Anal. Toxicol.*, 5, 6. DOI: 10.4172/2161-0525.1000329

Nair R.R., Hyun J.H., Kim J.H., Jung K.O., Kim D., 2025. Recent progress in the development of cellulose-derived organic-nanopolymer and coordination network platforms for application as optical chemosensors. *Adv. Compos. Hybrid Mater.*, 8, 30. DOI: 10.1007/s42114-024-01078-z

Sheraz M., Sun X.-F., Siddiqui A., Wang Y., Hu S., Sun R., 2025. Cellulose-based electrochemical sensors. *Sensors*, 25, 645. DOI: 10.3390/s25030645

Sozcu S., Frajova J., Wiener J., Venkataraman M., Tomkova B., Militky J., 2025. Synthesis of *Acetobacter xylinum* bacterial cellulose aerogels and their effect on the selected properties. *Gels*, 11, 272. DOI: 10.3390/gels11040272

Yang D., Chen Y., Che S., Wang K., 2025. Recent advances in non-enzymatic glucose sensors based on nanomaterials. *Coatings*, 15, 892. DOI: 10.3390/coatings15080892

Yu G., Shen S., Ni F., Guo Z., Qin X., Cao T., Zhu Z., Wang K., 2025. In-situ confined poly(p-phenylenediamine) within Mof pores for improved photocatalytic reduction of Cr(VI). *Colloids Surf., A Physicochem. Aspects*, 727, 138475. DOI: 10.1016/j.colsurfa.2025.138475

Chemical and Process Engineering: New Frontiers, 2026, 47(2), e138
DOI: 10.24425/cpe.2026.158136

Corrosive environments in municipal waste composting facilities: mechanisms, corrosivity and protection strategies

Andrzej Miszczyk, Michał Szociński, Kazimierz Darowicki

Gdansk University of Technology, Faculty of Chemistry, Department of Corrosion and Electrochemistry, Narutowicza 11/12, 80-233 Gdansk, Poland

* **Corresponding author, e-mail:** andrzej.miszczyk@pg.edu.pl

Article info:
Received: 26 March 2026
Revised: 16 May 2026
Accepted: 01 June 2026

Abstract
Although composting is a mature and economically favorable waste treatment technology, the controlled aerobic biodegradation of organic waste generates physicochemical conditions that are highly aggressive toward metallic and cementitious materials. This paper examines the corrosive environment in municipal solid waste composting facilities and its implications for material degradation and structural durability. Appropriate corrosion protection strategies were proposed based on the obtained results.
The corrosivity of composting atmospheres arises from both chemical and microbiological processes. Elevated temperatures (40–70 °C), persistent high relative humidity (>90%), and the presence of condensates enriched with organic acids, ammonia, carbon dioxide, and reduced sulfur compounds create an environment conducive to accelerated corrosion. Operational factors, including condensation–evaporation cycles and acid-laden runoff, accelerate corrosion kinetics and compromise protective coatings.
Given the limited empirical data on composting-specific atmospheric corrosivity, the corrosion rate of steel and zinc was determined under the conditions of a real operating composting plant according to the methodology described in the ISO 12944-2 standard and the appropriate corrosivity categories were defined. Based on this, optimized anti-corrosion systems were developed for new and renovated municipal solid waste composting facilities.

Keywords
corrosion, composting facilities, corrosivity category, anti-corrosion coatings

1. INTRODUCTION

Industrial environments and those associated with municipal infrastructure are often highly corrosive to structural materials due to their specific characteristics. It is therefore essential to implement appropriate protection methods. The first step in this process is to understand the composition, properties, and parameters of the environment, as well as its corrosivity as a key factor influencing the expected durability of the structure.

This paper is based on our practical experience with municipal composting facilities and builds on our portfolio of completed corrosion risk assessments and corrosion protection projects across various sectors, including the energy industry (Drozda and Miszczyk, 2022; Miszczyk and Darowicki, 2002; Miszczyk and Darowicki, 2012), museums and national heritage sites (Miszczyk et al., 2016; Szocinski et al., 2019), oil installations (Miszczyk et al., 2026; Orlikowski et al., 2024), and municipal water networks (Orlikowski et al., 2014).

The article outlines comprehensive steps for effectively protecting municipal organic waste composting facilities against corrosion. Due to insufficient understanding of the corrosive conditions present in such environments, many facilities deteriorate rapidly, leading to costly and disruptive repairs or reconstruction (Pajura, 2024).

Traditional waste treatment or disposal methods include composting (Avramidou et al., 2013; Hassen et al., 2001), anaerobic digestion (Abad et al., 2019; Jain et al., 2015), and landfilling (Behrooznia et al., 2018; Lee et al., 2017). Nontraditional technologies encompass incineration (Sharifah et al., 2013; Panepinto and Zanetti, 2018), pyrolysis (Lu et al., 2020; Yang et al., 2018), gasification (such as plasma gasification) (Lopes et al., 2018; Zhang et al., 2012), and hydrothermal processing (Anthraper et al., 2018; Peng et al., 2016).

Composting supports the circular economy by turning organic waste, such as food scraps and plant material, into nutrient-rich compost that improves soil quality. Instead of being discarded, organic waste is transformed into a valuable resource and returned to agricultural production. This process closes the environmental loop, reduces waste, and lessens environmental impact by sustainably reusing natural resources (Munir et al., 2021; Pajura, 2024; Pecorini et al., 2026).

Composting is a quite advanced technology for processing municipal solid waste. It has benefits like low initial costs, available land, lower contamination risks, and profitability from composted products (Ayilara et al., 2020; Gajalakshmi and Abbasi, 2008; Kumar, 2011; Lee et al., 2017). However, municipal waste composting facilities represent one of the most aggressive corrosive environments encountered in civil and industrial infrastructure (Agnew and Leonard, 2003;

© 2026. The Author(s). This is an open-access article distributed under the terms of the Creative Commons Attribution (CC-BY 4.0, https://creativecommons.org/licenses/by/4.0/), which permits unrestricted use, distribution, and reproduction in any medium, provided the original author and source are credited.

De Belie et al., 2000; Richard et al., 2002). These facilities are designed to accelerate the biological degradation of organic waste through controlled aerobic composting processes. But at the same time, the biochemical and physicochemical conditions that enable rapid biodegradation also create severe corrosion hazards for structural materials, mechanical equipment, and protective systems. Premature deterioration of steel and reinforced concrete elements has been widely reported in enclosed composting halls, tunnels, and bio-reactors, leading to increased maintenance costs, operational downtime, and, in extreme cases, structural safety concerns.

The corrosive environment in composting plants arises from a combination of high humidity, elevated temperatures, acidic and alkaline condensates, and biologically generated corrosive agents (Epstein, 1997; Rynk, 2022). Organic waste decomposition produces large quantities of water vapor, carbon dioxide, ammonia, organic acids (e.g., acetic, formic, and lactic acids), and reduced sulfur compounds. These substances accumulate in confined spaces and condense on cooler structural surfaces, forming aggressive electrolytes capable of attacking both metallic and cementitious materials.

A central question in the corrosion science of composting facilities concerns the role of biochemical reactions driven by compost-processing microorganisms. While corrosion itself is an electrochemical process, microbial activity is a primary upstream cause of corrosivity. Aerobic bacteria and fungi metabolize organic matter, releasing carbon dioxide and organic acids that lower local pH. In parallel, localized anaerobic microenvironments within compost piles can foster sulfate-reducing and sulfur-oxidizing bacteria, leading to the formation of hydrogen sulfide (H_2S). Subsequent oxidation of H_2S, either chemically or biologically, can produce sulfuric acid, a well-known agent of severe concrete degradation. This mechanism closely resembles microbiologically influenced corrosion (MIC) observed in wastewater infrastructure, although composting environments are typically more heterogeneous and transient.

The chemical processes that occur during composting include (Epstein, 1997; Epstein, 2011; Rynk, 2022):

- Decomposition of organic matter
  - Hydrolysis: Organic polymers such as cellulose, lignin, proteins, and fats are broken down into smaller molecules by enzymes secreted by microorganisms.
    - Cellulose → Glucose
    - Proteins → Amino Acids
    - Fats → Fatty Acids and Glycerol
  - Hydrolysis products become available for further metabolism by microorganisms.
- Degradation of Carbon Compounds
  - Aerobic Respiration: Microorganisms consume oxygen to oxidize carbon compounds into carbon dioxide (CO_2) and water (H_2O), releasing energy.

$$C_6H_{12}O_6 + 6O_2 \rightarrow 6CO_2 + 6H_2O + \text{Energy} \quad (1)$$

  - Anaerobic Processes (in the absence of oxygen): Gases such as methane (CH_4), hydrogen sulfide (H_2S), and organic acids are produced.
  - Decomposition of sulfur compounds: The decomposition of sulfur-containing proteins (e.g., cysteine) leads to the formation of hydrogen sulfide (H_2S) and sulfates (SO_4^{2-}).
- Organic acid production
  - Short-chain organic acids, such as acetic, butyric, and lactic acids, are formed as intermediate products in the fermentation process.
- Humification
  - Decomposition products, such as phenols, alcohols, and organic acids, are converted into stable humic compounds. This process involves:
    - Polycondensation of aromatic compounds.
    - Formation of stable organic complexes.
- Heat release
  - The decomposition of organic matter is an exothermic process. Due to the intense respiration of microorganisms, the compost temperature can rise to 60–70 °C, which helps eliminate pathogens and weed seeds.
  - Mineralization: Elements such as phosphorus, potassium, calcium, and magnesium are released in plant-available forms, making compost an excellent fertilizer.
- Gas release
  - During decomposition, gases such as carbon dioxide (CO_2), methane (CH_4), and ammonia (NH_3) are released, depending on aerobic or anaerobic conditions.

These chemical and biological processes work together to create nutrient-rich and stable compost. Maintaining the appropriate conditions (e.g., oxygen, moisture, temperature) is crucial for the process to proceed effectively.

Operational conditions within municipal composting facilities further exacerbate corrosion risk. Internal air temperatures commonly range from 40 to 70 °C, with localized compost core temperatures reaching up to 75 °C during thermophilic phases. Relative humidity is persistently high, often above 90% and frequently approaching saturation, particularly in enclosed or tunnel-based systems. These conditions promote continuous condensation–evaporation cycles on structural surfaces, which accelerate corrosion kinetics and undermine the long-term performance of protective coatings.

Due to the processes described above, the chemical and physical parameters of the composting environment change. Figure 1 schematically illustrates the changes in the following parameters: temperature and pH of the environment as a function of composting time, as well as the involvement of bacteria and fungi at various stages of the process (Epstein, 1997; Rynk,

2022). As the figure shows, in the initial period, bacteria are active, resulting in an increase in temperature and a decrease in the pH of the environment to approximately 5. In the second stage, the intensity of decomposition due to bacterial activity decreases, the temperature decreases, and fungi grow more intensively, leading to an increase in pH to approximately 8.5.

To mitigate these risks, composting facilities employ a combination of material selection, structural design, and corrosion protection systems. Load-bearing frameworks are typically constructed from structural carbon steel and reinforced concrete, while ancillary components may incorporate stainless steels (e.g., AISI 304L or 316L), aluminum alloys, or polymer-based materials such as high-density polyethylene (HDPE), polypropylene (PP), and fiber-reinforced plastics (FRP). In highly exposed zones, non-metallic materials are increasingly favored due to their inherent resistance to moisture and chemical attack.

Protective strategies for steel and concrete surfaces rely heavily on coating systems engineered for high humidity and chemically aggressive atmospheres. Common solutions include multilayer epoxy systems, epoxy–phenolic coatings, polyurethane topcoats, and vinyl ester or novolac epoxy linings. Typical dry film thicknesses range from 300 to 500 µm for atmospheric protection and may exceed 1000 µm for heavy-duty linings in areas exposed to condensate runoff or leachate. For concrete structures, polymer-modified cementitious coatings, epoxy coatings, and chemically resistant membranes are applied to limit acid ingress and moisture penetration.

Current best practice recommends an integrated anti-corrosion approach combining environmental control (ventilation and condensate management), robust coating systems, corrosion-resistant materials, and rigorous inspection and maintenance regimes. Early involvement of corrosion engineers during the design phase, along with adherence to relevant standards and exposure classifications, is critical for achieving an acceptable service life in these demanding environments.

Experience in this area is relatively limited, so principles developed earlier for industrial environments are applied here. To apply this approach, it is necessary to determine the corrosiveness of the atmosphere in various zones, and such data are lacking.

Composting plant design must be resistant to changing conditions. High humidity and air temperature must be properly considered in closed composting systems. The temperature inside the composting system is usually higher than the ambient temperature. Therefore, moisture in the air condenses on all surfaces, and the condensate contains aggressive acids and ammonia. The pH of the condensate changes from approximately 5 to 8.5 during the process. Typical anti-corrosion measures are ineffective in the composting process. Since these conditions are quite specific, it is necessary to perform measurements of the corrosive aggressiveness of the atmosphere in the composting plant, in accordance with the ISO 12944-2 standard, in order to propose an appropriate protection system.

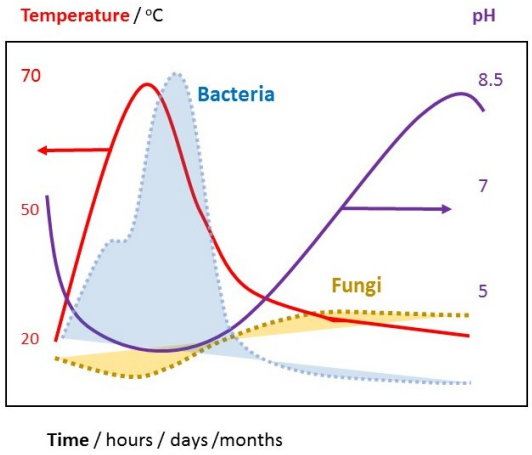


Figure 1. Schematic representation of changes in temperature and pH of the environment and the intensity of bacterial and fungal activity as a function of time in the composting process.

Based on this, it was decided to first characterize the chemical environment in the composting plant, then determine the corrosivity categories in different areas of the composting plant and, based on the data, propose protective systems necessary for proper protection of the structure in the conditions of the new and previously existing (renovation) composting plant structure. The research concerned composting plants processing municipal organic waste in Polish conditions.

2. EXPERIMENTAL DETAILS

The compost factory consists mainly of three halls that perform the functions necessary to carry out the entire process (Figure 2):

- Waste reception hall.
- Operational connector composting hall.
- Maturing and finishing hall.



Figure 2. Schematic representation of the structure of the composting installation

Corrosivity categories were assessed based on ISO 12944-2. They are determined based on the corrosion rate of mild carbon steel and/or zinc over a period of 1 year as shown in Table 1.

Table 1. Standard corrosion rates for mild steel and zinc in atmospheric conditions for different corrosivity categories.

Corrosivity		Corrosion rate [µm/year]	
Category	Description	Mild steel	Zinc
C1	Very low	≤ 1.3	≤ 0.1
C2	Low	> 1.3 to ≤ 25	> 0.1 to ≤ 0.7
C3	Medium	> 25 to ≤ 50	> 0.7 to ≤ 2.1
C4	High	> 50 to ≤ 80	> 2.1 to ≤ 4.2
C5	Very high	> 80 to ≤ 200	> 4.2 to ≤ 8.4
CX	Extreme	> 200 to ≤ 700	> 8.4 to ≤ 25

3. AIR COMPOSITION ANALYSIS IN THE INTERIORS OF COMPOSTING BUILDINGS

The contents of organosulfur compounds, hydrogen sulfide (H_2S), ammonia (NH_3), oxygen (O_2), carbon monoxide (CO), carbon dioxide (CO_2), methane (CH_4), and hydrogen (H_2) were determined inside the hermetic composting facility. Measurements were taken in the waste reception hall, the operational connector, and the maturation and finishing hall. The following equipment was used to determine the above-mentioned compounds: a MODEL WT8811 multigas concentration monitor, a Gas Data GFM Series multigas concentration monitor, and a Clarus 580 gas chromatograph (PerkinElmer, USA) with an ELITE-1MS capillary column (dimensions: 60 m × 0.32 mm × 1.0 µm) and an FPD flame photometric detector. The measurement results are presented in Table 2.

In addition to the total organosulfur compounds, which reached 6.36 ppm in the operational connector hall, qualitative determinations of the detected compounds were also made, identifying the presence of carbon disulfide, dimethyl sulfide, isopropyl mercaptan, and propyl mercaptan.

Analysis of the obtained results in terms of corrosion hazards led to the following observations:

- The carbon dioxide content in all composting halls was approximately 0.4%. This value is approximately one order of magnitude higher than that of atmospheric air (0.03%). The presence of carbon dioxide increases the corrosiveness of the environment, as CO_2 combined with water (moisture in the air) forms carbonic acid (H_2CO_3). This is an inorganic acid, relatively weak and unstable. However, due to the high carbon dioxide concentration and high humidity inside the composting halls, its formation in large quantities can pose a significant corrosion hazard. The highest carbon dioxide content was recorded in the operational connector hall, which translates into the greatest corrosion risk in this part of the composting plant.
- Carbon monoxide, whose higher concentrations were detected in the waste reception hall and connector hall compared to the maturation and final processing hall, is an inert gas (it does not form acids or hydroxides in the presence of moisture) and does not pose a corrosive threat to metals at atmospheric pressure (CO contaminated with sulfur compounds and combined with moisture can cause stress corrosion cracking under elevated pressure).
- The oxygen content in all composting halls remains at approximately 19%, which is lower than the oxygen content in outdoor atmospheric air. Oxygen is an essential element of the corrosion reaction (it participates in the cathodic reaction of the corrosion process), so its lower concentration in composting buildings does not increase the corrosion risk.
- The remaining compounds determined were present at concentrations below the detection limit of the measurement and analytical equipment used, meaning that their impact on the corrosiveness of the atmosphere inside the composting halls is negligible.

Table 2. Results of air composition measurements inside the hermetic composting facility.

Compound	Waste reception hall	Operational composting hall	Maturing and finishing hall
O_2 [%]	18.9	18.8	18.7
CO [µmol/mol of air]	16	17	3
H_2S [µmol/mol of air]	$< 0.1^*$	$< 0.1^*$	$< 0.1^*$
LEL (explosive gases) [%]	$< 0.1^*$	$< 0.1^*$	$< 0.1^*$
CO_2 [%]	0.4	0.5	0.4
CH_4 [%]	$< 0.01^*$	0.2	$< 0.01^*$
H_2 [ppm]	$< 1^*$	$< 1^*$	$< 1^*$
NH_3 [ppm]	$< 1^*$	$< 1^*$	$< 1^*$
Total volatile organosulfur compounds [ppm]	$< 0.1^*$	6.36	$< 0.1^*$

*means the detection limit of a given compound using the measuring equipment used

4. CORROSIVITY INSIDE COMPOSTING HALLS

A study was conducted to determine the corrosivity category in composting halls. For this purpose, a total of 40 samples made of S235JR carbon steel and steel coated with a 24.6 ($\pm$2.4) µm thick hot-dip zinc coating and measuring 20 cm $\times$ 5 cm $\times$ 1 mm were hung in various representative locations under the roof (within the roof structure), Figure 3. Additionally, for comparative purposes, two steel samples were hung in the connecting hall at a height of approximately 2 m from the floor, next to a wall shared with the reception hall. The exposure period was 48 days. After this period, the samples were removed (Figure 4), and the dirt and corrosion products of steel and zinc were removed in appropriate solutions, in accordance with the PN-74/H-04600 standard (10% HCl with 5% hexamine, 5% acetic acid solution, at 20 °C, respectively). The mass losses of steel and zinc were determined and converted into corrosion rates for steel and zinc (in µm/year). Figures 5 and 6 present the results for all galvanized and steel samples in the form of bar graphs to facilitate comparison of the corrosivity of each hall. Figure 7 indicates the corrosion rate averaged over all samples in a given hall.

Based on the conducted research, the corrosivity category for the reception hall and the operational composting hall is CX (extreme corrosivity). The maturation and final processing halls are C5. It should be noted that in some areas of the operational composting hall corrosivity is higher than that specified for CX (based on zinc results), meaning it falls outside the range of the accepted scales. These findings are also confirmed by the results obtained for steel, where the limiting value for this corrosivity category is a steel corrosion rate of 700 µm/year. This indicates that the initially applied protection, consisting of a 20 µm thick zinc coating, was sufficient for approximately one year. This is due to the range of pH values of condensates formed during the composting process, which vary from 5 to 8.5. As shown in Figure 8, this is the range in which zinc corrosion rates are significantly higher than in a neutral or near-neutral environment (pH around 7). This is facilitated by elevated temperature, high humidity (90–100% relative humidity), and the presence of corrosion stimulants in the form of salts (sulfates, chlorides, nitrates) formed as a result of chemical and biological processes.

Zinc corrosion rate studies have shown that protective layers of corrosion products form within a pH range of 6–12, with a minimum corrosion rate observed in the pH range of 10–12 (Figure 8). Water and increased amounts of organic and inorganic acids, a product of bacterial metabolism, condense under composting conditions on the internal surface of the roof structure, preventing the formation of a protective layer on the zinc surface. This causes accelerated corrosion of the zinc, which, therefore, no longer protects the steel surface after a short period of time. The steel continues to corrode due to the aggressive, corrosive atmosphere at an accelerated rate.



Figure 3. Steel and galvanized samples hung in the composting halls on the first day of exposure (2 steel and 2 galvanized).

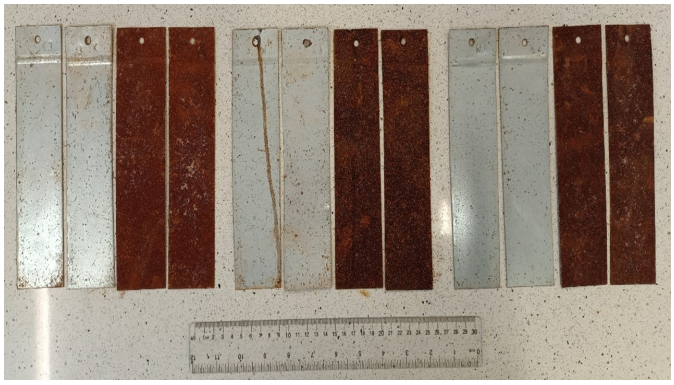


Figure 4. Appearance of some galvanized and steel samples after 48 days of exposure in composting halls.

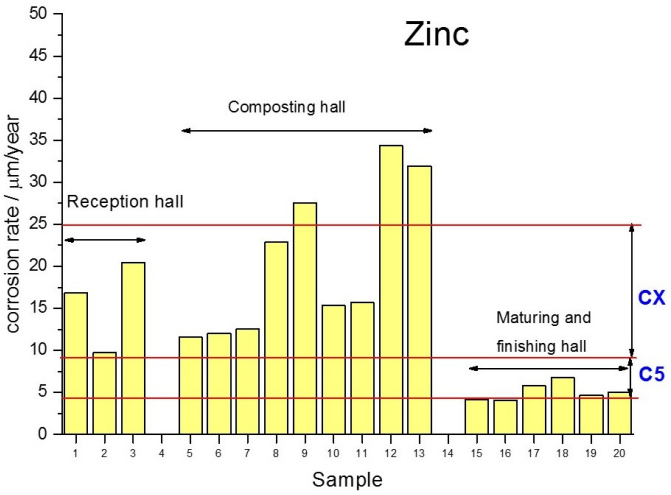


Figure 5. Corrosion rates of galvanized samples in the composting factory halls at different locations in each hall. The CX and C5 corrosivity ranges are marked according to the criteria of the ISO 12944-2 standard.

5. PROTECTION STRATEGIES

Municipal solid waste composting facilities, particularly enclosed (most common in central Europe) or tunnel-based systems, must be designed for a simultaneously aggressive

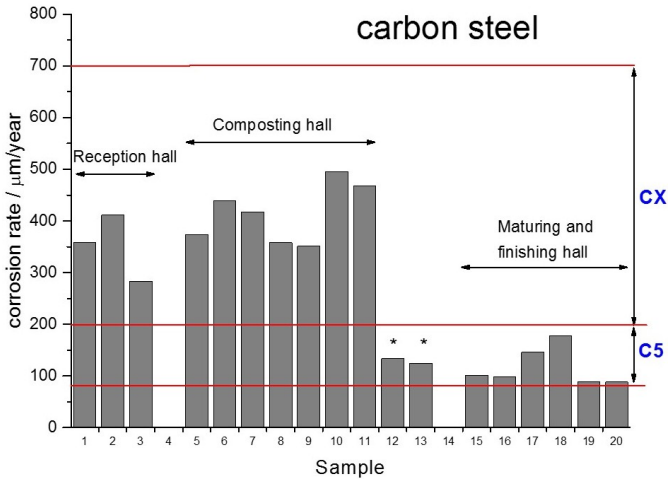


Figure 6. Corrosion rates of carbon steel samples in the composting factory halls at different locations in each hall. The CX and C5 corrosivity ranges are marked according to the criteria of the ISO 12944-2 standard. (*) refers to the corrosion rate of steel at a height of approximately 2 m above the floor.

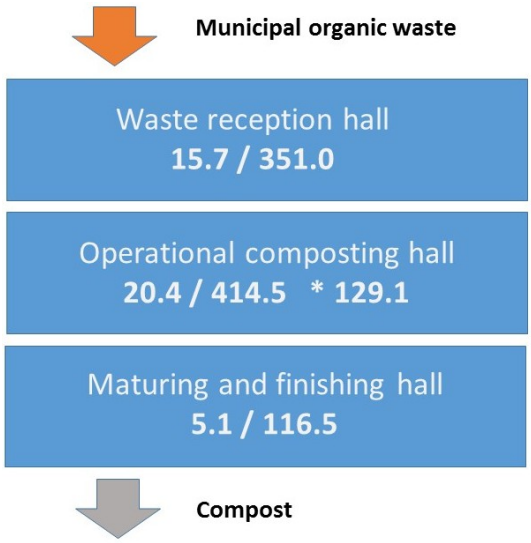


Figure 7. Average corrosion rates of zinc / steel within each hall, expressed in µm/year. The average value applies to all samples of a given type exposed in a given hall. The value with an asterisk (*) refers to the corrosion rate of steel at a height of approximately 2 m above the floor.

chemical, thermal, moisture, and mechanical environment. Structural solutions therefore differ substantially from conventional industrial halls. This is not always noticed, which results in corrosion problems later that are more difficult to repair. Roof design is critical due to:

- Condensation formation.
- Corrosive condensate dripping.
- High humidity exposure.
- Temperature gradients.

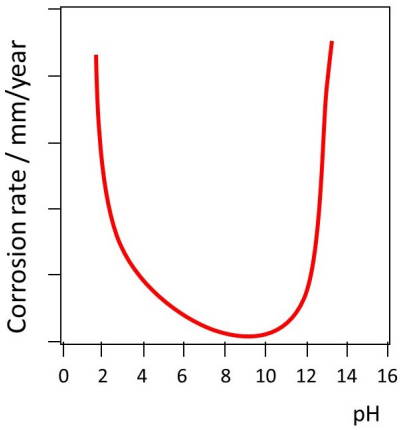


Figure 8. Schematic diagram of the zinc corrosion rate as a function of pH of the aquatic environment (based on Zhang, 1996).

A typical solution in this case are hot-rolled (Figure 9) or welded steel trusses. Stainless steel is only used selectively (due to cost). Reinforced concrete frames or hybrid steel-concrete structures are sometimes used. Lightweight openwork trusses are common structurally, but they are not "light" from a corrosion perspective, they require substantial protection. Subsections 5.1 and 5.2 propose protective coatings and their application methods appropriate to the conditions in a new composting plant and one requiring renovation, respectively.



Figure 9. Hot-rolled steel trusses connected with bolts used in one of the composting halls.

Multi-layer coating systems are an indispensable solution for anticorrosion protection, especially in heavy-duty environments, including municipal waste composting facilities. A single layer of any organic coating is not capable of providing an efficient and durable barrier in the long term. Selection of the coating system and its parameters is performed based on the respective standards, namely:

- ISO 12944-5 "Paints and varnishes – Corrosion protection of steel structures by protective paint systems – Part 5: Protective paint systems", which covers the types of paints

and systems (e.g., alkyd, epoxy, polyurethane) used for protecting steel in environments characterized by different corrosivity classes from C1 to C5.
- ISO 12944-9 "Paints and varnishes – Corrosion protection of steel structures by protective paint systems – Part 9: Protective paint systems and laboratory performance test methods for offshore and related structures", which relates to carbon steel structures and high-durability paint systems, typically those exposed to harsh environments of corrosivity class CX.

The standards contain the information about the minimum requirements (types of binders suitable for particular application, number of coating layers, dry thickness range for particular layers) for the coating systems for different durability variants. The standards have been created and are periodically updated based on practical experience collected from numerous application fields where organic coatings provide anticorrosion protection, for instance, atmospheric exposure, industrial applications, offshore structures, the transportation sector, etc. While searching for the optimum protection strategy for the municipal waste composting facility, we took into account the recommendations for C5 and CX corrosivity classes included in the ISO 12944 standards, and additionally confined our selection to epoxy- and polyurethane-based coatings. It is due to the specific environment identified inside the composting facility, especially significant variations in the pH that only these binders can withstand in the long-term exposure.

The presented approach is the primary method for designing coating protection. However, it requires knowledge of the corrosivity of the target atmosphere in which the protection is intended, taking into account specific environmental characteristics that may eliminate certain types of coatings (e.g., due to the unusual pH of the environment, most coatings will not guarantee adequate durability). First, the corrosivity of the atmosphere was precisely determined and other parameters of the composting environment that may affect the durability of coatings were examined. The approach presented in this manuscript includes all the necessary steps needed to design appropriate coating protection in accordance with the current state of knowledge.

The organic coating systems presented in the following chapters are typically designated for bare steel substrates. This situation occurs in structures intended for renovation. However, the same systems can be used to provide additional protection for new structures, which are inherently protected by a thin (approximately 25 μm) zinc coating on the steel elements. This type of protection is sufficient for similar warehouse structures, which are often used as a basis for composting plant halls. In this way, a duplex system is created, which provides even more efficient anticorrosion protection. Composting facilities are characterized by heavily corrosive conditions, in which the zinc layer alone is insufficient for effective protection, and thus application of the duplex systems is beneficial (van Eijnsbergen, 1994; Yu et al., 2020).

The presented systems were designed to be applied to both steel and galvanized steel surfaces, facilitating their application in different variants due to their versatility.

5.1. Anticorrosion protection of steel girders and trapezoidal roof sheet in the variant of erecting a new roof structure

Most frequently, the roof structure of a composting facility consists of trapezoidal steel sheet and steel girders. To ensure long-term durability, they must be adequately protected against corrosion in accordance with the ISO 12944-2 standard: CX for the waste reception hall and the operational connector hall, and C5 for the maturation and post-processing hall.

5.1.1. Requirements concerning the preparation of the steel substrate for painting and the conditions for applying coatings

Preparation of the metal substrate is one of the most crucial steps in achieving efficient, long-term anticorrosion protection. To provide good adhesion of paint coatings to the steel substrate, the following should be performed:

- abrasive blast cleaning using grit abrasives to the Sa$2\frac{1}{2}$ preparation grade in accordance with ISO 8501-1 standard,
- obtaining an intermediate surface roughness profile,
- washing steel elements with clean water to remove water soluble salts. The salt content on surfaces to be painted, determined according to the Bresle method (ISO 8502-6), should not exceed 50 mg/m^2.

Conditions for applying paint coatings shall comply with the requirements specified in the datasheet of the anticorrosion paints used. Nevertheless, certain conditions must be met regardless of the type of paint employed, such as during application and drying/curing of coatings, the relative air humidity should not exceed 85%, and the dew point temperature should be at least 3 °C higher than the temperature of the painted surfaces. It is recommended to prepare the surface and apply protective coatings to individual elements under controlled climatic conditions (for instance, inside the painting rooms) before their delivery and final installation on the composting plant buildings. It reduces the formation of flash rust after abrasive blasting of elements and provides fully hardened coatings before assembly. After installing the roof structure on the composting plant buildings, painting (using the same coating systems as on the rest of the structure) of the bolted joints should be performed. After final installation, it is recommended to inspect the coatings on the entire roof structure to identify and repair potential damage caused by installation.

5.1.2. Coating protection for the waste reception hall and for the operational connector hall

The minimum requirements for a coating system intended for use in the waste reception hall and in the operational connector hall should meet the CX corrosivity class (offshore) environment:

- the coating system should consist of a minimum of 3 layers,
- the total dry thickness of the coating system should not be less than 350 µm,
- the dry thickness of the primer coating should not be lower than 60 µm,
- it is recommended to use paints based on epoxy and/or polyurethane binders,
- it is recommended to apply a topcoat of a fire-retardant coating to prevent cellulose fire,
- the applied and cured coating system, after the conditioning period, should be characterized by an adhesion of not less than 5 MPa, measured with a pull-off test in accordance with ISO 4624 standard.

5.1.3. Coating protection of the maturation and post-processing hall

In the case of coating protection of the maturation and post-processing hall characterized by corrosivity class C5, it is recommended to choose one of the two longest durability periods: long (15–25 years) or very long (over 25 years). The minimum requirements for a coating system intended for use in a C5 corrosivity class environment, for a long life include:

- 1 layer of primer based on epoxy or polyurethane binder,
- the dry thickness of primer from 80 to 240 µm,
- 1–3 layers of coatings based on epoxy and/or polyurethane and/or acrylic binder,
- the total dry thickness of the coating system should not be less than 300 µm.

The minimum requirements for a coating system intended for use in a C5 corrosivity class environment, for a very long engulf:

- 1 layer of primer coating based on epoxy or polyurethane binder,
- the dry thickness of primer from 80 to 200 µm,
- 2–3 layers of coatings based on epoxy and/or polyurethane and/or acrylic binder,
- the total dry thickness of the coating system should not be less than 360 µm.

Additionally, in both variants, it is recommended to apply a topcoat of a fire-retardant coating to prevent cellulose fire.

5.1.4. Additional recommendations

Due to possible gaps at the connection points between individual elements of the roof structure, it is beneficial to protect these places with bridging fillers of high chemical resistance and flexibility. For larger gaps, using a filler with mesh should be considered. Due to the highly corrosive conditions in composting facilities, it is advised to carry out paint inspections of protective coatings once a year to assess the degree of their degradation and detect possible damage. This will enable repairs and renovations to be carried out at an early stage, allowing for lower financial outlays. It is also recommended to periodically, at least once a year, wash the roof structure with water at a pressure not exceeding 10 MPa. This will remove accumulated deposits and contaminants that contribute to the degradation of protective coatings.

5.2. Anticorrosion protection of steel girders and trapezoidal roof sheet in the variant of renovation of the existing roof structure

When renovating an existing roof structure, trapezoidal steel sheet and steel girders must be protected against corrosion in accordance with the atmospheric corrosivity class following the ISO 12944-2 standard: CX for the waste reception hall and the operational connector hall, and C5 for the maturation and post-processing hall. In this situation, the most important elements from the standpoint of obtaining effective and long-lasting coating protection are:

- thorough cleaning of the steel roof structure from corrosion products, deposits, and impurities, especially in difficult-to-access places and with complex geometry,
- ensuring appropriate climatic conditions at the coating application stage,
- ensuring suitable climatic conditions and the time necessary for the individual layers of the coating system to completely dry/cure before being put into service.

These elements become particularly important in a situation where the planned renovation will take place without suspending the technological process of waste processing, only with partial shutdown of parts of the facility for the duration of painting.

5.2.1. Requirements concerning the preparation of the steel substrate before painting and the conditions for applying coatings

In some facilities, due to design errors, the steel sections of the roof structure may have cavities directed towards the top of the structure. Moisture, deposits, and impurities accumulate inside them, causing severe corrosion. After protective coating application, these regions will still be exposed to accelerated degradation. In order to minimize this phenomenon, it is necessary to ensure drainage of these depressions by drilling holes allowing water to evacuate. During the recommended annual inspections of the coatings, the patency of drainage

holes should be checked, and the aforementioned corrosion-sensitive sections should be washed with water at a pressure not exceeding 10 MPa to remove any deposits.

Preparation of steel surfaces to obtain good adhesion of paint coatings should involve:

- abrasive blast cleaning using grit abrasives to the Sa2$\frac{1}{2}$ preparation grade in accordance with the ISO 8501-1 standard,
- obtaining an intermediate surface roughness profile,
- it is permissible to clean the surface to the Wa2$\frac{1}{2}$ grade by using a high-pressure water jetting (in accordance with the ISO 8501-4 standard),
- the acceptable flash rust intensity cannot exceed M grade in accordance with the ISO 8501-4 standard; it is recommended to apply a primer on the same day as the substrate preparation,
- particular attention should be paid to cleaning and preparing the area with cavities in the roof support structure,
- washing steel elements with clean water to remove water soluble salts. The salt content on surfaces to be painted, determined according to the Bresle method (ISO 8502-6 standard), should not exceed 50 mg/m^2.

Since the renovation usually takes place without suspending the technological process of waste processing, and only particular fragments of the facility are subjected to a shutdown during the steel substrate preparation, painting, and drying/curing of the coatings, it is recommended to use paints tolerating minimal surface preparation in case the required climatic conditions are not met.

Similarly to protecting new roof structure, conditions for applying paint coatings shall comply with the requirements specified in the datasheet of the anticorrosion paints used. During application and drying/curing of coatings, the relative air humidity should not exceed 85%, and the dew point temperature should be at least 3 °C higher than the temperature of the painted surfaces. Additional coating application should be made locally using a brush in difficult-to-access areas with complex geometry (all edges, corners, structural kinks) to provide good protection. This operation should be performed before applying each layer of the coating system.

5.2.2. Coating protection for the waste reception hall and for the operational connector hall

The minimum requirements for a coating system intended for use in the waste reception hall and in the operational connector hall should meet the CX corrosivity class (offshore) environment:

- the coating system should have a minimum of 3 layers,
- the total dry thickness of the coating system should not be less than 350 µm,
- the dry thickness of the primer coating should not be lower than 60 µm,
- it is recommended to use paints based on epoxy and/or polyurethane binders, tolerating the substrates with minimum preparation (presence of flash rust); the use of paints based on other binders is permitted provided that equivalent protective properties and tolerances of substrate are verified,
- it is recommended to apply a fire-retardant coating as a topcoat to prevent cellulose fire,
- the applied and cured coating system, after the conditioning period, should be characterized by an adhesion of not less than 5 MPa, verified with a pull-off test in accordance with the ISO 4624 standard.

5.2.3. Coating protection of the maturation and post-processing hall

Coating protection intended for corrosivity class C5, which is typical for the maturation and post-processing hall, requires selection between the two longest durability periods:

- long (15–25 years) or,
- very long (over 25 years).

The minimum requirements for a coating system intended for use in a C5 corrosivity class environment, for a long life engulf:

- 1 layer of primer based on epoxy or polyurethane binder tolerating the substrates with minimum preparation (presence of flash rust); the use of paints based on other binders is permitted provided that equivalent protective properties and tolerances of substrate are verified,
- the dry thickness of primer from 80 to 240 µm,
- 1–3 layers of coatings based on epoxy and/or polyurethane and/or acrylic binder; the use of paints based on other binders is permitted provided that equivalent protective properties and tolerances of substrate are verified,
- the total dry thickness of the coating system should not be less than 300 µm.

The minimum requirements for a coating system intended for use in a C5 corrosivity class environment, for a very long durability include:

- 1 layer of primer coating based on epoxy or polyurethane binder tolerating the substrates with minimum preparation (presence of flash rust); the use of paints based on other binders is permitted provided that equivalent protective properties and tolerances of substrate are verified,
- the dry thickness of primer from 80 to 200 µm,
- 2–3 layers of coatings based on epoxy and/or polyurethane and/or acrylic binder; the use of paints based on other binders is permitted provided that equivalent protective properties and tolerances of substrate are verified,
- the total dry thickness of the coating system should not be less than 360 µm.

Additionally, in both variants, it is recommended to apply a topcoat of a fire-retardant coating to prevent cellulose fire.

Figure 10 schematically illustrates an example of coating systems on galvanized steel (a new structure protection option) for environments with corrosiveness classes C5 and CX. This protective system is highly durable, exceeding the combined durability of its components (zinc coating and paint system) by 20–50% (van Eijnsbergen, 1994; Yu et al., 2020). Based

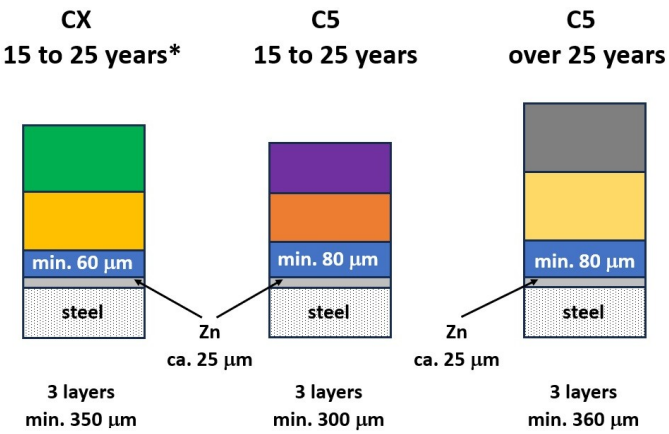


Figure 10. Graphical comparison of the requirements (total dry film thickness and number of layers) for the coating systems employed in corrosivity classes CX and C5. (*) refers to the durability "High" with expectancy of the first major coating failure between 15 and 25 years from the date of installation.

on the experience contained in the ISO 12944 standard and our own experience in contact with municipal composting plants and industrial environments, it is possible to estimate with great probability the protection effectiveness of the most common protective systems (Table 3). Undoubtedly, the most advantageous protective properties should be demonstrated by a "duplex" system thanks to the synergistic interaction of the zinc coating and the painting system consisting of epoxy and/or polyurethane coatings.

5.2.4. Additional recommendations

Similarly to maintenance of new roof structures, the following recommendations concern the renovated ones:

- it is suggested to protect the connection points between individual elements of the roof structure with bridging fillers of high chemical resistance and flexibility,
- it is advised carry out paint inspections of protective coatings once a year to assess the degree of their degradation and detect possible damage,
- it is recommended to periodically, at least once a year, wash the roof structure with water at a pressure not exceeding 10 MPa to remove accumulated deposits and contaminants; particular care should be taken when cleaning drainage holes and cavities in the roof structure sections.

6. CONCLUSIONS

Municipal composting facilities constitute a crucial element of waste management systems in urban and rural areas. The nature of biological and biochemical processes poses a serious risk to construction materials through corrosion degradation. Surprisingly, this problem seems to be underestimated as there are very few literature reports marginally relating to this topic. In this paper, we described a comprehensive approach, in which particular sections of the municipal composting facility were field tested for environment corrosivity class, corrosion rates were determined for steel and zinc, and anti-corrosion protection coating systems were selected for the protection of metal roof structures.

Corrosivity of the environment was determined based on the analysis of the biological and biochemical processes occurring in each part of the composting facility and the composition of ambient air collected in each section. Field exposure of steel and zinc samples inside the facility revealed corrosion rates characteristic of C5 and CX classes corresponding to high and very high corrosion risk, respectively. Then a protection with multi-layer organic coating systems was designed, taking into account two variants – new erected and renovated roof structures. It included the selection of coating types, number of coating layers, description of metal substrate preparation procedures, coating application conditions, and post-application, periodic maintenance recommendations.

The conditions inside the municipal composting facility include high humidity and temperature, presence of acidic and alkaline condensates, corrosion-enhancing microbiological activity, and

Table 3. Estimated approximate durability of anti-corrosion systems in compost factory halls.

Hall	Zinc coating/years	3-layer painting system*/years	Zinc coating + 3-layer painting system*/years
Waste reception	1–3 (25 µm)	15–25 360 µm	20–25 (25 + 360) µm
Operational composting	1–2 (25 µm)	15–25 (360 µm)	20–25 ((25 + 360) µm)
Maturing and finishing	4–6 (25 µm)	10–15 (300 µm) > 15 (360 µm)	15–25 ((25 + 300) µm) > 25 ((25 + 360) µm)

*applies to epoxy and/or polyurethane paints

mechanical impacts. To provide durable and efficient anti-corrosion protection of metal structures in these heavy-duty conditions, it is required to:

- perform a thorough metal surface preparation procedure before organic coating application, which will ensure Sa2$\frac{1}{2}$ preparation grade, an intermediate surface roughness profile, and water soluble salts concentration lower than 50 mg/m^2,
- apply at least a 3-layered organic coating system having a dry film thickness not less than 300 µm, depending on location and corrosivity class,
- use the coatings based on epoxy binders since the protection concerns indoor structures with minimal access to sunlight; they exhibit the highest resistance to the aforementioned harsh conditions; in some situations, polyurethane-based coatings are also acceptable,
- ensure high adhesion of the coating systems to the metal substrate equal to at least 5 MPa measured in a pull-off test.

Finally, long-term effective coating protection can be amplified by proper in-service maintenance, including annual washing of the structures with water at a pressure not exceeding 10 MPa to remove accumulated deposits and contaminants, followed by inspection for potential coating defects.

REFERENCES

Abad V., Avila R., Vicent T., Font X., 2019. Promoting circular economy in the surroundings of an organic fraction of municipal solid waste anaerobic digestion treatment plant: biogas production impact and economic factors. *Bioresour. Technol.,* 283, 10–17. DOI: j.biortech.2019.03.064.

Agnew J.M., Leonard J.J., 2003. The physical properties of compost. *Compost Sci. Util.*, 11, 238–264. DOI: 10.1080/1065657X.2003.10702132.

Anthraper D., McLaren J., Baroutian S., Munir M.T., Young B.R., 2018. Hydrothermal deconstruction of municipal solid waste for solid reduction and value production. *J. Cleaner Prod.,* 201, 812–829. DOI: 10.1016/j.jclepro.2018.08.116.

Avramidou P., Evangelou A., Komilis D., 2013. Use of municipal solid waste compost a growth media for an energy plant (rapeseed). *J. Environ. Manage.,* 121, 152–159. DOI: 10.1016/j.jenvman.2013.02.046.

Ayilara M.S., Olanrewaju O.S., Babalola O.O., Odeyemi O., 2020. Waste management through composting: challenges and potentials. *Sustainability,* 12, 4456. DOI: 10.3390/su12114456.

Behrooznia L., Sharifi M., Alimardani R., Mousavi-Avval S.H., 2018. Sustainability analysis of landfilling and composting-landfilling for municipal solid waste management in the north of Iran. *J. Cleaner Prod.,* 203, 1028–1038. DOI: 10.1016/j.jclepro.2018.08.307.

De Belie N., Sonck B., Braam C.R., Lenehan J.J., Svennerstedt B., Richardson M., 2000. Durability of building materials and components in the agricultural environment, Part II: Metal structures. *J. Agric. Eng. Res.,* 75, 333–347. DOI: 10.1006/jaer.1999.0521.

Drozda M., Miszczyk A., 2022. Selection of organic coating systems for corrosion protection of industrial equipment. *Coatings,* 12, 523. DOI: 10.3390/coatings12040523.

Epstein E., 1997. *The Science of composting*. CRC Press, Boca Raton, London, New York, Washington, D.C. DOI: 10.1201/9780203736005.

Epstein E., 2011. *Industrial composting: Environmental engineering and facilities management*. CRS Press, Taylor & Francis Group, Boca Raton, London, New York. DOI: 10.1201/b10726.

Gajalakshmi S., Abbasi S.A., 2008. Solid waste management by composting: state of the art. *Crit. Rev. Environ. Sci. Technol.,* 38, 311–400. DOI: 10.1080/10643380701413633.

Hassen A., Belguith K., Jedidi N., Cherif A., Cherif M., Boudabous A., 2001. Microbial characterization during composting of municipal solid waste. *Bioresour. Technol.,* 80, 217–225. DOI: 10.1016/S0960-8524(01)00065-7.

ISO 12944-2. Paints and varnishes – Corrosion protection of steel structures by protective paint systems – Part 2: Classification of environments, International Organization for Standardization, 2018.

ISO 12944-5. Paints and varnishes – Corrosion protection of steel structures by protective paint systems – Part 5: Protective paint systems, International Organization for Standardization, 2019.

ISO 12944-9. Paints and varnishes – Corrosion protection of steel structures by protective paint systems – Part 9: Protective paint systems and laboratory performance test methods for offshore and related structures, International Organization for Standardization, 2018.

ISO 4624. Paints and varnishes – Pull-off test for adhesion, International Organization for Standardization, 2023.

ISO 8501-1. Preparation of steel substrates before application of paints and related products -Visual assessment of surface cleanliness – Part 1: Rust grades and preparation grades of uncoated steel substrates and of steel substrates after overall removal of previous coatings, International Organization for Standardization, 2008.

ISO 8501-4. Preparation of steel substrates before application of paints and related products – Visual assessment of surface cleanliness – Part 4: Initial surface conditions, preparation grades and flash rust grades in connection with water jetting, International Organization for Standardization, 2020.

ISO 8502-6. Preparation of steel substrates before application of paints and related products – Tests for the assessment of surface cleanliness – Part 6: Extraction of water soluble contaminants for analysis (Bresle method), International Organization for Standardization, 2020.

Jain S., Jain S., Wolf I.T., Lee J., Tong Y.W., 2015. A comprehensive review on operating parameters and different pretreatment methodologies for anaerobic digestion of municipal solid waste. *Renewable Sustainable Energy Rev.,* 52, 142–154. DOI: 10.1016/j.rser.2015.07.091.

Kumar S., 2011. Composting of municipal solid waste. *Crit. Rev. Biotechnol.,* 31, 112–136. DOI: 10.3109/07388551.2010.492207.

Lee U., Han J., Wang M., 2017. Evaluation of landfill gas emissions from municipal solid waste landfills for the life-cycle analysis of waste-to-energy pathways. *J. Cleaner Prod.,* 166, 335–342. DOI: 10.1016/j.jclepro.2017.08.016.

Lopes E.J., Okamura L.A., Maruyama S.A., Yamamoto C.I., 2018. Evaluation of energy gain from the segregation of organic materials from municipal solid waste in gasification processes. *Renewable Energy,* 116, 623–629. DOI: 10.1016/j.renene.2017.10.018.

Lu J.-S., Chang Y., Poon C.-S., Lee D.-J., 2020. Slow pyrolysis of municipal solid waste (MSW): a review. *Bioresour. Technol.,* 312, 123615. DOI: 10.1016/j.biortech.2020.123615.

Miszczyk A., Darowicki K., 2002. Reliability of flue gas desulphurisation installations – the essential condition of efficient air pollution control. *Pol. J. Environ. Stud.,* 11, 205–209.

Miszczyk A., Darowicki K., 2012. Inspection of protective linings using microwave spectroscopy combined with chemometric methods. *Corros. Sci.,* 64, 234–242. DOI: 10.1016/j.corsci.2012.07.023.

Miszczyk A., Kuna M., Brillowska-Dąbrowska A., 2026. Early-stage biofilm prevention enabled by rapid microwave waveguide detection of planktonic microorganisms in diesel fuel. *Coatings,* 16, 101. DOI: 10.3390/coatings16010101.

Miszczyk A., Szocinski M., Darowicki K., 2016. Restoration and preservation of the reinforced concrete poles of fence at the former Auschwitz concentration and extermination camp. *Case Stud. Const. Mater.,* 4, 42–48. DOI: 10.1016/j.cscm.2015.12.002.

Munir M.T., Mohaddespour A., Nasr A.T., Carter S., 2021. Municipal solid waste-to-energy processing for a circular economy in New Zealand. *Renewable Sustainable Energy Rev.*, 145, 111080. DOI: 10.1016/j.rser.2021.111080.

Orlikowski J., Darowicki K., Mikołajski S., 2014. Multi-sensor monitoring of the corrosion rate and the assessment of the efficiency of a corrosion inhibitor in utility water installations. *Sens. Actuators B. Chem.,* 181, 22–28. DOI: 10.1016/j.snb.2013.02.015.

Orlikowski J., Jażdżewska A., Łuksa I., Szociński M., Darowicki K., 2024. Corrosion monitoring in petroleum installations—practical analysis of the methods. *Materials*, 17, 2663. DOI: 10.3390/ma17112663.

Pajura R., 2024. Composting municipal solid waste and animal manure in response to the current fertilizer crisis – a recent review. *Sci. Total Environ.,* 912, 169221. DOI: 10.1016/j.scitotenv.2023.169221.

Panepinto D., Zanetti M.C., 2018. Municipal solid waste incineration plant: a multi- step approach to the evaluation of an energy-recovery configuration. *Waste Manage.,* 73, 332–341. DOI: 10.1016/j.wasman.2017.07.036.

Pecorini I., Pasciucco F., Palmieri R., Panico A., 2026. Assessing the suitability of digestate and compost as organic fertilizers: a comparison of different biological stability indices for sustainable development in agriculture. *Sustainability,* 18, 1196. DOI: 10.3390/su18031196.

Peng N., Liu Z., Liu T., Gai C., 2016. Emissions of polycyclic aromatic hydrocarbons (PAHs) during hydrothermally treated municipal solid waste combustion for energy generation. *Appl. Energy,* 184, 396–403. DOI: 10.1016/j.apenergy.2016.10.028.

Richard T.L., (Bert) Hamelers H.V.M., Veeken A., Silva T., 2002. Moisture relationships in composting processes. *Compost Sci. Util.,* 10, 286–302. DOI: 10.1080/1065657X.2002.10702093.

Rynk R. (ed.), 2022. *The Composting Handbook. A how-to and why manual for farm, municipal, institutional and commercial composters*. Elsevier, Academic Press, London, San Diego, Cambridge, Oxford. DOI: 10.1016/C2019-0-05417-9.

Sharifah A.S.A.K., Yin C.-Y., Rosli Sulaiman M., Chen X., El-Harbawi M., 2013. Incineration of municipal solid waste in Malaysia: salient issues, policies and waste-to-energy initiatives. *Renewable Sustainable Energy Rev.,* 24, 181–186. DOI: 10.1016/j.rser.2013.03.041.

Szocinski M., Miszczyk A., Darowicki K., 2019. Condition of reinforced concrete structures and their degradation mechanism at the former Auschwitz concentration and extermination camp. *Stud. Conserv.*, 64, 174–186. DOI: 10.1080/00393630.2018.1557937.

van Eijnsbergen J.F.H., 1994. *Duplex Systems. Hot-dip Galvanizing Plus Painting.* Elsevier, Amsterdam, London, New York, Tokyo. DOI: 10.1016/C2009-0-10312-4.

Yang Y., Wang J., Chong K., Bridgwater A.V., 2018. A techno-economic analysis of energy recovery from organic fraction of municipal solid waste (MSW) by an integrated intermediate pyrolysis and combined heat and power (CHP) plant. *Energy Convers. Manage.,* 174, 406–416. DOI: 10.1016/j.enconman.2018.08.033.

Yu Z., Hu J., Meng H., 2020. A review of recent developments in coating systems for hot-dip galvanized steel. *Front. Mater.,* 7, 74. DOI: 10.3389/fmats.2020.00074.

Zhang Q., Dor L., Fenigshtein D., Yang W., Blasiak W., 2012. Gasification of municipal solid waste in the Plasma Gasification Melting process. *Appl. Energy,* 90, 106–112. DOI: 10.1016/j.apenergy.2011.01.041.

Zhang X.G., 1996. *Corrosion and electrochemistry of zinc.* Springer New York, NY. DOI: 10.1007/978-1-4757-9877-7.

Chemical and Process Engineering: New Frontiers, 2026, 47(2), e139
DOI: 10.24425/cpe.2026.158137

CRITICAL REVIEW

AI/ML in Chemical Engineering: From molecular design to industrial process optimization

Fatemeh Valizadeh Hajidehi*, Azam Mina

Department of Chemical Engineering, School of Allied Medicine, Tehran University, Tehran, Iran

Abstract

The integration of artificial intelligence and machine learning into chemical engineering represents a paradigm transformation that fundamentally reconceptualizes practice across molecular, process, and industrial scales. This comprehensive narrative review synthesizes recent advances in AI/ML methodologies, including graph neural networks, physics-informed neural networks, deep reinforcement learning, and generative artificial intelligence – and critically evaluates their applications spanning molecular property prediction, catalyst design, pharmaceutical development, reactor optimization, process control, and sustainability initiatives. Contemporary AI/ML approaches demonstrate unprecedented capabilities in navigating complex multi-scale phenomena while maintaining computational tractability and physical interpretability. Landmark achievements include 71% reduction in experimental iterations for reaction optimization through deep reinforcement learning, 98% accuracy in predictive maintenance using LSTM-based fault detection, sub-1% prediction errors in virtual metrology for semiconductor manufacturing, and substantial improvements in carbon capture efficiency through machine learning-guided materials discovery. Physics-informed neural networks address the critical challenge of plant-model mismatch by synergistically integrating mechanistic knowledge with data-driven learning, enabling extrapolation beyond training domains while respecting conservation laws. Explainable AI techniques, particularly SHAP analysis, enhance operational acceptance by 52% in safety-critical applications through transparent decision-making pathways. Despite remarkable progress, persistent challenges remain in data quality and standardization, model interpretability for regulatory compliance, computational scalability for real-time control, and integration with legacy industrial infrastructure. The review identifies transformative future directions including multi-modal learning frameworks, transfer learning for data-scarce applications, quantum machine learning for molecular design, and human-AI collaborative systems. Successful deployment demands interdisciplinary collaboration uniting chemical engineering domain expertise with computational intelligence, guided by principles of transparency, reproducibility, and responsible innovation to address sustainability imperatives while maintaining operational excellence and safety in chemical manufacturing.

* **Corresponding author, e-mail:** researchtahghigh6@gmail.com

Article info:

Received: 09 February 2026
Revised: 14 March 2026
Accepted: 27 May 2026

Keywords

Artificial Intelligence; machine learning; physics-informed neural networks; chemical process optimization; explainable AI

1. INTRODUCTION

Chemical engineering, a cornerstone of industrial innovation, has traditionally relied on first-principles modeling and empirical methods to design, optimize, and control chemical processes. However, the complexity and scale of modern chemical systems have pushed these classical approaches to their limits. In response, the integration of *Artificial Intelligence* (*AI*) and *Machine Learning* (*ML*) has emerged as a transformative development in the field. These data-driven tools are not only augmenting traditional modeling techniques but are increasingly enabling chemical engineers to perform tasks once thought too complex, non-linear, or data-intensive for conventional methods. *Artificial Intelligence* broadly refers to the simulation of human cognitive functions by machines, including reasoning, learning, and decision-making. Within *AI*, machine learning, especially supervised and unsupervised learning, has become particularly influential in scientific and engineering disciplines due to its ability to identify patterns and make predictions from large datasets. Chemical engineering, which generates vast quantities of experimental and operational data, is an ideal candidate for *AI* applications. *ML* models are being employed to accelerate reaction discovery, optimize reaction conditions, monitor process parameters, and enhance control strategies, all of which are central to chemical engineering practice. One of the earliest and most impactful areas where *AI* has shown promise is in reaction prediction. The ability to forecast reaction outcomes, yields, or even reaction pathways based on existing chemical data has traditionally required extensive domain expertise and trial-and-error experimentation. *AI*, particularly deep learning algorithms and neural networks, can be trained on large reaction databases to predict products, optimize reagents, and identify ideal conditions. This application is already accelerating drug development pipelines and green chemistry initiatives by enabling high-throughput screening and environmentally conscious process design (Mathur et al., 2021; Mondal 2024). These advancements are reducing reliance on energy-intensive laboratory experiments and minimizing waste, making the entire process more sustainable and cost-effective.

© 2026. The Author(s). This is an open-access article distributed under the terms of the Creative Commons Attribution (CC-BY 4.0, https://creativecommons.org/licenses/by/4.0/), which permits unrestricted use, distribution, and reproduction in any medium, provided the original author and source are credited.

In addition to molecular design and synthesis, *AI* is also revolutionizing process modeling and optimization. Traditional process models, based on differential equations and thermodynamic principles, often struggle with highly non-linear or multi-scale systems. *ML* algorithms, including support vector machines and ensemble methods, have demonstrated superior predictive power in modeling complex chemical kinetics and multiphase flows, especially when high-quality historical or real-time data is available (Benavides-Hernández and Dumeignil, 2024; Dobbelaere et al. 2021). These models offer faster computation, adaptability to new data, and, when integrated with optimization algorithms, can guide engineers toward optimal operating conditions with greater accuracy and speed than manual tuning or heuristics. A significant evolution in *AI*-driven chemical engineering is its use in process control and automation. Advanced control systems are essential in ensuring product quality, minimizing energy use, and maintaining safety. Traditionally, model predictive control (*MPC*) systems have relied on deterministic process models. However, these can be computationally intensive and inflexible to dynamic process variations. *AI*-enabled controllers, on the other hand, can adapt in real-time, learn from sensor feedback, and even anticipate process upsets before they occur (Boskabadi et al., 2025). With developments in reinforcement learning and digital twin technologies, *AI*-based systems are not only optimizing operations but also acting as decision-support tools for plant operators and engineers. Despite its potential, the integration of *AI* into chemical engineering is not without challenges. Key concerns include the lack of interpretability of black-box models, the quality and quantity of training data, and the limited *AI* literacy among chemical engineers. Additionally, data silos, privacy issues, and computational costs remain barriers to widespread adoption. Yet, education initiatives and interdisciplinary collaboration are beginning to close this gap. Several universities have started integrating *AI* into their chemical engineering curricula, aiming to prepare a new generation of engineers equipped with both domain knowledge and computational skills (Bozal-Ginesta et al., 2025).

This review aims to explore the expanding role of *AI* in chemical engineering, from reaction prediction and synthesis to process modeling, optimization, and real-time control. By examining current applications, identifying challenges, and discussing future directions, we hope to offer a comprehensive overview of how *AI* is reshaping the practice and potential of chemical engineering.

It is important, however, to approach these advances with critical realism. Despite remarkable progress, the gap between benchmark performance and practical industrial deployment remains substantial and is frequently understated in the primary literature. Many *ML* models are validated on curated datasets under idealized conditions that poorly reflect the noise, non-stationarity, and incomplete observability of real industrial processes. The reproducibility crisis documented across computational sciences is acutely relevant to chemical engineering *AI*, where molecular diversity and process variability are intrinsic rather than correctable features. Moreover, the uncritical reporting of performance metrics such as R^2, *AUROC*, and *MAE* risks obscuring whether a model has genuinely learned physically meaningful representations or has instead overfit to statistical artifacts of a particular training dataset. Absent prospective validation, uncertainty quantification, and adversarial testing under distribution shift, high benchmark scores provide limited assurance of real-world reliability. This review therefore aims to provide not merely an inventory of what *AI* can do in chemical engineering, but a calibrated and critical assessment: acknowledging landmark achievements while explicitly identifying where evidence remains preliminary, where generalization claims are unsupported, and where foundational challenges have received insufficient attention from the community.

2. AI AND ML FUNDAMENTALS FOR CHEMICAL ENGINEERS

The rapid integration of *AI* and *ML* into chemical engineering requires a foundational understanding of how these systems operate, especially as they diverge from traditional mechanistic modeling paradigms. Unlike first-principles approaches, *ML* models infer patterns from empirical data without explicit physical rules. For chemical engineers, this represents a shift from deterministic frameworks to probabilistic, data-driven inference – offering flexibility, speed, and scalability but introducing challenges in interpretability and data dependency.

At the heart of modern *AI* applications in chemical engineering are supervised and unsupervised learning paradigms. Supervised learning algorithms, such as feedforward neural networks, support vector machines, and gradient-boosted trees, require labeled data to map input features to desired outputs. These models excel in tasks like reaction yield prediction, fault classification in reactors, and sensor calibration. For instance, Dobbelaere et al. (2021) demanded the applicability of supervised *ML* in process modeling, where traditional approaches struggled with non-linearities and stochastic perturbations in high-throughput operations.

Unsupervised learning, on the other hand, is pivotal in exploratory data analysis. Techniques like principal component analysis, k-means clustering, and autoencoders are utilized to uncover latent patterns in spectral data, reaction databases, or sensor arrays without predefined outcomes. These tools assist in anomaly detection, feedstock characterization, and optimization of complex multi-variate systems. Recent studies have shown that unsupervised models can cluster reaction types or operational regimes based on historical plant data, providing actionable insights without expert-coded thresholds (Wieder et al., 2020).

Surpassing traditional *QSAR* models in both performance and generalizability (Wieder et al. 2020). Their ability to capture long-range dependencies and contextual information

makes them well-suited to model multi-step synthesis, offering probabilistic assessments of alternative routes (Al Sharah et al., 2024). To maximize yield while avoiding process instabilities – tasks that are traditionally managed through rule-based *PID* or *MPC* systems (Hoque et al., 2024).

Despite their power, these models introduce fundamental concerns for chemical engineers, especially regarding model interpretability and trust. Most deep learning systems operate as "black boxes," offering high accuracy but little explanation. This opaqueness conflicts with the engineering imperative for transparent, auditable, and physically grounded decision-making. As such, there is growing interest in interpretable *ML*, including attention mechanisms, Shapley values, and symbolic regression, which attempt to bridge the gap between statistical learning and mechanistic understanding.

Furthermore, the successful deployment of *AI* systems is contingent on data quality – a challenge in chemical engineering, where experimental datasets are often sparse, noisy, and heterogeneous. Transfer learning and data augmentation techniques are increasingly used to overcome these limitations by leveraging pretrained models or generating synthetic data. Nonetheless, robust model validation remains essential, requiring cross-validation, out-of-sample testing, and domain-specific sanity checks to ensure reliability in real-world deployment.

A dimension of *AI*/*ML* in chemical engineering that merits more critical attention than it typically receives is the distinction between interpolation and extrapolation performance. Neural networks and gradient-boosted tree models are powerful interpolators within their training distribution but are notoriously unreliable extrapolators. In chemical engineering, where scale-up, novel feedstocks, and changing process conditions routinely push systems outside the envelope of historical data, this distinction is not academic – it determines whether a deployed model provides reliable guidance or dangerously misleading predictions.

Gaussian process regression offers principled uncertainty quantification that explicitly signals when predictions are made far from training data, though its computational scaling has traditionally limited applicability to large datasets. Conformal prediction methods offer distribution-free, coverage-guaranteed uncertainty bounds for any underlying *ML* model and are beginning to attract attention in pharmaceutical and materials discovery contexts.

For chemical process monitoring, where an *ML* model must reliably detect anomalous operating regimes, the ability to characterize prediction uncertainty under distribution shift is arguably more important than point-prediction accuracy. These considerations should be central to the validation methodology of any *ML* system intended for deployment in safety-critical chemical processes.

Indeed, for chemical engineers to harness the full potential of *AI*, a hybrid approach is needed – combining domain expertise with data-centric modeling. While *AI* tools extend beyond the limitations of traditional methods, their responsible application requires a deep appreciation of their statistical nature, assumptions, and failure modes. This necessitates a curriculum shift that integrates *AI* literacy into core chemical engineering education, as advocated by Wu et al. (2023), who showed that targeted *AI* instruction improves both student outcomes and confidence in applying these tools in complex systems. Critically, however, this integration must be pursued with care: *AI* tools should serve as supplements to – rather than substitutes for – rigorous training in chemical engineering fundamentals, ensuring graduates retain deep domain expertise alongside computational proficiency.

3. MOLECULAR AND MATERIALS SCALE APPLICATIONS

3.1. Molecular property prediction and structure-property relationships

The prediction of molecular properties through quantitative structure-property relationships (*QSPR*) represents a foundational application of *ML* in chemical engineering at the molecular scale (Chinta and Rengaswamy, 2019). Traditional *QSPR* approaches, dating to the 1960s, have evolved dramatically with modern *ML* algorithms that can capture complex nonlinear relationships between molecular structure and physicochemical properties.

Contemporary *QSPR* methodologies employ diverse molecular representations including molecular descriptors, fingerprints, and graph-based encodings to establish predictive models (Yan et al., 2020; Yang et al., 2019). Graph neural networks (*GNNs*), particularly directed message-passing neural networks (*D-MPNNs*), have emerged as state-of-the-art architectures for molecular property prediction, demonstrating superior performance across diverse chemical datasets (Heid et al., 2024).

The Chemprop package, implementing *D-MPNN* architecture, provides accessible infrastructure for predicting properties ranging from solubility and reactivity to absorption, distribution, metabolism, excretion, and toxicity (*ADMET*) characteristics. These models achieve remarkable accuracy by learning hierarchical molecular representations that capture both local atomic environments and global molecular topology (Heid et al., 2024; Wieder et al., 2020).

Recent advances address the critical challenge of data scarcity through transfer learning and multi-task learning frameworks. Adaptive checkpointing with specialization (*ACS*) mitigates negative transfer in imbalanced datasets while preserving beneficial inter-task knowledge sharing, enabling accurate property prediction with as few as 29 labeled samples (Eraqi et al., 2025).

This capability proves particularly valuable for specialized applications such as sustainable aviation fuel design, where limited experimental data constrains conventional modeling approaches. The integration of physics-based descriptors with data-driven learning, exemplified by fastprop and similar frameworks – combines computational efficiency with interpretability, achieving state-of-the-art performance while maintaining domain relevance (Burns and Green, 2025).

3.2. Catalyst design and discovery

Heterogeneous catalysis represents one of the most impactful domains for *ML* applications in chemical engineering, where the complexity gap between theoretical models and experimental reality has historically impeded rational catalyst design (Benavides-Hernández and Dumeignil, 2024; Goldsmith et al., 2018). Machine learning approaches address multiple aspects of this complexity, including configurational space exploration, reaction pathway enumeration, active site identification, and performance prediction (Table 1).

The integration of *ML* with high-throughput experimentation (*HTE*) and computational methods creates synergistic workflows that dramatically accelerate catalyst discovery cycles (Benavides-Hernández and Dumeignil, 2024; Goldsmith et al., 2018). Modern *ML* applications in heterogeneous catalysis encompass several critical categories. First, *ML* models predict adsorption energies and *d*-band centers that serve as descriptors for catalytic activity, substantially reducing the computational expense of density functional theory (*DFT*) calculations for complex surface chemistries (Mou et al., 2023).

Machine-learned force fields (*MLFFs*) enable molecular dynamics simulations at near-*DFT* accuracy with orders of magnitude reduction in computational cost, facilitating exploration of reaction mechanisms and free energy landscapes (Omranpour et al., 2025). These approaches prove particularly valuable for screening large catalyst libraries where exhaustive *DFT* calculations remain prohibitively expensive.

Graph neural networks trained on large-scale databases such as the Open Catalyst Project (*OC*20) demonstrate remarkable capability in predicting catalyst properties and reaction pathways, achieving energy prediction errors below 0.05 *eV* relative to *DFT* benchmarks (Bozal-Ginesta et al., 2025).

The emergence of interpretable *ML* methods – incorporating physics-inspired feature engineering, Bayesian statistical learning, and theory-infused architectures – addresses the critical challenge of model explainability while maintaining predictive accuracy (Xin et al., 2023). These interpretable frameworks enable extraction of design principles and mechanistic insights that guide experimental catalyst development, bridging the gap between data-driven predictions and domain understanding.

3.3. Drug discovery and pharmaceutical engineering

ADMET property prediction has become a cornerstone application of *ML* in pharmaceutical development, addressing the critical bottleneck that contributes to high attrition rates in drug discovery pipelines (Terstappen and Reggiani, 2001; Vora et al., 2023). Modern *ML* platforms such as *ADMET-AI*,

Table 1. Representative ML applications in heterogeneous catalyst design.

Application domain	ML approach	Key achievement	Accuracy/Performance	Reference
Adsorption energy prediction	Graph Neural Networks	Universal binding energy models for multimetallic surfaces	$MAE < 0.15$ eV	Mou et al., 2023
Surface reaction mechanisms	Machine-Learned Force Fields	Automated reaction pathway exploration	$\Delta E_{error} \sim 0.05$ eV vs. *DFT*	Omranpour et al., 2025
Active site identification	Bayesian Optimization	Accelerated screening of single-atom catalysts	Speedup: 10–100× vs. *DFT*; $MAE < 0.1$ eV	Xin et al., 2023
Catalyst stability prediction	Gradient Boosting Regression	Thermal and chemical stability assessment	$R^2 > 0.85$	Goldsmith et al., 2018
Oxygen reduction reaction	Explainable AI (SHAP)	Descriptor importance ranking for ORR activity	$R^2 > 0.80$; experimental validation	Xin et al., 2023
CO_2 reduction	Transfer Learning	Performance prediction with limited data	$R^2 = 0.80$–0.90; 15–30% improvement	Bozal-Ginesta et al., 2025

HelixADMET, and commercial systems provide rapid, accurate predictions across 40 + *ADMET* endpoints, enabling efficient filtering of large chemical libraries generated through virtual screening and generative *AI* approaches (Swanson et al., 2024; Zhang et al., 2022).

These platforms employ sophisticated graph neural network architectures that achieve competitive performance on standardized benchmarks while maintaining computational efficiency sufficient for screening thousands of compounds in minutes.

The integration of *ML* into drug discovery workflows spans multiple stages, from hit identification through lead optimization. Multi-task deep neural networks simultaneously predict multiple *ADMET* properties, exploiting correlations among endpoints to improve predictive accuracy while reducing computational redundancy (Wenzel et al., 2019).

Transfer learning strategies prove particularly valuable for rare toxicity endpoints where limited training data is available, though care must be exercised to avoid negative transfer when applying models to narrow therapeutic areas or specialized compound classes (Niazi, 2025). Recent developments in quantum-informed molecular representations and transformer-based architectures further enhance prediction accuracy by capturing electronic structure information and long-range molecular interactions (Kim et al., 2024).

The pharmaceutical industry's adoption of in silico *ADMET* modeling reflects its demonstrated value in reducing late-stage failures and accelerating development timelines. The global in silico drug discovery market, valued at $ 3.61 billion in 2024, projects growth to $ 7.22 billion by 2030, driven by the imperative to "fail early, fail cheap" given that bringing a new molecular entity to market surpasses $ 2.6 billion (Pathan et al., 2025).

Regulatory acceptance of computational methods, exemplified by the *FDA*'s 2025 decision to phase out mandatory animal testing for many drug types, signals a paradigm shift toward increased reliance on validated in silico approaches for safety and efficacy assessment (Table 2).

Typical *ADMET* prediction accuracy ranges:

- Solubility: $R^2 = 0.75$–0.85
- Blood-brain barrier: $AUROC = 0.85$–0.92
- hERG blocking: $AUROC = 0.80$–0.88
- CYP inhibition: $AUROC = 0.82$–0.90
- Oral bioavailability: $AUROC = 0.75$–0.82

3.4. Novel materials development

3.4.1. Polymer design and characterization

Machine learning has catalyzed a paradigm shift in polymer materials research, enabling the systematic exploration of vast chemical design spaces that were previously inaccessible through traditional trial-and-error approaches (Gao et al., 2024; Yue et al., 2025). The *ML*-assisted polymer design workflow encompasses database construction, molecular representation, property prediction model development, virtual screening, and experimental validation.

This structured framework addresses the unique challenges posed by polymers' structural complexity, multiscale architecture, and limited availability of high-quality training data (Cao et al., 2026). Transfer learning and multitask learning strategies have emerged as essential techniques for overcoming data scarcity in specialized polymer applications.

Notable successes include the discovery of polymers with high thermal conductivity, where transfer learning from large databases (PoLyInfo, QM9) to limited thermal property data enabled identification and experimental validation of novel high-performance materials (Wu et al., 2019). Bayesian molecular design frameworks integrate uncertainty quantification with sequential optimization, guiding efficient exploration of chemical space while balancing exploitation of known favorable regions with exploration of uncharted territories.

Recent applications demonstrate *ML*'s transformative potential across diverse polymer domains. In membrane separation, *ML*-driven inverse design accelerates identification

Table 2. Performance metrics of state-of-the-art ADMET prediction platforms.

Platform	Architecture	Number of endpoints	Prediction speed	Key features	Reference
ADMET-AI	Chemprop-RDKit GNN	41	Fastest (45% faster)	DrugBank comparison	Swanson et al., 2024
HelixADMET	Self-supervised NNs	Multiple	High-throughput	Knowledge transfer	Zhang et al., 2022
ADMET Predictor	Multi-algorithm ensemble	175 +	Commercial-grade	Integrated PBPK	Venkataraman et al., 2025
PharmaBench	Large Language Models	11 datasets, 52 K entries	Benchmark-focused	LLM curation	Niu et al., 2024
Deep-PK/DeepTox	Graph-based multitask	PK and toxicity	Platform-dependent	Graph descriptors	Pathan et al., 2025

of polymeric materials with optimized permeability-selectivity trade-offs for gas separation and water treatment applications (Dangayach et al., 2025).

For energy storage, *AI*-guided discovery of dielectric polymers achieved simultaneous high energy density and thermal stability – properties traditionally considered mutually exclusive – through systematic exploration of polynorbornene and polyimide chemical spaces (Georgia Institute of Technology, 2024). Flame-retardant polymer discovery leverages operando analytical techniques integrated with virtual combustion generators to capture intermediate combustion information, enabling more accurate property prediction and rational design of fire-safe materials (Wang et al., 2024a).

3.4.2. Deep eutectic solvents and ionic liquids

Designer solvents, particularly deep eutectic solvents (*DES*) and ionic liquids (*ILs*), represent an emerging class of tunable materials where *ML* approaches accelerate property prediction and formulation optimization. Group contribution (*GC*) methods combined with *ML* algorithms predict temperature-dependent properties including viscosity, surface tension, thermal conductivity, and cytotoxicity with remarkable accuracy when appropriate data splitting schemes and algorithms are employed (Cao et al., 2024).

The critical challenge lies in capturing the complex non-additive interactions between cation-anion pairs or hydrogen bond donor-acceptor components that determine solvent properties.

Machine learning models for *IL* and *DES* properties must account for temperature dependence, ionic strength effects, and compositional variations across multicomponent systems. Point-based versus *IL*-based dataset splitting significantly impacts model performance for temperature-dependent properties, highlighting the importance of rigorous cross-validation strategies (Cao et al., 2024).

Random forest and extreme gradient boosting algorithms frequently emerge as optimal choices for *IL* property prediction, balancing predictive accuracy with computational efficiency. The integration of quantum mechanical descriptors and molecular dynamics-derived features further enhances model performance, particularly for properties governed by electronic structure and intermolecular interactions.

3.4.3. Nanomaterials and advanced functional materials

The extension of *ML* methodologies to nanomaterial design addresses unique challenges related to size-dependent properties, surface effects, and synthesis-structure relationships. Generative models create virtual libraries of nanoparticle compositions and morphologies, which are subsequently screened using *ML* property predictors trained on high-throughput computational or experimental data (Bozal-Ginesta et al., 2025). This approach has accelerated discovery of catalytic nanoparticles, quantum dots with tailored optical properties, and functional nanocomposites for energy conversion applications.

Integration of *ML* with autonomous experimental platforms – self-driving laboratories – enables closed-loop optimization where experimental results continuously refine predictive models and guide subsequent synthesis attempts. These cyber-physical systems combine robotic synthesis, in-line characterization, and adaptive algorithms to achieve accelerated materials discovery cycles measured in days rather than years (Boskabadi et al., 2025). The success of such platforms depends critically on developing robust models that generalize beyond training data while accounting for experimental variability and synthesis-property relationships.

4. REACTION AND PROCESS UNIT SCALE

4.1. Chemical reaction optimization

Deep reinforcement learning (*DRL*) has emerged as a transformative methodology for autonomous chemical reaction optimization, addressing the fundamental challenge of navigating vast experimental spaces efficiently. The Deep Reaction Optimizer (*DRO*) framework exemplifies this paradigm, employing modified long short-term memory architectures to iteratively record reaction outcomes and select new experimental conditions that maximize target objectives such as yield or selectivity (Zhou et al., 2017).

This approach demonstrated superior performance over conventional blackbox optimization algorithms, requiring 71% fewer experimental iterations while achieving optimal conditions in as little as 30 minutes when integrated with accelerated microdroplet reaction platforms. The stochastic exploration strategy incorporated within *DRL* frameworks mitigates the greedy policy limitation that causes entrapment in local optima, systematically balancing exploitation of promising conditions with exploration of uncharted parameter spaces (Zhou et al., 2017).

The *RE-EXPLORE* framework advances reaction optimization by integrating *DRL* with recurrent neural network-based generative models to identify novel reactants and catalysts that maximize yield or selectivity (Hoque et al., 2024). Pretrained on large chemical databases containing hundreds of thousands to blending millions of molecules, these generative models are enriched with diverse chemical knowledge that informs the search process.

The engineered reward function incorporates Tanimoto-based uniqueness factors within the reinforcement learning loop, addressing the critical challenge whereby standard *RL* methods prioritize immediate exploitation, resulting in repetitive generation of chemically similar molecules. This architectural

innovation enables efficient exploration of chemical space while maintaining focus on performance optimization objectives. The integration of user-defined core fragments further facilitates learning of specific reaction types, providing chemists with control over the molecular scaffolds explored during optimization (Hoque et al., 2024).

Multi-objective reinforcement learning extends single-objective optimization to address the realistic complexity of pharmaceutical lead optimization, where multiple competing objectives such as potency, selectivity, pharmacokinetics, and synthetic accessibility must be simultaneously optimized (Zhou et al., 2017). The *MolDQN* framework demonstrates this capability through direct molecular modifications that ensure 100% chemical validity while maximizing drug-likeness and maintaining structural similarity to lead compounds.

Recent extensions to catalytic reaction mechanism elucidation leverage high-throughput deep reinforcement learning integrated with first-principles calculations to autonomously predict reaction pathways with near-*DFT* accuracy at dramatically reduced computational cost (Lan et al., 2024). This reaction-agnostic framework demonstrates excellent generalizability across diverse catalytic systems, enabling efficient mechanistic investigations that traditionally required extensive human expertise and computational resources.

Despite impressive quantitative results, several important limitations of *DRL*-based reaction optimization deserve explicit discussion. First, the reward function design problem is nontrivial and directly determines what the *RL* agent optimizes. In pharmaceutical synthesis, the chemist's true objective involves multiple competing criteria including yield, selectivity, atom economy, reagent safety, solvent greenness, and scalability to manufacturing conditions.

Collapsing this multidimensional objective into a scalar reward inevitably privileges some criteria at the expense of others, and small changes in reward formulation can dramatically alter recommended conditions. Second, the structural coverage of pretrained generative models underlying frameworks such as *RE-EXPLORE* is heavily biased toward motifs dominating publicly available reaction databases such as *USPTO* and Reaxys, which are skewed toward medicinal chemistry.

This means *RL*-based methods may fail to generate genuinely novel molecular frameworks or conditions outside the represented chemistry – a form of extrapolation failure difficult to detect from within-distribution metrics. Third, integration of *DRL* with physical experimentation raises practical concerns: unlike simulation environments where failed experiments carry no cost, real flow chemistry platforms impose throughput limits, reagent constraints, and safety boundaries that must be explicitly encoded in the action space and constraint handling of the *RL* agent. These implementation details, critical to real-world deployment, are frequently minimized in published reports focused primarily on algorithmic performance.

4.2. Reactor design and modeling

Computational fluid dynamics (*CFD*) has evolved from a research tool to an indispensable component of modern reactor design and optimization, providing detailed insights into flow patterns, mixing behavior, residence time distributions, temperature gradients, and reaction kinetics within complex reactor geometries (Lodh, 2024). The integration of *CFD* with machine learning accelerates model development and enables real-time optimization capabilities previously unattainable with traditional computational approaches.

CFD simulations optimize stirred-tank reactor configurations by evaluating different impeller designs, agitation speeds, and baffle arrangements to achieve uniform mixing, maximize reaction rates, and minimize stagnant zones that degrade product quality and yield. A critical and frequently underappreciated limitation in *CFD–ML* integration is the turbulence closure problem. Conventional *CFD* relies on Reynolds-Averaged Navier–Stokes (*RANS*) models – most commonly $k-\varepsilon$ and $k-\omega SST$ variants – whose empirical constants were calibrated against canonical flows such as flat plates and pipe flows.

These models are well-documented to perform poorly in geometrically complex reactor environments with strong swirl, recirculation zones, and reactive multiphase interactions. Machine learning offers a physically motivated path to improved closures: data-driven models trained on high-fidelity Direct Numerical Simulation (*DNS*) or Large Eddy Simulation (*LES*) datasets can learn nonlinear stress–strain relationships that classical linear eddy-viscosity models are fundamentally incapable of representing.

However, *ML* turbulence closures trained on specific flow configurations may propagate prediction errors through coupled governing equations in ways that are complex to detect, particularly when deployed on reactor geometries outside their training distribution. Critically, a solution may satisfy numerical convergence criteria while producing physically incorrect species concentration fields and temperature profiles – a failure mode invisible to standard residual-based convergence monitoring.

This underscores the necessity of embedding hard physical constraints – realizability conditions for the Reynolds stress tensor, frame-invariance, and conservation law compliance – directly into any *ML* model augmenting *CFD* closure terms, rather than relying on soft loss penalization. For reactive flow systems – including tubular reformers, fluidized bed reactors, and gas–liquid bubble columns – the coupling between fluid mechanics, heat transfer, mass transfer, and chemical kinetics creates multiphysics complexity that exposes a foundational tension in *CFD–ML* surrogate strategies.

In steam methane reforming reactors, steep radial temperature gradients near tube walls, catalyst activity gradients along the bed, and pressure-dependent thermodynamic equilibrium of simultaneous endothermic reactions create a system

where errors in the predicted flow field propagate nonlinearly into conversion and selectivity predictions. *ML* surrogate models trained on isolated physical subsystems may achieve high individual accuracy while failing substantially when interconnected, because coupling terms introduce input variables absent from any single training distribution.

The most physically defensible approach involves operator learning frameworks – such as *DeepONet* or Fourier Neural Operators – that learn solution mappings for fully coupled *PDE* systems. However, their application to industrially complex reactive *CFD* remains at an early stage and awaits rigorous prospective validation. Scale-up further compounds these challenges: turbulence intensity, interfacial area-to-volume ratios, and axial dispersion all change non-trivially from bench to pilot to industrial scale, meaning *ML* surrogates validated at one scale cannot be reliably transferred to another without retraining on scale-specific simulation data – significantly diminishing the claimed cost savings of the surrogate approach.

Digital twins represent the apex of *CFD* integration into process engineering, creating virtual replicas of physical reactors that synchronize with real-time operational data to enable predictive control and optimization (De Carfort et al., 2024; Lodh, 2024). These cyber-physical systems combine mechanistic *CFD* models with data-driven machine learning algorithms to capture both fundamental physics and empirical relationships learned from operational history.

Samsung Biologics' bioprocess digital twin exemplifies this hybrid modeling approach, integrating advanced *CFD* with mechanistic cell kinetics models and deep learning systems to deliver highly accurate predictions tailored to individual biopharmaceutical products (Lodh, 2024). Unlike purely data-driven digital twins, mechanistic integration ensures physical consistency and enables extrapolation beyond training data, critical capabilities for managing process variations and optimizing novel production campaigns.

The computational demands of *CFD* traditionally constrained real-time applications, limiting digital twin implementations to offline analysis and periodic model updates. Recent methodological advances address this bottleneck through automatic generation of *CFD*-based compartment models that convert detailed three-dimensional flow field solutions into simplified systems of mass balance equations (De Carfort et al., 2024).

This reduced-order modeling approach preserves essential mixing characteristics and transport phenomena while achieving computational speeds faster than real-time, essential for predictive control applications. Validation studies demonstrate that *CFD*-derived compartment models accurately replicate tracer mixing profiles and, when coupled with biokinetic models, correctly predict the impact of substrate gradients on fermentation performance across scales from bench to production (De Carfort et al., 2024).

Artificial intelligence-enhanced *CFD* workflows further accelerate reactor optimization through surrogate modeling and automated design space exploration. Machine learning models trained on *CFD* simulation databases predict key performance indicators such as mixing time, heat transfer coefficients, and conversion efficiency at orders of magnitude faster than full *CFD* solutions, enabling rapid screening of thousands of design variants (Lodh, 2024).

The integration of physics-informed neural networks with *CFD* creates hybrid models that respect conservation laws while learning complex closure relationships from data, addressing the persistent challenge of turbulence modeling in reactive multiphase flows (Benavides-Hernández and Dumeignil, 2024). These advanced capabilities position *AI*-enhanced *CFD* as the foundation for next-generation autonomous reactor design systems that optimize performance while accounting for manufacturing constraints, safety requirements, and economic objectives simultaneously.

5. PLANT-LEVEL AND INDUSTRIAL APPLICATIONS

5.1. Process control and monitoring

Physics-informed neural networks have revolutionized model predictive control by enabling real-time optimization of nonlinear chemical processes while maintaining computational tractability (Patel et al., 2024). The *PINN*-based *MPC* framework integrates governing physical equations into the neural network loss function, creating hybrid models that leverage both approximate mechanistic knowledge and noisy measurement data.

When applied to solid oxide fuel cells, autocatalytic systems, and plug flow reactors, *PINN*-based *MPC* demonstrated superior performance compared to purely data-driven models, particularly in extrapolation scenarios where training data coverage was limited (Patel et al., 2024). The framework achieved real-time feasibility while maintaining prediction accuracy, addressing the long-standing trade-off between model complexity and computational cost that has constrained traditional *MPC* implementations.

Input convex neural networks further advance explicit *MPC* by formulating control optimization as convex problems, dramatically reducing computational burden while ensuring global optimality (Wang et al., 2024b). Unlike conventional neural network-based *MPC* that requires solving nonconvex optimization problems at each time step, *ICNN-MPC* converts the control problem into mixed-integer quadratic programming that can be solved orders of magnitude faster.

This computational efficiency proves critical for fast dynamic processes where millisecond-scale decision making is required. Industrial implementations demonstrate that *LSTM* and artificial neural network-based *MPC* models outperform traditional reduced-order approaches, achieving superior R^2 and *RMSE* metrics while maintaining computational speeds compatible with real-time control (Dan et al., 2025).

A critical assessment of *AI*-based process control deployments reveals that published performance metrics are frequently obtained under conditions substantially more favorable than those in routine industrial operation. Most reported *LSTM-MPC* and *PINN-MPC* benchmarks use simulation environments or laboratory-scale equipment with high sensor density, low noise, and stable disturbances. Real industrial processes involve intermittent sensor faults, actuator saturation, valve hysteresis, and feed composition disturbances that are complex to represent faithfully in training data.

The closed-loop stability guarantees available for linear *MPC* with terminal cost formulations do not extend straightforwardly to neural network-based controllers, whose relationship between network parameters and closed-loop behavior is opaque. Lyapunov-based stability certificates for neural network controllers require restrictive structural assumptions limiting practical applicability.

Perhaps the most underappreciated challenge is process nonstationarity: equipment aging, catalyst deactivation, and seasonal feedstock variation continuously shift the dynamics the *ML* controller was trained to handle, requiring either continuous online retraining – raising safety certification concerns – or periodic batch retraining with careful version management.

Regulatory frameworks for *AI*-based control in safety-critical chemical manufacturing, including COMAH sites in Europe and PSM-covered facilities in the United States, do not yet provide clear guidance on validation and change management requirements for adaptive *ML* controllers, creating a barrier to industrial adoption that technical performance alone cannot overcome.

5.2. Soft sensors and virtual metrology

Virtual metrology represents a critical enabler of Industry 4.0 manufacturing, providing cost-effective alternatives to physical measurements while enabling wafer-to-wafer control and early drift detection (Gentner et al., 2021; He and Wang, 2011). Deep learning architectures, particularly one-dimensional convolutional neural networks combined with bidirectional *LSTM* networks and attention mechanisms, have demonstrated exceptional capability in virtual metrology applications for semiconductor chemical mechanical planarization (*CMP*) (Breidung et al., 2025).

These architectures automatically extract relevant features from raw time-series sensor data, eliminating the need for manual feature engineering while achieving prediction errors below 1% for material removal rate estimation. The incorporation of attention mechanisms enables the model to focus on critical temporal patterns that most strongly influence product quality.

Hybrid virtual metrology frameworks that integrate physics-based models with machine learning achieve robust predictions across equipment variations and process conditions (Deivendran et al., 2025; Rahman et al., 2024). For *CMP* applications, physics-based models estimate critical but unmeasurable parameters such as slurry temperature and mean abrasive particle size from available sensor data, which then serve as inputs to *ML* soft sensors for material removal rate prediction.

This hybrid approach ensures physical consistency while leveraging *ML*'s capability to capture complex empirical relationships not captured by simplified mechanistic models. Domain adaptation techniques enable virtual metrology models trained on one equipment set to transfer effectively to identical-in-design systems with different data distributions, addressing the critical challenge of model scalability in multi-equipment manufacturing environments (Breidung et al., 2025) (Table 3).

The interpretability of virtual metrology models has emerged as a critical requirement for industrial acceptance and regulatory compliance. *SHAP* analysis applied to XGBoost and random forest models reveals that polishing time and carrier rotation speed are the most influential features for *CMP* non-uniformity prediction, with spatial material removal patterns exhibiting strong dependencies on local process conditions (Deivendran et al., 2025).

Table 3. Virtual metrology and soft sensor applications in industrial processes.

Application Domain	ML Architecture	Key Performance Metric	Industrial Impact	Reference
CMP Material Removal Rate	1*DCNN-BiLSTM* with Attention	$MAE < 1\%$	Wafer-to-wafer control	Breidung et al., 2025
Semiconductor *VM* (Multi-process)	Deep Learning Domain Adaptation	Model transfer	Scalable *VM* deployment	Breidung et al., 2025
Bioprocess Control	*LSTM*-based *MPC*	$R^2 > 0.90$	Maximizes product titer	Dan et al., 2025
Sugar Crystallization	*LSTM* Soft Sensor	2.12% residence reduction	Energy and CO_2 savings	Boskabadi et al., 2025
Chemical Vapor Deposition	*RBF* Neural Network	$MAPE = 0.34\%$, Max error $= 1.15\%$	Early drift detection	He and Wang, 2011
Plasma Etch Process	*RNN* with *POD*	Accurate profile prediction	Cycle time reduction	Xiao et al., 2021

This interpretability facilitates root cause analysis when quality deviations occur and guides process engineers in making informed adjustments to operational parameters. Advanced virtual sensor frameworks for batch crystallization processes demonstrate that *LSTM*-based soft sensors can reduce mean residence time by 2.12%, consequently decreasing energy consumption, CO_2 footprint, and increasing production capacity (Boskabadi et al., 2025).

5.3. Fault detection and predictive maintenance

AI-powered predictive maintenance has emerged as a high-value, low-risk application domain where chemical engineering companies achieve substantial return on investment (Xiao et al., 2021). T^2-*LSTM* frameworks for motor fault detection in chemical plants achieve 98% agreement between predicted and actual anomalies over multi-month operational periods, demonstrating practical viability for critical rotating equipment (Wang, 2024).

The Hotelling T^2 index calculated from triaxial vibration measurements provides a comprehensive health indicator, while *LSTM* trend modeling establishes adaptive warning thresholds that account for gradual equipment degradation patterns. This approach enables early intervention before catastrophic failures occur, preventing costly unplanned shutdowns and safety incidents.

Gaussian process regression with automatic kernel selection provides an advanced framework for fouling prediction in heat exchangers and distillation columns, enabling transition from reactive to prescriptive maintenance strategies (Negri et al., 2025). The *P-F* curve framework illustrates how predictive maintenance progressively anticipates failure events, with *AI*-based approaches detecting anomalies weeks before mechanical failure would manifest through traditional monitoring.

Companies like BASF and Dow report that *AI*-driven predictive maintenance for pumps, compressors, and heat exchangers detects minute vibration pattern anomalies weeks in advance, resulting in substantial cost savings and avoidance of production shutdowns (Negri et al., 2025).

Explainable *AI* techniques, particularly *SHAP* applied to adversarial autoencoders, enable transparent fault diagnosis in complex chemical processes (Sanjuan Gómez, 2021). The framework generates health indicators that capture overall plant condition, with *SHAP* attributing any significant fluctuation to specific process variables and fault types.

When tested on continuous stirred-tank reactors and the Tennessee Eastman Process, the explainable *AI* framework diagnosed catalyst decay, heat transfer fouling, feed disturbances, sensor faults, and valve stiction more accurately than previous methods. The transparency provided by explainable *AI* proves essential for building operator trust and meeting regulatory requirements in safety-critical applications.

6. SUSTAINABILITY AND ENVIRONMENTAL APPLICATIONS

Machine learning has emerged as a critical enabler for addressing sustainability imperatives in chemical engineering, particularly in carbon capture, waste valorization, and circular economy implementation ((Manikandan et al., 2025)). The integration of high-throughput computational screening with data-driven modeling, termed the *SMART* (Scalable Modeling, Artificial Intelligence, and Rapid Theoretical calculations) approach, combines expertise from chemical, materials, environmental, and data science to advance carbon capture technologies (Lei et al., 2023).

Multi-scale computational design frameworks employing genetic algorithms and machine learning identify metal-organic frameworks optimized for postcombustion CO_2 capture, with process-level modeling predicting performance in modified Skarstrom cycles (Deng and Sarkisov, 2024). These frameworks discover materials exhibiting high CO_2/N_2 selectivity through either size-exclusion mechanisms in small pores or multiple interaction sites in larger pores.

AI-driven optimization of carbon capture processes delivers substantial techno-economic and environmental benefits critical for scaling technologies to meet net-zero emissions targets. Machine learning models reduce capital and operational expenditures by optimizing process parameters and accelerating sorbent material discovery, addressing cost barriers that have historically impeded widespread adoption (Manikandan et al., 2025; Smart et al., 2025).

The Process-Informed design of tailor-made Sorbent Materials tool exemplifies this approach, using simulations and machine learning to identify cost-effective, sustainable material-process combinations while simultaneously evaluating economic and environmental impacts during the design phase rather than as post-hoc considerations. Artificial intelligence integration into wastewater treatment carbon capture systems demonstrates 97% accuracy in predicting CO_2 emissions and 95% accuracy for H_2S emissions, enabling real-time process optimization that reduces greenhouse gas emissions while recovering valuable resources.

Beyond carbon capture, machine learning is being applied across a wider spectrum of environmental challenges in chemical engineering, though the depth of critical validation varies greatly across application areas. In wastewater treatment, *ML*-based models have been applied to predict effluent quality, optimize coagulant dosing, and detect process upsets in activated sludge systems. Gradient boosting and *LSTM* architectures have demonstrated prediction accuracy above 90% for biochemical oxygen demand (*BOD*) and chemical oxygen demand (*COD*) under controlled experimental conditions.

However, a recurring weakness in this literature is the short evaluation boxes used for model validation: performance reported over weeks or months fails to capture seasonal feed composition shifts, microbial community evolution, and equipment aging effects that determine long-term operational reli-

ability. For life cycle assessment (*LCA*) and techno-economic analysis (*TEA*), *ML* models are increasingly used to fill data gaps and accelerate scenario screening.

Graph neural network-based *LCA* frameworks can propagate uncertainty across thousands of process configurations in minutes. Nevertheless, the quality of *ML*-accelerated *LCA* depends entirely on the completeness and geographic representativeness of the underlying inventory databases, which remain highly uneven across industrial sectors. The risk of perpetuating or amplifying existing data biases in sustainability assessments through *ML* automation deserves explicit attention from the research community.

The circular economy represents an emerging and particularly challenging application domain for *AI* in chemical engineering. Predicting the recyclability of complex polymer blends, optimizing chemical depolymerization pathways for mixed plastic waste, and designing processes for critical metal recovery from electronic waste all require *ML* models capable of handling highly heterogeneous input streams with variable composition, contamination, and degradation states – conditions fundamentally different from the homogeneous, well-characterized feedstocks on which most published models are trained.

Generative *AI* and reinforcement learning show conceptual promise for designing recycling-compatible polymer architectures and optimizing separation sequences for mixed waste streams, but prospective experimental validation of computationally generated recommendations remains rare. This gap between in silico promise and demonstrated experimental utility is the central unresolved challenge for *AI* in circular economy applications. Honest reporting of this gap is essential if the field is to channel resources productively toward tractable near-term opportunities rather than aspirational applications requiring foundational advances that have not yet been achieved.

7. PHYSICS-INFORMED AND HYBRID APPROACHES

Physics-informed neural networks (*PINNs*) address the fundamental challenge of plant-model mismatch in process systems by leveraging first-principles knowledge alongside data-driven techniques (Benavides-Hernández and Dumeignil, 2024; Moayedi et al., 2024). *PINNs* respect physical characteristics while yielding accurate dynamic models from process data, outperforming purely data-driven approaches like recurrent neural networks in predictive capability, particularly for extrapolation beyond training domains.

Applications to continuously stirred tank reactors and liquid-liquid separators demonstrate that *PINNs* infer immeasurable states with reasonable accuracy even when constitutive equations are unknown or incomplete (Moayedi et al., 2024; Velioglu et al., 2025). The decoupling-coupling training framework represents a methodological advance for modeling chemical reactor systems with multiphysics coupling (Wu et al., 2024). This approach decomposes complex physical domains into subdomains of fluid flow, heat transfer, and mass transfer combined with reaction kinetics, with each subdomain represented by specialized neural networks. Decoupling pre-training provides coarse but reasonable parameter distributions for initializing sub-networks before multiphysics coupling training, addressing the optimization challenges that arise when *PINNs* struggle with multiple coupled physical phenomena.

Physics-informed recurrent neural networks deployed with hyperparameter optimization enable modeling of dynamic processes by embedding physics through multi-objective loss functions or hybrid cell architectures performing Euler discretization (Asrav et al., 2023). These approaches achieve improved test performance and more robust architectures compared to purely data-driven alternatives, demonstrating particular value in the small-data regime common to chemical engineering applications.

Despite their theoretical appeal, physics-informed neural networks face a set of practical challenges that are frequently underemphasized in the literature. The primary difficulty lies in the formulation and weighting of the composite loss function, which must simultaneously minimize data mismatch, satisfy governing differential equations across the domain interior, and enforce boundary and initial conditions.

The relative weights assigned to these loss terms profoundly affect convergence behavior and solution quality, yet no principled, physics-agnostic method for selecting these weights currently exists. The *PINN* loss landscape is known to exhibit pathological behavior including saddle points, flat regions, and competing gradient magnitudes that cause training to stall or converge to physically spurious solutions.

For stiff chemical kinetics – where species concentrations evolve on timescales spanning many orders of magnitude, as in combustion or enzymatic reaction networks – standard gradient descent optimizers routinely fail to converge to physically correct solutions without problem-specific architectural modifications. Furthermore, published *PINN* validation studies in chemical engineering predominantly use forward problems with known analytical or numerical solutions as ground truth.

Inverse problems – inferring model parameters or unmeasured states from limited sensor data under realistic noise – represent the practically critical application, yet robust benchmarking of *PINN* performance on ill-posed inverse problems with proper uncertainty quantification remains sparse. Hybrid modeling – combining mechanistic first-principles models with data-driven components – is widely advocated as the pragmatic middle path between interpretable but inflexible white-box models and accurate but opaque black-box models.

The serial hybrid architecture, in which a mechanistic model generates primary state estimates subsequently corrected by an *ML* residual model, is particularly suited to chemical engineering where mass and energy balances are known but kinetic parameters are uncertain. This approach has been applied to fed-batch bioreactor modeling, distillation col-

umn optimization, and heat exchanger fouling prediction with demonstrated improvements in extrapolation accuracy.

The parallel hybrid architecture, in which mechanistic and *ML* components operate simultaneously and outputs are combined by a learned weighting function, offers greater flexibility but risks mode collapse where one component dominates. A critical and underreported limitation of both architectures is the error attribution problem: when a hybrid model fails in deployment, diagnosing whether the failure originated in the mechanistic component (wrong physical assumptions), the data-driven component (distribution shift), or the coupling mechanism (incorrect weighting) is non-trivial and often requires experiments specifically designed to isolate each component – a requirement rarely met in industrial deployment scenarios (Asrav et al., 2023; Wu et al., 2024).

8. EMERGING FRONTIERS

8.1. Explainable AI and interpretability

Explainable artificial intelligence (*AI*) has transitioned from academic curiosity to operational necessity in chemical engineering, with *SHAP* analysis increasing operational acceptance by 52% in safety-critical settings by visualizing neural network decision pathways (Romagnoli et al., 2024). Model-agnostic post-hoc interpretability methods enable identification of dominant material descriptors and feature contributions, building trust in *AI* predictions for high-stakes applications (Oviedo et al., 2022).

The *XpertAI* framework integrates *SHAP* with large language models to generate accessible natural language explanations of structure-property relationships, addressing the limitation that traditional *XAI* methods target technically oriented users rather than domain experts (Wellawatte and Schwaller, 2025). Applications to molecular property prediction, catalysis optimization, and materials design demonstrate that *SHAP* values reveal physically meaningful contributions.

For instance, *SHAP* analysis of *Pt* monolayer core-shell catalysts for oxygen reduction reactions voids the critical role of adsorbate resonance energies in chemical bonding, providing interpretable pathways for rational catalyst design (Omidvar et al., 2024). Regulatory agencies increasingly mandate transparency and accountability in *AI* systems supporting pharmaceutical development and chemical manufacturing.

The *FDA*'s 2025 draft guidance emphasizes traceable, context-aware validation throughout *AI* pipelines, positioning explainability not as luxury but prerequisite for deployment (Lavecchia, 2025). Hybrid approaches combining physics-based models with machine learning reduce prediction errors by 38–52% in catalysis simulations compared to pure data-driven methods while enhancing interpretability through incorporation of domain knowledge (Romagnoli et al., 2024).

This synergy proves particularly valuable in safety-critical reactor control and process optimization where understanding decision rationale enables rapid troubleshooting and regulatory compliance.

8.2. Digital twins and autonomous systems

Digital twin technology represents the convergence of mechanistic modeling, computational fluid dynamics (*CFD*), and machine learning to create virtual replicas that synchronize with real-time operational data (Lodh, 2024). Unlike purely data-driven surrogates, mechanistic integration ensures physical consistency and enables extrapolation beyond training data, essential capabilities for managing process variations and optimizing novel production campaigns.

Bioprocess digital twins demonstrate this integration by combining *CFD* with cell kinetics models and deep learning to deliver product-specific predictions, facilitating predictive control that maximizes product titer while respecting equipment constraints.

Despite transformative potential, *AI*/*ML* integration into chemical engineering confronts critical challenges that must be systematically addressed. Data quality, availability, and standardization remain persistent obstacles, with industrial plants collecting 12–15 sensor data types yet achieving interoperability in fewer than 40% of cases (Romagnoli et al., 2024). This fragmentation necessitates adaptive data pipelines reconciling vastly different sampling rates and formats.

More than half of industrial knowledge resides in paper records or experienced operators' tacit knowledge, requiring natural language processing and augmented reality approaches to capture decision-making heuristics. Model interpretability constitutes a fundamental concern where absence of unified validation protocols hinders industrial adoption (Dobbelaere et al., 2021; Romagnoli et al., 2024).

Industry consortia develop benchmark datasets across three dimensions, accuracy under variability, failure detection capability, and compatibility with existing control systems, supporting Safe-and-Sustainable-by-Design initiatives. The computational demands of sophisticated models, while diminishing with hardware advances, present barriers for real-time control requiring millisecond-scale decisions.

Integration with legacy infrastructure demands substantial capital investment and organizational change management, with successful implementation depending critically on collaboration between machine learning experts and domain practitioners. The trajectory of *AI*/*ML* in chemical engineering points toward several transformative directions.

Multi-modal learning frameworks integrating spectroscopic data, process sensor measurements, and mechanistic knowledge will enable more robust predictions across operational regimes. Transfer learning and few-shot learning approaches will extend model applicability to data-scarce applications, particularly for specialized products and emerging processes.

Quantum machine learning, though nascent, promises to revolutionize molecular property prediction and reaction pathway exploration by natively representing quantum mechanical phenomena. Human-*AI* collaboration frameworks will redefine

engineering practice, with *AI* systems augmenting rather than replacing human expertise through explainable recommendations and interactive optimization.

Educational transformation becomes imperative, requiring curricula that integrate data science, machine learning, and traditional chemical engineering principles while emphasizing critical evaluation of model assumptions and limitations. Industry-academia partnerships will accelerate deployment through co-development of validation frameworks, benchmark datasets, and best practice guidelines that balance innovation with operational reliability and regulatory compliance.

9. CONCLUSIONS

The integration of artificial intelligence (*AI*) and machine learning (*ML*) into chemical engineering represents not merely incremental advancement but fundamental reconceptualization of practice spanning molecular design through industrial operations. Contemporary methodologies – from physics-informed neural networks to generative *AI* – demonstrate unprecedented capability in navigating complex multi-scale phenomena while maintaining computational tractability and physical interpretability.

Applications across catalyst discovery, drug development, process control, and sustainability demonstrate transformative impact with quantifiable performance improvements including 71% fewer experimental iterations in reaction optimization, 98% accuracy in predictive maintenance, and substantial reductions in carbon emissions through intelligent process management. Critical challenges persist, demanding concerted efforts in data infrastructure development, interpretability enhancement, and validation protocol standardization.

The path forward requires interdisciplinary collaboration uniting chemical engineering domain expertise with computational intelligence, guided by principles of transparency, reproducibility, and responsible innovation. As the discipline navigates Industry 4.0 transformation toward autonomous, sustainable manufacturing, *AI*/*ML* emerges not as optional enhancement but essential infrastructure enabling the chemical industry to address 21st century imperatives of environmental stewardship, economic competitiveness, and societal benefit.

Success will be measured not only by predictive accuracy but by practical deployment creating measurable value while maintaining safety, sustainability, and operational excellence that define chemical engineering's enduring commitment to serving society. Several overarching observations emerge from a critical synthesis of the literature reviewed here.

First, the field would benefit substantially from a cultural shift toward prospective validation: studies that deploy *AI* models in genuine forward-prediction mode, without access to outcome data during model development, and report performance on truly held-out prospective datasets. The current dominance of retrospective cross-validated benchmarks provides an optimistic but potentially misleading picture of how *AI* systems will perform when confronted with novel process conditions, equipment states, and feedstock compositions not represented in historical data.

Second, the chemical engineering *AI* community needs domain-specific benchmarking standards analogous to those in computer vision (ImageNet) and natural language processing (GLUE). Without agreed benchmark tasks, standardized datasets, and common evaluation protocols, comparing methodologies across groups is unreliable, and apparent progress may partly reflect differences in evaluation rigor rather than genuine advances.

Third, the translation pathway from published algorithm to industrial deployment requires attention to software engineering quality, cybersecurity, operator interface design, and regulatory compliance – dimensions essentially absent from the academic literature but decisive for whether a promising model ever creates real-world value.

Looking forward, the most transformative advances are likely to emerge not from incremental improvements to individual architectures but from principled integration of chemical engineering domain knowledge into learning system design. This means embedding stoichiometric constraints, thermodynamic feasibility bounds, and transport phenomena directly into model structure; developing uncertainty-aware models that reliably distinguish confident in-distribution predictions from speculative extrapolations; and creating continual learning frameworks that adapt to evolving process conditions without catastrophic forgetting of previously validated behavior.

The long-term vision is of autonomous chemical systems combining reinforcement learning optimization, mechanistic model consistency, and explainable *AI* transparency into platforms that genuinely augment engineering practice. Realizing this vision demands that the community resist overstating near-term capabilities and instead invest in the foundational work of rigorous validation, honest benchmarking, and principled uncertainty quantification – the foundations that will ultimately determine whether *AI* becomes reliable infrastructure for chemical manufacturing or remains a collection of promising but fragile demonstrations.

ACKNOWLEDGEMENTS

The manuscript underwent editing by Claude. The author subsequently reviewed the content in its entirety and approved the final manuscript.

REFERENCES

Al Sharah A., Owida H.A., Alnaimat F., Hassan M., Abuowaida S., Alhaj M., Sharadqeh A., 2024. Application of machine learning in chemical engineering: outlook and perspectives. *IAES Int. J. Artif. Intell.*, 13, 619–630. DOI: 10.11591/ijai.v13.i1.pp619-630.

Asrav T., Aydin E., 2023. Physics-informed recurrent neural networks and hyper-parameter optimization for dynamic process systems. *Comput. Chem. Eng.*, 173, 108195. DOI: 10.1016/j.compchemeng.2023.108195.

Benavides-Hernández J., Dumeignil F., 2024. From characterization to discovery: artificial intelligence, machine learning and high-throughput experiments for heterogeneous catalyst design. *ACS Catal.*, 14, 11749–11779. DOI: 10.1021/acscatal.3c06293.

Boskabadi M.R., Murugaiah M., Nielsen T.R., Sivaram A., Sin G., Mansouri S.S., 2025. Virtual sensor for sustainable large-scale process monitoring. *Ind. Eng. Chem. Res.*, 64, 3902–3917. DOI: 10.1021/acs.iecr.4c03342.

Bozal-Ginesta C., Pablo-García S., Choi C., Tarancón A., Aspuru-Guzik A., 2025. Developing machine learning for heterogeneous catalysis with experimental and computational data. *Nat. Rev. Chem.*, 9, 601–616. DOI: 10.1038/s41570-025-00740-4.

Breidung M., Rothe T., Lauff A., Thieme P., Langer J., Günther M., Kuhn H., 2025. Process data-driven machine learning for non-uniformity prediction and virtual metrology in chemical mechanical planarization. *J. Intell. Manuf.* DOI: 10.1007/s10845-025-02753-8.

Burns J.A., Green W.H., 2025. Generalizable, fast, and accurate DeepQSPR with fastprop. *J. Cheminf.*, 17, arXiv:2404.02058v5. DOI: 10.48550/arXiv.2404.02058.

Cao P., Chen J., Chen G., Qi Z., Song Z., 2024. A critical methodological revisit on group-contribution based property prediction of ionic liquids with machine learning. *Chem. Eng. Sci.,* 298, 120395. DOI: 10.1016/j.ces.2024.120395.

Cao X., Zhang Y., Sun Z., Yin H., Feng Y., 2026. Machine learning in polymer science: A new lens for physical and chemical exploration. *Prog. Mater. Sci.*, 156, 101544. DOI: 10.1016/j.pmatsci.2025.101544.

Chinta S., Rengaswamy R., 2019. Machine learning derived quantitative structure property relationship (QSPR) to predict drug solubility in binary solvent systems. *Ind. Eng. Chem. Res.*, 58, 3082–3092. DOI: 10.1021/acs.iecr.8b04584.

Dan A., Liu B., Patil U., Manuraj B.N.M., Gandhi R., Buchel J., Chundawat S.P.S., Guo W., Ramachandran R., 2025. Machine learning model-based design and model predictive control of a bioreactor for the improved production of mammalian cell-based bio-therapeutics. *Control Eng. Pract.*, 156, 106198. DOI: 10.1016/j.conengprac.2024.106198.

Dangayach R., Jeong N., Demirel E., Uzal N., Fung V., Chen Y., 2025. Machine learning-aided inverse design and discovery of novel polymeric materials for membrane separation. *Environ. Sci. Technol.,* 59, 993–1012. DOI: 10.1021/acs.est.4c08298.

De Carfort J.L.N., Pinto T., Krühne U., 2024. An automatic method for generation of CFD-based 3D compartment models: towards real-time mixing simulations. *Bioengineering*, 11, 169. DOI: 10.3390/bioengineering11020169.

Deivendran B., Masampally V.S., Nadimpalli N.R.V., Runkana V., 2025. Virtual metrology for chemical mechanical planarization of semiconductor wafers. *J. Intell. Manuf.*, 36, 1923–1942. DOI: 10.1007/s10845-024-02335-0.

Deng Z., Sarkisov L., 2024. Multi-scale computational design of metal–organic frameworks for carbon capture using machine learning and multi-objective optimization. *Chem. Mater.*, 36, 9806–9821. DOI: 10.1021/acs.chemmater.4c01969.

Dobbelaere M.R., Plehiers P.P., van de Vijver R., Stevens C.V., van Geem K.M., 2021. Machine learning in chemical engineering: strengths, weaknesses, opportunities, and threats. *Engineering*, 7, 1201–1211. DOI: 10.1016/j.eng.2021.03.019.

Eraqi B.A., Khizbullin D., Nagaraja S.S., Sarathy S.M., 2025. Molecular property prediction in the ultra-low data regime. *Commun. Chem.*, 8, 201. DOI: 10.1038/s42004-025-01592-1.

Gao L., Lin J., Wang L., Du L., 2024. Machine learning-assisted design of advanced polymeric materials. *Acc. Mater. Res.*, 5, 571–584. DOI: 10.1021/accountsmr.3c00288.

Gentner N., Carletti M., Kyek A., Susto G.A., Yang Y., 2021. DBAM: Making Virtual Metrology/Soft sensing with time series data scalable through deep learning. *Control Eng. Pract.*, 116, 104914. DOI: 10.1016/j.conengprac.2021.104914.

Georgia Institute of Technology, 2024. Using AI to find the polymers of the future. *ScienceDaily*, 8 November 2024. Available at: https://www.sciencedaily.com/releases/2024/08/240819185140.htm

Goldsmith B.R., Esterhuizen J., Liu J.-X., Bartel C.J., Sutton C., 2018. Machine learning for heterogeneous catalyst design and discovery. *AIChE J.*, 64, 2311–2323. DOI: 10.1002/aic.16198.

He Q.P., Wang J., 2011. Statistics pattern analysis: a new process monitoring framework and its application to semiconductor batch processes. *AIChE J.*, 57, 107–121. DOI: 10.1002/aic.12247.

Heid E., Greenman K.P., Chung Y., Li S.-C., Graff D.E., Vermeire F.H., Wu H., Green W.H., McGill C.J., 2024. Chemprop: a machine learning package for chemical property prediction. *J. Chem. Inf. Model.*, 64, 9–17. DOI: 10.1021/acs.jcim.3c01250.

Hoque A., Surve M., Kalyanakrishnan S., Sunoj R.B., 2024. Reinforcement learning for improving chemical reaction performance. *J. Am. Chem. Soc.*, 146, 28250–28267. DOI: 10.1021/jacs.4c08866.

Kim J., Chang W., Ji H., Joung I.S., 2024. Quantum-informed molecular representation learning enhancing ADMET property prediction. *J. Chem. Inf. Model.*, 64, 5028–5040. DOI: 10.1021/acs.jcim.4c00772.

Lan T., Wang H., An Q., 2024. Enabling high throughput deep reinforcement learning with first principles to investigate catalytic reaction mechanisms. *Nat. Commun.*, 15, 6281. DOI: 10.1038/s41467-024-50531-6.

Lavecchia A., 2025. Explainable artificial intelligence in drug discovery: bridging predictive power and mechanistic insight. *WIREs Comput. Mol. Sci.*, 15, e70049. DOI: 10.1002/wcms.70049.

Lei Q., Li L., Chen H., Wang X., 2023. Emerging directions for carbon capture technologies: a synergy of high-throughput theoretical calculations and machine learning. *Environ. Sci. Technol.*, 57, 17189–17200. DOI: 10.1021/acs.est.3c05305.

Lodh B.K., 2024. The transformative role of Computational Fluid Dynamics (CFD) in chemical engineering. *Open J. Chem.*, 10, 1–3. DOI: 10.17352/ojc.000033.

Manikandan S., Kaviya R.S, Shreeharan D.H, Subbaiya R., Vickram S., Karmegam N., Kim W., Govarthanan M., 2025. Artificial intelligence-driven sustainability: enhancing carbon capture for sustainable development goals – a review. *Sustainable Dev.*, 33, 2004–2029. DOI: 10.1002/sd.3222.

Mathur A., Dave S., Dave S., 2021. Predicting chemical reactions with artificial intelligence and machine learning. In: Purohit S., Singh Jat D., Poonia R., Kumar S., Hiranwal S. (Eds.), *Proceedings of International Conference on Communication and Computational Technologies. Algorithms for Intelligent Systems*. Springer, Singapore, 445–458. DOI: 10.1007/978-981-15-5077-5_36.

Moayedi F., Chandrasekar A., Rasmussen S., Sarna S., Corbett B., Mhaskar P., 2024. Physics-informed neural networks for process systems: handling plant-model mismatch. *Ind. Eng. Chem. Res.*, 63, 13650–13659. DOI: 10.1021/acs.iecr.4c00690.

Mondal S., 2024. Exploring the synergistic potential of artificial intelligence and machine learning in chemistry. *Current Scientia*, 27, 68–85. DOI: 10.31357/vjs.v27i02.7839.

Mou T., Pillai H.S., Wang S., Wan M., Han X., Schweitzer N.M., Che F., Xin H., 2023. Bridging the complexity gap in computational heterogeneous catalysis with machine learning. *Nat. Catal.*, 6, 122–136. DOI: 10.1038/s41929-023-00911-w.

Negri F., Galeazzi A., Gallo F., Manenti F., 2025. Reshaping industrial maintenance with machine learning: fouling control using optimized Gaussian process regression. *Ind. Eng. Chem. Res.*, 64, 6633–6654. DOI: 10.1021/acs.iecr.4c04550.

Niazi S.K., 2025. Artificial intelligence in small-molecule drug discovery: a critical review of methods, applications, and real-world outcomes. *Pharmaceuticals*, 18, 1271. DOI: 10.3390/ph18091271.

Niu Z., Xiao X., Wu W., Cai Q., Jiang Y., Jin W., Wang M., Yang G., Kong L., Jin X., Yang G., Chen H., 2024. PharmaBench: enhancing ADMET benchmarks with large language models. *Sci. Data*, 11, 985. DOI: 10.1038/s41597-024-03793-0.

Omidvar N., Wang S.-H., Huang Y., Pillai H.S., Athawale A., Wang S., Achenie L.E.K., Xin H., 2024. Explainable AI for optimizing oxygen reduction on Pt monolayer core–shell catalysts. *Electrochem. Sci. Adv.*, 4, e202300028. DOI: 10.1002/elsa.202300028.

Omranpour A., Elsner J., Lausch K.N., Behler J., 2025. Machine learning potentials for heterogeneous catalysis. *ACS Catal.*, 15, 1616–1634. DOI: 10.1021/acscatal.4c06717.

Oviedo F., Ferres J.L., Buonassisi T., Butler K.T., 2022. Interpretable and explainable machine learning for materials science and chemistry. *Acc. Mater. Res.*, 3, 597–607. DOI: 10.1021/accountsmr.1c00244.

Patel R., Bhartiya S., Gudi R., 2024. Model predictive control using physics-informed neural networks for process systems. *IFAC-PapersOnLine*, 58, 775–780. DOI: 10.1016/j.ifacol.2024.08.431.

Pathan I., Raza A., Sahu A., Joshi M., Sahu Y., Patil Y., Raza M.A., 2025. Revolutionizing pharmacology: AI-powered approaches in molecular modeling and ADMET prediction. *Med. Drug Discovery*, 28, 100223. DOI: 10.1016/j.medidd.2025.100223.

Rahman A.U., Han X., Jia X., 2024. Enhanced data-driven virtual metrology on chemical mechanical planarization process using dual linear Kalman filter. *Proceedings of the ASME 2024 19th International Manufacturing Science and Engineering Conference*. Knoxville, Tennessee, USA. June 17–21, 2024. V002T05A009. ASME, 1–8. DOI: 10.1115/MSEC2024-125308.

Romagnoli J.A., Briceño-Mena L., Manee V., 2024. *AI in Chemical Engineering: Unlocking the power within data*. CRC Press. DOI: 10.1201/9781003455905.

Sanjuan Gómez A., 2021. *Fault diagnosis and fault-tolerant control of nonlinear dynamic systems using artificial intelligence techniques*. Doctoral dissertation, Departament d'Enginyeria de Sistemes, Automàtica i Informàtica Industrial, Universitat Politècnica de Catalunya (UPC). DOI: 10.5821/dissertation-2117-420260.

Smart E.E., Olayiwola D.E., Okwor U.D., Babatunde J., 2025. Revolutionizing carbon capture efficiency: a comprehensive review of AI-driven optimization strategies for CO2 capture and storage processes. *Int. J. Sci. Technol. Res. Arch.*, 9, 18–43. DOI: 10.53771/ijstra.2025.9.1.0043.

Swanson K., Walther P., Leitz J., Mukherjee S., Wu J.C., Shivnaraine R.V., Zou J., 2024. ADMET-AI: a machine learning ADMET platform for evaluation of large-scale chemical libraries. *Bioinformatics*, 40, btae416. DOI: 10.1093/bioinformatics/btae416.

Terstappen G.C., Reggiani A., 2001. *In silico* research in drug discovery. *Trends Pharmacol. Sci.*, 22, 23–26. DOI: 10.1016/S0165-6147(00)01584-4.

Velioglu M., Zhai S., Rupprecht S., Mitsos A., Jupke A., Dahmen M., 2025. Physics-informed neural networks for dynamic process operations with limited physical knowledge and data. *Comput. Chem. Eng.*, 192, 108899. DOI: 10.1016/j.compchemeng.2024.108899.

Venkataraman M., Rao G.C., Madavareddi J.K., Maddi S.R., 2025. Leveraging machine learning models in evaluating ADMET properties for drug discovery and development. *ADMET and DMPK*, 13, 2772. DOI: 10.5599/admet.2772.

Vora L.K., Gholap A.D., Jetha K., Thakur R.R.S., Solanki H.K., Chavda V.P., 2023. Artificial intelligence in pharmaceutical technology and drug delivery design. *Pharmaceutics*, 15, 1916. DOI: 10.3390/pharmaceutics15071916.

Wang C.-C., 2024. T^2-LSTM-based AI system for early detection of motor failure in chemical plants. *Mathematics*, 12, 2652. DOI: 10.3390/math12172652.

Wang R., Fu T., Yang Y.-J., Song X., Wang X.-L., Wang Y.-Z., 2024a. Scientific discovery framework accelerating advanced polymeric materials design. *Research*, 7, 0406. DOI: 10.34133/research.0406.

Wang W., Zhang H., Wang Y., Tian Y., Wu Z., 2024b. Fast explicit machine learning-based model predictive control of nonlinear processes using input convex neural networks. *Ind. Eng. Chem. Res.*, 63, 17279–17293. DOI: 10.1021/acs.iecr.4c02257.

Wellawatte G.P., Schwaller P., 2025. Human interpretable structure-property relationships in chemistry using explainable machine learning and large language models. *Commun. Chem.*, 8, 11. DOI: 10.1038/s42004-024-01393-y.

Wenzel J., Matter H., Schmidt F., 2019. Predictive multitask deep neural network models for ADME-Tox properties: learning from large data sets. *J. Chem. Inf. Model.*, 59, 1253–1268. DOI: 10.1021/acs.jcim.8b00785.

Wieder O., Kohlbacher S., Kuenemann M., Garon A., Ducrot P., Seidel T., Langer T., 2020. A compact review of molecular property prediction with graph neural networks. *Drug Discovery Today: Technol.*, 37, 1–12. DOI: 10.1016/j.ddtec.2020.11.009.

Wu M., Di Caprio U., Vermeire F., Hellinckx P., Braeken L., Waldherr S., Leblebici M.E., 2023. An artificial intelligence course for chemical engineers. *Educ. Chem. Eng.*, 45, 141–150. DOI: 10.1016/J.ECE.2023.09.004.

Wu S., Kondo Y., Kakimoto M.-A., Yang B., Yamada H., Kuwajima I., Lambard G., Hongo K., Xu Y., Shiomi J., Schick C., Morikawa J., Yoshida R., 2019. Machine-learning-assisted discovery of polymers with high thermal conductivity using a molecular design algorithm. *npj Comput. Mater.*, 5, 66. DOI: 10.1038/s41524-019-0203-2.

Wu Z., Li M., He C., Zhang B., Ren J., Yu H., Chen Q., 2024. Physics-informed learning of chemical reactor systems using decoupling-coupling training framework. *AIChE J.*, 70, e18436. DOI: 10.1002/aic.18436.

Xiao T., Wu Z., Christofides P.D., Armaou A., Ni D., 2021. Recurrent neural-network-based model predictive control of a plasma etch process. *Ind. Eng. Chem. Res.*, 61, 638–652. DOI: 10.1021/acs.iecr.1c04251.

Xin H., Mou T., Pillai H.S., Wang S.-H., Huang Y., 2023. Interpretable machine learning for catalytic materials design toward sustainability. *Acc. Mater. Res.*, 5, 22–34. DOI: 10.1021/accountsmr.3c00131.

Yan Y., Borhani T.N., Clough P.T., 2020. Chapter 14: Machine Learning Applications in Chemical Engineering, In: Cartwright H.M. (Ed.), *Machine learning in chemistry: The impact of artificial intelligence*. The Royal Society of Chemistry, 340–371. DOI: 10.1039/9781839160233-00340.

Yang K., Swanson K., Jin W., Coley C., Eiden P., Gao H., Guzman-Perez A., Hopper T., Kelley B., Mathea M., Palmer A., 2019. Analyzing learned molecular representations for property prediction. *J. Chem. Inf. Model.*, 59, 3370–3388. DOI: 10.1021/acs.jcim.9b00237.

Yue T, He J, Li Y. Machine-Learning-assisted molecular design of innovative polymers. 2025. *Acc. Mater. Res.*, 6, 1033–1045. DOI: 10.1021/accountsmr.5c00151.

Zhang S., Yan Z., Huang Y., Liu L., He D., Wang W., Fang X., Zhang X., Wang F., Wu H., Wang H., 2022. HelixADMET: a robust and endpoint extensible ADMET system incorporating self-supervised knowledge transfer. *Bioinformatics*, 38, 3444–3453. DOI: 10.1093/bioinformatics/btac342.

Zhou Z., Li X., Zare R.N., 2017. Optimizing chemical reactions with deep reinforcement learning. *ACS Cent. Sci.*, 3, 1337–1344. DOI: 10.1021/acscentsci.7b00492.